Simultaneous Analysis of Near and Far Detector Samples of the T2K Experiment to Measure Muon Neutrino Disappearance

by

Casey Bojechko
B.Sc., University of British Columbia, 2007

A Dissertation Submitted in Partial Fulfillment of the
Requirements for the Degree of

DOCTOR OF PHILOSOPHY

in the Department of Physics and Astronomy

Simultaneous Analysis of Near and Far Detector Samples of the T2K Experiment to Measure Muon Neutrino Disappearance

by

Casey Bojechko
B.Sc., University of British Columbia, 2007

Supervisory Committee

Dr. Dean Karlen, Supervisor
(Department Physics and Astronomy)

Dr. Mike Roney, Departmental Member
(Department Physics and Astronomy)

Dr. Scott McIndoe, Outside Member
(Department of Chemistry)

Supervisory Committee

Dr. Dean Karlen, Supervisor
(Department Physics and Astronomy)

Dr. Mike Roney, Departmental Member
(Department Physics and Astronomy)

Dr. Scott McIndoe, Outside Member
(Department of Chemistry)

ABSTRACT

The Tokai-to-Kamioka (T2K) experiment is a long-baseline neutrino-oscillation experiment that searches for neutrino oscillations with measurements of an off-axis, high purity, muon neutrino beam. The neutrinos are detected 295 km from production by the Super Kamiokande detector. A near detector 280 m from the production target measures the unoscillated beam. This thesis outlines an analysis using samples in the near detector and Super Kamiokande to measure the disappearance of muon neutrinos. To manage the complexity this analysis, a Markov Chain Monte Carlo framework was used to maximize a likelihood to estimate the oscillation parameters. T2K Run 1+2+3 data (3.010×10^{20} POT) is used for the analysis. The estimates for the oscillation parameters are:

$$(\sin^2(2\theta_{23}), \Delta m^2_{32}) = (0.999, 2.45 \times 10^{-3}[\mathrm{eV}^2]),$$

and the 90% 1D bayesian credible intervals:

$$0.9340 < \sin^2(2\theta_{23}) < 1.000$$
$$2.22 \times 10^{-3} < \Delta m^2_{32}[\mathrm{eV}^2] < 2.74 \times 10^{-3}$$

Contents

List of Tables

List of Figures

Contributions

At the beginning of my studies I was very active in the construction of the time projection chambers (TPCs). I helped with assembly and testing of the TPCs both at the TRIUMF and J-PARC facilities. I installed all of the targets for the TPC laser calibration system and developed a survey system to measured the location of the targets on the central cathode.

I stayed for an extended period of time in Japan, at the J-PARC lab for testing, installation and commissioning of the TPCs. This included installation of support services and cabling needed for the TPCs and other sub detectors as well a surveying the ND280 detector elements. Time was spent commissioning the detector after installation, developing procedures for powering up/down the TPCs and troubleshooting any problems in order to run the detectors stably.

I logged several shifts as on site TPC expert to ensure the TPCs were fully operational and to solve any problems arising during data collection. Time was also spent as the data acquisition expert shifter monitoring the data taking and resolving any crashes.

For analysis work I developed software to analyze the data from the laser calibration system for the calibration of magnetic field distortions in the TPCs, developing Monte Carlo software and performing validation studies. I performed studies to evaluate the effect of the magnetic field distortions on the momenta spectra of tracks reconstructed in the TPCs.

I also did the first T2K simultaneous analysis of the near and far detectors for muon neutrino disappearance.

ACKNOWLEDGEMENTS

I find it surreal that I was able to be a part of an endeavour asking some of the most fundamental questions about nature, and for nature to answer back. The driving force behind this endeavour was and continues to be the people involved. Inquisitive, passionate, kind people, some of which I'm proud to call my friends.

I would first and foremost thank my supervisor Dean Karlen for his help over the long journey that is grad school. Dean's insight into physics, attention to detail and persuasive discourse has given me a first hand account of what it means to be a world class scientist. I would like to thank him for his patience over the years navigating me through everything from conceptual issues to presentation techniques, even manuvering the early morning streets of Tsukuba to pick up a green graduate student who couldn't properly book a room at KEK. I am grateful for having had the opportunity to receive his instruction as well as collaborate with him.

I owe a great deal of thanks to my fellow UVic T2K grad students Andre Gaudin and Jordan Myslik for keeping me sane (for the majority of the time) during the long drives into JPARC. It would be hard to otherwise group together three people as different, so it was immensely enjoyable to learn these gentlemen's world view and connect over our shared love of science. It is with few people one gets to share such vexation and exaltation in such a short time.

Living in Japan and especially Naka-sugaya had its trials but I will forever look back fondly at the time spent in the Minouchi houses. Walking along the rows of houses, the air filed with debate and laugher instilled a sense of purpose in me that is hard to describe. I have the residences of Minouchi to thank for this. Special thanks goes to Brian Kirby, Patrick de Perio and other salty dog aficionados.

I would like to thank the several post docs that helped me along the way. Post docs are set on bringing the goals of the experiment to fruition still with the experience of graduate school fresh in their minds, making them a graduate students best resource. Thanks go to; Mike Wiliking for his insights to my work on the TPC calibration, his ready eagerness to help with any technical issues and his effortless ability to make people around him laugh while getting science done. Kendall Mahn for her tireless leadership and willingness to accommodate any requests in regards to my thesis or otherwise. Many people in the collaboration are indebted to Kendall's hard work and her consistent approach of leading by example. Anthony Hillairet for his keeping his office door open so I could bounce ideas off of him, his gentle pushes for me to market

myself more and his technical prowess in helping with all things reconstruction. Mark Hartz for his help with technical and conceptual aspects of making a fitter, a great deal of Mark's work provided a backbone for my thesis. Also to Thomas Lindner and Blair Jamieson for their expertise and enthusiasm to help out a fledgling student.

I received a great deal of help from professors in the T2K canada collaboration and those in particular at TRIUMF. Thanks goes to Hirohisa Tanaka, Akrika Konaka, Chris Hearty, Fabrice Retiere and Scott Oser. Although Scott was not directly supervising my thesis he always maintained an active interest and was quick to offer support of any kind. His casual but insightful deliberations on all things science never failed to provide perspective. I'm indebted to Scott for taking a chance on me when I was still an undergrad.

I was incredibly lucky to be teamed up with Asher Kaboth in doing the analysis for my thesis. His patience, humour and zeal for physics made for a relaxed but productive collaboration.

I also owe a great deal of gratitude to friends and family that helped my along the way. The countless people that humoured my rants, gripes and late night science discussions.

And to my beautiful Lauren, I couldn't imagine a brighter light at the end of the tunnel.

How wonderful that we have met with a paradox. Now we have some hope of making progress.

Niels Bohr

It doesn't matter how beautiful your theory is, it doesn't matter how smart you are. If it doesn't agree with experiment, it's wrong.

Richard Feynman

DEDICATION

To my parents, for unwavering support in everything I've done.

Chapter 1

Neutrino Physics

Neutrino physics is a fascinating and active field of research that may hold the key in understanding some of the currently unanswered questions in fundamental physics. The matter antimatter asymmetry observed in the Universe which is responsible for all of the baryonic matter we observe, is still a mystery. The neutrino may help us solve this mystery. A possible key component in the cause of the matter antimatter asymmetry, is CP violation in the lepton sector. In order to obtain information about CP violation, detailed knowledge of the properties of neutrinos is required. Over the past several decades experiments have been gaining more information about neutrinos, particles which are notoriously hard to measure. These efforts have paid off and the prospect of measuring CP violation with neutrinos seems to be within reach. In this chapter I will present the history of the neutrino as well as theoretical and experimental aspects of neutrino oscillations. I will then discuss ongoing research in the field of neutrino physics.

The neutrino, a particle with inauspicious beginnings, has become a cornerstone of high energy physics and has revealed deficiencies in the otherwise steadfast standard model. The neutrino was first postulated by Wolfgang Pauli in 1930 as a device to compensate for the apparent energy loss observed in nuclear beta (β) decay [1]. Pauli boldly theorized a new neutral particle at a time when the mere possibly of detecting neutral particles was in question. It was only two years later that James Chadwick discovered the neutron, however the neutron was far too massive to be the missing particle emitted in β decay [2]. Pauli expressed that his new particle must be much less massive than the neutron and Enrico Fermi coined the name neutrino to distinguish the two particles.

As an added detriment to the neutrino's detection, work done by Hans Bethe

and Rudolf Peierls showed that the cross section of the neutrino was billions of times smaller than that of an electron and on the order of $\sim 10^{-44}$ m^2 [3]. With such a small cross section Bethe and Peierls claimed that the neutrino may never be observed.

Over two decades after Pauli's introduction of a new neutral particle, the first experimental search for the neutrino was undertaken by F. Reines and C.L. Cowan. Initially proposing an atomic bomb as an intense source of neutrinos, the pair settled on a nuclear reactor source to measure the inverse β decay, $\bar{\nu_e} + p \rightarrow n + e^+$ [4]. In 1956, after 100 days of operation over the course of a year, using a detector composed of 1400 litres of liquid scintillator, Reines and Cowan detected the neutrino with a cross section agreeing closely with the theoretical prediction.

The theory of lepton flavour conservation led Pontecorvo to postulate the existence of another neutrino, the muon neutrino ν_μ, emitted in the decay of charged pions ($\pi^+ \rightarrow \mu^+ + \nu_\mu$) [5]. This was discovered at the Brookhaven National Laboratory (BNL) by Lederman et al. in 1962 [6]. In one of the first accelerator neutrino experiments a ~ 15 GeV/c^2 proton beam struck a target to create pions which decay into muons and subsequently muon neutrinos. Spark chambers placed behind thick shielding made the first observation of the muon neutrino. Much more recently, the DONUT experiment at Fermilab observed the tau neutrino (ν_τ) [7].

The $SU(2) \times U(1)$ gauge model proposed by Glashow [8] predicted the Z boson and the existence of weak neutral current interactions. The model predicted that the neutrino could interact by both charged and neutral current processes shown in Fig 1.1. The observation of neutral current neutrino interactions was first made by the Gargamelle experiment at CERN in 1973 [9].

Measurements of the invisible width of the Z boson, made by LEP experiments at CERN are consistent the existence of three light neutrino flavours [10]. The number of neutrino flavours also affects primordial nucleosynthesis which in turn affects the relative abundances of elements in the universe. Such cosmological observations set the number of neutrinos close to three, in agreement with data from the LEP experiments.

Beyond the simple detection of neutrinos, experiments have made the astonishing discovery of neutrino oscillation: the ability for neutrinos to change their flavour over time. Such a phenomenon requires that neutrinos have mass, a requirement that is not in agreement with the Standard Model of particle physics. The mechanisms of how neutrinos gain a tiny mass are not formulated in the Standard Model and new physics beyond the Standard Model (BSM) is needed to describe the nature of

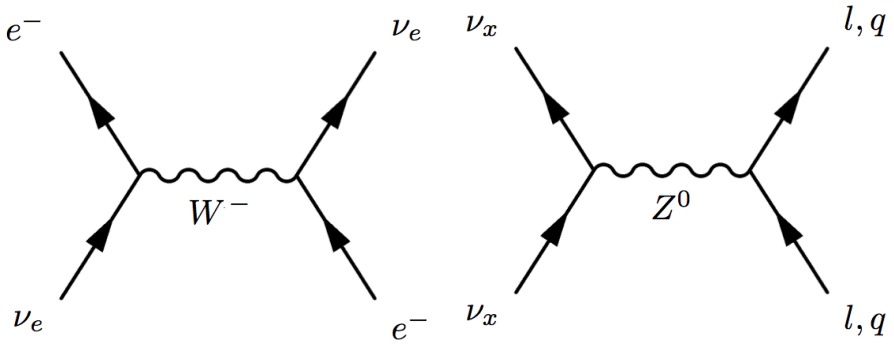

Figure 1.1: Feynman diagrams for Weak Charged Current (left) and Neutral Current (right) interactions. The charged current diagram plot shows electron neutrino scattering. Charge current vertices must couple a neutrino and lepton of the same flavour. The neutral current diagram shows a neutrino scattering off of a quark or lepton. Neutral current vertices must have the same ingoing and outgoing fermion (lepton or quark). In the figures time is running from the bottom to top.

neutrinos.

Another unusual property of neutrino oscillation is that lepton flavour is not conserved. Lepton flavour violation along with CP violation would make neutrinos a prime candidate for leptogenesis and a possible explanation for the observed excess of matter over antimatter in the Universe. The measurement of CP violation in neutrinos is experimentally very difficult and has not yet been performed.

Such unresolved questions make neutrino physics a very active field of research. The following sections outline results from different experiments measuring neutrino oscillation.

1.1 Solar Neutrino Problem

1.1.1 Homestake Experiment

Raymond Davis Jr. was the first person to attempt to measure neutrinos from the sun. In an ambitious experiment he used 390000 litres of liquid tetrachloroethylene (C_2Cl_4), 1478 m underground in the Homestake mine in South Dakota [11]. The experiment was setup to detect the reaction, $\nu_e + {}^{37}\mathrm{Cl} \rightarrow {}^{37}\mathrm{Ar} + e^-$, to measure the flux of neutrinos emitted from stellar fusion reactions. The technical challenge was to collect and correctly count the few ^{37}Ar atoms produced by neutrino interactions in such a vast detector. The ^{37}Ar atoms produced were radioactive and after data col-

lection were chemically extracted and measured with a low background proportional counter.

At the time of the Homestake experiment the flux of neutrinos emitted by the sun was described by the standard solar model (SSM) developed primarily by John Bachall [12].

Neutrinos are emitted in the nuclear fusion reactions in the core of the sun, a chain of reactions known as the *pp* chain, summarized by

$$4p + 2e^- \rightarrow^4 \mathrm{He} + 2\nu_e + 26.731\mathrm{MeV}. \tag{1.1}$$

In this reaction different sub-processes of the pp chain produce characteristic neutrino energy spectra. For experimental observation the most important neutrino producing steps in the *pp* chain are the *pp*, ^{8}B and ^{7}Be reactions [13]. The rates of reactions can be calculated through astrophysical models of the sun which can then be used to compute the total electron neutrino flux. Figure 1.2 shows the prediction of neutrino energy spectra from the *pp* chain.

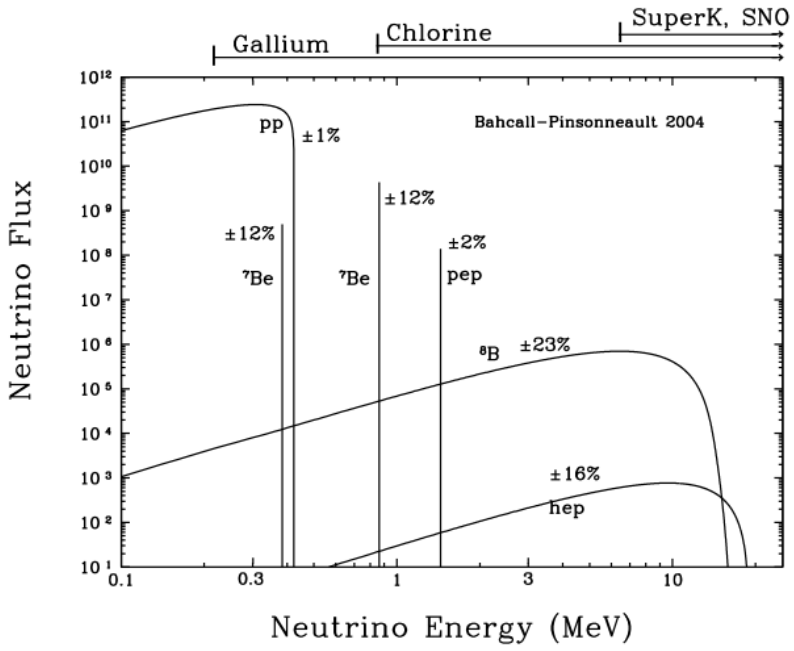

Figure 1.2: Neutrino energy spectra from the *pp* chain [12].

The dominant source of neutrinos measured by Davis's experiment were ^{8}B neutrinos. Initial results of the experiment measured a solar neutrino flux that was much

less than the predicted rate estimated by the standard solar model. In fact Davis measured $\sim 1/3$ of the neutrino flux that was predicted. The disparity between the prediction and measured flux became known as the solar neutrino problem. Initially, the Homestake experiment came under criticism that a measurement of such low rates of ^{37}Ar could not be made reliably. However, running for over 25 years (1970-1994) and introducing new measurement techniques, Homestake still measured a solar neutrino flux of about 1/3 of that predicted by the SSM with a significance of more than 3 standard deviations.

1.1.2 Other Solar Experiments

Observations from other experiments also observed a deficit in neutrino flux, but on different orders than the Homestake experiment, adding to the confusion surrounding the solar neutrino problem. Gallium based experiments GALLEX/ GNO [14], SAGE [15] and the large water Cherenkov detector Kamiokande [16] also made measurements of the solar neutrino flux. The gallium experiments used the reaction, $\nu_e + ^{71}\mathrm{Ga} \rightarrow ^{71}\mathrm{Ge} + e^-$. The energy threshold for gallium experiments is much lower than Davis's chlorine experiment making them sensitive to *pp* neutrinos. The gallium experiments also measured a deficit in neutrino flux compared to the solar models, however the deficit was of a different order than the Homestake experiment measuring a rate of about one half of that predicted by the SSM with a significance of 5 standard deviations.

The Kamiokande detector used water Cherenkov technology sensitive to $\nu - e$ scattering, $\nu_x + e^- \rightarrow \nu_x + e^-$. As be will discussed in Section 2.5, the Cherenkov detector can measure the direction of the neutrino helping to separate the solar neutrino signal from backgrounds. The energy threshold for Cherenkov detectors is much higher than for the gallium and chlorine experiments so that the Kamiokande experiments could measure ^8B neutrinos on the order of 10 MeV. The Kamiokande experiment also measured a deficit in the neutrino flux by one half of the SSM with a significance of 2 standard deviations. The measurement of a deficit in neutrino flux by different experiments suggested the solar neutrino problem was not the fault of the Homestake experiment. However a deficit in flux measurements of a different magnitude for different experiments made the situation all the more perplexing.

1.1.3 Atmospheric Neutrino Anomaly

In addition to the solar experiments, unexpected behaviour was seen in neutrinos produced in the atmosphere. The observation known as the 'atmospheric neutrino anomaly' was observed by the Kamiokande [17] and IMB experiments [18]. The experiments observed that the flux of neutrinos originating from pion decays in the upper atmosphere was dependent on the distance the neutrinos traveled to reach the detector. This showed that neutrinos independent from the sun also had strange behaviour not consistent with a massless Standard Model neutrino. Separate from any solar model the atmospheric neutrino anomaly began to shed light on a possible resolution of the solar neutrino problem.

1.2 Neutrino Oscillation

The proposed resolution for the solar neutrino problem was that neutrinos could oscillate, or transition from one flavour to another as a function of time. In the theory of neutrino oscillation, electron neutrinos coming from the sun would sometimes transition to neutrinos with a different flavour that would escape detection by the solar experiments. This would explain why a deficit in the number of neutrinos was observed by various experiments without the need to revise the SSM.

Neutrino oscillations were first proposed by B. Pontecorvo in 1957, inspired by the observation of neutral kaon oscillation $K^0 \leftrightarrows \bar{K^0}$ [19]. Ponetecorvo first postulated a mixing between neutrinos and antineutrinos $\nu \leftrightarrows \bar{\nu}$. Further work by M. Maki, M. Nakagawa and S. Sakata expanded by Pontecorvo, considered a two neutrino system in which ν_e and ν_μ are the mixture of two mass eigenstates, allowing oscillations to occur between flavour states [20], [21].

1.2.1 Neutrino Mixing Formulation

In the neutrino mixing formulation, a neutrino arising from a weak decay $W^+ \rightarrow l_\alpha^+ + \nu_\alpha$, results in a neutrino flavour state that can be expressed as a superposition of mass eigenstates [22],

$$|\nu_\alpha\rangle = \sum_k U_{\alpha k}^* |\nu_k\rangle, \tag{1.2}$$

where $\alpha = e, \mu, \tau$ corresponds to the lepton flavour states, U is the leptonic mixing matrix and k are the mass eigenstates. Assuming CPT invariance, the matrix U is unitary. Equation 1.2 can be inverted in order to express the mass eigenstates in terms of the flavour states:

$$|\nu_k\rangle = \sum_\alpha U_{\alpha k} |\nu_\alpha\rangle. \tag{1.3}$$

Massive neutrino states are eigenstates of the Hamiltionian and the Schrödinger equations

$$i\frac{d}{dt}|v_k(t)\rangle = H|v_k\rangle = E_k|v_k\rangle, \tag{1.4}$$

where the energy eigenvalues are $E_k = \sqrt{p^2 + m_k^2}$. Solving the Schrödinger equation shows that massive neutrinos evolve in time as a plane wave

$$|v_k(t)\rangle = e^{-iE_k t}|v_k\rangle. \tag{1.5}$$

If a neutrino is created at time 0 with a definite flavour it will then evolve in time according the equation

$$|v_\alpha(t)\rangle = \sum_k U^*_{\alpha k} e^{-iE_k t}|v_k\rangle. \tag{1.6}$$

Inserting Eq. 1.3 into Eq. 1.6 gives the result

$$|v_\alpha(t)\rangle = \sum_{\beta=e,\mu,\tau} \left(\sum_k U^*_{\alpha k} e^{-iE_k t} U_{\beta k} \right) |v_\beta\rangle. \tag{1.7}$$

The time evolution of a neutrino flavour state can therefore be described as a superposition of different flavour states. In the case that the mixing matrix U is diagonal, the neutrino flavour states will not mix. However if the off diagonal elements are nonzero this leads to mixing as the state $|v_\alpha\rangle$ evolves in time.

The transition amplitude between flavours, $\nu_\alpha \rightarrow \nu_\beta$ as a function of time is expressed by

$$A_{\nu_\alpha \rightarrow \nu_\beta} = \langle \nu_\beta | \nu_\alpha(t)\rangle = \sum_k U^*_{\alpha k} U_{\beta k} e^{-iE_k t}, \tag{1.8}$$

and the probability of transition is the square of the transition amplitude

$$P_{\nu_\alpha \to \nu_\beta}(t) = |A_{\nu_\alpha \to \nu_\beta}|^2 = \sum_{k,j} U^*_{\alpha k} U_{\beta k} U_{\alpha j} U^*_{\beta j} e^{-i(E_k - E_j)t}. \tag{1.9}$$

For the case of ultrarelativistic neutrinos the approximation $E_k \simeq E + \frac{m_k^2}{2E}$ can be made so that

$$E_k - E_j \simeq \frac{\Delta m^2_{kj}}{2E}, \tag{1.10}$$

where $\Delta m^2_{kj} = m^2_k - m^2_j$ is the mass squared difference. Neutrino oscillation experiments measure the distance travelled by the neutrino and not the time of flight, since neutrinos travel close to the speed of light the approximation t=L is made, using natural units.

Using the unitarity of U, the transition probability can be expressed in the useful form

$$\begin{aligned} P_{\nu_\alpha \to \nu_\beta}(L, E) = \delta_{\alpha\beta} - \quad & 4 \textstyle\sum_{k>j} \Re[U^*_{\alpha k} U_{\beta k} U_{\alpha j} U^*_{\beta j}] \sin^2\left(\frac{\Delta m^2_{kj} L}{4E}\right) \\ & \pm 2 \textstyle\sum_{k>j} \Im[U^*_{\alpha k} U_{\beta k} U_{\alpha j} U^*_{\beta j}] \sin\left(\frac{\Delta m^2_{kj} L}{2E}\right). \end{aligned} \tag{1.11}$$

Adding previously ignored factors of $\hbar$ and c and expressing the length and energy in useful units for experiment, the argument in the first sinusoidal function in Eq 1.11 can be expressed as

$$\Delta m^2_{kj} \frac{L}{4E} \simeq 1.27 \Delta m^2_{kj}(eV^2) \frac{L(km)}{E(GeV)}. \tag{1.12}$$

In Eq.1.11 the imaginary term contributes to CP violation, the $\pm$ differing neutrinos(+) from antineutrinos(-). CP violation arises in the neutrino oscillations if the imaginary term is nonzero.

Currently, it is believed that only three flavour states participate in neutrino oscillations. If an additional mixing with other light neutrino states does occur, those neutrinos would not interact with the Z boson [23]. Such unreactive neutrinos are known as sterile neutrinos. It should be noted that to date the majority of solar and atmospheric data exclude the single sterile neutrino case [24]. Since there are three flavour states, there must be equal to or greater than three mass states. For only

three massive neutrino eigenstates the leptonic mixing matrix is written as

$$U = \begin{bmatrix} 1 & 0 & 0 \\ 0 & c_{23} & s_{23} \\ 0 & -s_{23} & c_{23} \end{bmatrix} \begin{bmatrix} c_{13} & 0 & s_{13}e^{-i\delta} \\ 0 & 1 & 0 \\ -s_{13}e^{i\delta} & 0 & c_{13} \end{bmatrix} \begin{bmatrix} c_{12} & s_{12} & 0 \\ -s_{12} & c_{12} & 0 \\ 0 & 0 & 1 \end{bmatrix} \begin{bmatrix} e^{i\alpha_1/2} & 0 & 0 \\ 0 & e^{i\alpha_2/2} & 0 \\ 0 & 0 & 1 \end{bmatrix}, \tag{1.13}$$

where $c_{ij} = \cos\theta_{ij}$, $s_{ij} = \sin\theta_{ij}$ and θ_{ij} are the three mixing angles. δ, α_1 and α_2 are CP-violating phases, α_1 and α_2 are known as Majorana phases and are only present if neutrinos are Majorana particles (Majorana particles are discussed in Section 1.4.3). Every parameter in U can be measured by oscillation experiments except for Majorana phases. The matrix U is sometimes referred to as the Pontecorvo-Maki-Nakagawa-Sakata or PMNS matrix after the people who helped formulate it.

1.2.2 MSW Effect

Since ordinary matter is composed of a large number of electrons and no μ or τ particles, this has an effect on how neutrinos behave when travelling through matter, known as the MSW effect, named after Mikheyev, Smirnov and Wolfenstein [25] [26]. Inside matter, coherent forward scattering of neutrinos on electrons causes a change in the mixing so that it is not equal to the value in vacuum. An additional potential for charged current interactions of the electron neutrinos in matter is given by

$$V = \sqrt{2}G_F N_e, \tag{1.14}$$

G_F being the Fermi potential and N_e the number of electrons per unit volume in the matter. This only has an effect on the $\nu_e - \nu_e$ element of the mixing matrix.

For the case of a two neutrino oscillation, one neutrino being ν_e the other ν_x a linear combination of ν_μ and ν_τ, the effective Hamiltonian can be parameterized by a single angle θ. The Hamiltonian is modified to include a mixing potential as well as a matter induced potential

$$H = \frac{\Delta m^2}{4E} \begin{pmatrix} -\cos 2\theta & \sin 2\theta \\ \sin 2\theta & \cos 2\theta \end{pmatrix} + \begin{pmatrix} V & 0 \\ 0 & 0 \end{pmatrix} = \frac{\Delta m_M^2}{4E} \begin{pmatrix} -\cos\theta_M & \sin\theta_M \\ \sin\theta_M & \cos\theta_M \end{pmatrix}, \tag{1.15}$$

where m^2_M and θ_M are the effective mass splitting and effective mixing angle in matter. Similar to the treatment above, it follows that the leading term is

$$P_{\nu_e \to \nu_x} = \sin^2(2\theta_M) \sin^2 \left(\frac{\Delta m^2_M L}{4E} \right). \tag{1.16}$$

The MSW effect is important in solar neutrino experiments as the very dense matter in the interior of the sun modifies the oscillation characteristics from the behaviour seen in vacuum. Future terrestrial experiments with ever increasing baselines will also be sensitive to the MSW effect. For antineutrinos the interaction energy V in Eq. 1.14 becomes negative. In this fashion the effective mass splitting and effective mixing angles are different for neutrinos and antineutrinos so that within matter the oscillation probabilities will differ between neutrinos and antineutrinos.

1.3 Evidence for Neutrino Oscillation

1.3.1 Solar and Reactor Experiments

A definitive measurement of neutrino oscillations was made by the Sudbury Neutrino Observatory (SNO). The SNO detector was a water Cherenkov detector with a target of 1000 tons of heavy water (D_2O) [27]. The SNO detector was primarily sensitive to ^8B neutrinos which could interact with the deuterons in SNO via three interactions

$$\begin{aligned} \text{(Charged Current)} \quad & \nu_e + d \to p + p + e^- \\ \text{(Neutral Current)} \quad & \nu_x + d \to p + n + \nu_x \\ \text{(Elastic Scattering)} \quad & \nu_x + e^- \to \nu_x + e^-, \end{aligned} \tag{1.17}$$

where ν_x is any neutrino flavour [28]. The importance of the three different interaction channels is that the charged current is only sensitive to ν_e as in Davis's experiment but neutral current interactions are sensitive to all three neutrino flavours. Elastic scattering is also sensitive to all three flavours, however the interaction cross section of ν_μ and ν_τ is $\sim 1/6$ that of ν_e. From the different measured reactions, the flux of neutrinos in units of 10^6 neutrinos cm^{-2} s^{-1} was measured to be

$$\begin{aligned} \phi_{CC} &= 1.68 \pm 0.06(\text{stat})^{+0.08}_{-0.09}(\text{sys}), \\ \phi_{NC} &= 4.94 \pm 0.21(\text{stat})^{+0.38}_{-0.34}(\text{sys}), \\ \phi_{ES} &= 2.34 \pm 0.22(\text{stat})^{+0.15}_{-0.15}(\text{sys}). \end{aligned} \tag{1.18}$$

The NC flux is in good agreement with the solar model predictions, where as the CC and ES are $\sim 35\%$ of the ^8B neutrino flux, which is consistent with results from the Homestake experiment. The deficit of ν_e flux compared with total ν flux provides proof that neutrinos change flavour. The SNO experiment measured good agreement between the NC component and the SSM prediction as is shown in Fig. 1.3.

The survival probability of electron neutrinos can be approximated by the equation

$$P_{\nu_e \to \nu_e}(t) = 1 - \sin^2(2\theta_{sol}) \sin^2 \left(\frac{\Delta m^2_{sol} L}{4E} \right). \tag{1.19}$$

Generalizing to the three neutrino case $\Delta m^2_{sol} \simeq \Delta m^2_{21}$. The neutrino oscillation model fits the SNO data with the mixing parameters $\Delta m^2_{12} \approx 10^{-4} - 10^{-5}\text{eV}^2$ and $\tan^2 \theta_{12} \approx 0.4 - 0.5$, known as the Large-Mixing-Angle (LMA) solution.

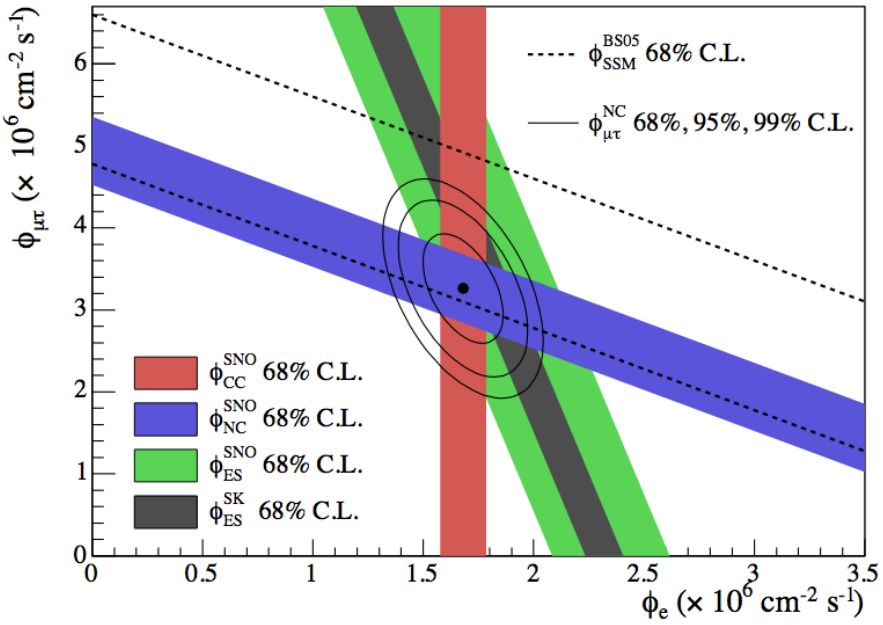

Figure 1.3: Flux of ν_μ and ν_τ versus flux of ν_e. The bands show the 68% CL flux of CC(red) NC(blue) and ES(green) interactions. The black band shows results from Super-Kamiokande experiment. The dotted lines show the bounds of the standard solar model (SSM) predictions. The solid line contours show the 68%, 95% and 99% joint probablity for $\phi(\nu_e)$ and $\phi(\nu_\mu$ and $\nu_\tau)$ [27].

A complication for neutrino oscillation models of the sun is that ^8B neutrinos will have a large MSW effect. For such large matter densities in the interior of the sun results in solar neutrinos undergoing further mixing and in fact neutrinos are emitted

from the sun in almost pure ν_2 state.

The results from solar neutrino experiments also suggest that neutrinos of an energy of approximately 1 MeV traveling on the order of $\simeq$ 100 km should also exhibit oscillation.

Nuclear reactors are an excellent source of $\bar{\nu}_e$, this was the motivation for the experimental setup to first detect neutrinos, conducted by Cowan and Reines. A nuclear reactor is powered by the fission of Uranium (U) and Plutonium (Pu), and electron neutrinos are produced by a chain of β decays of the fission products. A prediction of the antineutrino spectrum is quite difficult to make as the decay of each isotope produces a different neutrino energy spectrum. Knowledge of the thermal power of the reactor and the composition of the initial nuclear fuel and decay products is needed to estimate the antineutrino flux.

KamLAND is an experiment which measures the $\bar{\nu}_e$ flux of nuclear reactors scattered throughout Japan [29]. The KamLAND detector consists of 1200 m^3 of liquid scintillator surrounded by photo-multiplier tubes. Electron neutrinos are detected via the inverse β decay reaction, neutrinos above a threshold of 1.8 MeV can be detected. The distance from the detector to different reactors varies from 80 to 800 km with an average baseline of 180 km. The ratio of L/E of the KamLAND experiment makes it sensitive to the same Δm^2 as solar experiments.

Measuring the flux of reactor neutrinos, KamLAND observes an energy dependant suppression of $\bar{\nu}_e$ interactions. The L/E dependence of the $\bar{\nu}_e$ rate measured by KamLAND, divided by the expected rate with no neutrino oscillation is shown in Fig. 1.4. The overall observed rate is lower than the expected and there is an observed L/E dependance on the suppression of the $\bar{\nu}_e$ rate. The L/E dependance allows for a precise measurement of the Δm^2 parameter.

The observed rate is consistent with neutrino oscillation models with parameters corresponding to the LMA region found by solar experiments. The data from solar experiments and KamLAND are complementary, the solar experiments better constrain the mixing angle, $\tan^2\theta$ and KamLAND makes a precise determination of Δm^2, oscillation parameter contours from both are shown in Fig. 1.5.

A joint analysis of solar experiments and KamLAND gives $\Delta m^2_{21} = (7.59 \pm 0.21) \times 10^{-5}\text{eV}^2$ and $\tan^2\theta_{12} = 0.47^{+0.06}_{-0.05}$ [30].

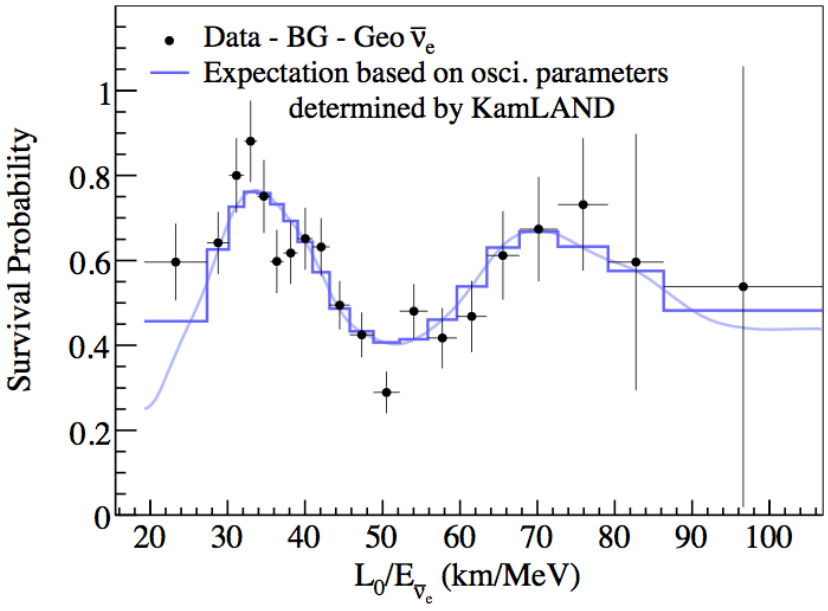

Figure 1.4: Ratio of the expected reactor $\bar{\nu}_e$ rate measured by KamLAND to the expected rate without oscillations, as a function of L/E [29].

1.3.2 Atmospheric and Accelerator Experiments

Neutrinos are also produced when high energy cosmic rays interact with nuclei in Earth's upper atmosphere. The incident cosmic rays are composed primarily of protons that collide with the atmosphere to create secondary hadrons, including a large number of charged pions. The produced pions decay most frequently into a muon and muon neutrino. Also, muons will decay into electrons, electron neutrinos and muon antineutrinos, this decay chain can be expressed as

$$\begin{aligned} \pi^+ &\rightarrow \mu^+ + \nu_\mu & \qquad \pi^- &\rightarrow \mu^- + \bar{\nu}_\mu \\ &\hookrightarrow e^+ + \nu_e + \bar{\nu}_\mu & &\hookrightarrow e^- + \bar{\nu}_e + \nu_\mu. \end{aligned} \tag{1.20}$$

A schematic view of the neutrino production is shown in Fig 1.6 [31].

The resultant neutrinos are on the order of ~1 GeV. The length of travel from the point of creation in the upper atmosphere to a detector near the surface of the earth ranges from 20 km, for neutrinos originating in the atmosphere directly above the

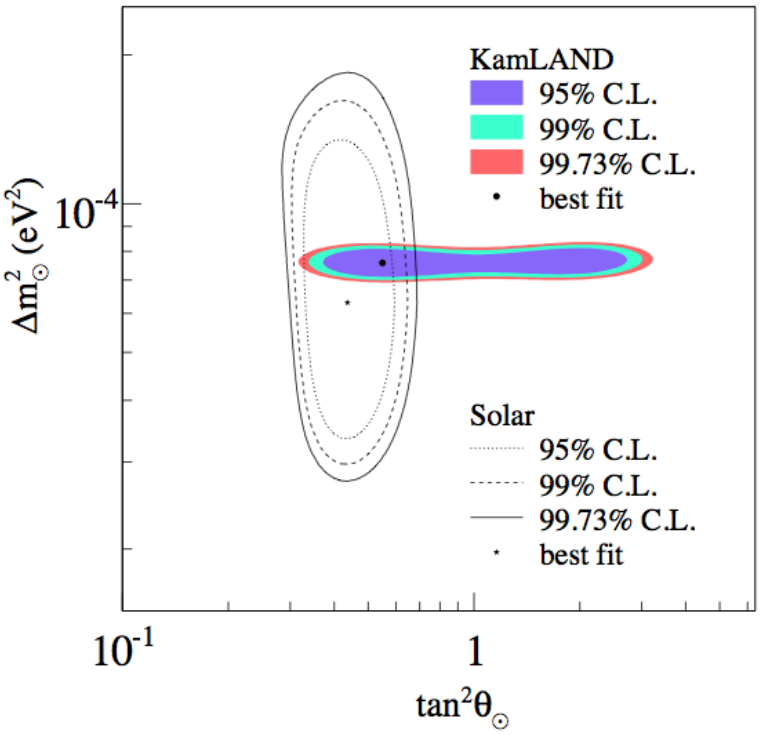

Figure 1.5: Oscillation parameter contours from solar neutrino experiments and the KamLAND experiment [30].

Earth's surface to 10^4 km, for neutrinos traveling through the Earth before detection. For atmospheric experiments, $L/E \simeq 10^4$ km GeV$^{-1}c^{-2}$, making the mass squared difference sensitive to $\Delta m^2 = 10^{-4}$ eV^2.

Compelling evidence for neutrino oscillation comes from the up down asymmetry measured at the Super Kamiokande detector. The Super Kamiokande detector was an upgrade to the Kamiokande detector and similarity is an underground water Cherenkov detector. Super Kamiokande is summarized in the description of the T2K experiment in Section 2.5. Super Kamiokande is able to distinguish between e-like and μ-like neutrino events based on the pattern of the Cherenkov light inside the detector. Without oscillation, the flux of downward traveling neutrinos, coming from the zenith angle θ_Z should be equal to the flux of upward going neutrinos, traveling through the earth, coming from an angle $\pi - \theta_Z$. However the zenith angle distributions of μ-like events show a clear deficit compared to the no oscillation expectation, shown in Fig 1.7.

Since the upward going ν_μ are created in the atmosphere on the other side of

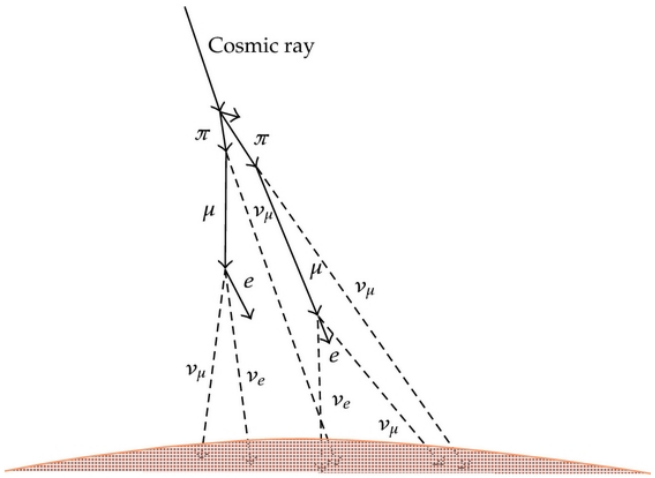

Figure 1.6: Neutrino production by cosmic-ray proton interactions in the atmosphere [31].

the Earth they have to travel a much farther distance to the detector. In this extra distance(time) of propagation the ν_μ have a higher probability to transition to other flavours and the measurement of a deficit of muon neutrinos is due to oscillation. Since an excess of electron neutrino interactions is not observed, atmospheric neutrino oscillation is analyzed as two-neutrino oscillation $\nu_\mu \rightarrow \nu_\tau$. At the L/E of atmospheric neutrino experiments the oscillation is not sensitive to the mass splitting measured for the oscillation of solar neutrinos and the survival probability of muon neutrinos can be expressed in the simplified form:

$$P_{\nu_\mu \rightarrow \nu_\mu}(t) = 1 - \sin^2(2\theta_{atm}) \sin^2\left(\frac{\Delta m^2_{atm} L}{4E}\right) \tag{1.21}$$

Analysis of the Super Kamiokande atmospheric data gives bounds on the atmospheric oscillation parameters $1.3\times10^{-3} < |\Delta m^2_{atm}| < 4.0\times10^{-3}\text{eV}^2$ and $\sin^2(2\theta_{atm}) > 0.95$ (90 % CL) [32].

Complementary to atmospheric observations are accelerator based long baseline experiments with a similar L/E. Particle accelerators can produce an intense beam of neutrinos in a desired energy range and well defined L/E making them an extremely useful tool in studying neutrino oscillation. Having an estimate of the Δm^2 of oscillation an accelerator experiment L/E ratio can be designed to maximize the oscillation probability. The way in which neutrino beams are produced from particle

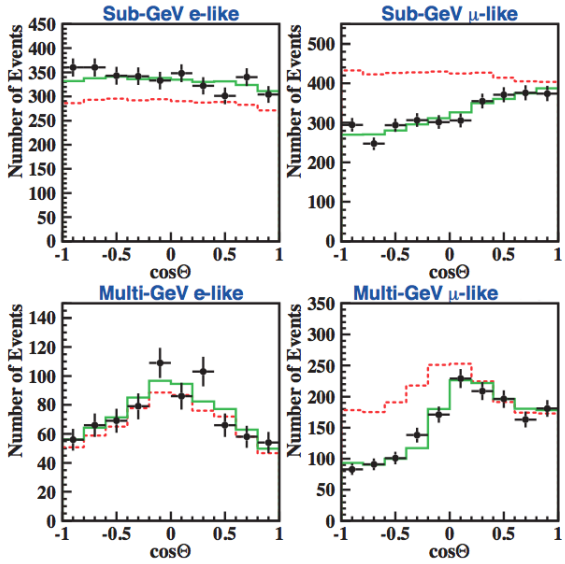

Figure 1.7: Fluxes of atmospheric ν_e and ν_μ as a function of zenith angle. The dashed shows the prediction with no oscillation and the solid line shows the best fit oscillation prediction [32] .

accelerators is described in Section 2.1.

Examples of acceleration based experiments include K2K and MINOS. The K2K (KEK to Kamioka) experiment measured a neutrino beam created at the KEK-PS facility. The neutrino beam was measured by a near detector composed of a 1 kton water Cherenkov detector and 6 ton scintillating fibre tracking detector, 300 m downstream of the production. The beam was also measured by the far detector Super Kamiokande, 250 km downstream from production. The beam had an average energy of $\langle E_\nu \rangle = 1.3$ GeV, giving L/E $\sim$ 200 km/GeV.

The MINOS experiment uses neutrinos produced from the NuMI facility at Fermilab. The neutrino beam is horn focused and has the ability to produce a varied neutrino energy spectrum. Like K2K, MINOS also makes use of two detectors, both the near and far detectors are iron-scintillating tracking calorimeters within a toroidal magnetic field. The near detector has a mass of 0.98 kton and the far detector 5.4 kton. The far detector is located in the Soudan Mine in South Dakota giving MINOS a baseline of 735 km. The K2K and MINOS measurements of the atmospheric oscillation parameters have been made from ν_μ disappearance, the oscillation of $\nu_\mu \rightarrow \nu_\tau$ is assumed with with no explicit observation of ν_τ appearance.

Both experiments observe an energy spectrum of muon neutrinos distorted with

respect to a no-oscillation scenario. Fig. 1.8 shows the confidence intervals for oscillation parameters from the Super Kamiokande atmospheric experiment and MINOS accelerator based experiment. Currently MINOS has made the most precise measurement of Δm^2_{atm} at $|\Delta m^2_{atm}| = (2.32^{+0.09}_{-0.10}) \times 10^{-3}\text{eV}^2$, $\sin^2(2\theta_{atm}) = 0.950^{+0.035}_{-0.036}$ (90% CL) [33].

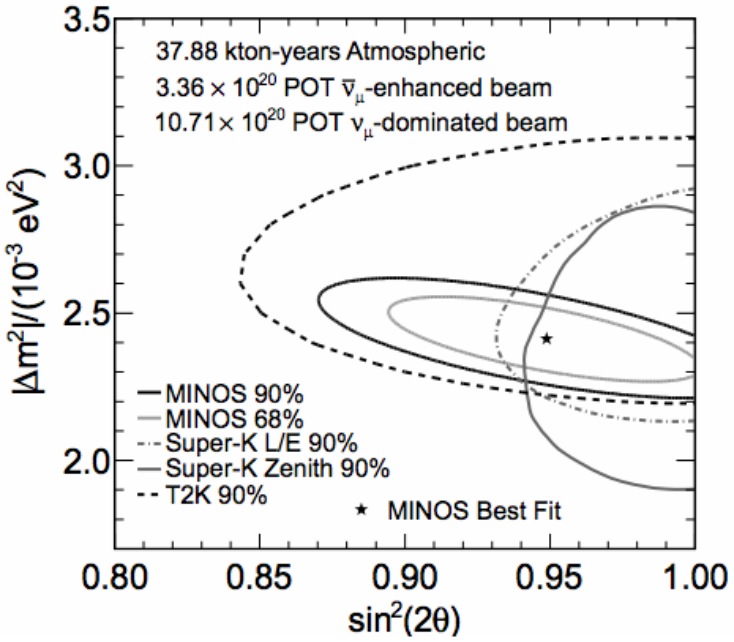

Figure 1.8: Confidence interval for $\nu_\mu \rightarrow \nu_\tau$ oscillation parameters for MINOS, Super-Kamiokande and T2K [33]. T2K 2011 result shown [34].

1.3.3 Measurement of θ_{13}

To date, solar and atmospheric results are well described by two-flavour mixing models, yet we know that there are at least three neutrino flavours and therefore at least three mass eigenstates. The aforementioned experiments while giving robust evidence of neutrino oscillation do not provide a full picture of 3x3 mixing models. At the frontier of neutrino physics is the measurement of the mixing angle θ_{13}, a parameter that is of particular interest since a nonzero value is required for there to be CP violation in the lepton sector, if neutrinos are not Majorana particles, as can be seen in Eq 1.13.

The parameter θ_{13} can be measured by reactor neutrino experiments by measuring

$\bar{\nu}_e$ disappearance at short baselines ($\sim$1 km), the probability of disappearance is

$$P_{\bar{\nu}_e \to \bar{\nu}_x}(t) \simeq 1 - \sin^2(\theta_{13}) \sin^2 \left(\frac{\Delta m^2_{13} L}{4E} \right). \tag{1.22}$$

In addition to reactor experiments, θ_{13} can be measured by long baseline accelerator experiments by looking for electron neutrino appearance ($\nu_\mu \to \nu_e$). For an L/E sensitive to Δm^2_{23} the oscillation probability is approximately

$$\begin{aligned} P_{\nu_\mu \to \nu_e}(t) &\simeq \sin^2(2\theta_{13}) \sin^2(\theta_{23}) \sin^2 \left(\frac{\Delta m^2_{32} L}{4E} \right). \\ &\sim \frac{1}{2} \sin^2(2\theta_{13}) \sin^2 \left(\frac{\Delta m^2_{32} L}{4E} \right). \end{aligned} \tag{1.23}$$

Accelerator experiments with a pure ν_μ beam can measure oscillation by searching for the appearance of a ν_e component at the oscillation maximum. The measurement of ν_e appearance is one of the main goals of the T2K experiment and a detailed explanation of the experiment is outlined in Chapter 2. In addition to T2K, another accelerator experiment NOνA is in the construction phase and will measure ν_e appearance in FermiLab's NUMI beamline [35].

It must be noted that Eq. 1.23 is an approximation and higher order terms in the ν_e appearance probability also depend on δ, the CP violating phase and the sign of Δm^2_{23}, parameters which are still unknown. For long baseline experiments where neutrinos travel through the earth's crust, matter effects must also be considered. Since multiple parameters still need to be determined, it is difficult to separate out the effects of each of these parameters on $\nu_\mu \to \nu_e$ oscillation. It is still possible to determine whether or not θ_{13} is nonzero, however experiments at different baselines and energies must be done to disentangle the effects of different parameters.

Prior to 2011 experiments were not yet sensitive the the small value of θ_{13} and the CHOOZ experiment gave the smallest upper limit at $\sin^2(2\theta_{13}) < 0.15$ at 90% C.L. [36].

The summer of 2011 saw the first indications of a nonzero θ_{13}, the initial result being announced by T2K in June. Measuring $\nu_\mu \to \nu_e$ appearance, T2K found a nonzero θ_{13} with a significance of 2.5 standard deviations [37]. Soon after the MINOS experiment measuring the same channel as T2K found that $\theta_{13} = 0$ was disfavoured

with a p-value of 0.11 [38]. In addition the Double CHOOZ experiment, measuring the disappearance of reactor $\bar{\nu}_e$, obtained a result ruling out the nonzero θ_{13} hypothesis with a p-value of 0.055.

In March 2012 the reactor neutrino experiment, Daya Bay in China announced their measurement of $\sin^2(2\theta_{13}) = 0.092 \pm 0.016(\text{stat}) \pm 0.005(\text{syst})$ giving a nonzero value for the neutrino mixing angle θ_{13} with a significance of 5.2 standard deviations [39]. Less than a month later the RENO reactor neutrino experiment in South Korea reported a result of $\sin^2(2\theta_{13}) = 0.113 \pm 0.013(\text{stat.}) \pm 0.019(\text{syst.})$ giving a nonzero θ_{13} with a significance of 4.9 standard deviations [40].

This flurry in activity in neutrino physics over the past few years has shown that θ_{13} is not zero. This is a very exciting result since it opens the door to a measurement of CP violation in the lepton sector.

1.4 Future Investigations in Neutrino Physics

1.4.1 Mass Hierarchy

In the current description of neutrino oscillation models, one of the parameters yet to be measured is the mass hierarchy of the neutrino mass eigenstates.

Solar and reactor neutrino experiments have determined that $\Delta m^2_{21} \approx 8.0 \times 10^{-5}$ eV^2, the sign is known from the MSW effect that occurs in the sun. From atmospheric and accelerator experiments, $|\Delta m^2_{32}| \approx 2.5 \times 10^{-3}$ eV^2, the sign of the mass squared difference has not been determined as experiments to date have not been sensitive to MSW effects.

There still remain two possibilities for the mass hierarchy of neutrinos. One possible hierarchy named 'normal' has two light neutrinos and one heavier neutrino, $m_1 < m_2 < m_3$. For the 'inverted' case there is one light neutrino m_3 and two heavier neutrinos, $m_1 < m_2$. A schematic diagram of the mass hierarchies is shown in Fig 1.9.

Future accelerator neutrino experiments such as NoνA, which will have a longer baseline (> 700 km) and higher energy neutrinos will be more sensitive to MSW effects and can possibly measure the mass hierarchy [35].

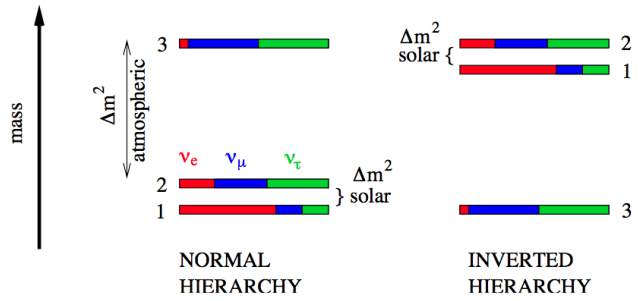

Figure 1.9: Normal and inverted neutrino mass hierarchies [13].

1.4.2 Absolute Neutrino Mass

Experiments attempting to directly measure the neutrino masses have set upper limits, roughly six orders of magnitude lighter than the electron.

Oscillation experiments give information about the differences in the square of the mass eigenstates, however they provide no information about the absolute mass scale of the neutrinos. Experiments measuring the β decay of tritium hold promise for finding the absolute mass scale of neutrinos. Observing the energy spectrum of the electron in β decay, the mass of the neutrino will limit the maximum energy of the outgoing electron. Currently the upper limit for the antielectron neutrino is 2.05 eV (95 % CL) [41], with a goal for further experiments such as KATRIN to increase the sensitivity of current mass measurements to 0.2 eV [42].

The Cosmic Microwave Background (CMB) data of the WMAP experiment, combined with other astronomical data can be used to obtain an upper limit on the sum of neutrino masses. Depending on the model used one obtains $\sum_j m_j \lesssim (0.3 - 1.3)$ eV, 95% CL. [43].

1.4.3 Dirac or Majorana Mass

The discovery that neutrinos oscillate shows that they can evolve as function of time. Such time evolution requires that the neutrino be moving slower than the speed of light and gives the profound result that they have a nonzero mass. The reason such a result is profound comes from the fact that the Standard Model which is very successful in predicting a wide array of physical phenomena makes the incorrect assumption that the neutrino mass is zero. The small mass of the neutrino still has unknown origins and therefore extensions to the Standard Model are needed to

explain the neutrino mass.

A feature of the weak interactions in the Standard Model is that they only couple to left handed neutrinos or right handed antineutrinos. In this scenario right handed neutrinos do not interact with matter and are sterile. In the Standard Model it has been postulated that the right handed neutrinos, instead of being sterile, do not exist at all.

The absence of right handed neutrinos has an effect on the formulation of the mass of the neutrino. The Standard Model Lagrangian mass term requires a coupling of right (ψ_R) and left (ψ_L) handed states

$$\mathcal{L} = -m\psi\bar{\psi} = -m(\bar{\psi_L}\psi_R + \bar{\psi_R}\psi_L). \tag{1.24}$$

If no right handed state exists the mass term in the Lagrangian cannot exist and the neutrino is a massless particle.

However after the discovery of neutrino oscillation, extensions to the Standard Model have been made to account for the neutrino's small mass. One extension known as the "*Minimally Extended Standard Model*" reintroduces the right handed neutrino state. The right handed states are sterile as they do not interact via the weak force or any other force. In this manner the mass term coupling right handed and left handed states can exist in the Lagrangian and the neutrino obtains its mass by the same mechanism as other particles, known as Dirac mass.

Another way to add mass to the neutrino is known as a Majorana mass term. A Majorana neutrino postulates that the neutrino is its own antiparticle, or that the neutrino and antineutrino differ only by their helicity.

In this formulation there are two Majorana fields, ν_L the 2 component field describing the left handed neutrino/right handed antineutrino state and ν_R the other Majorana field which describes the right handed neutrino/left-handed antineutrino state. In this formulation ν_R is independent of ν_L and does not couple to weak interactions. A ν_R and ν_L state can be coupled together to give rise to a mass term in the Lagrangian

$$\mathcal{L} = -m_D\bar{\nu_L}\nu_R - \frac{1}{2}m_L\nu_L^T C\nu_L - \frac{1}{2}m_R\nu_R^T C\nu_R + h.c.. \tag{1.25}$$

where C is the charge conjugation operator and $h.c.$ is the hermitian conjugate. The first term in Eq. 1.25 is known as the Dirac mass term, coupling the right handed and left handed fields. The couplings of $\nu_L^T\nu_L$ and $\nu_R^T\nu_R$ are also nonzero and give rise to

additional mass terms, known as Majorana mass terms. These Majorana couplings can occur only if the states are chargeless.

Expressing the mass terms as a matrix gives

$$M = \begin{bmatrix} m_L & m_D \\ m_D & m_R \end{bmatrix}. \tag{1.26}$$

Diagonalizing and obtaining the mass eigenvalues of the matrix: m_1, m_2 gives

$$m_{2,1} = \frac{1}{2}\left[m_L + m_R \pm \sqrt{(m_L - m_R)^2 + 4m_D^2}\right]. \tag{1.27}$$

In the limit where the Dirac mass is much less than the right handed Majorana mass ($m_D << m_R$) then $m_1 \approx \frac{m_D^2}{m_R}$ and $m_2 \approx m_R$. This is known as the see-saw mechanism. If m_D is on the order of the other fermion masses and m_R is on the order of GUT energy scales then m_2 will be very heavy and m_1 very light. This is an attractive formulation as it provides a possible explanation as to why neutrino masses are so much smaller than the other fermion masses. It also postulates the existence of a heavy right handed neutrino which has interesting further implications, discussed in Section 1.4.5.

1.4.4 Majorana Searches

The theory of neutrinos having a Majorana mass has given rise to an active field of research. Verification of neutrinos being Majorana in nature can be made by experimentally observing neutrino-less double β decay.

Two neutrino β decay occurs when a nucleus decays emitting two electrons and two $\bar{\nu}_e$,

$$N(A, Z) \rightarrow N(A, Z + 2) + 2e^- + 2\bar{\nu}_e. \tag{1.28}$$

Double β decay occurs when single β decay is forbidden but $|\Delta Z| = 2$ is allowed, one example being ^{76}Ge $\rightarrow^{76}$ Se.

If the neutrino is a Majorana particle (its own antiparticle) then it is possible for a virtual antineutrino to be emitted and reabsorbed as a neutrino. This would allow for a double β decay where two electrons and no neutrinos are emitted. Such a decay is expected to have a very small cross section however it would have an energy signature that is distinguishable from two neutrino double β decay.

Currently there has been no detection of neutrino-less double β decay. Several next generation experiments are being considered to increase the sensitivity of neutrino-less double β decay searches, such as EXO [44] and MAJORANA [45].

1.4.5 CP Violation

From the simple observation that the Universe's baryonic matter is composed entirely out of matter and not antimatter, one can conclude that the Universe contains an inherent asymmetry. This asymmetry can be quantified from early Universe cosmology, the excess is described by the parameter η, which relates the baryon, antibaryon number density (n_B, $n_{\bar{B}}$) and the photon number density n_γ

$$\eta = \frac{n_B - n_{\bar{B}}}{n_\gamma} = (6.21 \pm -0.16) \times 10^{-10}. \tag{1.29}$$

From the predicted abundances of the light elements D, ^{3}He, ^{4}He and ^{4}Li and observations of the Cosmic Microwave Background gives the result that there was only a slight excess of matter over antimatter in the early universe. This slight excess, not destroyed by matter antimatter annihilations, now comprises the entirety of the baryonic matter in the Universe.

One possible explanation for this observed matter antimatter asymmetry, is that initially the Universe started with zero asymmetry and the excess of matter over antimatter evolved in the very early stages of it's development.

This asymmetry can be generated if the following conditions, known as the Sakharov conditions are met. These three conditions are

- Baryon Number is violated.
- C and CP violation.
- Interactions happen out of thermal equilibrium.

The weak interaction has been shown to violate C and CP in the quark sector, observed in Kaon and B meson systems [46], [47]. However the magnitude of CP violation in the quark sector is not large enough to account for the observed asymmetry. Another proposed source of CP violation which has not yet been observed is in the lepton sector.

The strong motivation to measure the $\nu_\mu \rightarrow \nu_e$ appearance channel is that the oscillation is dependant on the CP violating phase δ. Since θ_{13} is nonzero it is then possible that CP violation can exist in neutrino oscillations and δ can be probed by comparing $P(\nu_\mu \rightarrow \nu_e)$ and $P(\bar{\nu}_\mu \rightarrow \bar{\nu}_e)$. The CP asymmetry for ν_e appearance is given by

$$\mathcal{A}_{CP} = \frac{P(\nu_\mu \rightarrow \nu_e) - P(\bar{\nu_\mu} \rightarrow \bar{\nu_e})}{P(\nu_\mu \rightarrow \nu_e) + P(\bar{\nu_\mu} \rightarrow \bar{\nu_e})} \simeq \frac{\Delta m^2_{21} \sin 2\theta_{12}}{4E_\nu \sin \theta_{13}} \sin \delta. \tag{1.30}$$

The size of $\mathcal{A}_{CP}$ measured by oscillations sensitive to Δm^2_{32} also depends on solar neutrino parameters Δm^2_{21}, θ_{12}, so that a measurement of CP violation requires a complete knowledge of neutrino oscillations.

Baryon number violation or baryogenesis has not yet been observed in any physical system. The discovery of neutrino oscillation and a nonzero neutrino mass have led to an interest in leptogenesis as an indirect way to violate baryon number.

In standard leptogenesis an asymmetry in the number of leptons and antileptons arises from the decays of heavy neutrinos, theorized by the see-saw mechanism that can occur if neutrinos are Majorana particles, described in Section 1.4.3. In leptogenesis a heavy right handed neutrino N_i can decay into a charged Higgs and charged lepton

$$N_i \rightarrow H + l_\alpha, \tag{1.31}$$

where $\alpha = (e, \nu, \tau)$. For the decay of the lightest right handed neutrino, N_1 with a mass of M_1, the out of thermal equilibrium Sakharov condition requires that the rate of decay be small compared to the expansion rate of the Universe, at a temperature $T = M_1$. As the temperature of the early universe drops below M_1, the lepton violating decays $\Gamma(N_i \rightarrow H + l_\alpha)$ and $\Gamma(N_i \rightarrow \bar{H} + \bar{l}_\alpha)$ have different decay rates giving CP violation. The resultant effect of the CP violation is an excess of leptons over antileptons [48].

In this formulation the lepton number asymmetry is converted into a baryon number asymmetry by the sphaleron process [49].

The ongoing search for CP violation in the lepton sector as well as Majorana neutrinos will provide further insight to the nature of neutrinos. If such phenomena are observed, the case for letpogenesis will be even stronger and the keys to answering mystery of the matter antimatter asymmetry in the Universe ever closer.

1.5 Outline

In this thesis the results of an oscillation measurement done at T2K is presented. In Chapter 2 the T2K experiment will be outlined and in Chapter 3 the Time Projection Chambers used in the experiment will be described. Chapter 4 will summarize studies done to calibrate and assess the errors due to magnetic field distortions in the Time Projection Chambers. Chapter 5 discusses the techniques used to perform the oscillation analysis and presents the measured results. Chapter 6 outlines studies done to determine errors that could limit the precision of future oscillation analyses done at T2K. Concluding remarks are given in Chapter 7.

Chapter 2

T2K

The Tokai-to-Kamioka (T2K) long-baseline neutrino oscillation experiment searches for neutrino oscillation with measurements of an off-axis, high purity, muon neutrino beam [50]. The neutrino beam is produced at the J-PARC site in Tokai, Japan and is measured by the Super Kamiokande (SK) detector located in the Kamioka mine. A near detector, known as ND280, located 280 m from the production target measures the unoscillated neutrino beam. Fig 2.1 shows a schematic diagram of the layout of T2K.

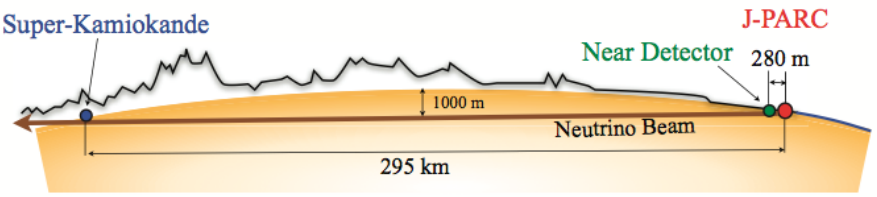

Figure 2.1: Schematic diagram of a neutrino's path, produced at the J-PARC facility and traveling through the ND280 detector (green dot) and the far detector Super-Kamiokande (blue dot) [50].

2.0.1 Physics Goals

T2K is the most sensitive long-baseline neutrino oscillation experiment to look explicitly for the appearance of electron neutrinos in a muon neutrino beam. Electron neutrino appearance is a measure of θ_{13} the last mixing angle in the lepton sector to be measured.

The physics goals of the T2K experiment are

- Precise determination of the oscillation parameters $\sin^2(2\theta_{23})$ and Δm^2_{32} by measuring $\nu_\mu \rightarrow \nu_x$ disappearance. The T2K precision goals are $\delta(\Delta m^2_{32}) \sim 10^{-4}$ eV^2 and $\delta(\sin^2(2\theta_{23})) \sim 0.01$.

- Increase the sensitivity of the θ_{13} measurement by an order of magnitude on the upper limit set by the CHOOZ experiment [36], in hopes of a positive observation through the search of $\nu_\mu \rightarrow \nu_e$ appearance (In the case of $\theta_{13} = 0$ a sensitivity of $\frac{1}{2}\sin^2 2\theta_{13} < 0.004$ at 90% confidence level for CP violating phase of $\delta = 0^o$). In response to recent observations of θ_{13}, T2K's goal is to measure a nonzero $\sin^2(2\theta_{13})$ with a significance of 5σ or greater.

- Confirmation of $\nu_\mu \rightarrow \nu_\tau$ oscillations and searches for sterile components in ν_μ disappearance by measuring neutral current events in Super-Kamiokande.

T2K's peak energy of E_ν ~1 GeV is in the region where neutrino interactions transition from resonance production to deep inelastic scattering. This will allow T2K to also conduct interesting neutrino interaction studies. Further detail on neutrino interactions is described in Section 2.3.

2.1 T2K Neutrino Beam

A 30 GeV proton beam, extracted from the JPARC synchrotron, is directed to hit a graphite target which produces a shower of hadrons, mainly pions, which are focused by three electromagnetic horns. The polarity of the horns selects the charge of the hadrons to be focused, positive hadrons are focused while negative hadrons are defocused in order to create a muon neutrino beam with little antineutrino contamination. The focused hadrons decay in flight in a 96 m decay tunnel, the positively charged pions primarily decaying to an antimuon and muon neutrino,

$$\pi^+ \rightarrow \mu^+ + \nu_\mu. \tag{2.1}$$

At the end of the decay tunnel the antimuons and other charged particles are captured by a beam dump. The result is a focused muon neutrino beam directed towards the ND280 and SK detectors.

2.1.1 Off-Axis Neutrino Beam

The T2K experiment uses a clever orientation of the beamline in order to obtain a more desirable spectrum of neutrinos. When hadrons decay, the energy of the outgoing neutrino is dependent on its direction. For example, in the decay of a pion (Eq. 2.1), the neutrino energy is given by

$$E_\nu = \frac{(1-(m_\mu/m_\pi)^2)E_\pi}{(1+\gamma^2\theta^2)}, \tag{2.2}$$

where m_μ is the mass of the muon, π is the decaying pion, and θ is the angle of the neutrino relative to the direction of the pion in the lab frame [51]. Eq 2.2 can also be applied to two body decays of other hadrons.

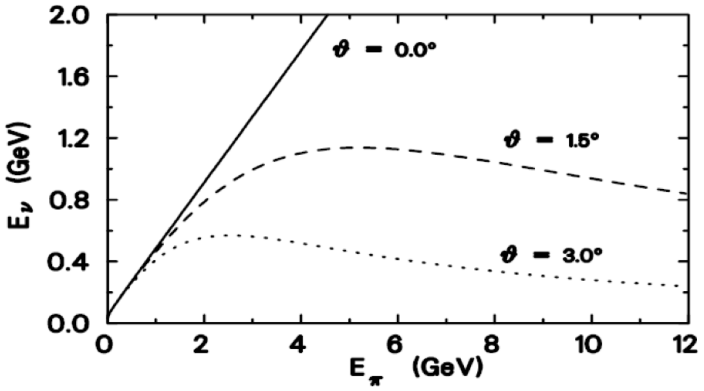

Figure 2.2: Energy of a neutrino coming from a pion decay as a function of pion energy, for different decay angles [51].

When produced in the same direction as the parent, the neutrino's energy is proportional to the parent pion energy. Neutrinos produced at an angle of a few degrees from the parent direction have a relatively small dependence on the pion energy. Figure 2.2 shows the neutrino energy (E_ν) as a function of pion energy (E_π) for different decay angles, described by Eq. 2.2.

The decay kinematics of hadrons in flight allows a broad-band pion beam to create an off-axis narrow band neutrino beam. As the off-axis angle increases, the energy peak narrows and moves to lower energies. This is extremely useful for neutrino oscillation experiments since by choosing the appropriate angle, the energy spectrum peak can be selected to correspond to the oscillation maximum. The T2K off-axis beam (OAB) configuration has been set to 2.5^o. Figure 2.3 shows the expected

neutrino spectrum for different off-axis angles plotted with the muon neutrino survival probability for T2K, displaying the peak of the neutrino spectrum for a 2.5^o off-axis beam coincides with the oscillation maximum [52].

In addition to selecting the peak energy, detectors situated in an off-axis configuration have the following benefits:

- Off-axis neutrino flux at a desired energy (oscillation maximum) will be greater than on-axis.
- Background of intrinsic ν_e is less at the off-axis position.
- Fewer higher energy neutrinos which can be mis-reconstructed as lower energy neutrinos or produce NC π^0 that can contribute to the ν_e backgrounds at SK (described in Section 2.5.1).

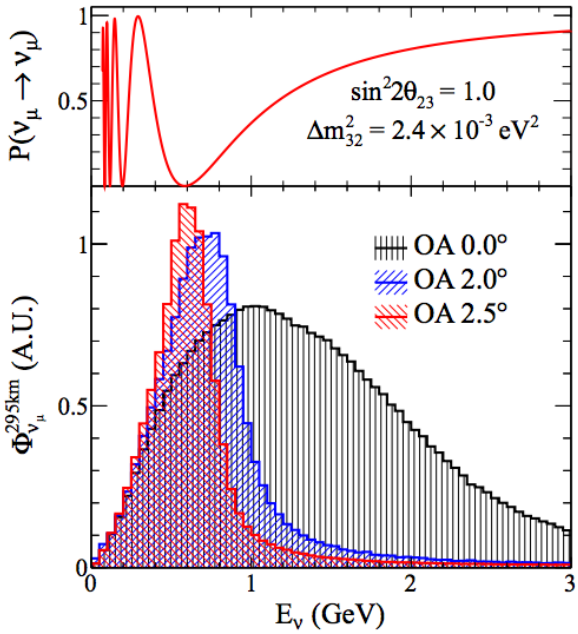

Figure 2.3: Muon neutrino survival probability at 295 km and neutrino energy spectra for different off-axis angles: on axis (black), 2 degrees off-axis (blue) and 2.5 degrees off-axis (red) [52].

2.1.2 JPARC Accelerator

The T2K neutrino beam is produced at the Japan Proton Accelerator Research Complex (J-PARC) in Tokai Japan.

To accelerate the protons to their desired energy, the primary beamline uses several acceleration steps. A linear accelerator, accelerates H^- atoms up to an energy of 181 MeV. The beam is converted to H^+ atoms by a charge stripping foil at the injection to the Rapid Cycling Synchrotron (RCS) which accelerates the protons up to 3GeV. The RCS feeds protons into the Main Ring (MR) proton synchrotron which further accelerates the protons to 30 GeV. Protons are extracted from the MR in two points, slow extraction for the hadron beamline and fast extraction for the neutrino beamline.

In fast extraction, eight proton bunches are extracted in a single revolution of the MR, this gives the extracted beam a distinct timing signature. Table 2.1 gives the parameters of the J-PARC main ring used for fast extraction.

Circumference	1567 m
Beam power	$\sim$ 750 kW
Beam kinetic energy	30 GeV
Beam intensity	$\sim 3 \times 10^{14}$ p/spill
Spill cycle	$\sim$ 0.3 Hz
Number of bunches	6 or 8/spill
RF Frequency	1.67 - 1.72 MHz
Spill width	$\sim$ 5 μsec

Table 2.1: J-PARC Main Ring (MR) parameters for fast extraction [50].

2.1.3 Neutrino Beamline

The protons are extracted into the neutrino beamline, which consists of two sections, the primary beamline that guides the proton beam so that it is directed towards the T2K detectors and the secondary beamline, where protons strike a target to produce secondary hadrons, which are focused by electromagnetic horns, and decay in flight to produce neutrinos. A sketch of the neutrino beamline is shown in Fig 2.4.

Primary Beamline

The primary beamline consists of a preparation section (54 m), an arc section (147 m), and a final focusing section (37 m). In the preparation and arc sections the beam

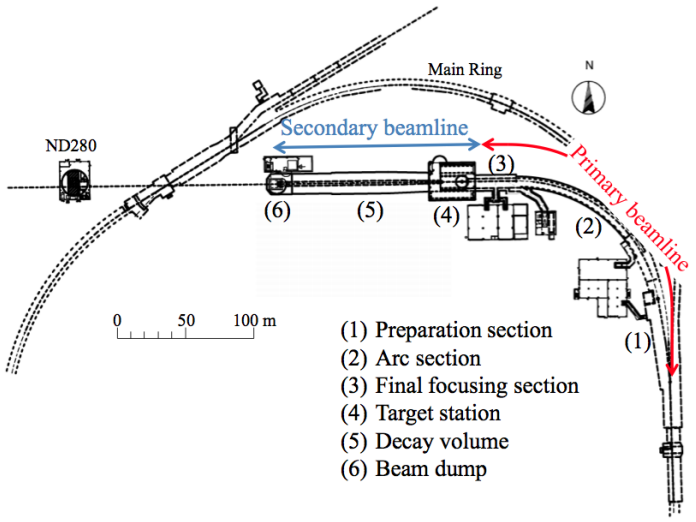

Figure 2.4: T2K neutrino beamline [50].

is steered and focused with dipole and quadrapole magnets. In the arc section the beam is bent by 80.7 degrees so that it is directed towards ND280 and SK. In the final focusing section the beam is guided and focused onto the target.

To ensure that the primary beam losses are low and that stable neutrino beam production is maintained, the primary beam is monitored at several locations. The intensity, position, profile and beam loss are measured by five current transformers (CTs), 21 electrostatic monitors (ESMs), 19 segmented emission monitors (SSEMs) and 50 beam loss monitors (BSMs) respectively.

Secondary Beamline

The secondary beamline shown in Fig 2.5, consists of three sections; the target station, decay volume and beam dump.

The target station contains:

- An optical transition radiation (OTR) monitor which measures the beam profile just upstream of the target.
- The target which produces secondary hadrons.
- Three electromagnetic horns used to focus the secondary hadrons.
- A baffle which is a collimator to protect the magnetic horns.

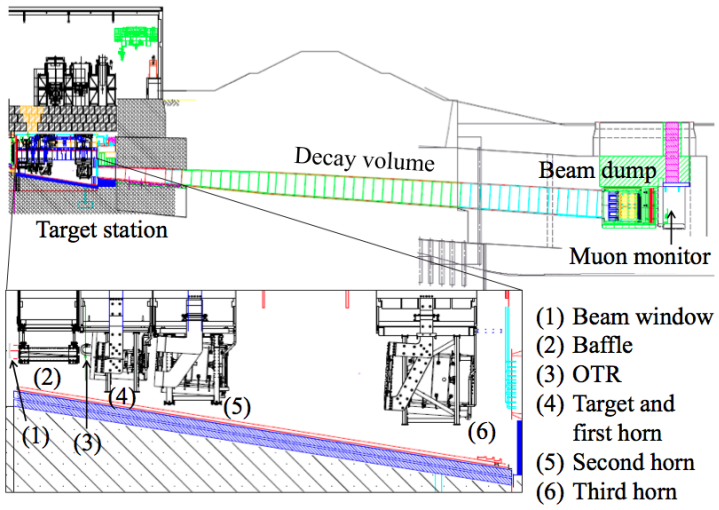

Figure 2.5: Secondary beamline [52].

Target

The target core is a 914 mm long and 26 mm diameter graphite rod (1.8 g/cm^3). The length corresponds to 1.9 pion interaction lengths and 80% of the protons incident on the target interact to produce primarily pions and kaons. Graphite was chosen for its high melting point and good thermal stress resistance. The core is surrounded by a 2 mm graphite tube sealed inside a titanium case and the target is cooled with helium gas flowing between the core and tube. The target is installed inside the inner conductor of the first horn.

Horns

There are three horns in the secondary beamline. The first horn collects the hadrons produced from the target and the second and third horns provide additional focusing.

Each horn consists of two coaxial (inner and outer) conductors which enclose a volume. The horn material is an aluminium alloy, made as thin as possible to minimize pion absorption, yet the horns must be strong enough to withstand the Lorentz force from 320 kA current pulses (presently running at 250 kA) and thermal shock from the beam. The maximum field inside the horns is 2.1 T and varies as 1/r where r is the distance from the horn axis.

Turning on the horns increases the flux of neutrinos at SK by a factor of ∼16 at

the peak energy of the spectrum .

Decay Volume

The majority of pions decay in flight in a volume of helium gas at 1 atm. Helium is used instead of air to reduce pion absorption and tritium production. The decay volume is a steel tunnel 96 m long. The cross sectional area of the decay volume is 1.4 m wide by 1.7 m high at the upstream end and 3.0 m wide by 5.0 m high at the downstream end. The volume is surrounded by 6 m of reinforced concrete for shielding purposes.

Beam Dump

The beam dump is located at the end of the decay volume, it is 75 tons of graphite (1.7 g/cm^3) that measures 3.174 m long, 1.94 m wide and 4.69 m high. Iron plates 2.40 m thick are placed downstream of the graphite core. Downstream of the iron plates is the muon monitor. Muons with a momentum greater than 5.0 GeV/c will be able to pass through the beam dump and can be measured by the muon monitor.

Muon Monitor (MUMON)

The MUMON detector consists of two components, ionization chambers and semi conductor detectors. They measure the profile of the muons on a bunch by bunch basis to monitor the neutrino beam intensity and direction. The goal of the muon monitor is to measure the neutrino beam direction to a precision of 0.25 mrad, corresponding to a 3 cm precision on the muon profile centre. The system measures the neutrino beam intensity indirectly, only observing the portion arising from high energy hadrons.

2.2 Neutrino Flux Simulation

The prediction of the neutrino flux and spectrum at the T2K detectors is based on a simulation that begins with the primary proton beam before it hits the target and ends with the decay of hadrons or muons that produce neutrinos [52].

The simulation of the primary interactions of the 30 GeV proton beam on the target is based on NA61/SHINE data [53]. Hadronic interactions where the beam interacts with the target or baffle are simulated by FLUKA [54]. Kinematic information for particles emitted from the target is saved and transferred to the JNUBEAM

	Particle Decay Products	Branching Fraction (%)
π^+	$\rightarrow \mu^+\nu_\mu$	99.9877
	$\rightarrow e^+\nu_e$	1.23×10^{-4}
K^+	$\rightarrow \mu^+\nu_\mu$	63.55
	$\rightarrow \pi^0\mu^+\nu_\mu$	3.353
	$\rightarrow \pi^0 e^+\nu_e$	5.07
K^0_L	$\rightarrow \pi^-\mu^+\nu_\mu$	27.04
	$\rightarrow \pi^- e^+\nu_e$	40.55
μ^+	$\rightarrow e^+\bar{\nu_\mu}\nu_e$	100

Table 2.2: Neutrino-producing decay modes considered in JNUBEAM and their branching ratio in percentage. The π^-, K^- and μ^- modes are the charge conjugates of π^+, K^+ and μ^+ respectively [52].

simulation. In JNUBEAM a detailed geometry of the secondary beamline is implemented using GEANT3 [55]. Further hadronic interactions in JNUBEAM that occur outside of the target are simulated using GCALOR [56]. In the simulation, particles are propagated through the decay volume until they interact or decay.

In JNUBEAM, $\pi^\pm$, $K^\pm$,$K^\pm_L$ and $\mu^\pm$ decays are considered as sources of neutrinos, the branching fractions of the decays listed in Table 2.2. The neutrino kinematic variables and probability are based on the decay phase space density and branching fractions. The neutrino energy in the centre of mass frame is assigned based on the decay kinematics, the neutrino is then boosted into the laboratory frame under the assumption that it points towards the T2K detectors.

Figure 2.6 shows the predicted flux at SK, for different neutrino flavours. Also Table 2.3 gives the prediction of the relative fractions of each flavour, in bins of $0-1.5$, $1.5-3.0$ and >3.0 GeV. The ν_e flux, which constitutes an irreducible background for the study of $\nu_\mu \rightarrow \nu_e$ oscillations, accounts for less than 1% of the flux below 1.5 GeV, and the $\bar{\nu}_\mu$ contamination is $\sim 5\%$. In the intermediate ($1.5-3.0$ GeV) and high energy bin, the relative fraction of ν_e increases as the contribution from the decays of focused kaons becomes significant. Also in the intermediate energy bin weakly focused forward going pions, including π^-, become more significant increasing the flux of $\bar{\nu}_\mu$. Fig 2.7 shows the ν_μ flux at SK broken down into the parent particle that produces the neutrino, it can be seen at higher energies the contribution from kaons plays a significant role.

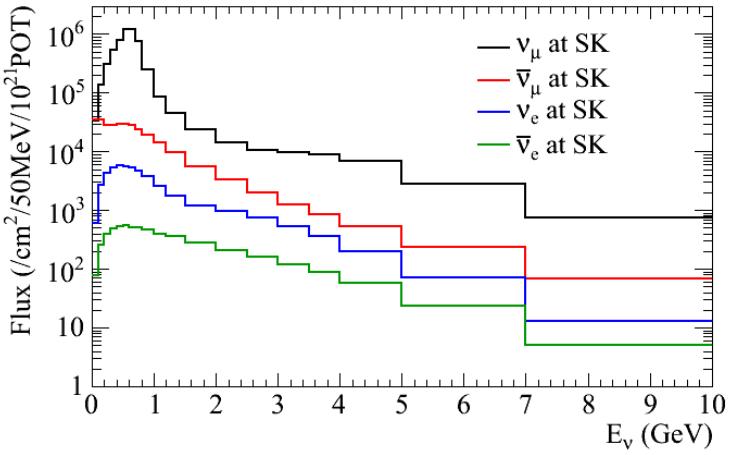

Figure 2.6: Neutrino flux prediction for all flavours at SK [37].The flux is expressed in terms of cm^2/50 MeV/ 10^{21} protons on target (POT).

	Energy Range (GeV)		
Flavour	0 -1.5	1.5 - 3.0	>3.0
ν_μ	0.9363	0.7719	0.8821
$\bar{\nu}_\mu$	0.0542	0.1729	0.0795
ν_e	0.0085	0.0451	0.0304
$\bar{\nu}_e$	0.0010	0.0100	0.0080

Table 2.3: The fraction of the total flux by flavour in bins of neutrino energy [52].

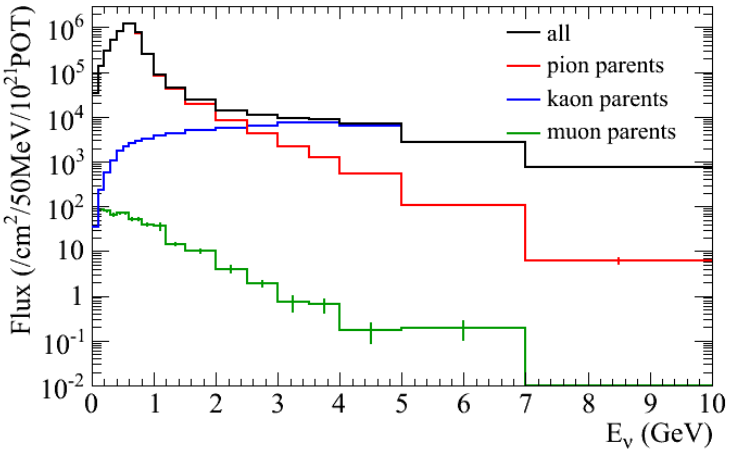

Figure 2.7: ν_μ flux prediction at SK broken down into the parent particle that produces the neutrino [57]. The flux is expressed in terms of $cm^2/50$ MeV/ 10^{21} protons on target (POT).

2.3 Neutrino Interactions

Neutrinos can interact via the weak force with atomic nuclei through a variety of processes. The dynamics of the nuclear targets are very complex and not fully understood, making uncertainties in neutrino interaction models one of the main sources of error for neutrino experiments.

Figure 2.8 shows the charged current neutrino cross sections as a function of energy, broken down into the quasi-elastic (dashed), single pion (dot-dash) and deep inelastic scattering (dotted) processes. It can be seen that near the peak energy of T2K, $\simeq 0.7$ GeV the dominant neutrino interaction is Charged-Current Quasi-Elastic (CCQE) [58].

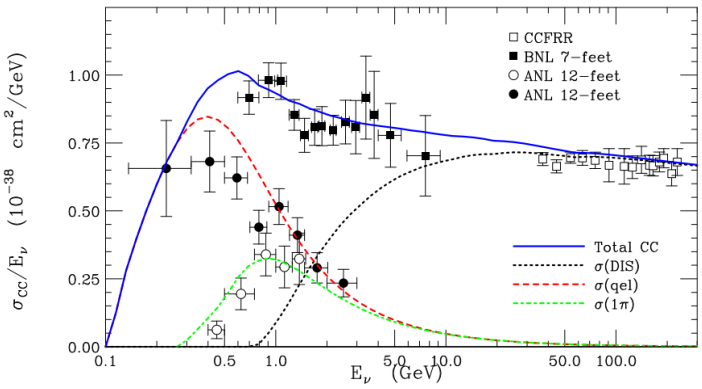

Figure 2.8: Charged current neutrino cross sections as a function of energy (in GeV). Shown are the contributions from quasi-elastic (dashed), single pion (dot-dash) and deep inelastic scattering (dotted) processes. Also plotted is data from various neutrino cross section experiments [58].

The CCQE interaction is of the form

$$\nu_\ell + n \rightarrow \ell^- + p, \tag{2.3}$$

where ℓ is the lepton flavour. Experimentally, this interaction is favourable since the initial neutrino energy can be determined from the outgoing lepton momentum and angle. Ignoring Fermi momentum, the neutrino energy can be reconstructed from

$$E_\nu^{QE} = \frac{m_p^2 - (m_n - E_b)^2 - m_l^2 + 2(m_n - E_b)E_l}{2(m_n - E_b - E_l + p_l \cos(\theta_l))}, \tag{2.4}$$

where m_p is the proton mass, m_n the neutron mass and E_b is the binding energy of

a nucleon inside the target nucleus. The index l indicates the outgoing lepton and θ_l is the angle the outgoing lepton makes with respect to the direction of the neutrino in the lab frame. This makes CCQE interactions the preferred channel and is the primary way in which neutrinos are measured at the T2K experiment. A selection of CCQE interactions is made at both ND280 and SK in order to do oscillation studies.

Neutrino energies are incorrectly determined when other interactions are misidentified as CCQE. These include resonant 1π production where a neutrino interacts with a target nucleus, exciting it to a resonance. The resonance generally decays to a nucleon and pion. This can be misidentified as a CCQE interaction if the pion is misidentified. A related process is coherent pion production, where the neutrino interacts with the nucleus as a whole to produce the final state pion. Another interaction, deep-inelastic scattering becomes a dominant interaction mode at higher energy scales where the neutrino interacts with individual partons as opposed to the entire nucleon, this leads to the nucleon breaking apart and a large number of particles in the final state. These backgrounds can occur through both CC and NC channels.

Further complications come from secondary interactions in the nucleus, known as final state interactions. These interactions can modify the event topology masking the true nature of the neutrino interaction.

Fig 2.9 shows the expected reconstructed ν_μ neutrino energy distribution, for selected events at SK, in the case of no oscillation. The unfilled region is from CCQE interactions while the hatched area is non-QE contribution.

2.3.1 Interaction Simulation

Neutrino interactions in the T2K detectors are simulated primarily by the NEUT neutrino event generator [60]. The NEUT package, produces a list of neutrino interactions and their product particles from a given neutrino flux and energy spectrum. The neutrino generator includes all neutrino interaction models and cross section information that is needed to simulate neutrino interactions in the different detector materials of ND280 and SK.

NEUT models neutrino interactions in a two step process. Firstly a primary neutrino-nucleon interaction produces a set of particles. Those particles then undergo secondary interactions as they travel through the nucleus. In NEUT the following interactions are considered:

- Charged/neutral current (quasi-)elastic scattering, ($\nu N \rightarrow lN'$)

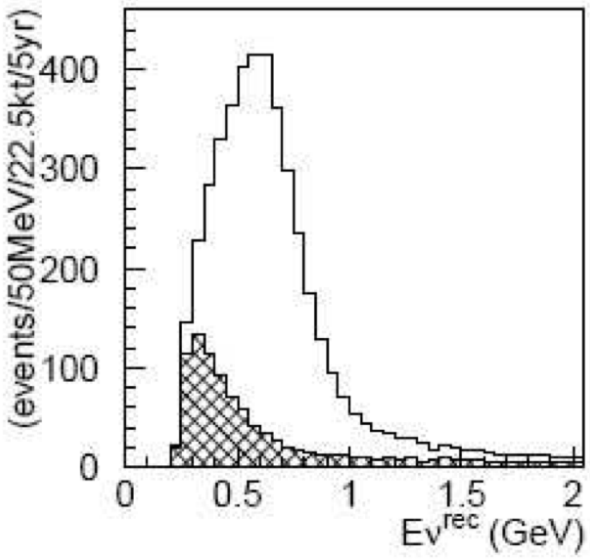

Figure 2.9: The expected reconstructed neutrino energy distribution for no oscillation at SK. The hatched area shows the non-CCQE component [59].

- Charged/neutral current single π production, ($\nu N \rightarrow lN'\pi$)
- Charged/neutral current single γ production, ($\nu N \rightarrow lN'\gamma$)
- Charged/neutral current single K production, ($\nu N \rightarrow l\Lambda K$)
- Charged/neutral current single η production, ($\nu N \rightarrow lN'\eta$)
- Charged/neutral current deep inelastic scattering,($\nu N \rightarrow lN'$hadrons)
- Charged/neutral current coherent production, ($\nu^{16}\mathrm{O} \rightarrow l\pi X$)

where N and N' are nucleons, l is the lepton and X is the remaining nucleus.

For free nucleons, CCQE primary interactions are simulated using the Llewellyn-Smith model [61]. In the case of bound nucleons the relativistic Fermi gas model by Smith and Moniz [62] is used to simulate the nuclear medium effects. The principal parameter for modelling quasi-elastic cross sections is the axial mass form factor M_A.

Resonant pion production processes are simulated using the Rein and Sehgal model [63] which considers the amplitude and decay probabilities of different baryon resonances. Coherent pion production is modelled by the neutrino interacting with the nucleus as a whole [64]. For deep-inelastic scattering, the cross section is modelled using the nucleon structure functions [65]. For secondary interactions, a Woods-Saxon

model of the nucleon density distribution is used to simulate the particles produced from primary interaction propagating through the nucleus [66].

2.4 ND280 Detector Complex

The neutrino spectrum, flavour content and interaction rates of the unoscillated beam are measured at ND280, 280 m downstream from the production target. These measurements are used to constrain information about the expected interactions at SK. There is also an on-axis detector INGRID used to measure the direction, profile and intensity of the neutrino beam. The near detectors are crucial in reaching the physics goals of T2K, stated in Section 2.0.1.

The detectors are located in an excavated shaft in the ND280 hall shown in Fig 2.10. The shaft has a diameter of 19 m and a depth of 37 m. The bottom of the shaft is split into 3 levels; B1, 24 m below the surface, is the site of the off-axis detector, SS, 33 m from the surface, is the site of the horizontal modules of the INGRID detector and B2, 37 m from the surface, is the site of the bottom modules of the vertical INGRID detector.

2.4.1 On-Axis Detector: INGRID

The Interactive Neutrino GRID (INGRID) is designed to measure the direction, profile and intensity of the neutrino beam. The detector consists of fourteen modules placed in a horizontal and vertical cross pattern which samples an area of 10×10 m^2 and with the centre on-axis with the neutrino beam. Two additional modules are located at off-axis positions outside the main cross, used to check the azimuthal symmetry of the neutrino beam. The INGRID detector is shown in Fig. 2.11. Each INGRID module consists of alternating planes of plastic scintillator and iron plates. Muons originating from neutrino interactions within the detector produce light in the scintillator bars that is readout by wavelength shifting (WLS) fibres. Each module contains veto planes to reject muons originating from outside the detector.

The neutrino beam centre is measured to a precision better than 10 cm. This corresponds to 0.4 mrad precision at the near detector pit, a crucial measurement in reducing the systematic error arising from the uncertainty of the beam direction.

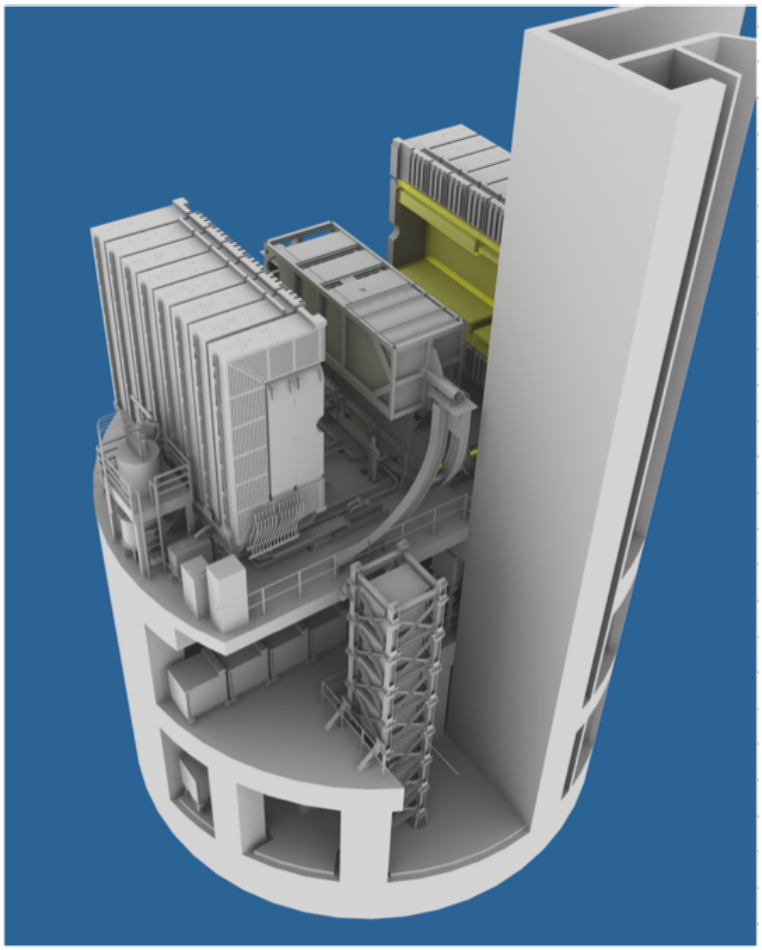

Figure 2.10: ND280 detector complex. Off-axis detector is on upper level surrounded by UA1 magnet. INGRID detector is on the lower two levels [50].

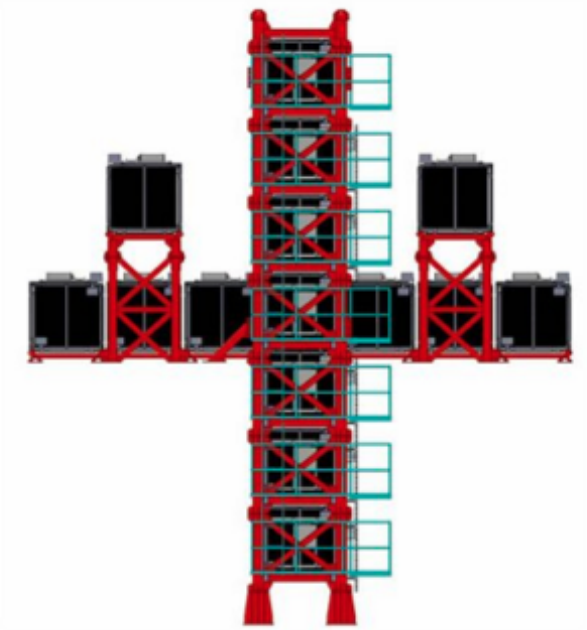

Figure 2.11: The Interactive Neutrino GRID (INGRID) [50].

2.4.2 Off-Axis Detector

The ND280 off-axis detector has been designed to measure the neutrino beam spectrum and flavour content as well as interaction cross sections. ND280 is pivotal in constraining properties of the neutrino beam used in oscillation analyses.

ND280 measures the main backgrounds for the ν_e appearance measurement which are intrinsic ν_e and neutral current interactions that produce a π^0. Also to reduce the uncertainties in the ν_e appearance and ν_μ disappearance analyses, the ν_μ event rate and spectrum are measured at ND280.

The ND280 detector comprises several sub-detectors, shown in Fig. 2.12, with the neutrino beam entering from the left. For reference the ND280 coordinate system is a right handed system with the z axis in the direction of the neutrino beam and the y axis opposing the direction of gravity. A brief summary of each sub-detector and their purpose is as follows:

- Magnet: The ND280 sub-detectors are operated within the UA1 magnet which produces a field of 0.2 T aligned perpendicular (+x direction) to the neutrino beam direction. The magnetic field is produced by aluminium coils operated

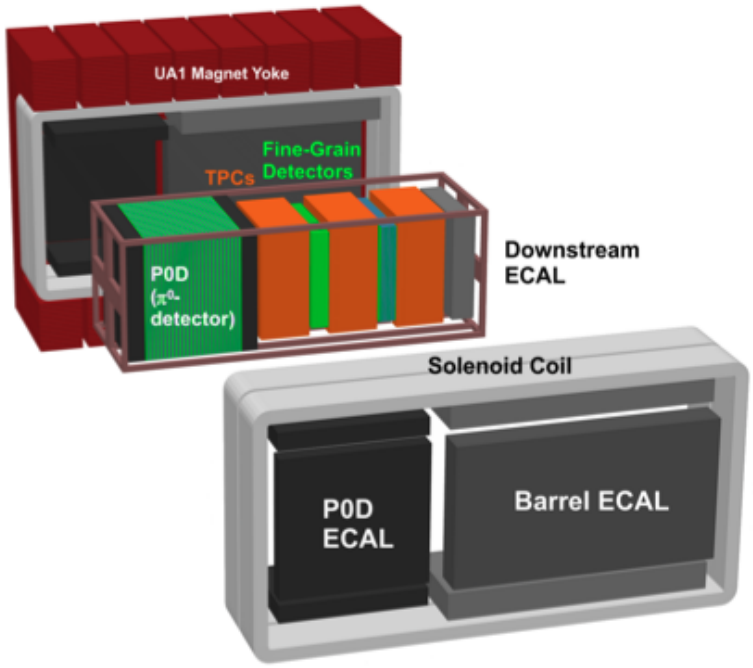

Figure 2.12: ND280 off-axis detector [50].

with a current of ∼3 kA. The inner dimensions of the magnet , where the ND280 sub detectors are installed, is 3.5 m × 3.6 m × 7.0 m. Charged particles will curve in the magnetic field allowing for a measurement of the momentum. A more detailed explanation of the magnet is outlined in Section 4.1.1.

- Tracker: The tracker is designed to measure the spectrum of particles produced in neutrino interactions, most importantly muons and electrons from CCQE interactions. The tracker is composed of

  – Time Projection Chambers (TPCs): There are 3 TPCs that measure the charge and momenta of charged particles. Also the TPCs measure energy loss to identify particles, in particlular to separate muons and electrons. An in-depth description of the TPCs is given in Chapter 3.

  – Fine Grained Detectors (FGDs): The FGDs are placed upstream of the 2nd and 3rd TPCs. They provide the target mass for neutrino interactions as well as tracking of charged particles originating from an interaction vertex. The FGDs consist of finely segmented polystyrene scintillator bars. The bars are 9.61 mm × 9.61 mm × 1864.3 mm and have a wave-

length shifting fibre traveling down the centre of the bar. Each wavelength shifting fibre is readout at one end by a silicon multi-pixel photon counter (MPPC) while the other end has a reflective aluminium mirror. The bars are arranged in planes which are orientated perpendicular to the beam direction in alternating x and y directions. Alternating x and y layers allows for the tracking of charged particles within the FGD. Since the detector is highly segmented it can measure the direction and ranges of short tracks which is important for measuring recoil protons from CCQE interactions. The measurement of energy loss within the scintillator bars can be used for particle identification. Each FGD has outer dimensions of 2300 mm × 2400 mm × 365 mm (width × height × depth in beam direction) and contains ∼1.1 tons of target material. The upstream FGD consists of scintillator bars, arranged into 30 layers of 192 bars each. The downstream FGD consists of 14 layers of plastic scintillator alternating with six 2.5 cm thick water panels. The panels are made from thin walled hollow corrugated polycarbonate: they are included to determine the relative neutrino cross sections for carbon and water by comparing the interaction rates in the two FGDs.

- Pi-Zero Detector (PØD): The PØD is a tracking scintillator detector which provides a large target mass, located upstream of the tracker. The main role of the PØD is to measure neutral current neutrino interactions that produce neutral pions of the form, $\nu_\mu + N \rightarrow \nu_\mu + \pi^0 + X$. There are large layers of water within the PØD so that π^0 production for water can be measured, which is an important systematic uncertainty for the SK detector. The PØD consists of x and y tracking planes made from plastic scintillator, readout by wavelength shifting fibres. Situated between the scintillator planes are lead and brass foils as well as fillable water target bags. The metal sheets are included to increase the conversion probability for photons to e^+, e^- pairs so that they can be tracked. The scintillator bars are segmented to provide tracking of charged particles and electromagnetic showers from electrons and photons produced from π^0s. The up and downstream sections of the PØD are called the upstream ECAL and central ECAL respectively. They are composed of alternating layers of scintillator planes and lead sheets. The central region of the PØD contains the upstream and central water targets, these are made up of alternating scintil-

lator planes, water bags and brass sheets. This configuration makes for good containment of electromagnetic showers originating in the water layers and also provides a veto region. The dimensions of the active target of the entire PØD are 2103 mm × 2239 mm × 2400 mm (width × height × length). The mass of the detector with and without water is 16.1 tons and 13.3 tons respectively. A schematic diagram of the PØD is shown in Fig. 2.13.

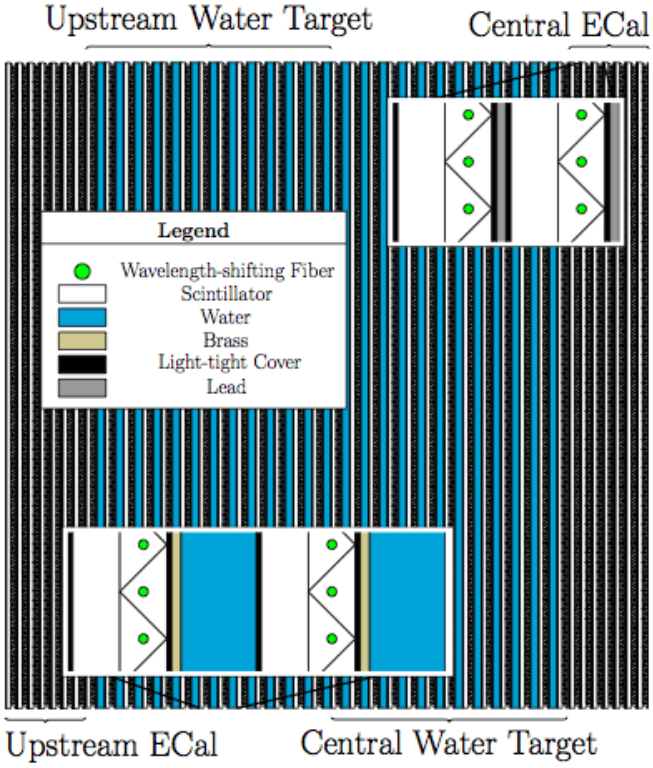

Figure 2.13: A schematic diagram of PØD, beam direction moving from left to right [50].

- Electromagnetic Calorimeter (ECal): The ECal surrounds the PØD and tracker on all sides. The role of the ECal is to detect photons and charged particles exiting from the tracker and to reconstruct π^0s produced in the tracker that cannot be measured by the PØD. The ECal can help determine the particle type for particles exiting the tracker and also provides a veto layer for background interactions occurring outside of the tracker. The ECal is made of 16 modules of three different types. Each module is made up of alternating layers of scintillator bars glued to lead sheets. All scintillator bars have a 40 mm × 10 mm cross

section with an elliptical hole in the centre for a wavelength shifting fibre. The three types of modules are

  - Ds-ECal: Positioned downstream of the tracker the Ds-ECal consists of 34 alternating x, y scintillator layers interspersed with lead sheets 1.75 mm in thickness. The Ds-ECal has a total thickness of 10.6 interaction lengths (X_0) .
  - Barrel ECal: There are six barrel ECals surrounding the tracker on the four sides parallel to the beam axis. Each module has 31 alternating x, y layers each with lead sheets of 1.75 mm thickness for a total of 9.7 X_0.
  - PØD-ECal: Another six PØD-ECal modules surround the PØD on four sides parallel to the beam axis. Each PØD-Ecal module is made of six active scintillator layers separated by five layers of 4 mm thick lead, giving 3.6 X_0.

  The barrel and PØD-ECal modules are mounted on the inside of the UA1 magnet yokes.

- Side Range Muon Detector (SMRD): The SMRD is installed inside the yokes of the magnet and provides tracking for muons leaving the tracker at large angles with respect to the beam axis. The SMRD can reconstruct muon momenta by measuring the range of the particles in the magnet yoke. This gives kinematic information of muons only partially crossing or completely missing the TPCs. The SMRD also provides a trigger for cosmic rays traveling through ND280 and can also determine neutrino events originating from interactions within the magnet. The SMRD is made up of scintillator modules placed in air gaps in the magnet iron yoke. An S-shaped groove has been machined into each scintillator where a wavelength shifting fibre sits. The wavelength shifting fibre is readout by a MPPC.

All of the detectors aside from the barrel and PØD-ECal are supported by a metal basket structure of dimension $6.5\,\mathrm{m} \times 2.6\,\mathrm{m} \times 2.5\,\mathrm{m}(\mathrm{width} \times \mathrm{height} \times \mathrm{length})$. A display of a track passing through all of the detectors in the basket is shown in Fig 2.14.

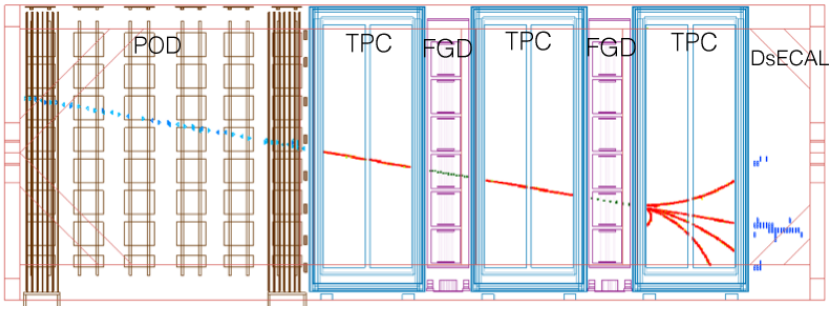

Figure 2.14: This event display shows an event with a muon track entering via the front face of the PØD detector, continuing to the tracker (TPC and FGD) region and producing secondary particles on the way. The secondary particles are then stopped in the DsECal detector [50].

2.4.3 ND280 Monte Carlo

For Monte Carlo simulations, interfaces have been built between the neutrino beam simulation, the neutrino interaction generator NEUT and ND280 software. The neutrino fluxes estimated from beam MC described in Section 2.2 are passed through the ND280 detector geometry and cross section information for the different materials present in the magnet and sub-detectors are used to generate the spatial distribution of neutrino interactions. The propagation of the final state particles from the neutrino interactions are then simulated with GEANT4 [67]. The detailed response of the active detectors, such as scintillator bar light propagation and the electronics response is simulated by a custom software package. The software package also simulates electrons drifting due to electromagnetic fields in the TPCs which is further detailed in Section 4.2.

2.5 Far Detector: Super-Kamiokande

Super-Kamiokande (SK) is the world largest land based water Cherenkov detector, consisting of 50 kton of pure water. The detector is located 1000 m underground (2700 meters of water equivalent or m.w.e.) in the Kamioka mine in the Gifu Prefecture, Japan. SK has been running since 1996 and has made measurements of flavour oscillations in atmospheric, solar and accelerator produced neutrinos.

Charged particles produced from neutrino interactions within the detector, travel through the water at ultra relativistic speeds and emit Cherenkov radiation. Cherenkov

photons travel to the walls of the detector and produce a ring-shaped pattern where they are measured by Photo Multiplier Tubes (PMTs). The hit pattern can be used to measure the vertex, direction, momenta and particle type of the recoil particle.

The detector is cylindrical in shape, 39.3 m in diameter and 41.4 m in height. Figure 2.15 gives the schematic view of Super-Kamiokande. SK is segmented into the outer detector (OD) which is 18 kton of water that surrounds the 32 kton inner detector (ID). The inner detector makes measurements of Cherenkov radiation with 11129, 50 cm diameter PMTs. The PMTs are Hamamatsu R3600 hemispherical PMTs which give a combined quantum and collection efficiency of 20%. The large number of PMTs in the ID gives a 40% coverage so that there is sufficient spatial resolution to obtain important physics quantities. The outer detector contains 1885, 20 cm diameter PMTs [68]. The purpose of the OD is to reject through going cosmic ray muons, it is a cylindrical space about 2 m thick radially and on the cylinder axis on both ends. The ID and OD are separated by a cylindrical structure made of steel scaffolding covered by plastic sheets that optically separate the ID and OD.

The SK detector is calibrated with a number of different sources included cosmic rays and introduced laser light.

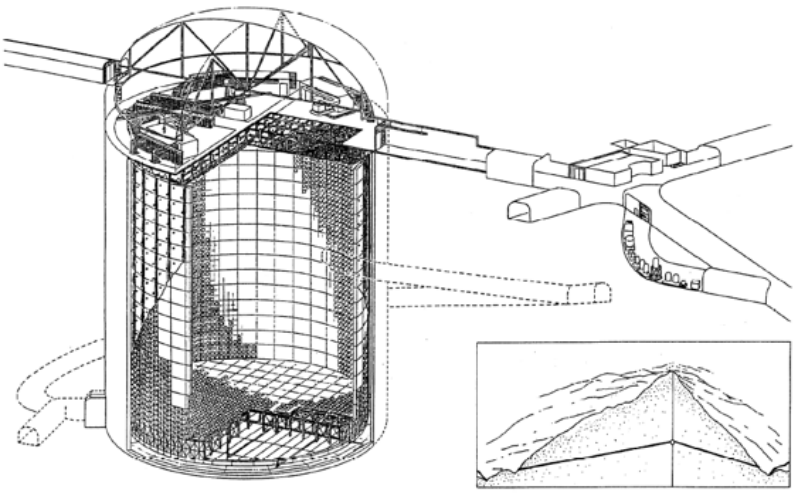

Figure 2.15: Drawing of Super-Kamiokande Detector [50].

2.5.1 Cherenkov Radiation Detection

For a particle to emit Cherenkov radiation the speed of the particle must exceed the velocity of light in that medium, $v_{particle} > \frac{c}{n}$,where n is the index of refraction and c is the speed of light in a vacuum. When this condition is met the particle creates an electromagnetic shock wave similar to the phenomena of a sonic boom occurring for objects moving faster than the speed of sound. The Cherenkov light emitted forms a conical shape and is emitted at a definite angle with respect to the trajectory of the particle given by

$$\cos\theta_C = \frac{1}{\beta n(\omega)}, \tag{2.5}$$

where n is the index of refraction dependent on the wavelength ω and β is the speed of the particle. The energy loss of a particle due to Cherenkov radiation is negligible compared to collisional losses.

The Cherenkov cone produces ring shaped pattern on the walls of SK and there are distinct patterns for the Cherenkov ring emitted by electrons and muons. Muons starting and stopping within the detector produce a sharp well defined Cherenkov ring. Electrons undergo much more multiple scattering due to their small mass and almost always induce an electromagnetic shower, the shower produces a fuzzy ring pattern due to many Cherenkov rings overlapping. Event displays of muon-like and electron-like events measured by SK are shown in Fig. 2.16.

The Cherenkov light can be used to reconstruct the location where the recoil particle originated, the direction of the particle as well as its momenta and type. One major background for ν_e appearance at SK originates from π^0s produced in neutrino interactions. When a π^0 is produced it decays into 2 photons, which appear as electron-like rings in SK. When only one of the photons is reconstructed these events look the same as ν_e events.

2.5.2 Super-Kamiokande Monte Carlo

Similar to ND280, interfaces have been built between the neutrino beam simulation, the neutrino interaction generator NEUT and SK detector Monte Carlo. The propagation of particles in SK generated by NEUT is handled by SKDETSIM, software based on the GEANT3 package [55]. The package also simulates the propagation of the Cherenkov light through the water. For hadronic interactions in water the

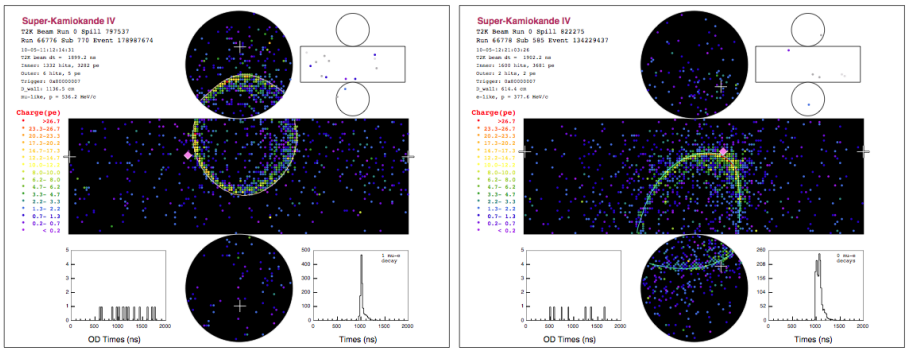

Figure 2.16: Super-Kamiokande events showing a muon like ring (left) and electron like ring(right). Each coloured point represents a PMT the colour corresponding to the amount of charge. The reconstructed cone is represented by a white line [50].

CALOR package is used [69].

The parameters used in the detector simulation have all been tuned with various laser calibration sources. Various samples including the reconstructed momentum spectrum of electrons from the decay of cosmic ray muons, neutral pions created from atmospheric neutrinos and cosmic ray muons which have been determined to stop inside the inner detector all show agreement between data and simulation to be within a few percent.

Chapter 3

The T2K Time Projection Chambers

The T2K Time Projection Chambers are critical in the measurement of the unoscillated neutrino spectrum and flavour content. In order to interpret how these measurements are made and how to assess the associated errors, one must be familiar with the physical processes that occur in Time Projections Chambers. A description of gaseous detector principles is included in this chapter along with a general summary of how TPCs operate. Also presented is a detailed description of the design and performance of T2K TPCs and their subsystems.

3.1 Gaseous Detector Principles

3.1.1 Primary Ionization

For a charged particle passing through matter, the particle will lose energy through inelastic collisions with the atomic electrons of the material.

For a given collision an atom in the material will either undergo excitation or ionization. For the ionization of an atom X, a free electron and ion are created, described by the reaction

$$X + p \rightarrow X^{+} + p + e^{-}, \tag{3.1}$$

where p is a charged particle. Electrons and ions created by the incident particle are known as primary ionization. In these ionizations a large amount of energy can be

transferred to the electron so that it can ionize other atoms creating additional ion-electron pairs. These high energy electrons are called delta-rays and the ion-electron pairs that they produce are known as secondary ionization.

The occurrence of ionization reactions is statistical in nature so a useful quantity of measure is the average number of ion-electron pairs created for a given energy loss. For gases, the average is approximately 1 ion-electron pair per 30 eV of energy lost. The average value does not depend very strongly on the incident particle type and only weakly on the type of gas.

The ionization process has an energy threshold and since low energy transfers are more probable, excitation reactions generally dominate. No free electrons or ions are created in excitation, however the excited molecule may undergo further reactions that do result in ionization [70].

3.1.2 Energy Loss by Atomic Collisions

The inelastic collisions that cause either ionization or excitation are statistical in nature, however the number of collisions per macroscopic path length is very large and the fluctuations in the total energy loss within a material is small. A quantity of interest is the average energy loss per path length, dE/dx, which is given by the Bethe-Bloch formula

$$-\frac{dE}{dx} = 4\pi N_A r_e^2 m_e c^2 z^2 \frac{Z}{A}\frac{1}{\beta^2}\left[\frac{1}{2}\ln\frac{2m_e c^2\beta^2\gamma^2 T_{max}}{I^2} - \beta^2 - \frac{\delta(\beta\gamma)}{2}\right], \tag{3.2}$$

where z is the charge of the incident particle, Z is the atomic number of the absorbing material, A is the atomic mass number, N_A is Avogadro's number, r_e is the classical electron radius, m_e is the electron mass, I is the mean excitation energy of the atom and β and γ are relativistic kinematic variables. T_{max} is the maximum kinetic energy that can be imparted to a free electron and δ is a function that takes into account corrections from density effects. The density effect arises from the fact that the electric field of the incident particle can polarize atoms along its path. This polarization will shield electrons that are far away from the full electric field intensity [71].

The energy loss for a muon in copper for a wide range of momenta is shown in Fig. 3.1 [71]. At non-relativistic energies, dE/dx is dominated by the $1/\beta^2$ term (Eq. 3.2) and decreases with increasing velocity until $v \simeq 0.96c$ where a minimum

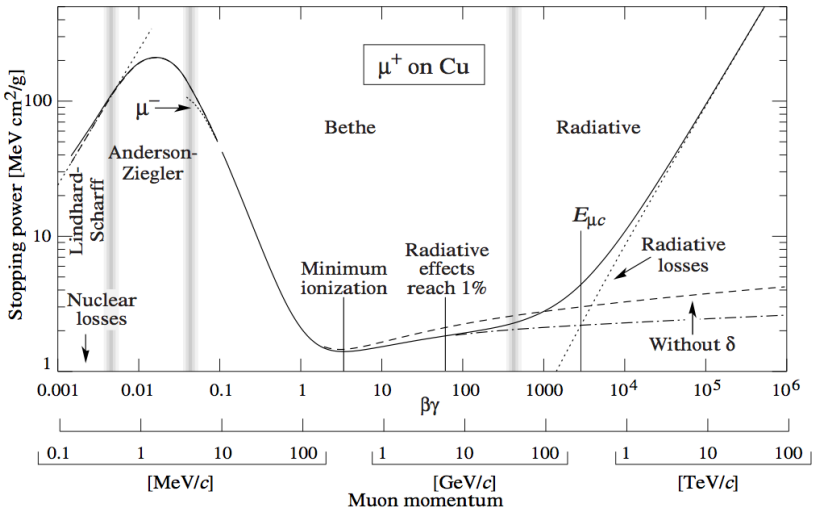

Figure 3.1: Average energy loss given by the Bethe-Bloch formula as a function of $\beta\gamma$ for μ^+ on copper [71].

is reached. Particles in this region are known as minimum ionizing. As the energy increases beyond this point, $1/\beta^2$ becomes almost constant and dE/dx rises again due to the logarithmic term, an effect is known as the relativistic rise. This rise is slightly canceled by the density effect.

The dE/dx as a function of momentum for different particles in the minimum ionizing region is shown in Fig. 3.2 [71]. It can be seen that by reconstructing the energy loss and momentum one can distinguish one particle type from an other.

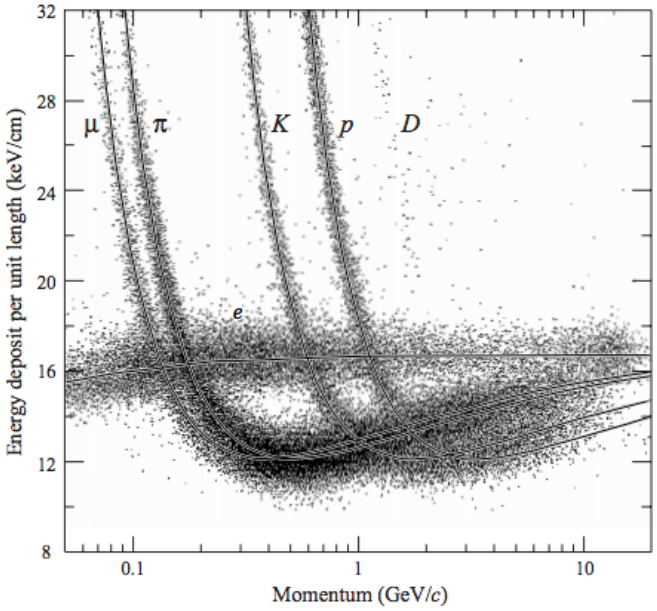

Figure 3.2: Energy deposit measurements, in the minimum ionizing region, made by the PEP4/9-TPC at the Stanford Linear Accelerator. Energy loss is shown for several different incident particles [71].

3.1.3 Energy Loss Distribution

The Bethe-Bloch equation describes the mean value of the energy loss per path length, however the statistical fluctuations in the number of collisions and the energy transferred in each collision will cause energy losses not equal to the mean.

For a mono-energetic beam of particles passing through a given material there will be a distribution for the energy loss. The distribution is asymmetric about the peak since there is a possibility of large energy transfers in a single collision. These events are rare but add a long tail to the high energy side of the distribution. Therefore the

mean energy loss is not at the peak of the distribution but is displaced due to the high energy tail, while the position of the peak gives the most probable energy loss. The energy loss distribution for particles traversing a thicker portion of material can represented by the straggling function. Figure 3.3 shows the straggling function for particles traversing 1.2 cm of argon gas [72].

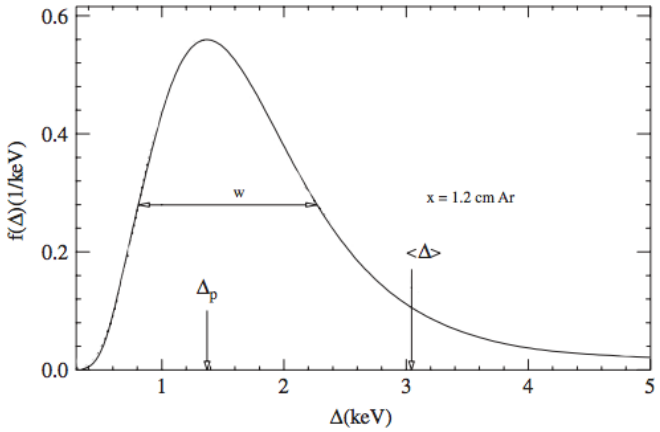

Figure 3.3: Straggling function, $f(\Delta)$ for particles with $\beta\gamma = 3.6$ traversing 1.2 cm of Ar gas. Δ_p is the most probable energy loss while $\langle\Delta\rangle$ represents the mean energy loss [72].

Section 3.3.9 outlines how the energy loss distribution and Bethe-Bloch formula provide the necessary information to perform particle identification in the TPCs.

3.1.4 Transport in Gases

Drift

In the presence of an electric field, the electrons and ions freed in ionization reactions are accelerated along the field lines. This acceleration is interrupted by collisions with gas molecules which limit the maximum velocity that can be reached by the ionization products. The average velocity of the electrons is known as the drift velocity. Compared to thermal velocities the drift velocity is much smaller. The mobility, μ, of the ions is defined as

$$\mu = \frac{v}{E}, \tag{3.3}$$

where v is the drift velocity and E the electric field strength. For an electron charge e, mass m that drifts through the gas with a mean collision time of τ, the drift velocity

can be expressed as

$$v = \frac{eE\tau}{m}, \tag{3.4}$$

known as the Townsend expression.

Diffusion

Drifting electrons undergo multiple collisions with gas molecules altering the direction of the velocity of the particles, causing a grouping of charge to diffuse as it travels in a gas. For an initial point-like cluster of charge, the distribution of the charge after diffusing a time t spreads out to become Gaussian. The linear distribution of charge is given by

$$\frac{dN}{dx} = \frac{N_o}{\sqrt{4\pi Dt}} \exp\left(\frac{-x^2}{4Dt}\right), \tag{3.5}$$

where N_o is the total number of charges, x is the distance from the point of creation and D is the diffusion coefficient. The rms of the spread is therefore

$$\sigma_x = \sqrt{2Dt}. \tag{3.6}$$

The diffusion is related to the mobility by the Einstein relation

$$\frac{D}{\mu} = \frac{kT}{e}, \tag{3.7}$$

where k is the Boltzman constant and T is the temperature. Using Eqs. 3.3, 3.4 and assuming the average velocity squared for an ideal gas $\langle v^2 \rangle = 3kT/m$ the diffusion can be expressed as

$$D = \frac{1}{3}v^2\tau = \frac{1}{3}v\lambda, \tag{3.8}$$

where λ is the mean free path between collisions.

The diffusion and drift velocity are strongly dependent on the atomic properties of the gas.

Electron capture

While the electrons drift in the gas there are two processes that can recapture the electrons, recombination and electron attachment. Recombination occurs when an ion-electron pair attracted by electric force recombine. Electron attachment occurs when electrons are captured by molecules and form negative ions. For molecules with an almost full outer electron shell, adding an electron is energetically favourable and such molecules are known as electronegative. The presence of any electronegative molecules in a gas can reduce the efficiency of the electron collection in a gas detector. Such gases include H_2O and O_2.

3.1.5 Amplification

Electron multiplication can occur in gaseous detectors when ionization electrons acquire enough energy from the electric field to also ionize the gas. The resultant secondary electrons can cause further ionization and so on. This results in an ionization cascade or avalanche. If λ_I is the mean free path of the electron for secondary ionization then $\alpha = 1/\lambda_I$ is the probability of ionization per unit path length. For n electrons traveling a path length dx there will be

$$dn = n\alpha dx, \tag{3.9}$$

electrons created. Integrating gives the number of electrons created in a path length x,

$$n = n_0 \exp(\alpha x), \tag{3.10}$$

where n_0 is the original number of electrons. The multiplication factor or gain is

$$M = n/n_0 = \exp(\alpha x). \tag{3.11}$$

The number of electron-ion pairs in an avalanche is a proportional amplification of the primary and secondary ionization electrons. The resulting current after amplification is greatly increased and therefore less sensitive to noise and more desirable for signal processing.

3.2 Time Projection Chambers

Time projection chambers are the most sophisticated of the gaseous ionization detectors. They were invented by David Nygren in the late 1970's [73]. TPCs provide three dimensional tracking, giving the spatial location of several points along a charged track path and the energy loss, dE/dx within the detector gas. A uniform electric field drifts ionization electrons in either a gas or liquid towards 2D segmented readout planes. The third coordinate is given by the drift time of the electrons. The detector design usually has a high voltage cathode at the centre with anodes corresponding to the readout planes. Gaseous TPCs often operate within a magnetic field so that the track curvature can give an estimation of a particle's momentum. Ionization measurements made along the length of the track can be combined to identify the type of particle, given the momentum.

TPCs generally have large drift distances, which provides a large active volume of the detector but also presents some challenges. The long distances can make the device sensitive to small distortions in the electric field. Distortions can arise from imperfections in the TPC construction such as deformations of the readout surface. Also for detectors with large drift distances, some events can have long readout times possibly reducing the sampling rate of the detector.

A strong magnetic field parallel to the electric field can reduce transverse displacements due to distortions in the electric field, for stronger fields the electrons follow the magnetic field lines. In this regime the device is sensitive to small distortions in the magnetic field, so it is necessary to precisely measure the magnetic field. Corrections to non-uniformities in the fields can be determined from control samples such as photoelectrons produced on the cathode, or ionizing the gas with a UV laser.

The spatial resolution of the detector is determined by several factors. A larger transverse diffusion will degrade the spatial resolution, using a magnetic field parallel to the electric field can reduce the diffusion by a factor of

$$\sigma_{D_x}(B)/\sigma_{D_x}(0) = \frac{1}{\sqrt{1+\omega^2\tau^2}}, \tag{3.12}$$

where τ is the mean collision time and ω is the Larmor frequency.

More finely segmented detectors at the readout plane allow TPCs to have a better spatial resolution and a greater number of ionization measurements to improve the particle identification. The spatial resolution degrades for tracks at an angle to the readout pad boundaries because ionization fluctuations lead to an increase in the

variance of charge sharing between neighbouring pads. For experiments where there is a preferred track direction the pad boundaries are aligned in this direction to reduce the effect.

The drift gas of the TPC must remain very pure in order to avoid electron capture from electronegative gases. For example, O_2 must be kept below a few parts in 10^5 or a large fraction of the drifting electrons will be captured, greatly reducing the performance of the detector.

At the readout plane, gas amplification on the order of $10^3 - 10^4$ is needed to boost signals for conventional charge sensitive amplifiers.

3.2.1 Micro Pattern Detectors

The micromesh gaseous detector (Micromegas) was invented by I. Giomataris, G. Charpak, and collaborators in 1995 [74]. The Micromegas is a thin parallel plate avalanche counter. Electrons from primary ionizations in the TPC drift through the micromesh holes into the multiplication region where they gain enough energy to produce an ionization avalanche. The multiplication region, which is on the order of 100 μm is the space between a thin metal grid known as a micromesh and the readout electrode. The field gradient in the multiplication region is approximately 25 kV/cm. This region gives a narrow avalanche which is excellent for spatial resolution. A schematic drawing of primary ionization being amplified in a Micromegas is shown in Fig. 3.4.

Like all proportional gaseous detectors, Micromegas are operated with a quench gas, like isobutane, to absorb UV photons produced in the amplification region which can cause a large ionization avalanche and discharge the gas creating a spark across the amplification region. Sparks saturate the output, masking any information about the signal and can potentially damage the detector. The Micromegas used in the T2K TPCs are described in Section 3.3.5.

3.3 T2K TPCs

In the ND280 tracker there are 3 TPCs, one placed downstream of the PØD, the other two downstream of the FGD modules as is shown in Fig 2.12 and Fig 2.14.

The main purpose of the TPCs in the ND280 tracker is to measure the spectrum of muons and electrons produced from CCQE interactions in the near detector [76].

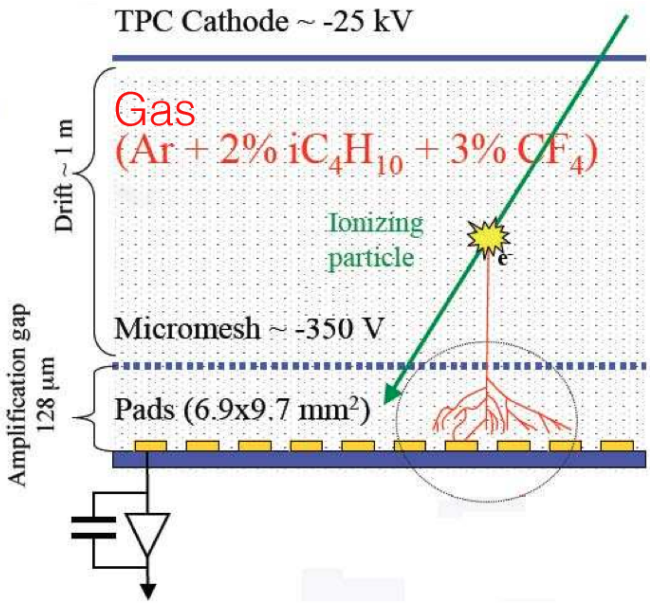

Figure 3.4: Schematic drawing of primary ionization being amplified in the Micromegas detector [75].

To meet the objectives of ND280 and T2K as a whole, the TPCs have the following performance goals:

- Energy estimates of CCQE neutrinos are limited to precision of ∼10% due to Fermi motion of the target nuclei. This limitation sets the momentum resolution goal of the TPCs to $\delta p_\perp/p_\perp = 0.1 p_\perp$ [GeV/c] ($p_\perp$, momentum in plane perpendicular to the magnetic field direction).

- The overall momentum scale needs to be known to the level of 2%. This requirement is set in order not to limit the precise determination of Δm^2_{32}. A photoelectron calibration system is in place to calibrate electromagnetic field distortions and remove any biases to the reconstructed momentum introduced by such distortions.

- At ∼1 GeV the energy loss of electrons in argon is 45% percent greater than that for muons. An energy loss resolution of better than 10% gives a good separation of muons and electrons so that the ν_e contamination of the T2K beam can be determined.

The physics goals of the TPCs can be met while operating with a gas mixture of

Ar : CF_4 : iC_4H_{10} (95:3:2) in a magnetic field of 0.2 T with a sample length of $\sim$ 700 mm and readout pad segmentation of 70 mm^2.

The following sections describe different aspects of the TPC design and performance.

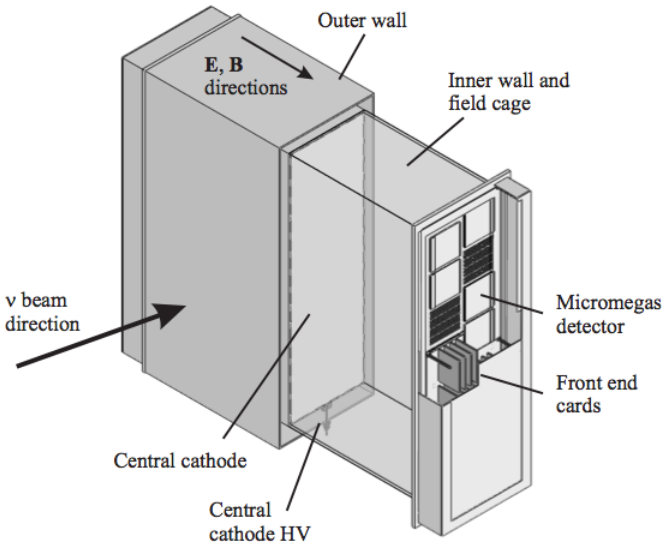

Figure 3.5: Drawing of a single TPC showing the important elements of the detector [76].

3.3.1 Mechanical Structure

The TPCs have a double box design, the inner box serving as the drift volume for the detectors and the outer box providing insulation for the high voltage as well as preventing atmospheric contaminants from entering the inner volumes. The outer box is at ground potential so the volume between the outer and inner box is filled with CO_2 which acts as an insulator as it has a high break down voltage.

Bulk Micromegas are used for the gas amplification of the primary electrons. On each readout plane of the TPCs are 12 Micromegas modules arranged in two columns of 6 modules vertically offset from one another, providing an active tracking length of 720 mm for horizontal particles. The analog data produced from the Micromegas modules is digitized by frontend electronics and data is transported with optical links to the ND280 data acquisition system. Fig 3.5 shows a schematic drawing of the TPC.

Inner Box

The inner box is divided in half by the central cathode, creating two drift volumes for each TPC. At each anode end of the inner box the 12 Micromegas modules are arranged in a plane parallel to the central cathode. A photo of the inner box during construction, before the installation of the Micromegas is shown in Fig 3.6

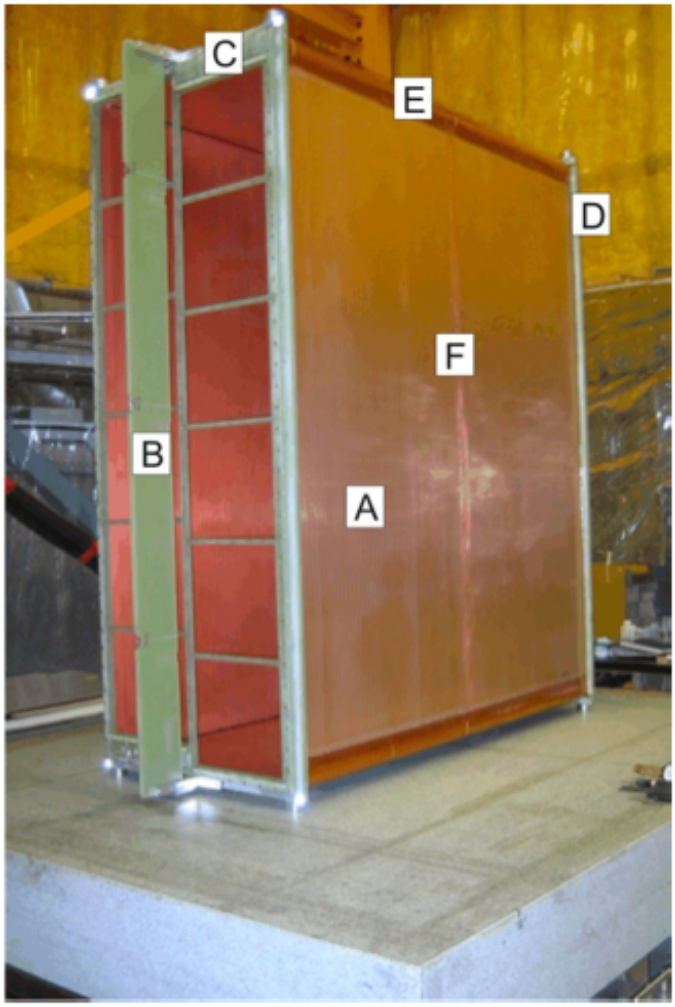

Figure 3.6: TPC inner box A: one of inner box walls; B: module frame stiffening plate; C: module frame; D: inner box endplate; E: field-reducing corners; F: central cathode location [76].

The four walls and the central cathode of the box are made from copper-clad-G10/rohacell panels. The central cathode has two mesh covered cutouts to allow gas flow between the two drift volumes. The panels provide a stiff frame that will not

deflect under pressure variations of the TPC gas. The panels are also low in density to minimize the multiple scattering of particles entering and exiting the TPCs. In order to create the electric field gradient in the drift volume the conductive panel surface on the walls between the central cathode and readout plane is divided into strips with a pitch of 11.5 mm and pairs of 20 MΩ resistors are connected in parallel between each two copper strips as is shown in Fig 3.7.

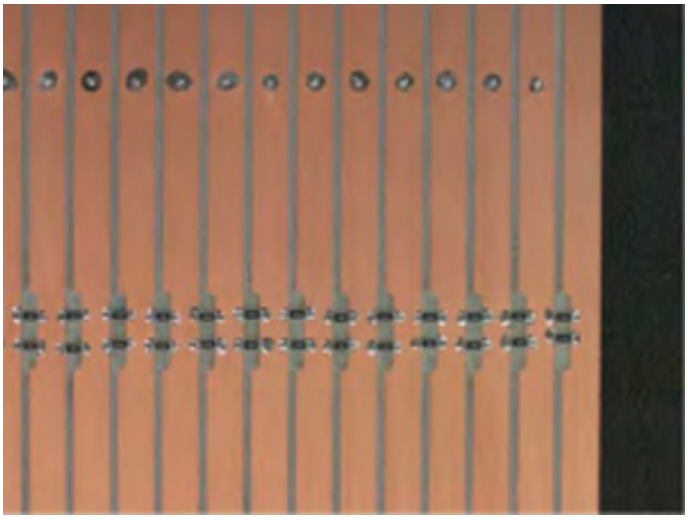

Figure 3.7: The copper strips on G10 walls of the inner box, resistor chain soldered on to the strips [76].

The mechanical design and construction of the inner box was performed to minimize the electric field distortions. Studies performed with Comsol Multiphysics [77] were done to optimize the the field cage design. The goal of the TPCs is to have distortions in the reconstructed position of primary electrons to be less than 0.2 mm, small compared the nominal space point resolution of 0.7 mm and small enough to effect the momentum scale by less than 2%. These limits on the electric field distortions require that the different elements of the TPCs be aligned with sub-mm precision. It is required that:

- The central cathode is flat to within 0.1 mm.
- The central cathode and Micromegas plane are parallel to within 0.2 mm.
- The Micromegas plane should be flat to 0.2 mm.
- Resistor pairs along the side walls of the inner box should be matched to 0.1%.

In addition to being well aligned, the inner box must be gas tight so that gas contaminants cannot diffuse in. The oxygen level in the drift volume must be below 10 ppm. It is also desirable to keep the CO_2 concentration low so that the purification filters have a long lifetime.

The ends of the four walls are glued to endplates, solid G10 rectangular frames. These hold O-rings that make a gas tight seal between the module frame and the field cage.

The central cathode is held at -25 kV and the Micromegas at -350 V. The maximum drift distance is 897 mm which creates a drift field of approximately 275 V/cm close the the saturation point for the T2K gas, so that the drift velocity is less sensitive to changes in the gas composition.

The cathode holds aluminium targets that are used for the calibration system described in Section 3.3.12.

Module Frame

The 12 Micromegas modules are mounted into individual cutouts in the module frame at the end of the inner box. O-rings provide a gas seal between the Micromegas and the frame. The module frame is held rigid by attaching it to the endplate and a stiffening plate that spans the height of the TPC. The module frame supports the optical packages for the laser calibration system as well as the gas inlet and outlet manifolds. Figure 3.6 shows the module frame without Micromegas installed as well as the stiffening plate.

Outer Box

The front, back, top and bottom panels of the outer box are constructed with aluminium -rohacell laminate panels 14.3 mm thick. These panels provide low density material while still providing solid mechanical connections. The panels are also constructed to be sufficiently rigid as the CO_2 in the outer volume is kept at 0.2 mbar above atmospheric pressure. At each end of the TPCs, a solid aluminium rectangular frame or endplate is glued. The outer box endplates provide support points for the connection of the TPCs with the ND280 detector basket. Screwed to each endplate with an O-ring seal are service spacers. The overall size of the outer box including service spacers is $2303 \times 2400 \times 974$ mm in $x \times y \times z$.

The gap between the inner and outer boxes is 68 mm on three surfaces and 118 mm

on the bottom, where extra space is required for the cathode high voltage connection. The electric field in the region between the inner and outer boxes is designed to be a factor of 3 below the CO_2 nominal break down voltage of 20 kV/cm.

The outer box and inner box walls combined have a thickness of 3.3% of a radiation length for particles entering the TPCs. A photo of the outer box with the inner box partially installed and service spacers attached is shown in Fig. 3.8.

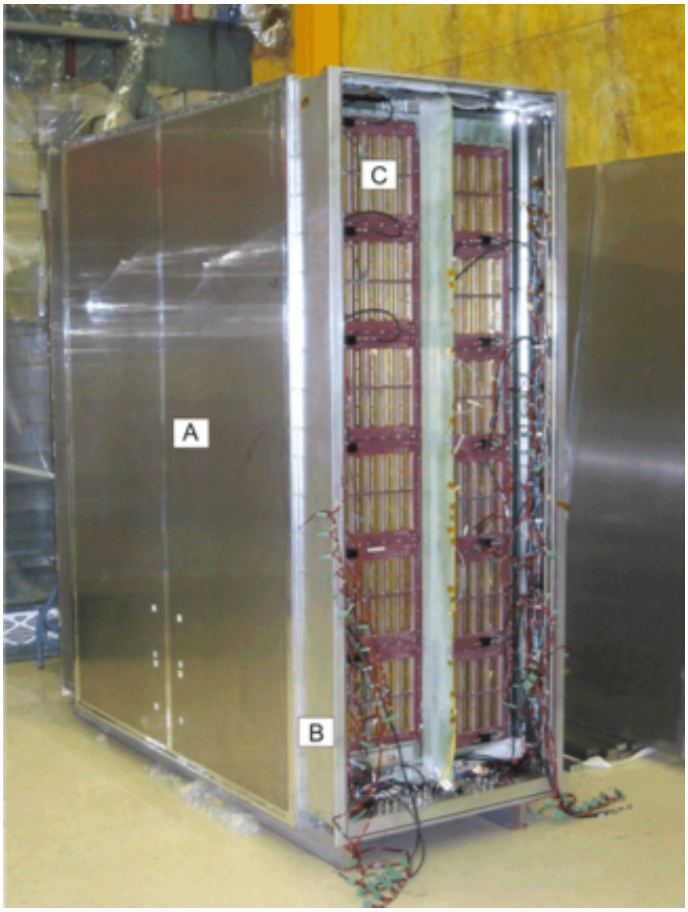

Figure 3.8: TPC outer box. A: one of the outer box walls; B: service spacer; C: one of the Micromegas modules inserted into the module frame [76].

Service spacers

The service spacers provide space in the outer volume for the front end electronics. All services to the TPCs aside from the central cathode high voltage, such as electronics power, readout cooling water, laser fibre optics and optical cables enter the TPCs

through the bottom of the service spacers. All service spacers have a cover with an O-ring seal which can be removed to access the electronics or other services.

3.3.2 T2K Gas

The T2K gas was chosen to have a high drift speed as well as low transverse diffusion to obtain a low enough space point resolution. Also the gas has a suitable gain at a relatively low amplification field of 27 kV/cm in the Micromegas. Gas in the T2K TPCs is composed of

- Argon (95%): Is a good gas for primary ionization, the mean energy for an ion-electron pair to be formed is 26 eV. The ionization energy loss of electrons in 1 atm argon gas is roughly 45% larger than for muons over the momentum range of interest, giving a good separation. Also since it is a noble gas, argon will not capture drifting electrons. These properties along with the low cost of argon make it the main component of the gas.

- CF_4 (3%): Used to reduced the transverse diffusion and increase the drift velocity of the electrons in the gas. Molecules of CF_4 have large inelastic cross sections at moderate energies. For nobel gases the probability of collision between the electrons and gas atoms reaches a minimum value for electrons with a certain amount of kinetic energy ($\sim$ 0.5 eV for argon). This is known as the Ramsauer-Townsend effect. Inelastic collisions reduce the energy of the electrons, in turn reducing their cross section with argon atoms and counterintuitively increasing the drift speed. The cooling of the electrons also reduces the transverse diffusion.

- iC_4H_{10} (isobutane) (2%): Used as a quench gas for operating the Micromegas modules. Isobutane is added to absorb UV photons to prevent any ionization avalanches.

3.3.3 Gas System

The TPC gas system is a very complex sub-system with almost 250 active devices, it mixes the gas components in the correct proportion, while maintaining the design flow rates, differential pressures and gas purity. Systems must be in place to provide several interlocks to prevent damage to the detectors that could arise from mechanical or

human failure during operation. The majority of the gas system devices are monitored with a programmable logic controller.

Differential pressure between the inner and outer volume can cause the inner box walls to deflect causing changes in the electric field cage. Measurements have shown that the Micromegas module frames deflect by about 2 μm/mbar. For this reason the TPC gas system is designed to keep the differential pressure stable to within $\pm$0.10 mbar.

To reduce the diffusion of contaminants the inner volume is operated at a slight over pressure of 0.4 mbar compared to the outer volume.

The gas mixture is set by mass flow controllers. Including errors from the response of the mass flow controller to temperature, the mixture stability is $(95.00 \pm 0.01)\%$ Ar, $(3.00 \pm 0.005)\%$ CF_4 and $(2.00 \pm 0.005)\%$ iC_4H_{10} meeting the projected goals. The concentrations of O_2 and H_2O are less than 2 ppm at the output of the purifiers and concentrations of CO_2 have been observed to vary between 20 and 120 ppm.

3.3.4 Gas Monitor Chambers

Installed in the TPC gas system are mini TPCs that are used for the monitoring of the TPC gas. One of the chambers samples the supply gas of the detectors, while the other chamber samples the exhaust gas. The monitor chambers are operated at the same drift field and mesh voltage of the main TPCs. Each chamber measures the drift velocity and amplification of the gas.

To measure the drift velocity in each chamber there are two sources of ^{90}Sr with scintillator fibre triggers that are separated by a well defined distance. The sources emit β decay electrons producing tracks with different drift times. The difference between the drift times is used to estimate the drift velocity of the gas.

To measure the gas amplification a source of ^{55}Fe emitting 5.9 keV X-rays is installed in each chamber.

Measurements of the drift velocity and gain are sent to the ND280 slow control system and the information is used as reference for the large TPCs.

3.3.5 Micromegas Modules

To reach the TPC performance goals, it is required that; the Micromegas have small dead areas, there is gas gain uniformity at the level of a few % and planarity at the detection surface. The total detection surface covered in the three TPCs is about 9

m^2 with a pad segmentation of 70 mm^2. For practical purposes the detection surface is broken up into 12 bulk Micromegas modules per readout plane, setting each module surface to 0.12 m^2. Each bulk Micromegas module contains 1728 pads arranged in 48 rows of 36 pads and covers a sensitive area of 36×34 cm^2.

The Micromegas consist of a thin micromesh separated from a printed circuit board (PCB) by a small distance $\mathcal{O}(100\ \mu m)$. This mesh creates a large field gradient for amplification. At nominal TPC operation the micromesh is set to -350 V setting the field gradient in the amplification region to 27.4 kV/cm.

The modules on the same readout plane are operated at the same voltage to minimize electric field distortions near the readout plane. This requires good reproducibility of the small amplification gap from one module to another.

With low noise electronics, the Micromegas can be operated with a gain of 1000 and have detection efficiencies of close to 100% for minimum ionizing particles.

Production

The bulk Micromegas technique consists of laminating a woven mesh on a PCB covered by a photoimageable film. The steps for producing a bulk Micromegas module are shown in Fig. 3.9 [78].

The bulk Micromegas undergo UV exposure with a mask followed by chemical development. At the end of the photoimaging process, the micromesh is held in place by a 2 mm coverlay border and by 20736 regularly distributed pillars, maintaining the amplification gap of 128 μm.

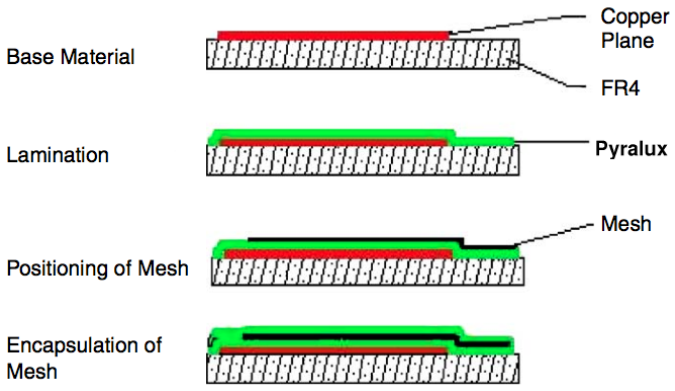

Figure 3.9: Production sequence of a bulk Micromegas [75].

To minimize electric field distortions near the edges of the TPC and between adjacent modules a 2 mm wide copper strip called the Border Frame Mesh (BFM) is located at the micromesh plane and surrounds the active area of the detector. The BFM is kept at the same potential as the micromesh.

After development the bulk Micromegas detector underwent cleaning and baking to achieve full polymerization of the Pyralux material.

To ensure mechanical rigidity and planarity of the module the PCB is was reinforced by a stiff frame of FR5 glass epoxy, which also provides anchorage for a guiding, fixing and extraction system for the readout electronics.

A complete Micromegas module ready to be mounted is shown in Fig 3.10.

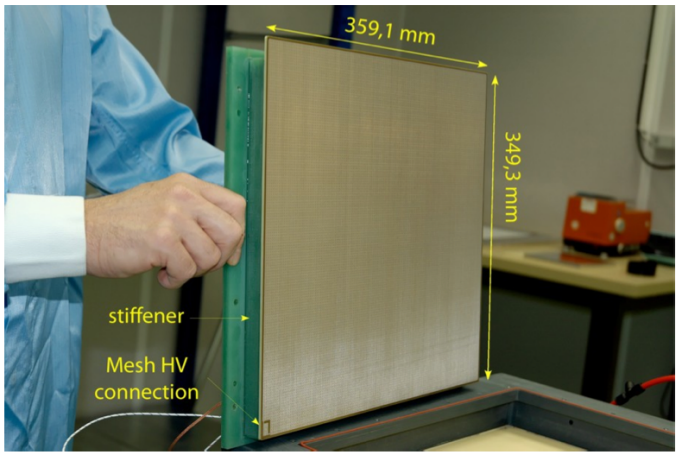

Figure 3.10: A bulk Micromegas detector module for the T2K TPC [76].

Testing

For the testing of the Micromegas detectors, a dedicated test bench was used at the T2K Micromegas production laboratory at CERN [79]. To test each bulk Micromegas performance a X-Y scanning system was used to measure the response of a single module pad when illuminated by a collimated 185 MBq ^{55}Fe source, producing 5.9 keV X-rays. For testing, the detector module is inserted in a gas tight box filled with a mixture of the T2K gas. The 5.9 keV X-ray source was mounted on an external motorized head, the source able to move from one pad to the next by positioning the head in front of the target pad centre.

Fig 3.11 shows the typical energy spectrum measured by a single pad. A very good resolution of about 8% at 5.9 keV is seen.

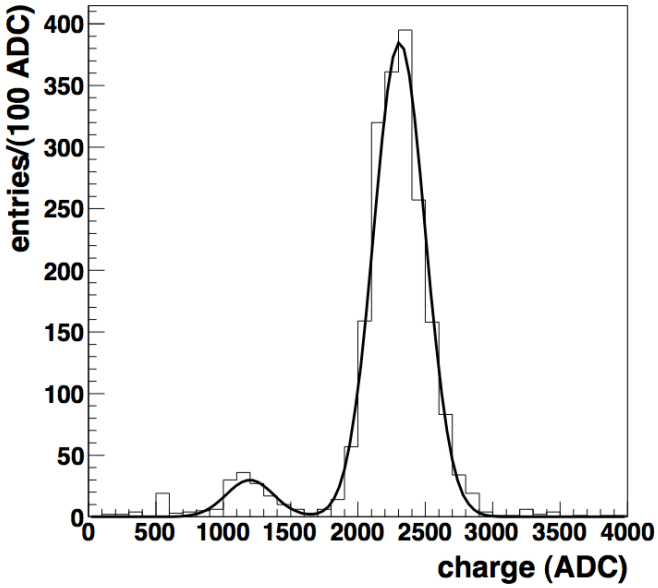

Figure 3.11: ^{55}Fe energy spectrum (in ADC counts) measured from a single pad [76].

Studying the uniformity over the active pads of a module yields a RMS of the mean energy to be 3% and the RMS in the energy resolution of $\sim$ 6%

At the nominal operation voltage of -350 V the gas gain was measured to be about 1500 and a spark rate lower than 0.1/h, while operating with the T2K gas. Sparks typically lasted a few millseconds with a few volts drop ($<$ 5 V) on the micromesh.

3.3.6 Front End Electronics and Data Acquisition

There are 72 Micromegas modules that cover the 3 TPCs, each module is segmented into 36 $\times$ 48 pads giving a total of 124,416 readout channels.

To reach the performance requirements of the TPCs, the desired dynamic range is 10 times a Minimum Ionizing Particle (MIP) with a signal to noise ratio of 100. The readout electronics acquire 500 time samples during the maximum drift time of electrons. The raw event size from the TPCs is $\sim$ 125 MB, which is too large for network throughput and storage for a nominal trigger rate of 20 Hz. To reduce event size, zero suppression is applied in which only signals above a threshold are passed to the data acquisition system. This reduces the data size by a factor of $\sim$ 1000 and

fits within a 50 ms time budget.

The front end electronics have a modular design which is repeated 72 times for each Micromegas. Figure 3.12 shows a schematic overview of the TPC frontend electronics for one Micromegas.

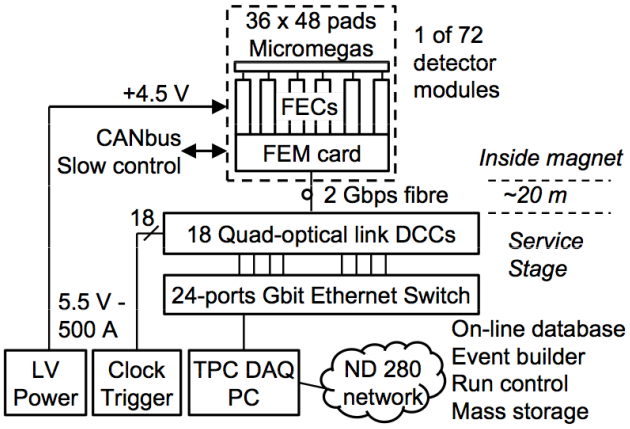

Figure 3.12: TPC readout electronics [76].

Each module is composed of 6 Front End Cards (FECs) and one Front-End Mezzanine (FEM) card which connects to the FECs and controls their readout. The basic component of the readout system is the 72 channel Application Specific Integrated Circuit (ASIC) called "AFTER".

The signals on each pad are sampled and stored in a 511 time bin switched capacitor array (SCA). The SCA is used as a circular buffer in which each analog channel is continuously sampled and stored at the sampling rate, which can be up to 100 MHz.

Four AFTER chips are mounted to the FEC giving 288 channels. The output of the four AFTER chips is digitized at 20 MHz by a quad-channel 12-bit analog to digital converter (ADC).

The FEM boards collect the data from 6 FECs, perform zero suppression and send the remaining data via an optical link to a Data Concentration Card (DCC). The FECs and the FEM are attached to an aluminium plate for support which is cooled by circulating water.

The DCCs collect the data from the 72 modules and send the data to a standard personal computer which is linked to the global ND280 data acquisition system.

3.3.7 Reconstruction Software

The patterns of ionization collected by the pads are used to reconstruct tracks of particles that passed through the TPCs. The first step in the reconstruction is the application of the gain calibration constants and the removal of dead or noisy channels. The output of this process is a waveform which contains information of the charge collected on a readout pad versus time. The calibration runs on a raw data MIDAS file format [80] and outputs the results in a ROOT file with the ND280 event format [81].

The next step is the clustering of waveforms. Waveforms from Micromegas pads in the same column(row) are grouped into vertical(horizontal) clusters that are then joined together into tracks by a pattern recognition algorithm. The track parameters are then estimated by maximizing the likelihood of the charge sharing within the clusters. In order to determine the position of the track in the x coordinate, the drift distance must be known and information about the tracks T_0 must be obtained from other detectors such as the FGD or PØD. The final part of the reconstruction uses the charge information of clusters to calculate the energy loss per unit length for particle identification.

Clustering

The first step in TPC reconstruction is the clustering of the waveforms. This is done with a simple criterion of connectivity: waveforms must overlap in time and be consecutive in space. The clustering is done primarily in the vertical Micromegas pad columns. Vertical clustering is preferred because it is perpendicular to the main direction of particles coming from neutrino interactions. Figure 3.13 shows a schematic diagram of the clustering method. For tracks with a large angle with respect the the beam direction, horizontal pad rows instead of columns are used to create clusters.

Hits are associated to a common cluster if the following conditions are met:

- The waveform ADC is above a certain threshold, nominally set to zero since the pedestal cut gives enough suppression.
- The waveforms are in the same Micromegas column and are contiguous in y.
- The waveforms overlap in time for ADC values above pedestal. Also the number of time samples between two waveforms maxima is less than a certain threshold.

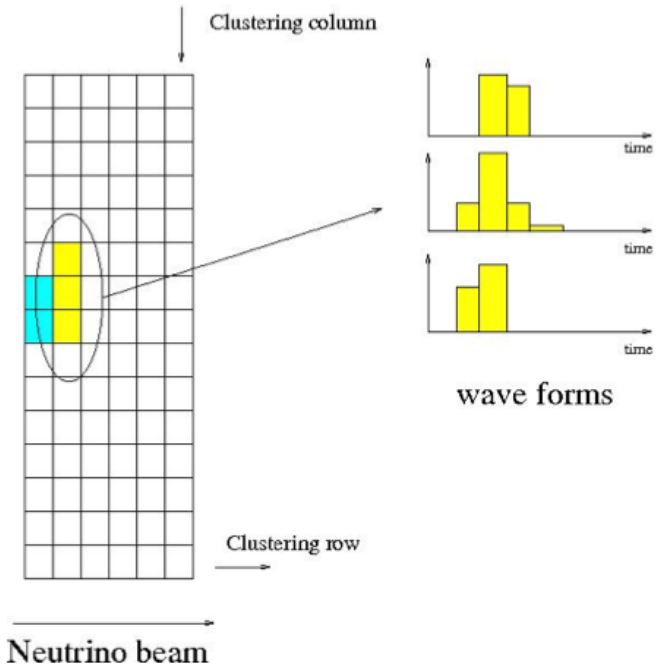

Figure 3.13: Sketch of the clustering method. Clustering in vertical direction is shown [82] .

Track Pattern Recognition

Tracks are characterized as a series of clusters that overlap. The pattern recognition, which is based on a cellular automaton algorithm, connects the clusters and creates tracks segments. The algorithm has been adapted from the SciBar detector in K2K and SciBooNE, the same algorithm is also used in FGD reconstruction.

Clusters consecutive along the z direction are joined if the follow conditions are met:

- Clusters are close in the y coordinate with a distance less than a threshold set in reconstruction settings.
- Clusters have waveforms that overlap in time.
- Clusters have one pair of waveforms with their peaks separated in time by less than a threshold set in reconstruction settings.

Also clusters not in contiguous columns can be joined if:

- Clusters waveforms overlap in time.
- Clusters are continuous along the y coordinate.

The cellular automaton first creates segments connecting clusters in contiguous columns, a segment defined as a pair of clusters in two columns. Segments are connected if they share a common edge, the central column. Once segments are connected the algorithm navigates along the list of connected segments and selects the combination that gives the longest reconstructed track segment.

The algorithm is also able to find branches corresponding to hard δ ray emission.

Track Parameter Seeding

Proper seeding of the track parameters is important for the likelihood fit to succeed. Seeding is computed in two ways and the fit selects one that best describes the trajectory of clusters based on a χ^2 cut.

The first is a simple determination of the track parameters from three points on a track, the two extremes in z and the centre point.

For the second method the YZ projection of the track is mapped onto a Riemann sphere, if the points are in a circular trajectory in the YZ plane then they will map

to a 3D helix when projected onto the sphere and the position, angle and curvature of the track can be calculated analytically [83]. The second method is more robust than the first except if the track is short.

Single TPC Likelihood Fit

The likelihood method is based on a model detailed in [84] describing the charge deposition and electrons drifting in a gas. The overall TPC track is described by a helix model which is detailed in [82].

As an approximation the charge distribution in a Micromegas column is modelled by a multinomial. This approximation is well motivated when the diffusion within and after the Micromegas is small compared to the diffusion in the drift region, and the fluctuations due to electronics noise are small compared to primary electron statistics.

The number of electrons collected by a pad i with a pad gain g_i is defined as

$$n_i = ADC_i/g_i, \tag{3.13}$$

where ADC_i is the charge collected in pad i in ADC units, The number of primary electrons per column is on the order of 100. These units are non-integer but a direct continuum of the multinomial distribution. This yields the log likelihood function

$$\log L^y_{col} = \sum_i n_i \log p_i + \text{constant}, \tag{3.14}$$

where p_i is the probability of a primary electron from the track to be associated to the pad i given by

$$p_i = Q_i(\vec{x}, \vec{p}, \sigma)/\sum_j Q_j(\vec{x}, \vec{p}, \sigma), \tag{3.15}$$

where $Q_i(\vec{x}, \vec{p}, \sigma)$ is the predicted charge deposited in the pad i with coordinate $\vec{x}$, momentum $\vec{p}$ and charge cloud with a width of σ; j runs over all the pads in the cluster containing pad i.

The fit includes all clusters from a track segment found from the pattern recognition algorithm. The negative log likelihood is minimized with the MINUIT software package [85] to obtain track coordinates, direction and momentum. Also the σ of the charge cloud is not strongly correlated to the track parameters and is also fitted.

To make the track fit robust to spurious signals the probability is modified adding

a small constant p_{noise}

$$p_i \rightarrow \frac{p_i + p_{noise}}{1 + n_{pad} p_{noise}}, \tag{3.16}$$

where n_{pad} is the number of pads in a cluster. The introduction of p_{noise} causes the σ of the charge cloud to be slightly underestimated.

X coordinate

The time the track is created, T_0 can be determined from hits in adjacent scintillator detectors such as the FGD, ECAL and PØD or tracks crossing the central cathode. The track in the TPC is extrapolated in the YZ plane to other detectors to find the hit that gives the lowest matching residual, computed by the RECPACK kalman filter software [86]. The timing of the hit is then taken as the T_0. If available all three T_0 values from the different scintillator detectors are stored. The FGD value is preferred followed by the ECAL then PØD values. If the T_0 cannot be found from the scintillator detectors the time at which the track crossed the central cathode is used. The error on the T_0 from the scintillator detectors is less than the cathode crossing calculation and is the preferred method.

3.3.8 Momentum measurement

For a particle traveling in a magnetic field $\vec{B}$ the resultant trajectory will be a helix. The equation relating transverse momentum, p_t and curvature of a helix is given by

$$p_t = \frac{0.3B}{\rho}, \tag{3.17}$$

where B is the strength of the magnetic field in Tesla, ρ is the inverse of the radius of curvature of the track in m^{-1} and transverse momentum is in units of GeV/c.

A quantity of interest is the sagitta of the track which refers to the depth of an arc shown in Fig 3.14.

Relating the sagitta s to the radius of curvature r in the limit that the sagitta is small compared to the length of the chord L, ($s << L$) the transverse momentum can be expressed as

$$p_t = \frac{0.3BL^2}{8s}. \tag{3.18}$$

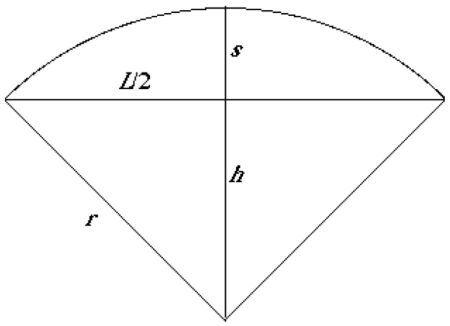

Figure 3.14: Diagram of an arc showing the radius of curvature r, chord length L and sagitta s.

The diffusion of the gas adds Gaussian noise to the distribution of the measured sagitta and therefore also the distribution of inverse transverse momentum.

The resolution of the transverse momentum and sagitta are given by

$$\frac{\sigma_{p_t}}{p_t} = \frac{\sigma_s}{s} = \sigma_{xy}\frac{p_t}{eBL^2}\sqrt{\frac{720}{N+4}}, \tag{3.19}$$

where σ_{xy} is the point resolution in the transverse plane and N is the number of points on a track [87].

The total momentum can be expressed by measuring the polar angle Θ between the track and the direction of $\vec{B}$,

$$p = \frac{p_t}{\sin\Theta}. \tag{3.20}$$

The momentum resolution for a single TPC, computed with a Monte Carlo sample of simulated neutrino events, is shown in Fig. 3.15. The sample includes tracks that have at least 50 of the 72 pad columns in a TPC. The resolution is found comparing the truth and reconstructed momenta. The figure is plotted with the resolution goal of $\delta p_\perp/p_\perp = 0.1 p_\perp$ [GeV/c] ($p_\perp = p_t$).

Studies measuring the difference in the inverse transverse momentum between two TPCs for tracks that cross multiple TPCs shows good agreement between data and MC for the momentum resolution [88].

Muons at the energy of the neutrino oscillation maximum $\simeq$ 1 GeV travelling in a magnetic field of 0.2 T have a curvature of 6.0×10^{-2} m^{-1}. A track traversing a TPC (length of chord 720 mm) with this curvature will have a sagitta of $\sim$4 mm. The goal of the momentum scale uncertainty is roughly 2% at 1 GeV, or 0.02 GeV^{-1} expressed

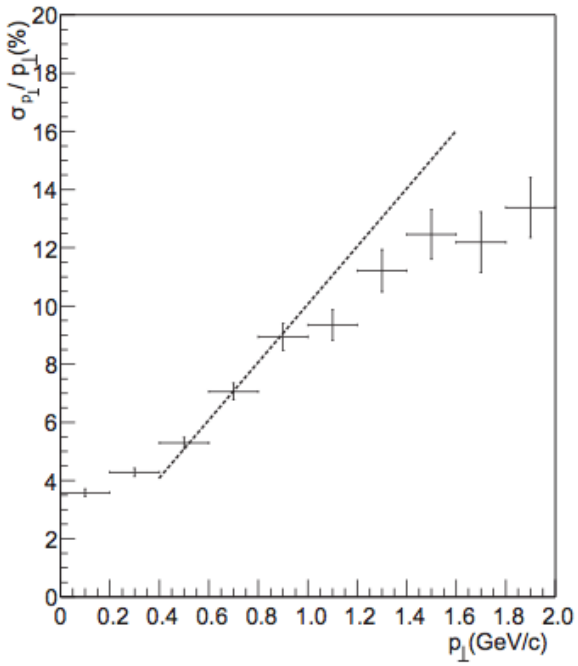

Figure 3.15: Momentum resolution for a single TPC is shown as a function of momentum perpendicular to the magnetic field. The dashed lines represents the momentum resolution goal [76].

in terms of inverse transverse momentum. This corresponds to a goal to understand spatial distortions on the order of 0.1 mm.

3.3.9 Particle Identification

As is stated in Section 3.2 the energy loss of a given particle is a characteristic function of its speed so that particles can be identified by measuring their momentum and energy loss.

Particle identification in the TPC uses the truncated mean of the ionization collected in the clusters described earlier. The distribution of ionization energy loss per cluster will follow a straggling function distribution as is described in Section 3.1.3. The truncation reduces the relative variance of the estimator for the most probable energy loss. Clusters near the edge of a Micromegas or the central cathode are rejected since an unknown amount of charge is not collected due to insensitive areas. The charge collected is corrected for variation in the gas temperature and pressure.

The truncated mean energy deposit C_T per horizontal segment is:

$$C_T = \frac{1}{\alpha N} \sum_{i}^{\alpha N} C_c(i) \tag{3.21}$$

where $C_c(i)$ is the energy in cluster i, ordered according to increasing energy, N is the number of clusters and α is the truncation fraction.

The lowest 70% of the values are used to compute the truncated mean, the fraction determined from optimization studies done with Monte Carlo simulation and test beam data. The length of the track samples are used to give the truncated mean energy loss per unit length. The distribution of truncated mean energy loss per unit length is shown in Fig 3.16, the resolution for minimum ionizing particles is 7.8 $\pm$ 0.2% which is better than the 10% goal.

The energy loss per unit length is used to compute the pull "$\delta_E(i)$", the number of standard deviations the measurement is away from the expected value for particle type i at the observed momentum.

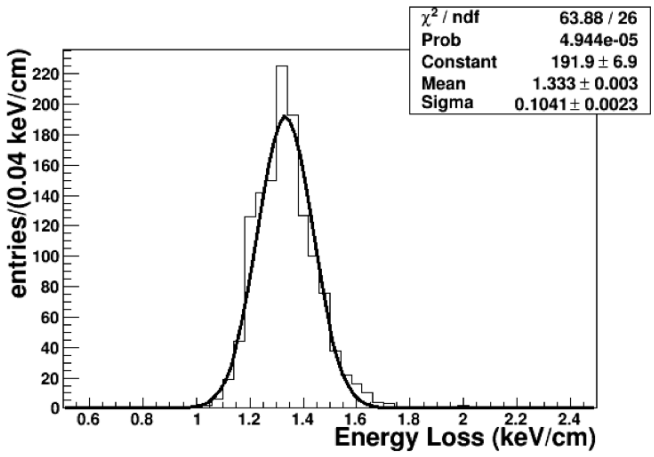

Figure 3.16: Distribution of the energy loss per unit length for negatively charged particles with momenta between 400 and 500 MeV/c [76].

The energy loss resolution gives excellent separation between muons and electrons, the probability of identifying a muon as an electron is 0.2% for the criteria, $-1 < \delta_E(e) < 2$ for tracks below 1 GeV/c. Figure 3.17 shows the distribution of energy loss pull for the electron hypothesis as a function of momentum for a sample of through going muons.

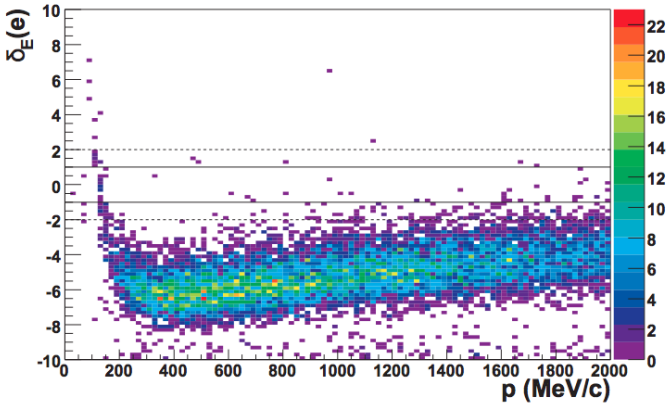

Figure 3.17: Distribution of the energy loss pull in the electron hypothesis for a sample of through going muons. The solid and dashed lines indicate $|\delta_E(e)| < 1$ and $|\delta_E(e)| < 2$ respectively [76].

The distribution of the energy loss for negatively charged particles as a function of the momentum for data taken during the first T2K physics run is shown in Fig. 3.18. The figure also shows the expected energy loss curves for muons, electrons, pions and protons. It can be seen that the sample is primarily muons and different particle types can be clearly separated.

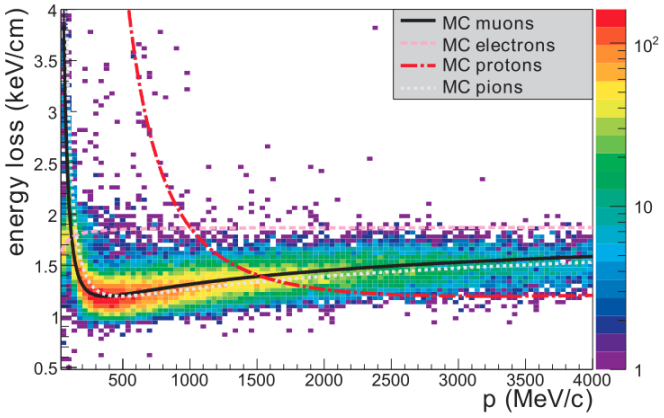

Figure 3.18: Distribution of the energy loss as a function of the momentum for negatively charged particles produced in neutrino interactions, compared to the expected curves for muons, pions, electrons and protons [76].

3.3.10 Space Point Resolution

The spatial resolution of the TPCs is estimated comparing the transverse coordinate obtained from a track fit using the entire TPC to one obtained from a fit of a single cluster of charge in one Micromegas column. The space point resolution as a function of drift distance is shown in Fig. 3.19.

The degradation in resolution at short drift distances is due to a large fraction of single pad clusters. At short drift distances transverse diffusion has a small effect and signals are often not shared between two pads. At larger drift distances charge sharing between adjacent pads occurs more frequently, but the resolution slowly degrades as the transverse diffusion increases with drift distance. Good agreement is seen between the data and MC and the resolution goal of ~ 0.7 mm is met.

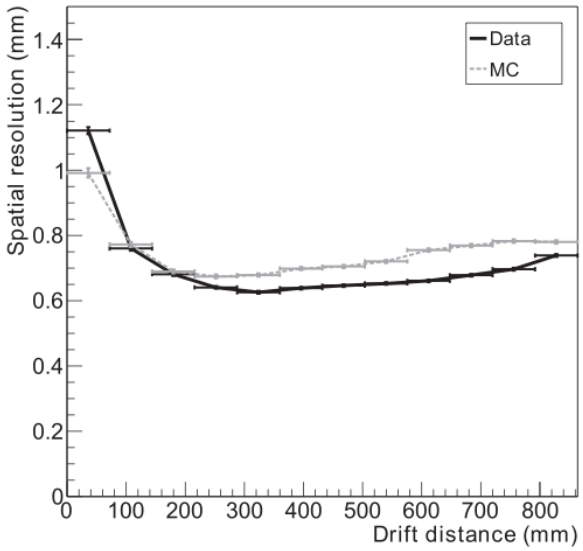

Figure 3.19: Spatial resolution as function of the drift distance for data (black line) and MC (grey dashed) [76].

3.3.11 Transverse Diffusion

The transverse diffusion is fit at the same time as the track kinematics. Figure 3.20 shows the distribution of transverse diffusion measurements for magnet field on and off, plots are generated with cosmic tracks with a drift distance greater than 30 cm.

It can be seen that transverse diffusion is less when the magnetic field is present as was described in Section 3.2. Using Eq. 3.12 the transverse diffusion measurements

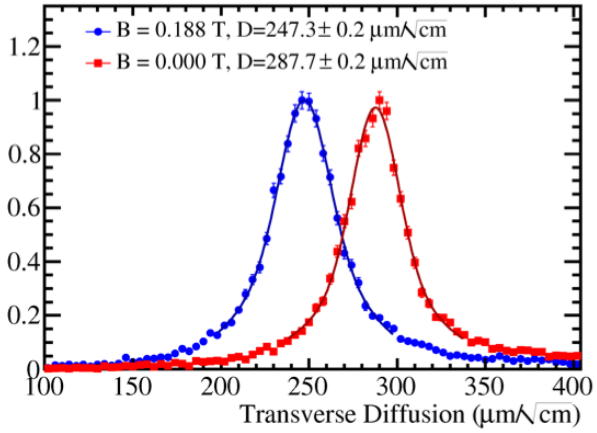

Figure 3.20: Distribution of diffusion constant estimates from samples of cosmic rays with mean drift distance of more than 30 cm with magnetic field on and off [76].

can be used to find the product $\omega\tau$ of the TPC gas.

3.3.12 The Photoelectron Calibration System

The photoelectron calibration system of the TPCs is designed to produce a control sample of photoelectrons used for understanding properties related to the transport of electrons. The system can be broken down into three sub parts: a laser, a distribution system, and aluminium targets.

The calibration system laser is a pulsed Nd:YAG laser that is frequency quadrupled yielding a 266 nm beam that produces photoelectron from the aluminium targets. A motorized variable attenuator is used to adjust the pulse energy and so the number of photoelectrons. The laser beam is distributed to the TPCs through a set of 18 silica fibre optics cables, three for each of the service spacers. At the laser, the 18 fibres are arranged in a linear array and a motorized multiplexer couples the laser light into a single fibre at a time. At the service spacer, each of the fibre optic cables couples to a short internal fibre, running along the stiffener plate. The fibres terminate at optical packages that defocus the light onto the central cathodes. The individual optical packages illuminate the targets for a set of 4 Micromegas, corresponding to single DCC. A schematic diagram of the laser system is shown in Fig. 3.21

The calibration system targets are sets of 53 dots and 2 strips affixed to the surfaces of the central cathodes and made of die-cut aluminium tape. Figure 3.22 shows the base pattern, which is duplicated on the cathodes for each Micromegas.

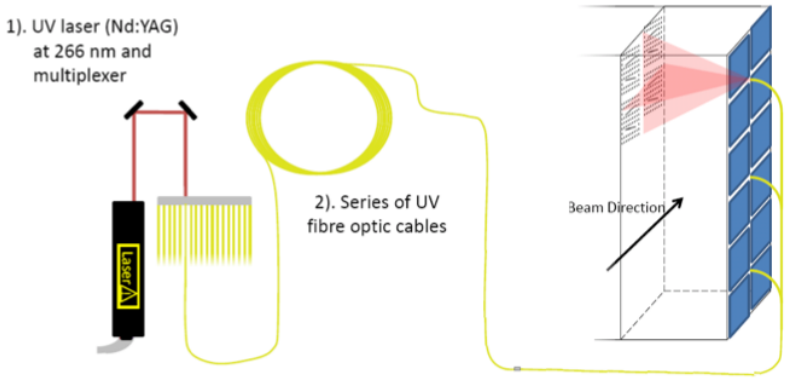

Figure 3.21: TPC laser photocalibration system [89].

The targets, 8 mm in diameter, produce images at the corners of 4 Micromegas pads to improve spatial resolution through charge sharing. Figure 3.23 shows a photo of a single calibration dot placed on the central cathode. The strips are 4 mm wide and angled relative to the Micromegas pad axes. During the TPC construction the targets were manually placed on the central cathodes at locations marked using an industrial router. The final location of the targets were then determined through a survey using a camera mounted on the arm of the router.

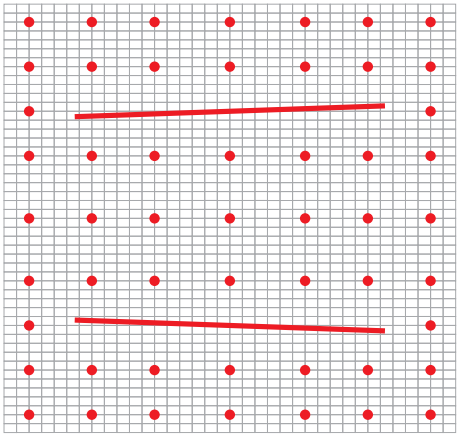

Figure 3.22: The base aluminium target pattern of targets and strips shown superimposed on the projected pads of a corresponding Micromegas [76].

Laser data sets for studying the spatial distortions require approximately 200 laser flashes per set of Micromegas. To obtain approximately 100 photoelectrons per target

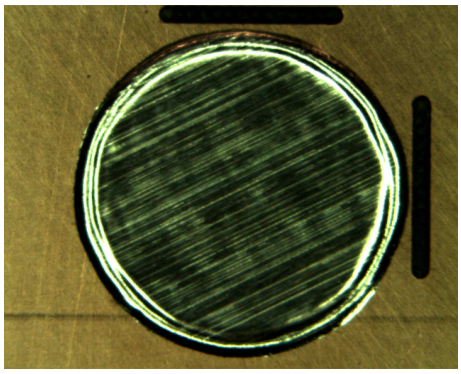

Figure 3.23: Photo of a single aluminium target on the central cathode. Also shown are the scribe marks used for the placement of the target.

the laser's attenuator is used to adjust the energy density on the central cathode targets to $\sim$ 10 nJ/cm^2. Acquisition of a data set requires 2 hours for a dedicated TPC run and 4 hours during normal ND280 runs. An example event display image for three laser events on one side of a TPC is shown in Fig. 3.24.

Calculation of Calibration Target Centre

The position of a calibration target is found by measuring the charge on the 4 pads closest to the intended target centroid. In the case of an ideal drift the image of the target is shared equally by the 4 pads. Only 4 pads are chosen since the vast majority of charge from the 8 mm diameter target will be within the 4 pads. Using 16 pads one uses pads that are farther from the target and subject to contamination from photoelectrons emitted from the copper. It should be noted that there is a good contrast between copper and aluminium, the Al emitting 2 photoelectrons/mm^2 whereas Cu emits 0.03 photoelectrons/mm^2. However some regions of the central cathode copper do emit a higher density of photoelectrons for reasons not yet understood.

For each dot, a maximum likelihood fit is done to find the centroid that corresponds to the distribution of charge sharing on the 4 pads. The transverse diffusion, σ of the gas is an input parameter to the fit and is essential to correctly determining image centres.

The expected charge collected by a rectangular pad is determined by integrating a 2 dimensional gaussian density function over the physical region of the pad and is proportional to

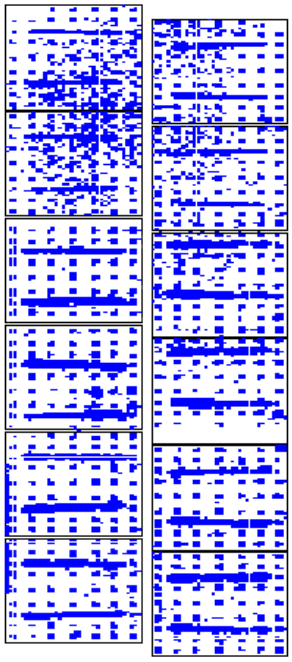

Figure 3.24: Example of three laser events artificially stitched together and illuminating a full TPC central cathode side.

$$
\begin{aligned}
&I(b,c,\sigma,h,w) \\
&\qquad = \int_{-w/2}^{w/2}\int_{-h/2}^{h/2} \frac{dxdy}{2\pi\sigma} \times \\
&\qquad \exp(\frac{-(x-b)^2}{2\sigma^2}) \exp(\frac{-(y-c)^2}{2\sigma^2}) \\
&\qquad = \eta(b,c,\sigma,h,w) - \eta(b,c,\sigma,-h,w) \\
&\qquad + \eta(b,c,\sigma,-h,-w) - \eta(b,c,\sigma,h,-w)
\end{aligned} \tag{3.22}
$$

$$
\eta(b,c,\sigma,h,w) = \xi((b+\frac{w}{2}),(c+\frac{h}{2}),\sigma) \tag{3.23}
$$

$$
\xi(u,v,\sigma) = \frac{1}{4} Erf(\frac{u}{\sqrt{2}\sigma}) Erf(\frac{v}{\sqrt{2}\sigma}) \tag{3.24}
$$

where b and c are respectively the horizontal and vertical distance of the target centroid from the overall centre of the 4 readout pads and h and w are the height

and width of the pads.

In order to calculate the likelihood of the observed charge distribution on the 4 pads an approximate model is used. As in the likelihood fit for track reconstruction the distribution of charge is assumed to be multinomial with n observations. Analogous to Eq. 3.14 the log likelihood of the multinominal distribution is used, where p_i is the probability for a primary electron from the target to be associated to pad i, such that

$$p_i = I_i(b, c, \sigma, h, w) / \sum_j I_j(b, c, \sigma, h, w) \tag{3.25}$$

where $I_i(b, c, \sigma, h, w)$ is the predicted charge on pad i and j runs over all 4 pads associated with the target. The gain for each pad is assumed to be equal so that the ADC counts N_i are used in the maximum likelihood function instead of the primary electrons n_i .

Several measurements of the centroid from many laser flashes can be averaged to get the precision of 0.1 mm needed. Analysis of measuring the image of the targets show a resolution of better than 0.5 mm. A sample of data with 400 flashes gives an error in the mean to better than 0.025 mm. Fig 3.25 shows the results from 400 flashes on a single target fitting for the centroid in z and y as well as a 2 dimensional scatter plot.

Systematic errors in the measurement of the target location include error in the determination of the transverse diffusion coefficient, variations in the pad to pad gain of the Micromegas and contamination from the photoelectrons being emitted from the copper of the central cathode.

The centroids of the targets were measured with the magnetic field on and off, taking the difference cancels out the systematic errors related to the centroid location and gives displacements in electron drift due to magnetic field distortions. Figure 3.26 shows the difference between target centroids for magnetic field on and magnetic field off. The circles represent the nominal, field off positions of the targets and the lines represent the difference between magnetic field on and off (the lines are magnified by a factor of 20 to make visible on the figure). The figure was generated using data taken on November 26th 2010.

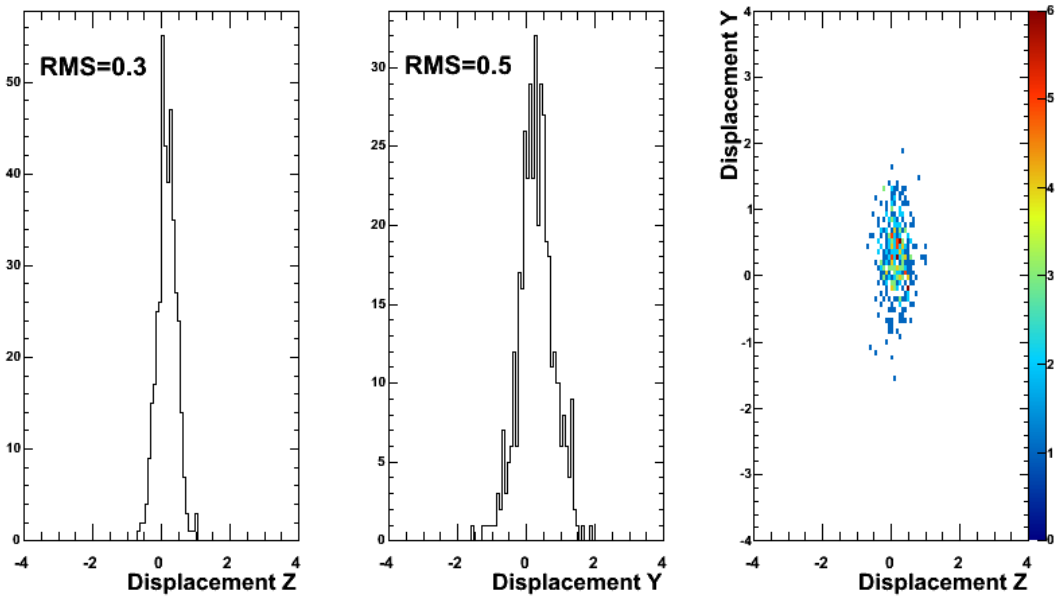

Figure 3.25: Estimates for the centroid in z and y and scatter plot of estimates for a single target (units in mm).

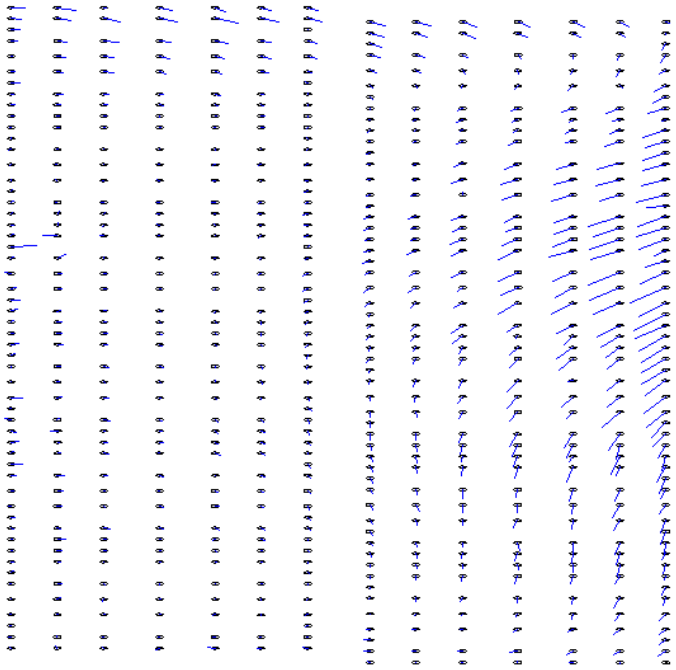

Figure 3.26: The difference between target centroids for magnetic field on and magnetic field off. Circles give nominal positions of calibration targets and lines give direction of magnetic field distortion (magnitude magnified by a factor of 20). Distortions shown for TPC 3 RP 0. Data taken on Nov. 26th 2010.

Chapter 4

Magnetic Field Distortions

4.1 Introduction

The magnet used at ND280 was previously used at CERN for the UA1 and NOMAD experiments and provides a dipole 0.2 Tesla field.

The magnet consists of water-cooled aluminium coils which creates the horizontally oriented dipole field and a flux return yoke. The inner dimensions of the magnet are 7.0 m × 3.5 m × 3.6 m. The external dimensions are 7.6 m × 5.6 m × 6.1 m and the total weight of the magnet is 850 tons.

The magnet consists of two mirror-symmetric halves. The coils are split into four elements, two for each half and are mechanically supported but electrically isolated from the return yoke. The two half yoke pieces consist of eight C-shaped elements made of low-carbon steel plates which stand on moveable carriages. The carriages are fitted onto rails and operated by hydraulic movers so that each half of the magnet is independent and can be moved to open and closed positions separately. When the magnet is open the inner volume is exposed allowing access to the detectors. A sketch of the open magnet is shown in Fig. 4.1.

4.1.1 Magnetic Field Mapping

A simulation is used to model the drift of the electrons within the TPC gas from the point of ionization to the readout plane. The simulation uses information from the survey of the magnetic field. The following section gives a summary of the measurement and analysis of the magnetic field data done by the Bern T2K group. More detailed information can be found in [90].

Figure 4.1: UA1/NOMAD magnet used in ND280 in the open position [59].

Measurement of Magnetic Field

The magnetic field was surveyed using Hall probes mounted on a custom survey device. The Hall probes measured the induced voltage from the Hall effect for each component of the magnetic field (B_x, B_y, B_z).

For the Hall probe calibration performed at CERN, each card was placed in a highly uniform field whose strength was monitored by a nuclear magnetic resonance (NMR) probe with a precision of better than 1 Gauss.

The probes were mounted on 3 arms spanning the width (x direction) of the ND280 detector region. To prevent undesired field distortions, all of the equipment was built of non-magnetic material such as aluminum and stainless steel. The arms were moved with three pneumatic motors in the y and z directions to measure the magnetic field in a region slightly larger than the instrumented region of the ND280 basket. The information on the position of the mapping device during its operation was read out by four optical encoders which allowed the user to control the movement of the equipment.

The magnetic field was mapped in early September 2009. At the volume centre the field was mapped in steps of 200 A of the coil's current during two full cycles of ramp-up to 1000 A and back down to 0 A. Another ramping cycle was done with 250 A steps and a 10 cm B field measurement grid through the whole instrumented

region. A 10 cm grid means that the mapping device was moved in steps of 10 cm in the beam direction (z) as well as in the vertical direction (y). The 5.7 cm distance of the probes in the third dimension (x) is determined by the fixed points of the cards on the arms of the mapping device.

A detailed field map of the region of the TPCs was done at a current of 1000 A ($\simeq$ 0.07 T), consisting of more than 250,000 measurement points, which corresponds to a 5 cm grid.

Figure 4.2 shows the mapped B-field as a function of y and z in the region of the TPCs.

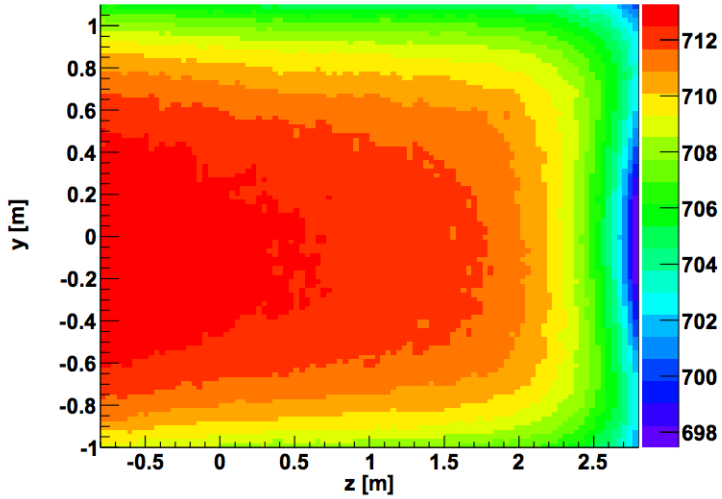

Figure 4.2: The colour plot shows a slice (x = 0, the basket central plane) of the mapped B-field (in Gauss) in the TPC region. The neutrino beam is entering the picture from the left [90].

Fitting of Data

In the absence of electric currents and with a quasi-static electric field the Maxwell equations for the magnetic field take the form, $\vec{\nabla} \cdot \vec{B} = 0$ and $\vec{\nabla} \times \vec{B} = 0$.

The geometry of the magnet has symmetries in cartesian coordinates with the origin at the centre of the magnet as the point of symmetry. Exploiting this feature and using the separation of variables technique, one obtains the following expression of the magnetic potential, Φ_M, which fulfills the Maxwell conditions:

$$\Phi_M = \sum_{nm} A_{nm} \sin(a_n x + \alpha_n) \cos(b_m y + \beta_m) \cosh(c_{nm} z + \gamma_{nm}), \qquad (4.1)$$

with the constraint $\alpha_n^2 + \beta_m^2 = \gamma_{nm}^2$ and n, m running to infinity.

The parameters a_n, b_m, c_{nm}, and A_{nm} are free parameters which are determined by the fit.

Since the material of the basket is not completely non-magnetic, regions nearby do not fulfill the criteria for the fitting function. Therefore the fit was only in a central region of the mapped volume (with a minimum distance of 20 cm from all distorting materials), where no distorting effects are observed. The region in which the fit was applied is shown in Fig. 4.3.

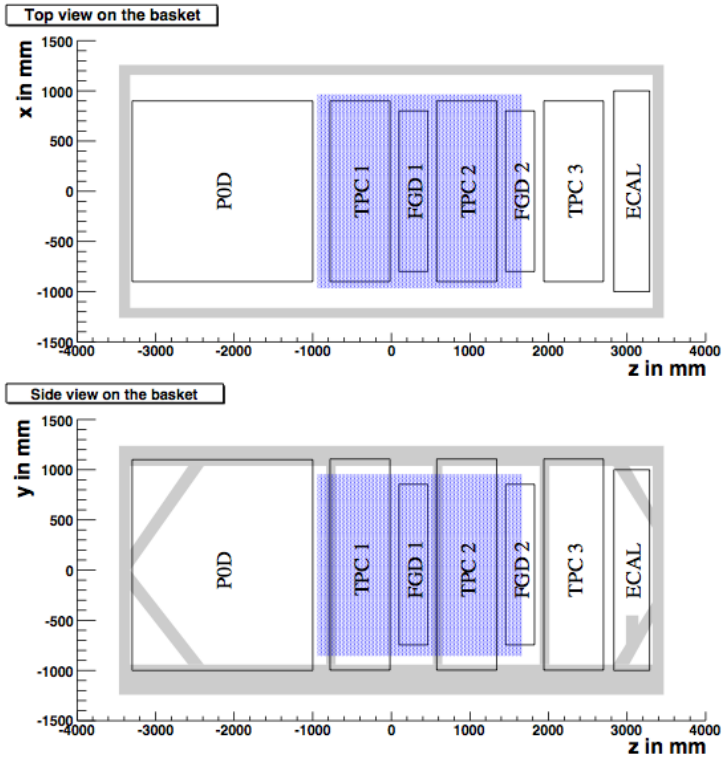

Figure 4.3: Top view (top) and side view (bottom) of the ND280 basket (in grey) and its containing detectors. The blue dotted region indicates the volume, for which the data fitting is applied [90].

A χ^2 fit was done using MINUIT for minimization. The fit converged at an order of two for the polynomial, higher orders not improving the fit. The residuals, $B_{c,i}^{measured} - B_{c,i}^{fit}$ are shown in Fig. 4.4, i runs over all measured points and c is the component index. The RMS of the residuals is of the same order of magnitude as the intrinsic uncertainty of the Hall probes (0.2 Gauss), indicating that the fit is appropriately describing the data.

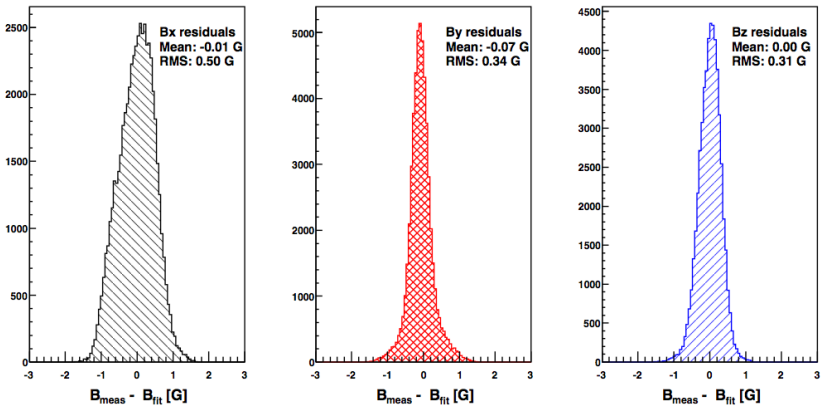

Figure 4.4: Distribution of residuals for each B-field component of the measurements done at the field magnitude of 700 Gauss (0.07 T). The widths of the distributions which is 0.5 G for the B_x component and even smaller for B_y and B_z are a measure for the fit quality [90].

For areas outside of the central region of the mapped volume the modelling of the data uses an interpolation between the measured data points. With a maximum distance of only 5.7 cm between two neighbouring measurement points, a linear interpolation is sufficient to describe the data.

4.2 Drift Simulation

For a particle with charge q and mass m moving in a gas with an electric field $\vec{E}$ and magnetic field $\vec{B}$ the force can be characterized by the equation of motion

$$m\frac{d\vec{v}}{dt} = q\vec{E} + q(\vec{v} \times \vec{B}) - K \cdot \vec{v}, \tag{4.2}$$

where the force on the particle is the vector sum of the electric field, the Lorentz force and a 'frictional' force caused by the deceleration of particles through collisions with gas molecules. The constant K > 0 and $m/K = \tau$ has a dimension of time and characterizes the mean time between collisions of the particle with the gas molecules.

A solution for $t >> \tau$ can be given by the steady state solution $d\vec{v}/dt = 0$ and the drift velocity is determined by the equation

$$\frac{1}{\tau}\vec{v} - \frac{q}{m}(\vec{v} \times \vec{B}) = \frac{q}{m}\vec{E}. \tag{4.3}$$

Equation 4.3 can be written in the matrix form $M\vec{v} = E$ where

$$M = \begin{bmatrix} m/q\tau & -B_z & B_y \\ B_z & m/q\tau & -B_x \\ -B_y & B_x & m/q\tau \end{bmatrix}. \tag{4.4}$$

To solve for $\vec{v}$, M is inverted to give,

$$\vec{v} = M^{-1}E,$$

$$M^{-1} = \alpha^2 \frac{1}{1+\alpha^2|B|^2} \begin{bmatrix} 1+B_x\alpha^2 & B_z\alpha + B_xB_y\alpha^2 & -B_y\alpha + B_xB_z\alpha^2 \\ -B_z\alpha + B_xB_y\alpha^2 & 1+B_y\alpha^2 & B_x\alpha + B_yB_z\alpha^2 \\ B_y\alpha + B_xB_z\alpha^2 & -B_x\alpha + B_yB_z\alpha^2 & 1+B_z\alpha^2 \end{bmatrix}, \tag{4.5}$$

where $\alpha = \frac{q\tau}{m}$. In the case of electrons the equation is generally written in terms of the Larmor frequency $\omega = eB/m_e$ giving

$$\vec{v} = \frac{e}{m_e}\frac{\tau}{1+\omega^2\tau^2}\left(\vec{E} + \frac{\omega\tau}{B}(\vec{E}\times\vec{B}) + \left(\frac{\omega\tau}{B}\right)^2(\vec{E}\cdot\vec{B})\vec{B}\right), \tag{4.6}$$

known as the 'Langevin Equation'.

The simulation of the drift of electrons using the Langevin equation is done by an incremental stepping of the electron position. For an electron at a given location in the magnetic field, the velocity and the position of the next step are calculated using a 4th-order Runge Kutta method with a fixed step size. This process is done for each step, propagating the electron until its position reaches the x coordinate of the TPC readout plane.

4.2.1 Impact

The impact of inhomogeneities in the ND280 magnetic field on the momentum scale is characterized by a Monte Carlo study. The study is done for a sample of tracks in the TPC's, simulating the drift of electrons with two magnetic fields; a perfect magnetic field ($B_x = 0.2$ T) and the magnetic field obtained from the survey. The reconstruction is done for the output of the two simulations, comparing the bias in the inverse transverse momentum. The study is done for both the central TPC (TPC 2) and the most downstream TPC (TPC 3).

The studies use a sample of MC particles generated to simulate the outgoing particles passing the selection of CCQE events described in T2K internal note T2K-TN-015 [91]. The MC truth information of the muon momentum, position and direction when entering the TPCs is used to generate a sample of muons that are input into GEANT4 and then the drift simulation. The electron drift simulation is run twice for a single GEANT4 output, once simulating with a magnetic field $B_x = 0.2$ T with no magnetic field inhomogeneities (perfect field) and once with the measured magnetic field generated from the survey and fit (measured field) described in Section 4.1.1. Since GEANT4 and the drift simulation are rerun, introducing statistical fluctuations in the MC events, cuts described in Section 4 of T2K-TN-015, which select the highest momentum track with a momentum above 50 MeV/c, are performed in order to acquire the desired sample.

Both instances of the field simulation used the Langevin equation (Eq. 4.6) with input parameters listed in Table 4.1.

Parameter	Value
μ	28600 cm$^2/Vs$
v_{drift}	7.85 cm/μs
$\sigma_{Transverse}$	0.0286 cm/$\sqrt{}$(cm)
$\omega\tau$	0.42

Table 4.1: Values for parameters used the MC field simulation.

The parameter $\sigma_{Transverse}$ is found from measurements of the transverse diffusion from reconstructed TPC tracks. The product $\omega\tau$ is found from measuring the difference in the transverse diffusion with the magnetic field on and off input into Eq. 3.12. The drift velocity which is found from laser calibration data is used with the mobility, μ to give the magnitude of the electric field via Eq.3.3. The electric field in the MC is simulated as homogeneous, the direction of the field is set to be and parallel or antiparallel to the x coordinate axis for readout plane 1 and 0 respectively.

Figures 4.5 to 4.10 show the residuals in the inverse transverse momentum ($1/p_{t\,reco} - 1/p_{t\,true}$) for both field simulations plotted as function of different kinematic variables, the residuals in units of GeV^{-1}.

Figures 4.5, 4.6 and 4.7 show the residuals in $1/p_t$ verses true momentum, $\cos\theta$ and the upstream x position respectively for TPC 2. The angle θ is the polar angle with respect to the +z axis and the x coordinate is orientated along the drift direction, the

origin corresponding to the TPC central cathode. It can be seen from these figures that the magnetic field distortions do not introduce a significant bias in $1/p_t$ and the measured field simulation is consistent with the perfect field case.

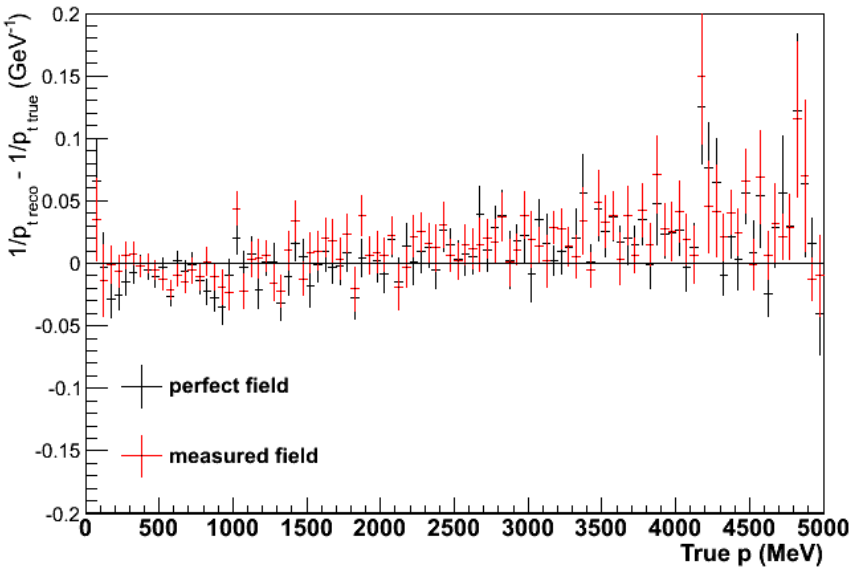

Figure 4.5: The residuals in $1/p_t$ as a function of true momentum in TPC 2. The residuals in $1/p_t$ are shown for both the perfect field and measured field used in the TPC drift simulation.

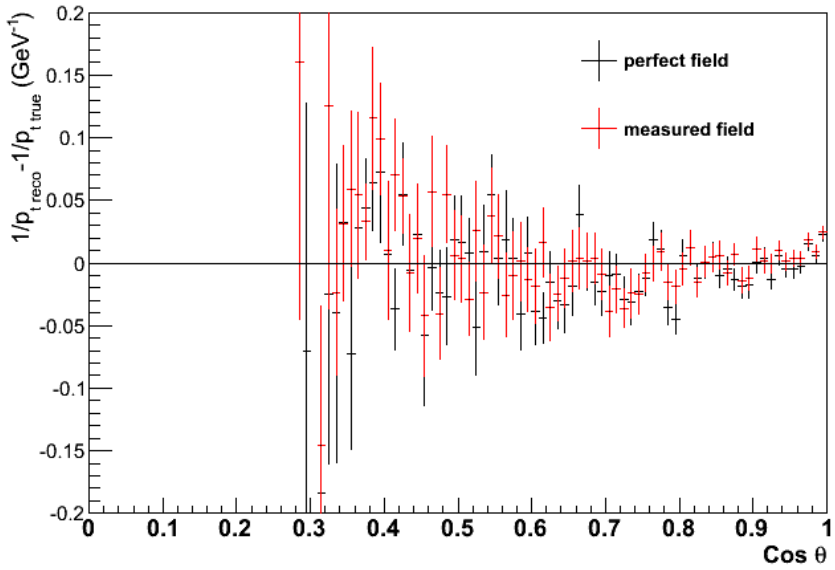

Figure 4.6: The residuals in $1/p_t$ as a function of the reconstructed $\cos\theta$ of the track in TPC 2. The residuals in $1/p_t$ are shown for both the perfect field and measured field used in the TPC drift simulation.

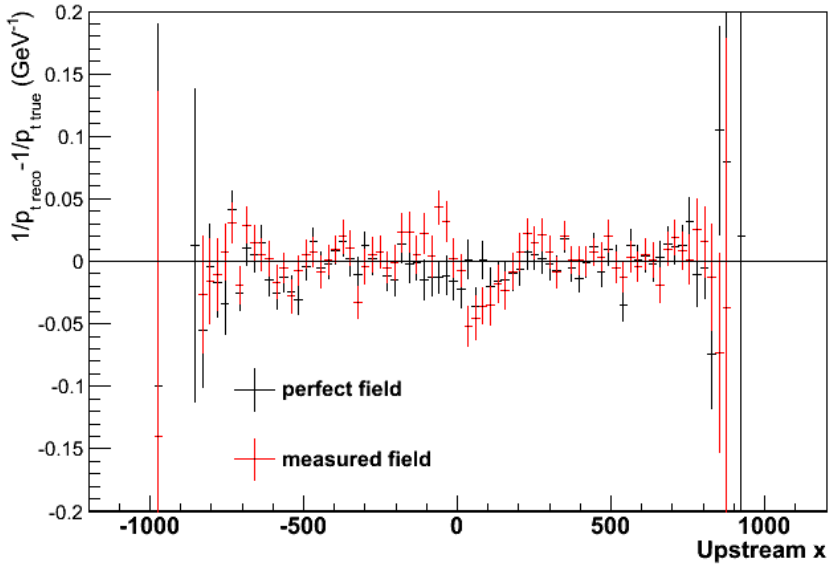

Figure 4.7: The residuals in $1/p_t$ as a function of the most upstream reconstructed x position in TPC 2. The residuals in $1/p_t$ are shown for both the perfect field and measured field used in the TPC drift simulation.

Figures 4.8, 4.9 and 4.10 show that for TPC 3, the measured field simulation

introduces a significant bias in $1/p_t$, on the order of $\sim 0.1\ \mathrm{GeV}^{-1}$.

From the calibration system, the largest magnetic field distortions have been measured in TPC 3 and it is expected to have the largest momentum bias of the 3 TPCs. The cause of this can be seen in Fig. 4.2 where the downstream end of the basket which is occupied by TPC 3 has a less uniform magnetic field compared to the centre region which is occupied by TPC 2.

Figure 4.8 shows the residuals as a function of true momentum of the track, it can be seen that the bias is larger for high momentum tracks. Tracks with higher momenta have less curvature than low momenta tracks so that any distortions in the track shape will cause a larger relative change in the momentum.

Figure 4.9 shows the residuals as a function of $\cos\theta$ of the track, the largest bias can be seen for forward going tracks.

Figure 4.10 shows the residuals as a function of the most upstream reconstructed x position. The measured field simulation introduces the largest bias for tracks at large drift distances.

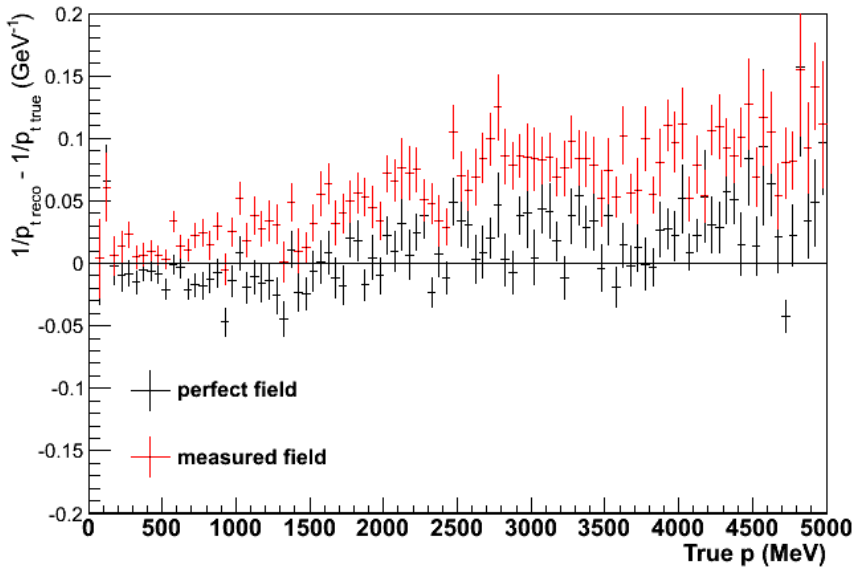

Figure 4.8: The residuals in $1/p_t$ as a function of true momentum in TPC 3. The residuals are shown for both the perfect field and measured field used in the TPC drift simulation.

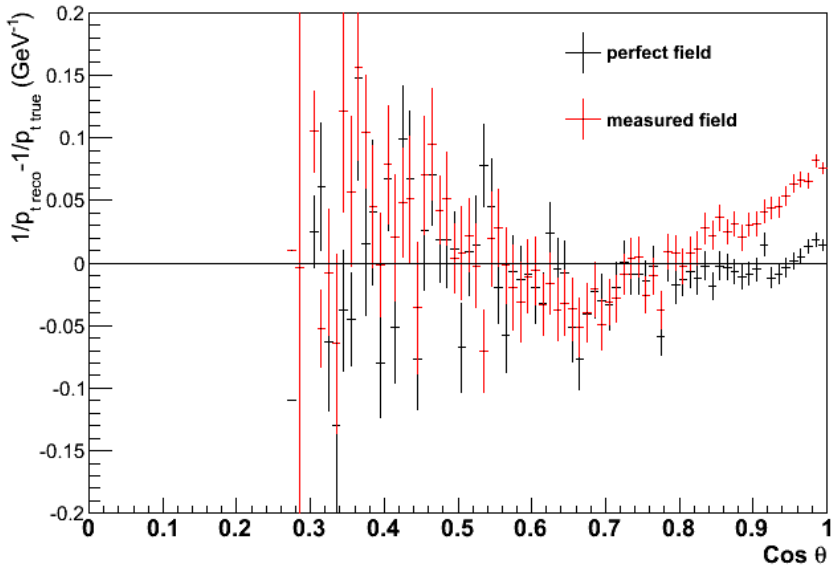

Figure 4.9: The residuals in $1/p_t$ as a function of the reconstructed $\cos\theta$ of the track in TPC 3. The residuals are shown for both the perfect field and measured field used in the TPC drift simulation.

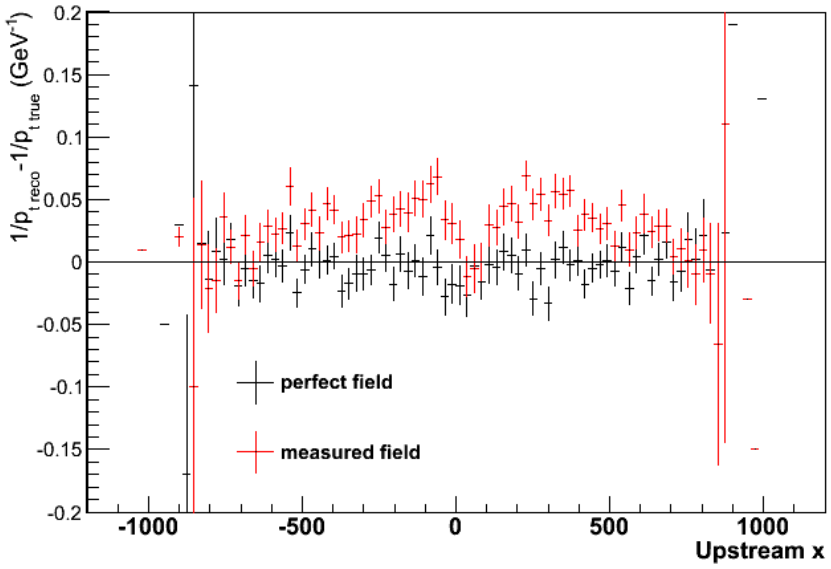

Figure 4.10: The residuals in $1/p_t$ as a function of the most upstream reconstructed x position in TPC 3. The residuals are shown for both the perfect field and measured field used in the TPC drift simulation.

Using a simplified MC sample with tracks orientated parallel to the +z direction

and monoenergetic at 1 GeV shows that to first order the bias introduced by the magnetic field distortions is linear with the drift distance. Fig 4.11 shows residuals in $1/p_t$ vs the upstream x position on one readout plane, for the simple MC sample, using the two different magnetic field simulations.

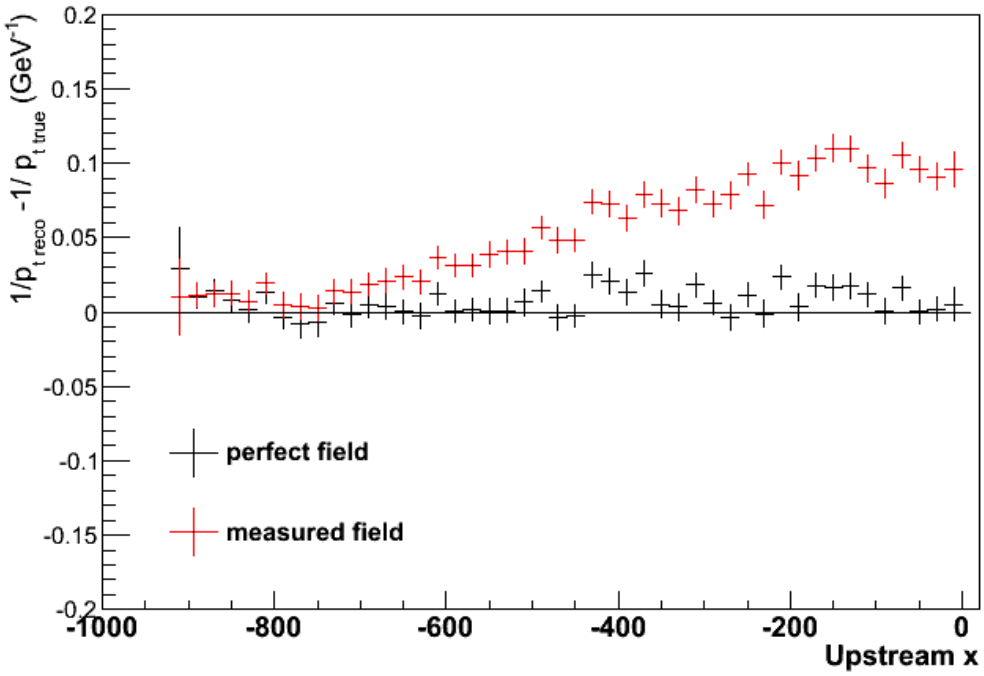

Figure 4.11: The residuals in $1/p_t$ as a function of the reconstructed most upstream reconstructed x position in TPC 3 RP0. The residuals are shown for both the perfect field and measured field used in the TPC drift simulation. This plot is generated using a MC sample of tracks all parallel to the +z direction and monoenergetic at 1 GeV.

4.3 Corrections to Magnetic Field Distortions

In order to reduce the bias in the momentum and to reach the goal of 0.02 GeV^{-1} in the inverse transverse momentum bias uncertainty the magnetic field distortions need to be corrected for. Tools have been developed to account for spatial distortions caused by imperfect fields and are implemented in the TPC reconstruction algorithm (Section 3.3.7).

4.3.1 Field Correction

Corrections applied using the measured magnetic field information and drift simulation are called the "field correction". Prior to the likelihood fit, the seed track parameters are used to select points with which to evaluate the displacements of ionization. At each point where the seed track crosses the z-coordinate that corresponds to the centre of a Micromegas pad column, a hypothetical particle is transported using the same 4th-order Runge Kutta method described in Section 4.2. The particle starts at the readout plane and is drifted back to the reconstructed x position of the seed track. The hypothetical particle has a positive charge in order for the simulation to move the particle away from the readout plane. The displacement in y and z, compared to its starting point, is recorded. The likelihood fit to the observed ionization pattern on the Micromegas plane takes into account the distortions by adjusting the expected ionization pattern by using the displacements recorded for the seed track. The approach does not re-evaluate the displacements for each track hypothesis considered, as it is too time consuming. Since the seed track is close to the fitted track, this is a good approximation.

4.3.2 Field Correction Validation

For the validation of the field correction the same samples used for the impact studies in Section 4.2.1 are considered. The studies are done for TPC 3 where the measured field introduces a significant bias.

Again the simulation of the drift is run twice on the same MC files using two different magnetic fields; the perfect and measured fields. Over those simulation files the reconstruction is run once in the case of perfect magnetic field and twice in the case of the measured field map, with and without the field correction applied. In this way the results of the reconstruction are compared for three cases:

1. Using the perfect magnetic field in the drift simulation *without applying* the field correction in the reconstruction.

2. Using a measured magnetic field in the drift simulation *without applying* the field correction in the reconstruction.

3. Using a measured magnetic field in the drift simulation *applying* the field correction in the reconstruction..

In this approach the field correction tool should remove any biases from the inhomogeneities in the measured field simulation and the reconstructed inverse transverse momentum distribution should be comparable to the perfect field case. A measure of the residuals $(1/p_{t\,reco} - 1/p_{t\,truth})$ is used to observe the effects of the applied field correction.

Figures 4.12, 4.13 and 4.14 show the residuals as a function of true momentum, $\cos\theta$ and the upstream x position respectively. The figures show the residuals for the perfect field and measured field used in the drift simulation, plotted with the residuals after applying the field correction. It can be seen from the figures that the field correction reduces the bias in $1/p_t$ and the results are consistent with the perfect field case, showing that the field correction technology is working as intended.

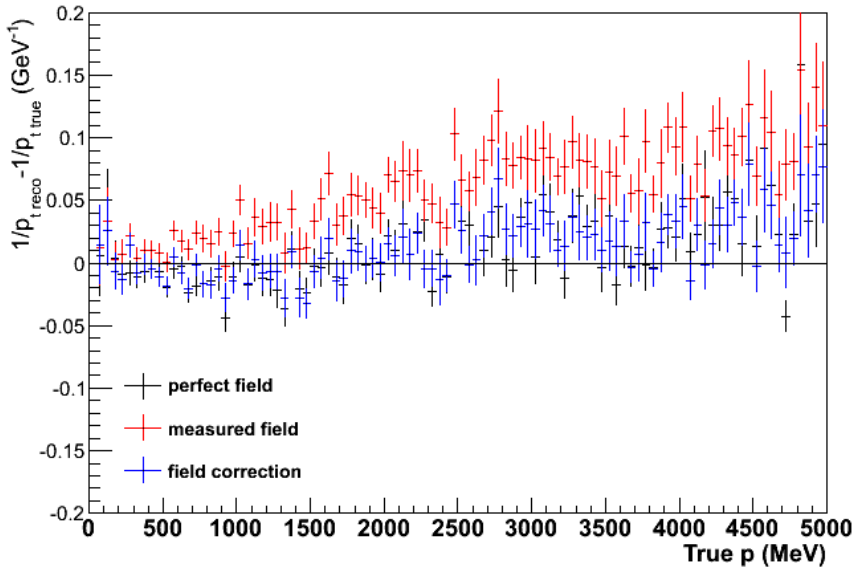

Figure 4.12: The residuals in $1/p_t$ as a function of true momentum in TPC 3. The residuals are shown for the perfect field simulation and the measured field simulation with and without the field correction.

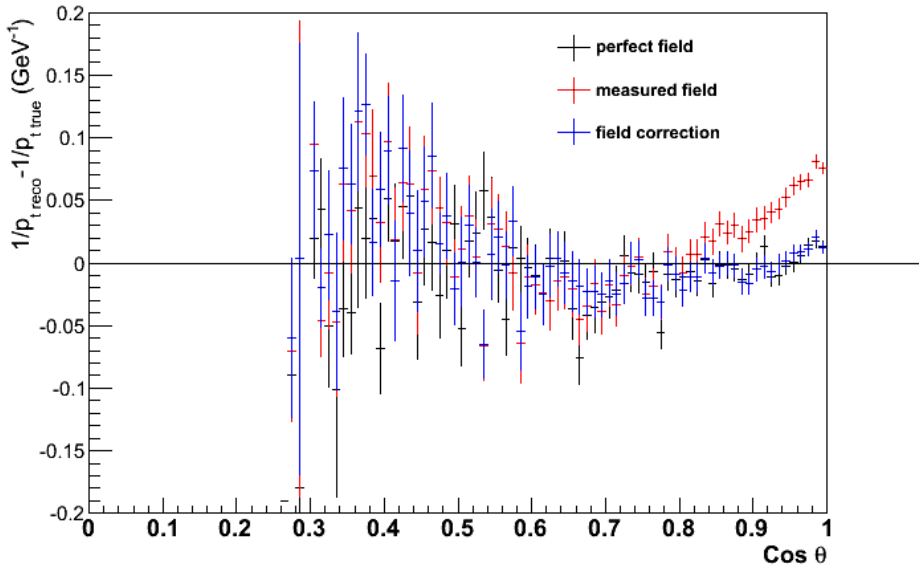

Figure 4.13: The residuals in $1/p_t$ as a function of $\cos\theta$ in TPC 3. The residuals are shown for the perfect field simulation and the measured field simulation with and without the field correction.

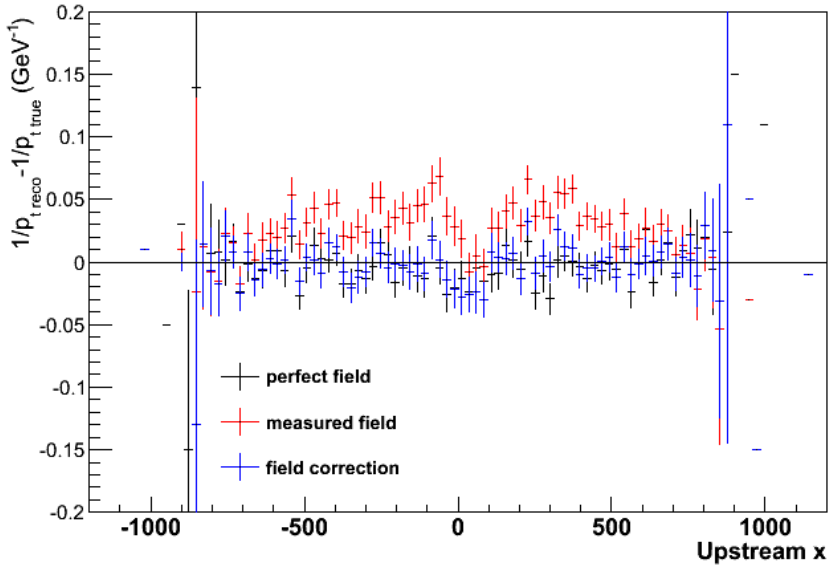

Figure 4.14: The residuals in $1/p_t$ as a function of the upstream x position in TPC 3. The residuals are shown for the perfect field simulation and the measured field simulation with and without the field correction.

4.3.3 Empirical Correction

In order to define the systematic uncertainty on the field correction an additional empirical correction is used. The differences in the magnetic field distortions between the data and the MC are not understood and represent the uncertainty of magnetic field distortions. The empirical correction quantifies the differences in the magnetic field distortions and is used as a tool to evaluate the systematic uncertainty.

The photocalibration system described in Section 3.3.12, is used to measure the magnetic field distortions in each TPC, the distortions are compared to a MC simulation of the photocalibration data and the differences between the two are analyzed to create an empirical distortion map. The map contains nominal yz position for each calibration dot and the differences in the displacements in the yz plane.

The method to find the displacements in the electron drift due the magnetic field distortion is outlined in Section 3.3.12. For both the data and MC simulation the photoelectrons originate at the central cathode so that the displacements are integrated over the entire drift length. Figure 3.26 shows the displacements due to magnetic field distortion for TPC 3 readout plane 0 and appendices A and B show the displacements for MC and data respectively, for all readout planes.

Using information from the empirical distortion map the empirical correction is applied in the TPC reconstruction at the same stage as the field corrector. As in the case for the field corrector, before the likelihood fit is done, the seed track parameters are used to select points with which to evaluate the corrections. The correction for each point is found by a bi-linear interpolation of the empirical distortion map, with the magnitude multiplied by the fraction of the full drift distance for that point. The linear dependance of the empirical correction with the drift distance is assumed because this is the general form of the distortions observed for the measured field simulation studies as seen in Fig. 4.11.

Figures 4.15 through to 4.20 show the differences in the displacements in z and y as a function of y for all readout planes. Each point on the plots represents a calibration target dot. The laser calibration data used was collected on November 26st 2010, running with a magnetic current of 0A and 2900A, the MC simulation used the parameters listed in Table 4.1.

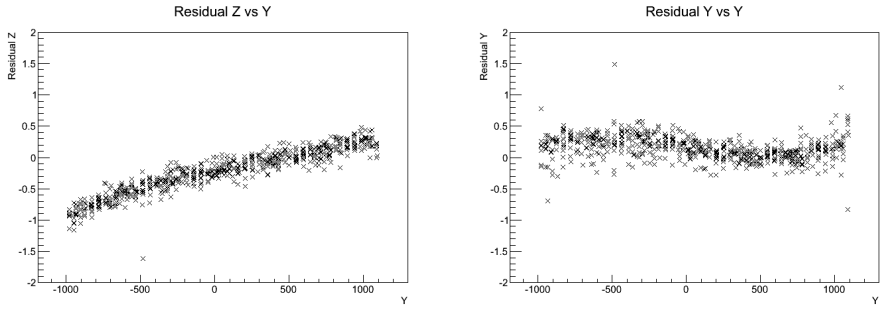

a: Z Residual b: Y Residual

Figure 4.15: Displacement residuals comparing data and MC, TPC 1 readout plane 0.

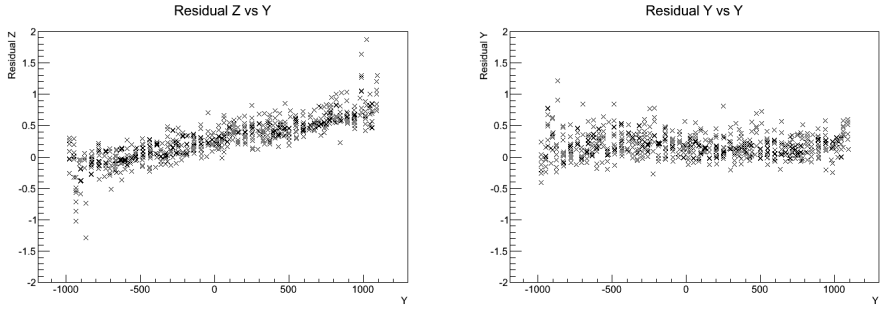

a: Z Residual b: Y Residual

Figure 4.16: Displacement residuals comparing data and MC, TPC 1 readout plane 1.

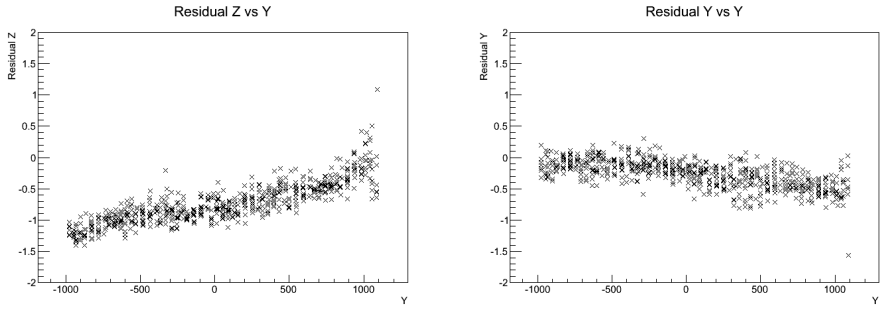

a: Z Residual b: Y Residual

Figure 4.17: Displacement residuals comparing data and MC, TPC 2 readout plane 0.

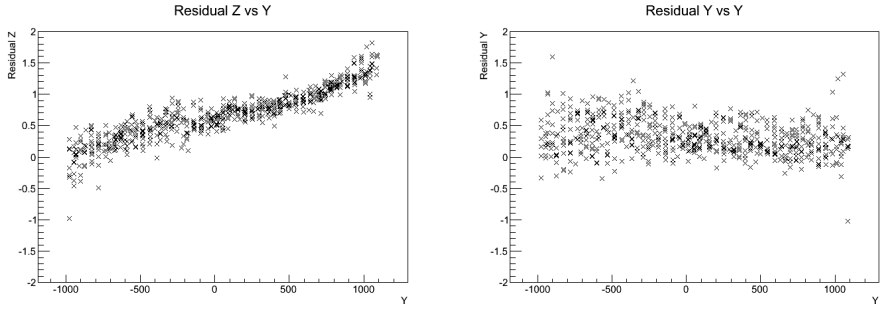

a: Z Residual b: Y Residual

Figure 4.18: Displacement residuals comparing data and MC, TPC 2 readout plane 1.

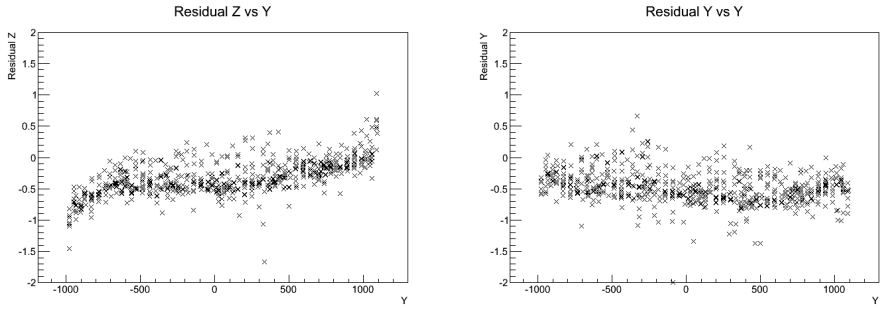

a: Z Residual b: Y Residual

Figure 4.19: Displacement residuals comparing data and MC, TPC 3 readout plane 0.

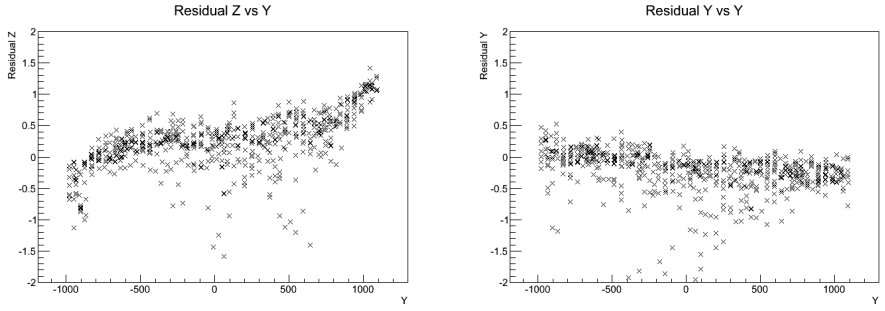

a: Z Residual b: Y Residual

Figure 4.20: Displacement residuals comparing data and MC, TPC 3 readout plane 1.

The origin of the non-zero residuals between data and MC is unknown, possible sources could include:

- Magnetic materials in the detectors, installed after the magnetic field survey causing further distortions in field.
- Non-uniformities in the electric field.
- Realignment of the magnetic coils after opening and re-closing magnet.
- Errors in the inputs to the MC simulation.

It should be noted that the scaling of the magnetic field strength in the MC will not affect the simulated displacements and is not a possible source of the non-zero residuals. With all other parameters constant, a multiplicative scale factor of the magnetic field will cancel out in the drift simulation, which can be seen from inspecting the Langevin equation.

Due to the unknown source of the discrepancies, the residuals between data and MC are used to evaluate the systematic uncertainty of the momentum scale due to displacements from the magnetic field distortions. A study evaluating the uncertainty is outlined in Section 4.5.1.

4.3.4 Empirical Correction Validation with MC

The empirical correction technology is tested by applying the correction to a MC sample with a known field distortion to ensure that the correction is behaving as expected. For this specific study the measured field simulation is used.

A test empirical correction map used to correct the MC is made in the following manner:

- The drift of photoelectrons originating from the target dot locations on the central cathode, traversing the full length of the TPC is simulated.
  - The simulation is done for both the perfect field and measured field.
- For both simulations the dot centroids are fit.
- The distortions in the yz plane are computed by calculating the differences in the measured centroids for the two different field simulations.

The procedure provides a map that describes the differences between the perfect and measured field simulation integrated over the drift length. Implementing this test empirical correction map in the reconstruction should correct for any biases in the reconstructed inverse transverse momentum introduced by the measured field drift simulation.

As in the studies for the field corrector the test empirical correction map is applied to the sample of tracks described in Section 4.2.1 for TPC 3.

A measure of the residuals $(1/p_{t\,reco} - 1/p_{t\,truth})$ is used to observe the effects the test empirical correction map. Figures 4.21, 4.22 and 4.23 show the residuals as a

function of true momentum, $\cos\theta$ and the upstream x position respectively. The figures show the residuals for the perfect field and measured field used in the drift simulation for TPC 3, plotted with the residuals after applying the test empirical correction map at the reconstruction stage. It can be seen from the figures that the test empirical correction map reduces the bias in $1/p_t$ and the results are consistent with the perfect field case, showing that the empirical correction technology is working as intended.

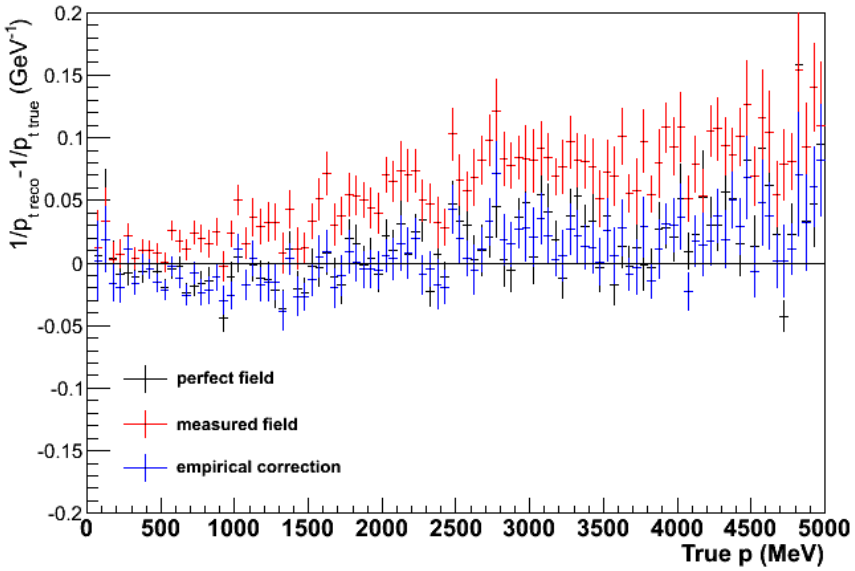

Figure 4.21: The residuals in $1/p_t$ as a function of true momentum in TPC 3. The residuals are shown for the perfect field simulation and the measured field simulation with and without the empirical correction.

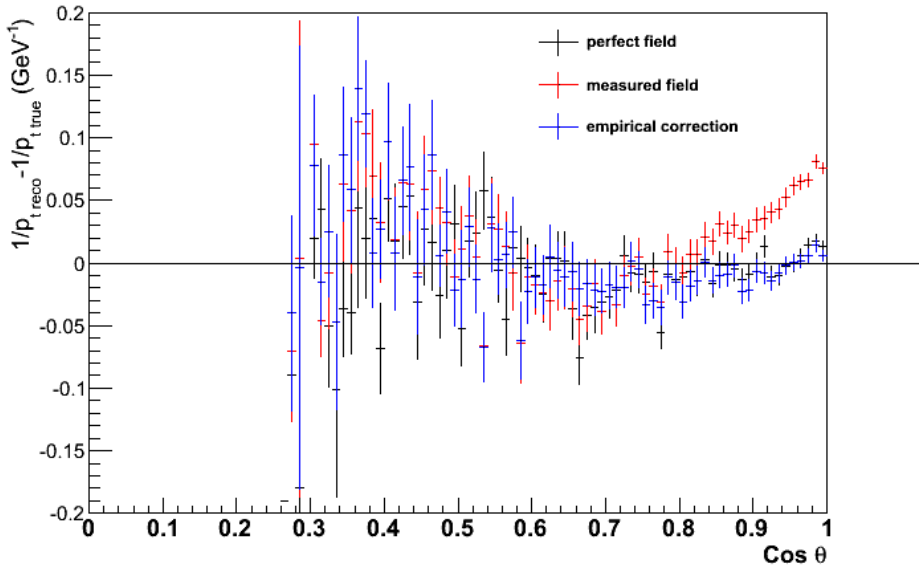

Figure 4.22: The residuals in $1/p_t$ as a function of $\cos\theta$ in TPC 3. The residuals are shown for the perfect field simulation and the measured field simulation with and without the empirical correction.

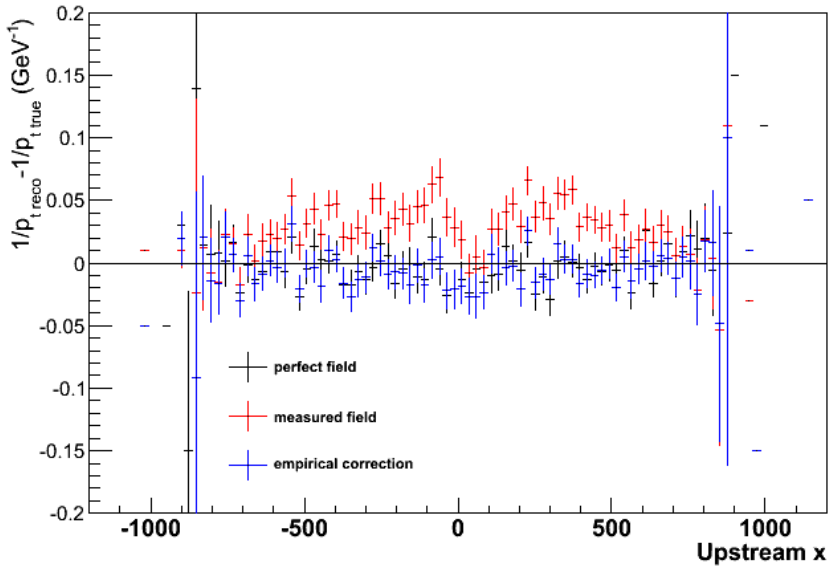

Figure 4.23: The residuals in $1/p_t$ as a function of the upstream x coordinate in TPC 3. The residuals are shown for the perfect field simulation and the measured field simulation with and without the empirical correction.

4.4 Validation for Data

4.4.1 Reconstructed Inverse Momentum Bias Between TPC 2 and TPC 3

For data, a study is done comparing the reconstructed inverse momentum in TPC 3 using information from two different sources. For tracks traveling through both TPC 2 and TPC 3, the inverse momentum in TPC 3 is calculated by:

- Using the reconstructed inverse momentum found in TPC 3 ($1/p_{rec}$).
- Using the reconstructed inverse momentum found in TPC 2, applying an energy loss correction due to the tracks passage through the downstream FGD ($1/p_{cor}$).

The large magnetic field distortions observed in TPC 3 will create a bias in the quantity $1/p_{rec}$ and in the residuals of ($1/p_{cor}$ - $1/p_{rec}$).

MC Cross Check

A Monte Carlo study is done in order to determine the effect of the displacements in the electron drift from the magnetic field distortions on the bias of the residuals $(1/p_{cor} - 1/p_{rec})$. In the study tracks are selected with the following cuts:

- Exactly one track in TPC 2 and TPC 3.
- Greater than 68 clusters in each track.
- Both tracks reconstructed in the forward going direction.
- Muon Pull $|\delta_E(\mu)| < 2.5$.

Furthermore tracks reconstructed in TPC 2 are extrapolated into TPC 3 to ensure the tracks are contained within the TPC 3 volume. Conversely tracks reconstructed in TPC 3 are also extrapolated into TPC 2.

The energy loss correction applied to the inverse momentum found in TPC 2 takes into account the downstream FGD (FGD 2) active material as well as the dead material in FGD and the TPCs. The expected energy loss for MIP's travelling between TPC 2 and TPC 3 is shown in Table 4.2. The dE/dx in each material varies as a function of momentum according to the Bethe-Block equation.

Material	dE/dx	width
FGD 2 Active	0.1929 MeV/mm	333.67 mm
FGD 2 End Plates (x2)	0.4456 MeV/mm	6.27 mm
TPC Dead Volumes (Front/Back)	0.01465 MeV/mm	96.12 mm
Total E loss	72.76 MeV	

Table 4.2: Expected energy loss for a MIP passing from TPC 2 to TPC 3, traversing FGD2.

In the MC study the residuals $(1/p_{cor} - 1/p_{rec})$ are computed for two different magnetic field simulations, the perfect field and measured field. Figure 4.24 shows the distribution of the residuals for the perfect and measured field, as well as the mean residual for each field simulation. The units for the inverse momentum are in GeV^{-1}. The figure shows that for the measured field simulation the bias in the residuals is larger. This is due to the bias in the inverse transverse momentum caused by magnetic field distortions in TPC 3 as seen in previous studies.

The MC check shows that distortions on the order of the measured magnetic field simulation will have a significant effect on the residuals $(1/p_{cor} - 1/p_{rec})$.

Applying Correction to Data

For data the same cuts are applied to the tracks as in the MC study. The momentum distribution of the sample is slightly different than the MC since the data sample contains muons originating from interactions in material upstream of the detector, which are not simulated in the MC. The momenta distributions for data and MC are shown in Fig. 4.25.

Figure 4.26 shows the distribution and mean value of the residuals when no correction is applied, applying the field correction and applying both the field and empirical corrections to data. From the mean value of the residuals it can be seen that when applying the field corrector the bias is smaller than when no correction is applied. When additionally applying the empirical correction the bias is somewhat greater, an unexpected behaviour since the combined field and empirical corrections should be a better representation of the magnetic field distortions in data. Although it is larger than the case where only the field correction is used, applying both the field and empirical correction the bias remains less than 0.016 GeV^{-1} and is an improvement on the bias present with no correction applied.

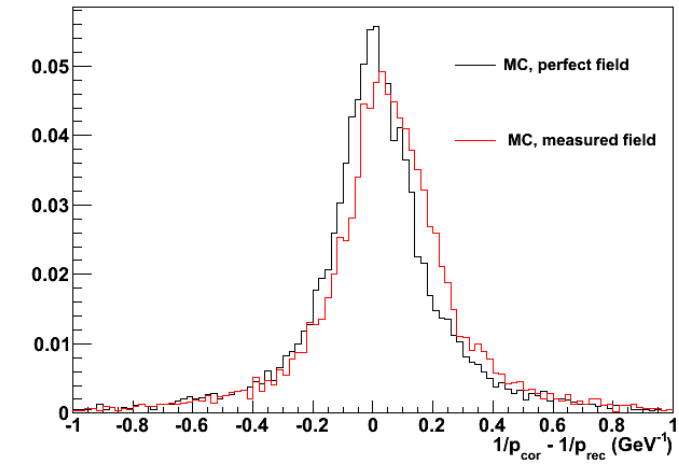

(a)

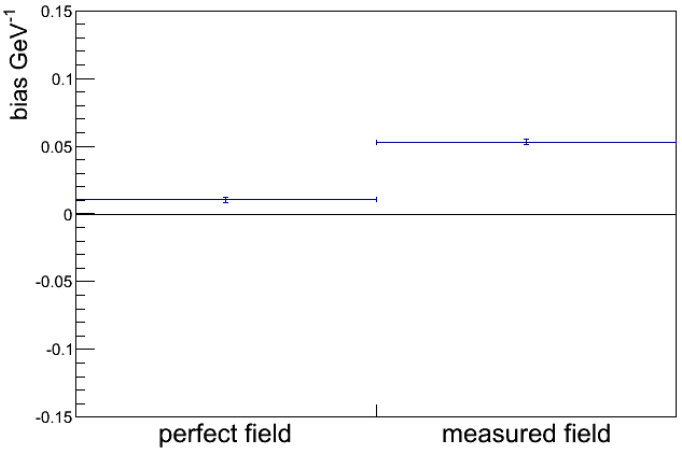

(b)

Figure 4.24: Residuals for $1/p_{cor} - 1/p_{rec}$ for perfect field and measured field simulation (a) mean residuals (b) for MC.

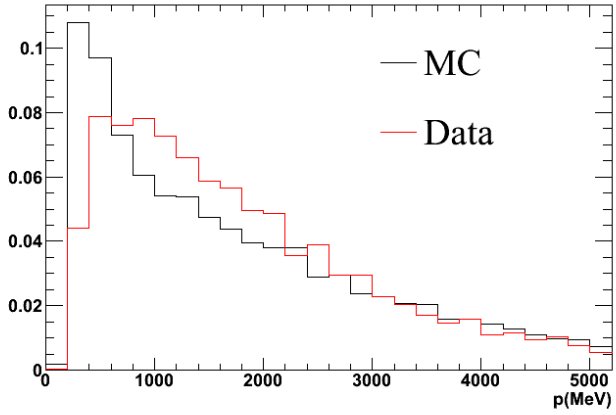

Figure 4.25: Data and MC momentum distributions used in correction study.

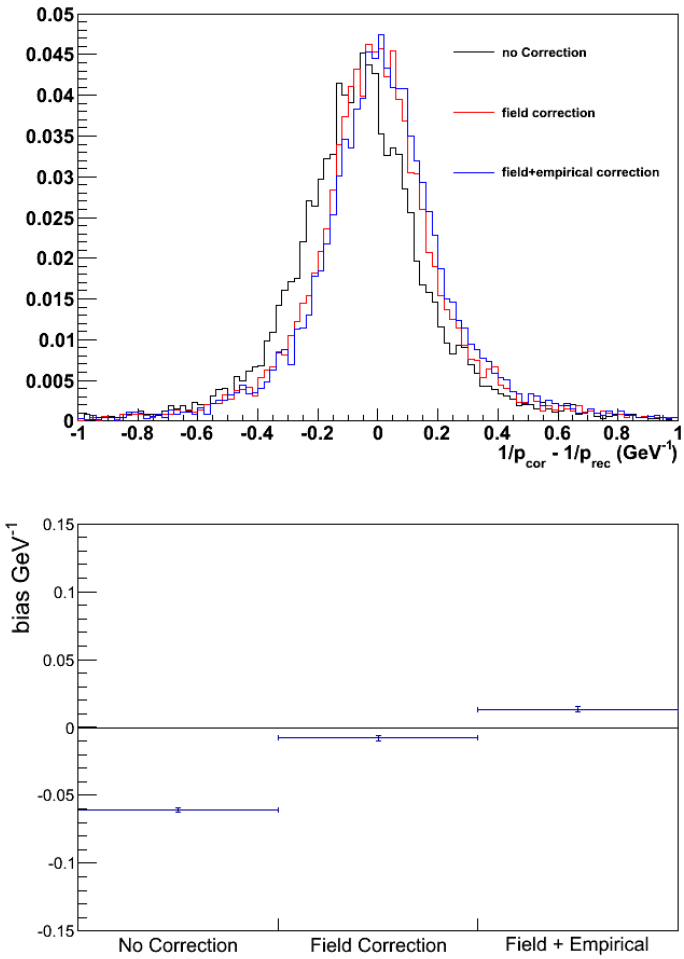

Figure 4.26: Residuals for $1/p_{cor} - 1/p_{rec}$ for data with no correction field correction and field + empirical correction (a) mean residuals (b) for data.

When measuring the mean value of the residuals in terms of the two readout planes as shown in Fig. 4.27 it can be seen that there is very different behaviour on readout plane 0 and 1. For readout plane 0 the mean after the field correction and field and empirical correction cases both have a small bias of similar magnitude but opposite sign. For readout plane 1 applying the field correction results in a small bias, however when adding the empirical correction a large bias is introduced. Additionally Fig. 4.28 shows the bias in $(1/p_{cor} - 1/p_{rec})$ versus the most upstream x position of the track in TPC 3, where readout plane 0,1 correspond to negative and positive x respectively. In this plot it is also observed that adding the empirical correction introduces a bias on readout plane 1, showing that the bias is larger for tracks close to x=0 which corresponds to tracks with the largest drift distance.

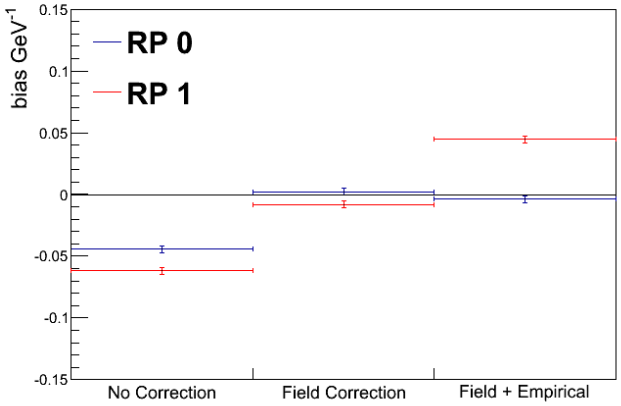

Figure 4.27: Mean of residuals $(1/p_{cor} - 1/p_{rec})$ for readout plane 0 (blue) and readout plane 1 (red) for data.

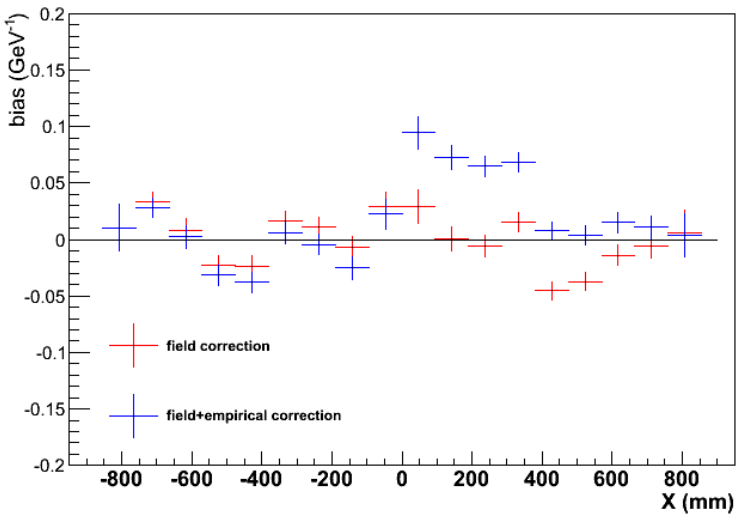

Figure 4.28: Residuals for $1/p_{cor} - 1/p_{rec}$ vs upstream x.

The source of the bias introduced by the empirical correction on TPC 3 RP 1 is not fully understood however one possible explanation could be due to the drift length of TPC 3. While doing a survey of the TPC's it is found that the drift volume of TPC 3 is 0.8 mm longer than the other TPCs. It is possible that if the extra length is on readout plane 1 this could cause electric field distortions close to the readout plane. Distortions concentrated at the readout plane will be incorrectly handled by the empirical correction since the distortions are modelled to be linear with drift distance.

Since it was observed that the bias in the inverse transverse momentum is smallest for the field correction only case, in the future the TPC reconstruction algorithm will only include this correction when fitting data.

4.5 Momentum Distortion Systematic

Due to the complexities of the displacements in the electron drift due to magnetic field distortions it is not possible to determine the effect they will have on the spectrum and momentum scale in a general way. The biases introduced by the field distortions are dependent on the spectrum of the particles as well as the angular and spatial distributions within the TPCs. This complexity requires that the systematic uncertainty be found for each unique sample of tracks that is used in physics analyses. The

following section describes how the uncertainty is calculated for a ν_μ CC sample used for the oscillation analyses reported in this thesis.

4.5.1 ν_μ CC Sample Momentum Distortion Systematic

For oscillation studies a sample at ND280 is selected, composed of tracks originating from ν_μ CC interactions in the upstream FGD. The sample is binned in terms of p_μ, θ_μ and broken up into QE-like and non-QE-like event selections, a more detailed description of the sample is given in Section 5.2 and in T2K-TN-093 [92]. For the selection only tracks in TPC 2 are considered, and MC separated into Run 1 and Run 2 is used for the evaluation of the systematic. The Monte Carlo statistics are equivalent to 54.5×10^{19} POT for Run 1 and 110.5×10^{19} POT and are simulated with different average intensity, 50 kW for Run1 and 120 kW for Run2. Figure 4.29 shows the momentum and angular distributions for the inclusive CC sample for Run 1 and Run 2 together, data and MC broken into neutrino interaction components are shown.

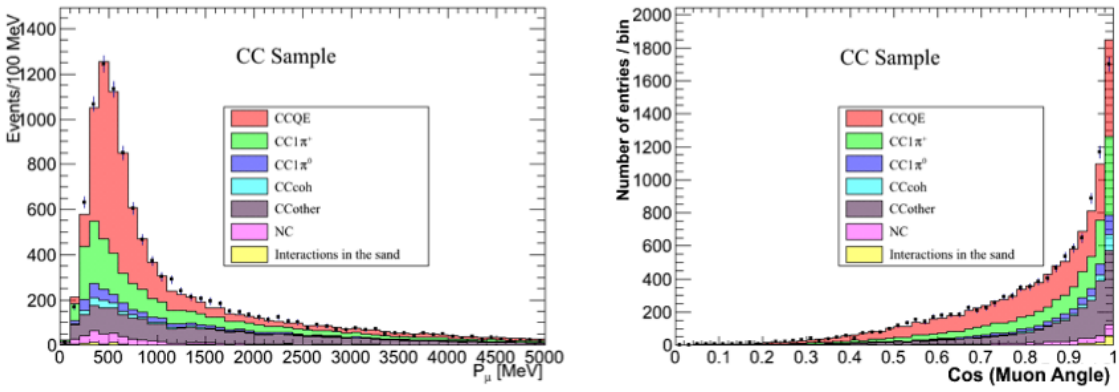

Figure 4.29: Data and MC p_μ (left) and $\cos\theta_\mu$ (right) distributions for the ν_μ CC sample for Run 1 and 2 for MC (solid line) and data (dot) [92].

The evaluation of the error on the momentum scale and any biases due to magnetic field distortions is important in conducting oscillation studies.

The MC truth information of the muon momentum, position and direction when entering the TPCs is used to generate a sample of muons that are input into GEANT4 and the TPC drift simulation. For a single GEANT4 output sample, the drift simulation is run twice, using the perfect and measured magnetic field simulations.

The perfect field is used as the default magnet field in the MC simulation of the drift, so to better model the data a migration in terms of the p_μ, θ_μ bins is applied to the ν_μ CC selection. The representation of data is found using the magnetic field in the drift simulation and applying the empirical correction in the reconstruction to account for the differences seen in the photocalibration data between data and MC. The migration applied to MC is found by comparing the reconstructed number of events in each p_μ, θ_μ bin for the perfect field simulation and the measured field simulation with empirical correction. The systematic error in the migration is found by comparing the number of events in each bin, for the measured field simulation, with and without the empirical correction applied.

Evaluation of systematic error

For the uncertainty that is used in further oscillation studies a systematic covariance matrix is calculated in terms of the 40 p_μ, θ_μ bins. The systematic error in the magnetic field distortion is given by 100% of the empirical correction since the source of the non-zero residuals between data and MC are not fully understood (Section 4.3.3). The systematic covariance is calculated following the prescription given by Eq. 6 in TN-093

$$v_{ij} = \frac{\Delta_i \Delta_j}{n_{pred,i} n_{pred,j}}, \tag{4.7}$$

where n_i is the number of events in bin_i and Δ_i is the difference in the number of events in bin_i with and without the empirical correction applied, $\Delta_i = n_{empirical_{on},i} - n_{empirical_{off},i}$.

Evaluation of statistical error

Due to the finite statistics of the MC sample and the re-simulation of GEANT4 and the drift simulation, the migration of events from one bin to another caused by the magnetic field distortions also have associated statistical errors. For the statistical fluctuations of the number of events in a given bin, one must take into account the variation in the number of events that migrate out of that bin to all other bins, resulting in a loss in the number of events in a bin, as well as the variations in the number of events entering a given bin from all other bins, resulting in the increase in the number of events in a bin.

The probability of an event migrating from one bin to another is evaluated by finding instances where a truth event is reconstructed in bin_i for the perfect field simulation and is reconstructed in bin_j for the measured field simulation with empirical correction. Here the indices indicate the p_μ, θ_μ bin. The probability of an event migrating from bin_i to bin_j is given by p_{ij}.

For bin_i with a number of entries N_i the probability of events migrating to bin_j is given by

$$p_{ij} = \frac{n_{ij}}{N_i}, \tag{4.8}$$

where n_{ij} is the number of events migrating from bin_i to bin_j. Summing over j for $j \neq i$ gives the total probability that an event in bin_i will migrate to another bin denoted by p_{loss_i}. The number of events migrating out of bin_i follows the binomial distribution and has a variance of $\sigma^2_{loss_i} = N_i p_{loss_i}(1 - p_{loss_i})$.

For the opposing situation where an event in bin_j migrates *into* bin_i. The probability is given by $p_{ji} = \frac{n_{ji}}{N_j}$ (noting that n_{ji} indicates that an event in bin_j migrates to bin_i).

Events migrating from bin_j to bin_i follow the Poisson distribution with a mean and variance equal to $N_j p_{ji}$. Summing the variances for each over bin_j ($j \neq i$) give the total variance of the number of events entering bin_i. This gives the total variance in the number of events in bin_i as

$$\sigma_i^2 = N_i p_{loss_i}(1 - p_{loss_i}) + \sum_{j \neq i} N_j p_{ji}. \tag{4.9}$$

The statistical errors for the different bins are organized into a covariance matrix where the off diagonal elements are given by

$$\sigma_{ij}^2 = -\frac{N_i p_{ij} + N_j p_{ji}}{N_i N_j}, \tag{4.10}$$

and the diagonal elements are given by Eq. 4.9. The statistical error is evaluated separately for the QE-like and non-QE-like subsamples.

Total error

The statistical and systematic errors are combined to give the total error on the migration. The change in the fraction of events in the 20 bins for QE-like and non-

QE-like samples is shown in Figs. 4.30 and 4.31 plotted with the statistical and combined statistical and systematic errors for each p_μ, θ_μ bin. It can be seen from the figures that the statistical component is the dominant error.

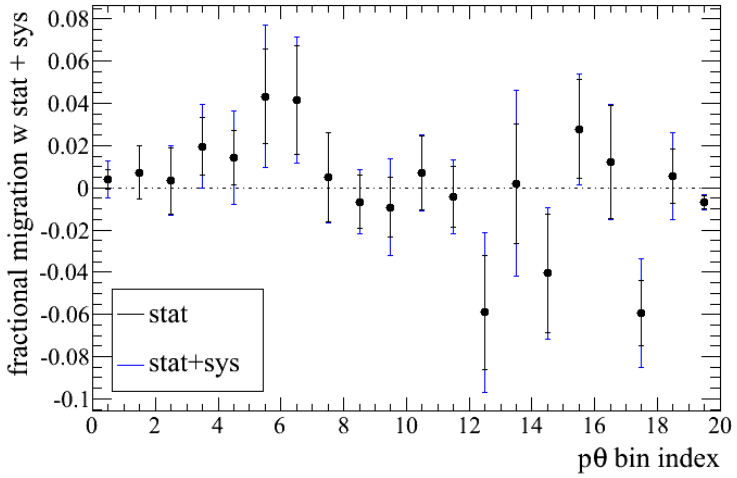

Figure 4.30: Migration of events for CCQE-like bins.

The statistical and systematic covariances described above are shown in the form of a 40x40 covariance matrix in Figs. 4.32 and 4.33. The total covariance which is the sum of the statistical and systematic components is shown in Fig. 4.34. The total covariance matrix is combined with other systematic uncertainty matrices to create the overall uncertainty in the ND280 detector used as an input to the oscillation analyses.

In future data processing the field and empirical corrections will be included in the reconstruction phase of processing. This removes the need for any re-simulation steps in the error calculation and will reduce the statistical uncertainties.

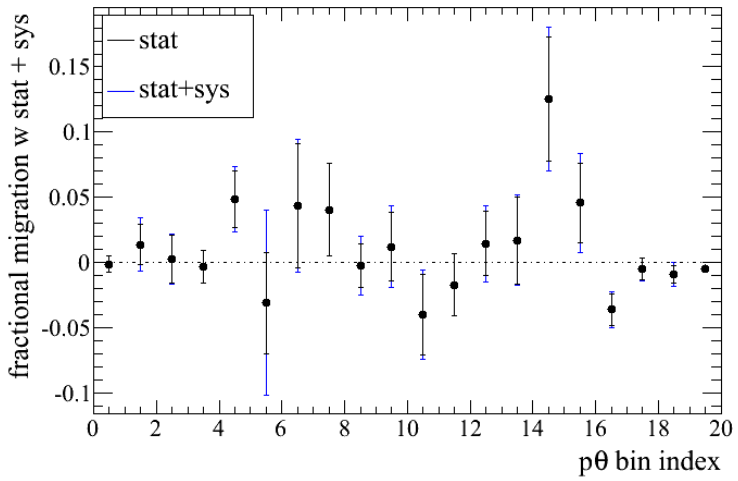

Figure 4.31: Migration of events for CCnonQE-like bins.

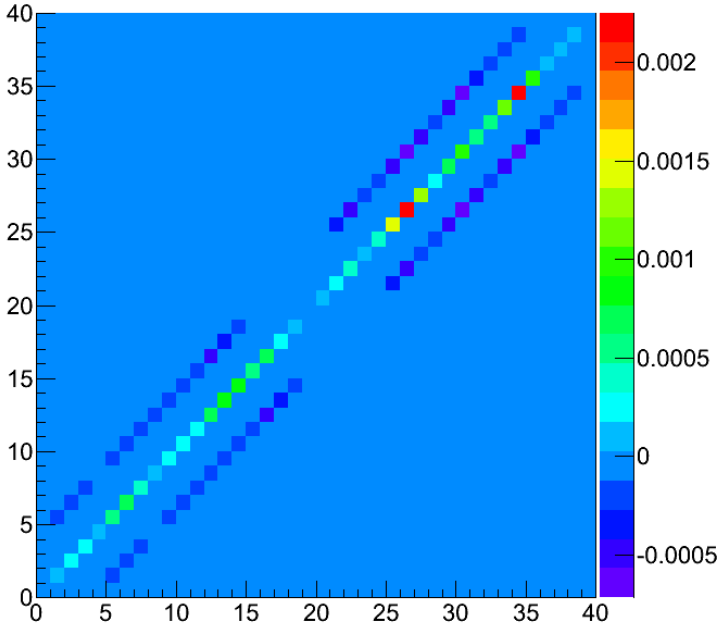

Figure 4.32: Statistical covariance due to finite size of MC sample.

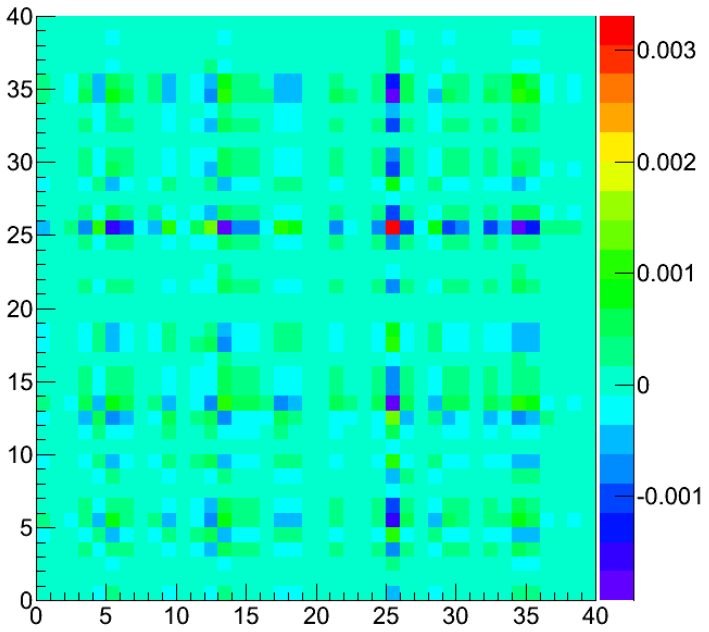

Figure 4.33: Systematic covariance due to uncertainty in the magnetic field distortions.

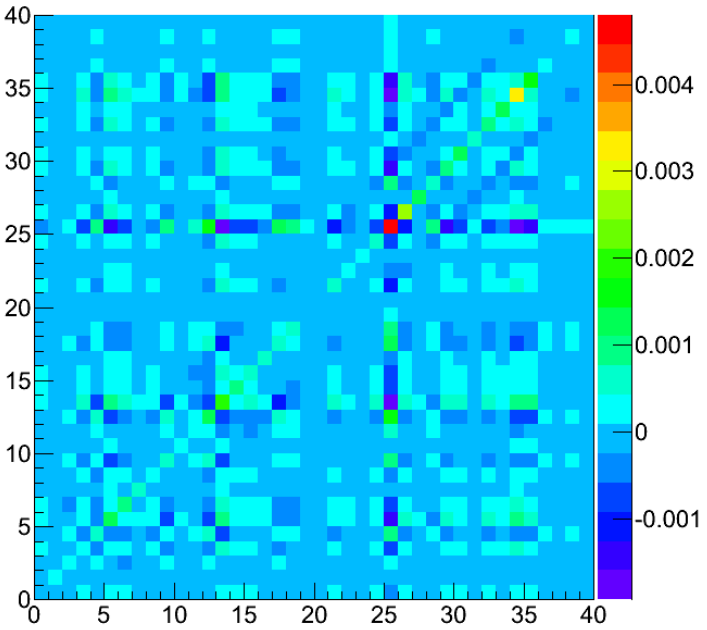

Figure 4.34: Total covariance.

Chapter 5

ν_μ Disappearance Measurement at T2K

An analysis of the ND280 and Super-Kamiokande detector samples is done to measure ν_μ disappearance at T2K. This approach differs from the majority of T2K oscillation analyses, which deal with the detector samples separately. A Markov Chain Monte Carlo(MCMC) framework is used for this analysis and the approach is motivated by the large number of systematic parameters.

Other T2K, oscillation analyses have been performed in a piecewise manner: first constraining systematic parameters using the ND280 sample, and then propagating those parameters as inputs for an oscillation analysis using the SK sample. In the piecewise approach, for the parameters propagated from the near detector, the expected number of events is approximated to be a linear function of the nuisance parameters assuming the log-likelihood behaves quadratically near the maximum. In the case of the MCMC approach, the nuisance parameters are marginalized over, and there is no need for such approximations.

However, treating both detector samples simultaneously means that both near and far detector systematics must be included, greatly increasing the number of parameters. Minimizers such as MINUIT are more likely to fail to converge in non-linear, large-dimensional spaces, and thus the need for alternative analysis techniques arises.

One such technique is a Metropolis-Hastings algorithm Markov Chain Monte Carlo, which allows for efficient sampling of the joint probability distribution of an arbitrary number of parameters. The following sections give an overview of Markov Chains and the Metropolis-Hastings algorithm, followed by a description of the like-

lihood used in the analysis.

5.1 Markov Chains and the Metropolis-Hastings Algorithm

5.1.1 Markov Chains

A Markov chain [71], [93], [94], is a stochastic sequence of states in which the probability of the next state depends only on the present state. This is expressed as:

$$\begin{aligned} P\{X_{n+1} = \phi | X_n = \theta, X_{n-1} = \theta_{n-1}, \ldots, X_1 = \theta_1, X_0 = \theta_0\} &= P\{X_{n+1} = \phi | X_n = \theta\} \\ &= P_{\theta\phi}. \end{aligned} \tag{5.1}$$

Since the process must make a transition from the state θ into some state ϕ, the sum over all transition probabilities is unity:

$$\sum_{\phi}^{\infty} P_{\theta\phi} = 1. \tag{5.2}$$

5.1.2 Metropolis-Hastings algorithm

The Metropolis-Hastings algorithm MCMC is a method to obtain a random sequence that follows a known probability distribution. It is particularly useful when sampling from multi-dimensional distributions, especially when the dimension is high and techniques such as rejection sampling become unfeasible.

To create a Markov chain, one must define a transition kernel from state θ to ϕ, $p(\theta, \phi)$ with the property that the equilibrium distribution of states will follow the probability density function of interest, π.

The Hastings algorithm requires a time-reversible chain with a kernel p that satisfies

$$\pi(\theta)p(\theta, \phi) = \pi(\phi)p(\phi, \theta). \tag{5.3}$$

The kernel $p(\theta, \phi)$ can be written as the product of two elements, a transition density $q(\theta, \phi)$ and a probability $\alpha(\theta, \phi)$,

$$p(\theta, \phi) = q(\theta, \phi)\alpha(\theta, \phi). \tag{5.4}$$

The density $q(\theta, \phi)$ is a p.d.f. from which independent random values ϕ can be generated and also contains θ.

The acceptance probability is defined such that when combined with the arbitrary transition kernel, it gives a reversible chain. The expression for the acceptance probability is

$$\alpha(\theta, \phi) = min\left(1, \frac{\pi(\phi)q(\phi, \theta)}{\pi(\theta)q(\theta, \phi)}\right). \tag{5.5}$$

For the Metropolis-Hastings algorithm, q defines a symmetric transition $q(\phi, \theta) = q(\theta, \phi)$ and the acceptance probability becomes:

$$\alpha(\theta, \phi) = min\left(1, \frac{\pi(\phi)}{\pi(\theta)}\right). \tag{5.6}$$

In practice, the sampling of a distribution π is done in the following manner:

1. An initial state θ_t is set.

2. A new state θ_{t+1} is proposed given by the transition density $q(\theta_t, \theta_{t+1})$

3. The acceptance probability $\alpha(\theta_t, \theta_{t+1})$ is evaluated by Eq. 5.6. If $\alpha \geqslant 1$, the proposed state is automatically accepted; if $\alpha < 1$, the proposed state is accepted with probability α. If the proposed state is not accepted the chain remains in the state θ_t.

4. The chain is continued by returning to step 2.

For the application of parameter estimation, the states are points in parameter space, and given by the posterior probability distribution, $P(\theta)$, Eq. 5.6 becomes

$$\alpha(\theta_t, \theta_{t+1}) = min\left(1, \frac{P(\theta_{t+1})}{P(\theta_t)}\right). \tag{5.7}$$

It is more favourable for the Markov chain to accept points towards the maximum of the probability distribution, so the Metropolis-Hastings MCMC acts as a directed random walk. It is notable that the transition p.d.f. $q(\theta, \phi)$ chosen will determine how many steps it takes to arrive at a suitable approximation of the equilibrium distribution, $P(\theta)$.

The end result of the MCMC is a set of points which are distributed according to the desired probability distribution. With a large number of points, representative quantities of the distribution can be inferred, as described in Section 5.5.

The full posterior probability function designated as the equilibrium function for this analysis is described in Section 5.4.

5.1.3 Step Size and Burn In

The rate of acceptance is important to the success of the method. Driving the chain with small displacements in the transition kernel will result in a high acceptance rate; however, very small moves will take many iterations to traverse the full parameter space. By contrast, large displacements will cause the chain to fail in the tail of the posterior distribution because of low acceptance probabilities. Additionally, for a very low acceptance rate, the chain can stay in the same state for a long time, which can result in a need for long chains to ensure the distributed sample of the equilibrium distribution.

Since the initial state of the MCMC begins at an arbitrary state, a finite number of steps is required for the chain to converge to where it is correctly sampling from the distribution. In practice, a number of initial steps or "burn-in" period is discarded and not used in the chain.

5.2 ND280 Sample

The analysis uses a sample of ND280 events consistent with ν_μ charged-current events originating in FGD 1. This sample is subdivided into "QE-like" and "non-QE-like" samples, based upon the track multiplicity and on the presence or absence of Michel electrons in the FGD.

The QE-like and non-QE-like samples are binned by both muon momentum and angle, and so provide constraints on both the shape of the neutrino energy spectrum as well as the normalization. The subdivision of the events into QE-like and non-QE-like samples also provides a basic cross section constraint on the QE/non-QE ratio as a function of muon momentum and angle. These measurements thereby simultaneously constrain both the neutrino flux and the cross sections, when combined with beam model flux predictions and uncertainties.

The binning for the samples is as follows:

- Momentum: 0–400 MeV/c, 400–500 MeV/c, 500–700 MeV/c, 700–900 MeV/c, 900–10,000 MeV/c
- Angle: $-1 < \cos\theta < 0.84$, $0.84 < \cos\theta < 0.9$, $0.9 < \cos\theta < 0.94$, $0.94 < \cos\theta < 1$

This binning was optimized for this data set by a previous T2K analysis, known as the BANFF analysis [95]. The BANFF analysis uses only the ND280 sample to provide a constraint on the flux and cross section models, the results are used in the prediction of the SK samples for other oscillation analysis. The ND280 portion of the posterior probability used in the simultaneous analysis is almost identical to the BANFF likelihood as is discussed in Section 5.7.

In the BANFF analysis each bin was required to have an expectation of least 20 events, have a similar number of expected events as the other bins in the sample, and to have a width in momentum larger than the resolution at that momentum.

5.2.1 ND280 Selection

A sample of events consistent with ν_μ charged current interactions in FGD 1 are selected by demanding the following:

- Data quality flag: Full spill has a good global ND280 data quality flag to ensure the ND280 detectors are in a stable state.
- Bunching: Tracks are grouped together in bunches according to their times corresponding to the 8 bunches (6 bunches for Run 1) per beam spill.
- Negative track in FGD 1's fiducial volume: There is at least one negative track with FGD and TPC components that starts inside FGD 1's fiducial volume. The vertex is defined as the upstream end of the track, unless the track is identified as backwards-going by the time difference between the two FGDs.
- TPC track quality: Track has more than 18 vertical clusters in the TPC, which rejects short tracks for which the reconstruction is less reliable.
- Backwards-going tracks and TPC 1 veto: If the highest-momentum negative track starting in the FGD 1 fiducial volume is backward-going (end position upstream of start position) the event is rejected. The event is also rejected if a track is found in TPC 1.

- TPC particle identification (PID): Given the estimated momentum of the muon candidate, the energy loss function is calculated for the different particle hypotheses rejecting electrons at energies below 500 MeV and protons and pions for all energies.

Two additional criteria divide the events into CCQE-like and CCnonQE-like. The CCQE-like events are characterized by

- There should only be one matched TPC-FGD track. For true CCQE events, the recoiling nucleon usually stops in the FGD and doesn't reach the TPC. The fact that a second track reached the TPC makes it more likely that it was a pion.

- There should be no electrons originating from muon decay (Michel electrons) in FGD 1. Michel electrons are identified by looking for a time-delayed FGD 1 hit cluster. This aids in rejecting pions that do not leave the FGD. Pions stopping in the FGD decay into muons that then decay into electrons.

Any event that fails one of these two criteria is classified as CCnonQE-like. The CCnonQE events are particularly important for constraining the high energy part of the neutrino flux, since relatively few CCQE interactions result from higher energy neutrinos.

5.2.2 ND280 tracker ν_μ MC samples

The predicted number of events in each p_μ, θ_μ bin at ND280 is evaluated with a Monte Carlo simulation of the ND280 detector response with flux and cross section inputs as described in Section 2.4.3. The Monte Carlo sample is predominantly composed of events generated from the predicted neutrino flux incident on the region enclosed by the ND280 magnet. There is also a small contribution from the simulation of interactions in the material upstream of ND280. The magnet simulation is carried out separately for different T2K data taking periods, Run 1, Run 2, Run 3b and Run 3c. Run 1 and 2 periods used MC files with the PØD water bags filled, while the Run 3b and Run 3c periods used MC files with the PØD water bags empty. Inefficiency due to multiple neutrino interactions occurring in the same bunch, known as pile-up are calculated for each run period. Table 5.1 summarizes for each run the number of protons on target for simulation and data, plus the corresponding pile-up weights.

The error on the protons on target (POT) is included in the flux parameter errors. Fig. 5.1 [95] shows the MC CCQE-like and CCnonQE-like samples as a function of true neutrino energy, along with the relevant interaction modes.

	Run1	Run2	Run3b	Run 3c	Upstream Interactions
POT (Data)	2.939E+19	7.858E+19	2.136E+19	1.3424+20	2.6357E+20
POT (MC)	5.45E+20	1.104E+21	1.66E+20	9.30E+20	2.0E+20
MC POT weight	0.05393	0.07110	0.12870	0.14435	1.3178
Pile-up weight	0.99558	0.99212	0.99153	0.99065	1.0

Table 5.1: The number of protons on target for each run period and MC simulation set for the ND280 ν_μ sample. The MC POT weight is the ratio of POT (Data) to POT (MC) and is used to normalize the Monte Carlo to the data. The pile-up weight accounts for inefficiency arising from multiple neutrino interactions happening in the same bunch.

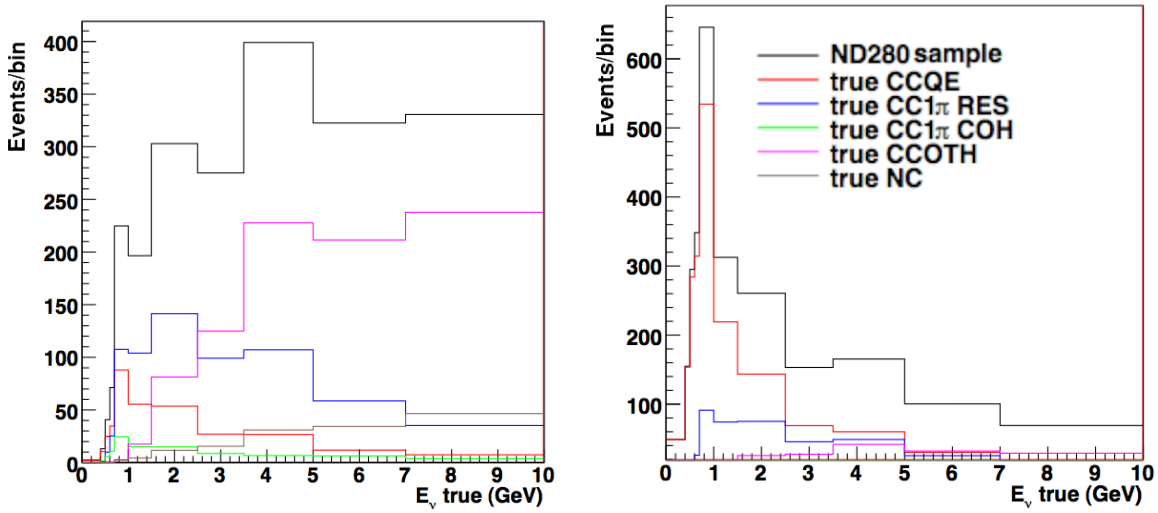

Figure 5.1: Left: ND280 CCnonQE enhanced (non-QE-like) sample vs. true neutrino energy, broken down by interaction mode. Right: CCQE enhanced (QE-like) sample. Events with neutrino energy > 10 GeV have been placed in the 7–10 GeV bin, but are not a large fraction of that bin [95].

5.3 SK sample

The selection criteria used for the ν_μ disappearance sample in the SK detector is as follows:

1. Require that the event passes SK DAQ T2K timing cuts, so that event is associated with a T2K beam spill.

2. Require the event be fully contained. This selects neutrino interactions inside the inner detector (ID) of SK. Also, particles are required to stop within the ID.

3. Reconstructed vertex and particle stopping points are inside the nominal fiducial volume, which is defined as 2 m inside the ID boundary (22.5 kton).

4. The number of reconstructed Cherenkov rings is 1 (single ring).

5. Particle ID of the reconstructed Cherenkov ring is μ-like.

6. Number of decay electrons is less than or equal to one.

7. Reconstructed momentum of the muon is above 200 MeV/c. This is to ensure performance of the PID and remove contamination of the decay electrons from muons below Cherenkov threshold.

All events are binned in terms of reconstructed momentum (E_{reco}). In total 73 E_{reco} bins are used, the bin boundaries are as follows:

- 50 MeV bins: 0.00–3.00 GeV
- 250 MeV bins: 3.00–4.00 GeV
- 500 MeV bins: 4.00–6.00 GeV
- 1 GeV bins: 6.00–10.00 GeV
- High Energy bin: 10.00–30.00 GeV

.

The binning was optimized so that finer binning is used near the expected oscillation peak.

5.3.1 SK MC simulation, flux prediction used in the analysis

The beam flux prediction is scaled by the number of POT over Run1+2+3, which corresponds to 3.010×10^{20}. The SK MC is binned in terms of true neutrino energy to apply the oscillation probabilities. In total, 84 true neutrino energy bins were used and they are as follows:

- 50 MeV bins: 0.00–0.30 GeV
- 25 MeV bins: 0.30–1.00 GeV
- 50 MeV bins: 0.30–1.00 GeV
- 100 MeV bins: 3.00–4.00 GeV
- High energy bins: 4.00–5.00,5.00–7.00,7.00–10.00,10.00–30.00 GeV

Table 5.2 shows the expected number of events for each event category for SK MC simulation with and without oscillation, and Fig 5.2 shows the reconstructed energy spectrum with and without oscillation for each event category. The rate of events with neutrino oscillations is calculated using the Prob3++ software, which includes matter effects [96].

The oscillation parameters used to generate Table 5.2 and Fig. 5.2 are summarized in Table 5.3 [97]. Fig. 5.3 shows a comparison of the reconstructed energy spectrum with and without oscillation and the ratio of the two spectra.

	# of pre-calculated events	
Event category	without oscillation	with oscillation
Total	210.46	59.39
CC ν_μ signal	200.55	52.17
CC $\bar{\nu}_\mu$ background	6.37	3.56
CC ν_e background	0.03	0.03
CC $\bar{\nu}_e$ background	0.00	0.00
Appearance ν_e background	0.00	0.12
NC background	3.51	3.51

Table 5.2: Predicted number of events for different event categories in the SK MC simulation in the case of Run 1+2+3 POT $= 3.01 \times 10^{20}$ and the oscillation parameters shown in Table 5.3.

Parameter	Value
Δm^2_{32}	$2.4 \times 10^{-3}\text{eV}^2$
Δm^2_{21}	$7.6 \times 10^{-5}\text{eV}^2$
$\sin^2(2\theta_{23})$	1.0
$\sin^2(2\theta_{12})$	0.8704
$\sin^2(2\theta_{13})$	0.1
δ_{CP}	0^o
Earth matter density	2.6 g/cm^3
Mass hierarchy	normal
Base-line length	295 km

Table 5.3: Neutrino oscillation parameters and earth matter density used for the calculation of the expected number of events at SK.

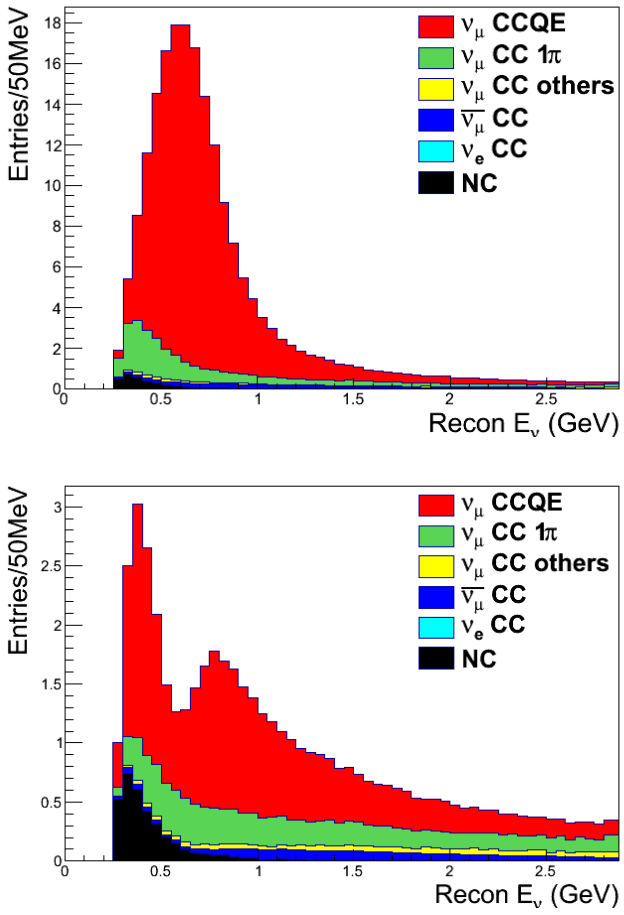

Figure 5.2: Distribution of the number of events as a function of reconstructed energy. Upper plot: Spectrum in the case of no oscillation. Lower plot: Spectrum in the oscillation case using parameters in Table 5.3. Red is ν_μ CCQE, green is ν_μ CC1π, yellow is ν_μ CC others, blue is $\bar{\nu}_\mu$ CC all , purple is ν_e CC all, and black is NC interactions of all neutrino flavours.

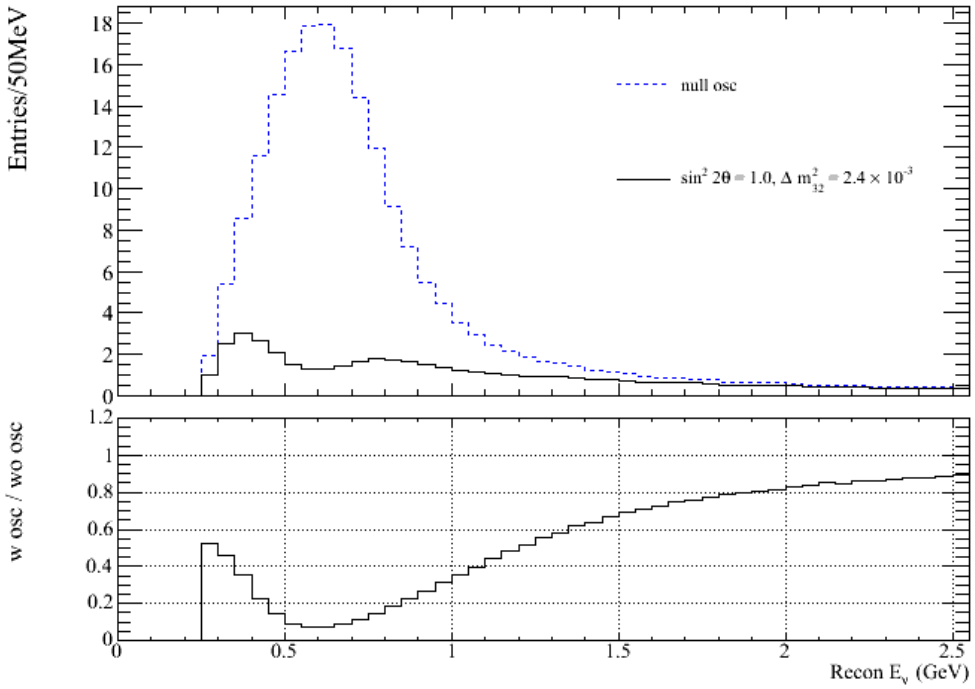

Figure 5.3: Upper plot: Reconstructed neutrino energy spectrum for no oscillation (blue dotted line) and with oscillation using parameters in Table 5.3 (black). Lower plot: Ratio of the energy spectra with oscillation to without oscillation.

5.4 Combined ND280 and SK Likelihood Function

The distribution that is sampled with the MCMC in the disappearance analysis is the the posterior probability density, given by the product of the likelihood function and the prior probability density. The likelihood, $L(\sin^2(2\theta_{23}), \Delta m^2_{32}, \vec{f})$ is dependent on the oscillation parameters and nuisance parameters $\vec{f}$. To deal with oscillation parameter estimation in the presence of unknown nuisance parameters, a Bayesian framework is adopted.

For this ν_μ disappearance oscillation analysis, only the oscillation parameters $\vec{o} = (\sin^2(2\theta_{23}), \Delta m^2_{32})$ are of interest as a final result. The nuisance parameters, $\vec{f}$, can be broken up in terms of other oscillation parameters $(\vec{o'})$, flux $(\vec{b})$, cross section $(\vec{x})$, and detector $(\vec{d})$ parameters. The likelihood written in terms of the oscillation parameters, the nuisance parameters , and the binned ND280 data, $\vec{M}^{ND280}$, and SK data, $\vec{M}^{SK}$, samples can be expressed as:

$$L(\vec{o},\vec{f}|\vec{M}^{ND280},\vec{M}^{SK}) = L(\vec{f}|\vec{M}^{ND280})L(\vec{o},\vec{f}|\vec{M}^{SK}) = \prod_i p(M_i^{ND280}(p,\theta)|\vec{f}) \prod_j p(M_j^{SK}(E_{rec})|\vec{o},\vec{f}) \tag{5.8}$$

where $p(M_i^{ND280}(p,\theta)|\vec{f})$ and $p(M_j^{SK}(E_{rec})|\vec{o},\vec{f})$ are the probability mass functions of the data given the parameters. The indices i and j refer to the bins in ND280 and SK respectively.

The posterior probability for the oscillation and nuisance parameters is given by:

$$P(\vec{o},\vec{f}|\vec{M}^{ND280},\vec{M}^{SK}) = \frac{L(\vec{o},\vec{f}|\vec{M}^{ND280},\vec{M}^{SK})\pi(\vec{f})\pi(\vec{o})}{\int L(\vec{\tilde{o}},\vec{\tilde{f}}|\vec{M}^{ND280},\vec{M}^{SK})\pi(\vec{\tilde{f}})\pi(\vec{\tilde{o}})d\tilde{f}d\tilde{o}}, \tag{5.9}$$

where $\pi(\vec{o}),\pi(\vec{f})$ are the prior probability density functions for the parameters. The denominator is a normalizing factor that does not need to be evaluated directly.

Broken up into the separate nuisance parameter contributions, $\pi(\vec{o'})$, $\pi(\vec{b}),\pi(\vec{x})$ and $\pi(\vec{d})$ are assumed to be multivariate Gaussian distributions that describe the prior uncertainty. For example,

$$\pi(\vec{b}) = (2\pi)^{-k/2}|V_b|^{-1/2}e^{-\frac{1}{2}\Delta b V_b^{-1}\Delta b^T}, \tag{5.10}$$

where V_b is the covariance that describes uncertainties and correlations for the $\vec{b}$ parameters, Δb is the deviation from nominal for the $\vec{b}$ parameters and k is the dimension of $\vec{b}$.

Taking the natural log of Eq. 5.9, expressing it in terms of the nuisance parameters $\vec{o'},\vec{b},\vec{x},\vec{d}$ and dropping the denominator which does not depend on the parameters, gives

$$\begin{aligned}\ln[P(\vec{o},\vec{o'},\vec{b},\vec{x},\vec{d}|\vec{M}^{ND280},\vec{M}^{SK})] = &\ln[L(\vec{b},\vec{x},\vec{d}|\vec{M}^{ND280})] + \ln[L(\vec{o},\vec{o'},\vec{b},\vec{x},\vec{d}|\vec{M}^{SK})] \\ &- \frac{1}{2}\Delta b V_b^{-1}\Delta b^T - \frac{1}{2}\Delta x V_x^{-1}\Delta x^T \\ &- \frac{1}{2}\Delta d V_d^{-1}\Delta d^T - \frac{1}{2}\Delta o' V_{o'}^{-1}\Delta o'^T.\end{aligned} \tag{5.11}$$

The individual likelihoods for ND280 and SK are evaluated from the observed and expected number of events in each bin, N_i^d and N_i^p respectively. The detector parameters for ND280 and SK can be separated and the negative log-probability density is written as

$$\begin{aligned} -\ln(P) = & \sum_{i}^{ND280bins} N_i^p(\vec{b^{nd}}, \vec{x}, \vec{d^{nd}}) - N_i^d \ln[N_i^p(\vec{b^{nd}}, \vec{x}, \vec{d^{nd}})] \\ & + \sum_{j}^{SKbins} N_j^p(\vec{b^{sk}}, \vec{x}, \vec{d^{sk}}, \vec{o}, \vec{o'}) - N_j^d \ln[N_j^p(\vec{b^{sk}}, \vec{x}, \vec{d^{sk}}, \vec{o}, \vec{o'})] \\ & + \frac{1}{2}\Delta b(V_b^{-1})\Delta b + \frac{1}{2}\Delta x(V_x^{-1})\Delta x + \frac{1}{2}\Delta d^{nd}(V_{d^{nd}}^{-1})\Delta d^{nd} \\ & + \frac{1}{2}\Delta d^{sk}(V_{d^{sk}}^{-1})\Delta d^{sk} + \frac{1}{2}\Delta o'(V_{o'}^{-1})\Delta o'. \end{aligned} \tag{5.12}$$

The first two summations are the result of taking the natural log of the probability of observing N_i^d events from Poisson distributions with a of mean N_i^p in each bin, where Sterling's approximation is made. Terms that do not depend on the parameters are not included in the equation. The Δb, Δx, Δd, and $\Delta o'$ are the deviations of the flux, cross section, detector, and nuisance oscillation parameters from their nominal values. The nuisance parameters are treated with Gaussian priors, except for the spectral function systematic for both ND280 and SK. These are given a uniform prior. The spectral function is described in Section 5.6.4.

The oscillation nuisance term includes the errors on $\sin^2(2\theta_{12}), \sin^2(2\theta_{13})$ and Δm^2_{21}. The errors $V_{o'}$ were acquired from the Particle Data Group summary of leptons [71] outlined in Section 5.6.6. It is assumed that correlations are negligible so that $V_{o'}$ is diagonal.

The parameters $\vec{b^{nd}}, \vec{b^{sk}}$ allow the predicted spectra of neutrinos passing through ND280 and SK to be adjusted. The covariance between the ND280 and SK flux parameters are determined through studies that incorporate uncertainties related to hadron production and beamline components.

The detector parameters $\vec{d}$ are split up into ND280 and SK detector parameters. At ND280, $\vec{d^{nd}}$ are multiplicative factors for each p_μ, θ_μ bin to account for uncertainties in the detector response bins and $\vec{d^{sk}}$ parameterize the reconstruction efficiencies and other detector errors at SK.

The predicted number of events N_i^p at ND280 in a given p_μ, θ_μ bin depends only

on the nuisance parameters and can be expressed as

$$N_{pred}^{ND280}(p,\theta,d,b,\vec{x}) = \vec{d}^{nd}(p,\theta) \sum_{i}^{E_\nu bins} \sum_{j}^{Int.modes} \vec{b}^{nd}(E_i^{nd}) \times X^{norm}(E_i^{nd}, I_j) \times w(\vec{x}, E_i^{nd}, I_j, p, \theta) \times T_{ND}(E_i^{nd}, I_j, p, \theta). \quad (5.13)$$

At SK the data sample is binned in reconstructed energy and the predicted number of events can be expressed as the following:

$$N_{pred}^{SK}(E_{rec},o,d,b,x) = d_{E-scale}^{sk}(E_{true},E_{rec}) \sum_{k}^{\nu type} \sum_{i}^{E'_\nu bins} \vec{b}^{sk}(E_i^{sk},\nu_k) \times \sum_{j}^{Int.modes'} P_{osc}(E_i^{sk},\nu_k,I_j,\theta_{23},\Delta m^2_{32},\vec{o'}) \times X^{norm}(E_i^{sk},\nu_k,I_j) \times w(\vec{x},E_i^{sk},\nu_k,I_j,E_{rec}) \times \vec{d}^{sk}(\vec{x},I_j,E_{rec}) \times T_{SK}(E_i^{sk},\nu_k,I_j,E_{rec}), \quad (5.14)$$

where

E_i^{nd},E_i^{sk} : True neutrino energy bins. At ND280 there are 11 bins in true ν_μ energy as described in Section 5.6.3. At SK there are 84 true energy bins for all neutrino types. The 84 bins are used to calculate the oscillation probability, outlined in Section 5.3.1. These bins are grouped together for the modelling of the flux (Section 5.6.3) and cross section reweighting (Section 5.6.5).

E_{rec} : Reconstructed neutrino energy. At SK there are 73 bins given in Section 5.3.

I_j : Neutrino interaction mode groups.

For ND280 there are 7 modes:

- Charged current quasi-elastic (CCQE)
- Charged current resonant (CC1π)
- Charged current coherent (CC coherent)
- Charged current multi pion (CCNπ)

- Charged current deep inelastic scattering (CCDIS)
- Neutral current neutral pion (NC1π^0)
- Neutral current other (NC others)

For SK there are 6 modes :

- Charged current quasi-elastic (CCQE)
- Charged current 1 pion (CC1π)
- Charged current coherent (CC coherent)
- Charged current other (CC others)
- Neutral current pion (NC1π)
- Neutral current other (NC others)

ν_k: True neutrino type. Types considered are $\nu_\mu, \bar{\nu}_\mu, \nu_e$ and $\bar{\nu}_e$.

$\vec{x}$: Neutrino interaction cross section parameters, described in Section 5.6.4.

$X^{norm}(E_i^{nd}, I_j), X^{norm}(E_i^{sk}, \nu_k, I_j)$: Energy dependent multiplicative factors for each type of neutrino interaction cross section.

$w(\vec{x}, E_i^{nd}, I_j, p, \theta)$,$w(\vec{x}, E_i^{sk}, \nu_k, I_j, E_{rec})$: "response functions" describe the response of the detectors to changes in the cross section parameters. They are the fractional change to the templates, T_{ND}, T_{SK} under a change to the cross section parameters $\vec{x}$. A detailed description of response functions is outlined in Section 5.6.5.

$P_{osc}(E_i^{sk}, \nu_k, I_j, \theta_{23}, \Delta m^2_{32}, \vec{o'})$: Oscillation Probability. In practice the disappearance probability is modelled by calculating the oscillation probabilities for signal and background. For charged current interactions, oscillations are considered for

- $\nu_\mu \rightarrow \nu_\mu$ oscillation for ν_μ signal,
- $\bar{\nu}_\mu \rightarrow \bar{\nu}_\mu$ oscillation for $\bar{\nu}_\mu$ background,
- $\nu_e \rightarrow \nu_e$ oscillation for ν_e background,
- $\bar{\nu}_e \rightarrow \bar{\nu}_e$ oscillation for $\bar{\nu}_e$ background and
- $\nu_\mu \rightarrow \nu_e$ oscillation for ν_e background.

No oscillation is applied for neutral current events.

$\vec{b}^{nd}(E_i^{nd}), \vec{b}^{sk}(E_i^{sk}, \nu_k)$: Energy dependent multiplicative factors on the neutrino flux at ND280 and SK.

$\vec{d}^{nd}$: Systematic parameters for the ND detector response and final state interactions.

$\vec{d}^{sk}$: Systematic parameters for SK detector response and final state interactions.

$d^{sk}_{E-scale}(E_{true}, E_{rec})$: Systematic parameters for momentum scale uncertainty at SK.

$T_{ND}(E_i^{nd}, I_j, p, \theta)$: Gives the predicted number of events in a given bin of true E_i^{nd}, I_j, p_μ, θ_μ for ND280 for the POT indicated in Table 5.1.

$T_{SK}(E_i^{sk}, \nu_k, I_j, E_{rec})$: Gives the predicted number of events in a given bin of E_i^{sk}, I_j, E_{rec} for unoscillated neutrino type ν_k for SK for 3.010×10^{20} POT.

There is no separation of "background" events in the templates T_{ND}, so the T_{ND} include some small fraction out of fiducial volume events. In practice T_{ND}, T_{SK} are pre-calculated with MC simulation.

5.5 Marginalization, Parameter Estimation

5.5.1 Marginalization

Frequentist analyses often use a profile likelihood method to deal with nuisance parameters when estimating confidence intervals.

For the profile likelihood method, suppose the likelihood $L(\theta, \beta)$ depends on parameters of interest θ and nuisance parameters β. The nuisance parameters can be effectively removed from the problem by constructing the profile likelihood, defined by

$$L_p(\theta) = L(\theta, \beta(\hat{\hat{\theta}})), \tag{5.15}$$

where $\beta(\hat{\hat{\theta}})$ is given by the β that maximizes the likelihood for fixed θ. The profile likelihood may then be used to construct intervals for the parameters of interest based on a likelihood ratio approach. In this approach, it is assumed that the log-likelihood is well-approximated by a Gaussian and the resulting intervals for the parameters

of interest are not guaranteed to have exact coverage for all values of the nuisance parameters [71].

A different method for dealing with the systematics, the one used in this analysis, is to marginalize over the nuisance parameters. For parameters of interest θ and nuisance parameters β, the marginal likelihood or data, x, is given by

$$L_m(x|\theta) = \int L(x|\theta,\beta)\pi(\beta)d\beta. \tag{5.16}$$

In this approach, the systematic uncertainty due to a limited knowledge of the nuisance parameters is included and does not need to be approximated with a Gaussian [98]. The marginalization method is used for parameter estimation as well as the interval determination.

In practice, the MCMC produces a set of points distributed in parameter space according to the posterior probability density function, given by

$$p(\theta|x) = cL_m(x|\theta)\pi(\theta), \tag{5.17}$$

where c is a normalization constant, and $\pi(\theta)$ is the prior degree of belief. Projecting the points onto one parameter axis gives the posterior probability distribution for that parameter, marginalized over all other parameters.

5.5.2 Credible Intervals

The posterior probability may be used to determine regions that will have a given probability of containing the true value of a parameter. For the example of one parameter, a Bayesian or credible interval can be determined which contains a given fraction $1-\alpha$ of the posterior probability,

$$1-\alpha = \int_{\theta_{lo}}^{\theta_{up}} p(\theta|x)d\theta. \tag{5.18}$$

Sometimes an upper or lower limit is required so that θ_{lo} or θ_{up} is set to a physical boundary. Highest posterior density (HPD) intervals are constructed so that $p(\theta|x)$ is higher everywhere inside the interval than outside [71].

The credible interval refers directly to the probability of a parameter θ being in an interval, conditional on the data observed in an experiment. By contrast, in a confidence interval, the interpretation is considered in the case of a hypothetical

ensemble of experiments, where the constructed intervals will contain true value in the specified percentage of experiments.

5.5.3 Point Estimation for Parameters

In this analysis, point estimates for parameters are given by the maximum of the posterior probability density, marginalized onto 1- or 2- dimensions. For the nuisance parameters, the estimate of the parameter is determined by fitting the projected posterior with a Gaussian over a restricted range centred at the maximum value of the distribution. A limited range is used to account for non-Gaussian tails seen in a few of the nuisance parameters marginal likelihood.

For the final oscillation parameters of interest, the posterior probability distribution is projected onto a 2 dimensional plane in $\Delta m^2_{32} - \sin^2(2\theta_{23})$. The value of the parameters at the maximum value of the 2-D marginal likelihood gives the oscillation parameter estimation. Due to the physical limit at $\sin^2(2\theta_{23}) = 1.0$ the 2-D marginal likelihood is not fit with a Gaussian.

In some cases parameter estimates obtained by marginalizing over all other parameters may not represent the point of the parameter space with the largest posterior density.

5.6 Systematics

The systematic uncertainties in the prediction of the p_μ, θ_μ distribution at ND280 and the E_{rec} distribution at SK are implemented by varying systematic parameters such as $\vec{b^{nd}}, \vec{b^{sk}}, \vec{x}, \vec{d^{nd}}\vec{d^{sk}}, d^{sk}_{E-scale}$ as described in Section 5.4. As shown in Eqs. 5.13 and 5.14 these parameters are multiplicative factors , which are dependent on event category, true neutrino energy, neutrino interaction mode, as well as either muon momentum and angle at ND280 or reconstructed energy at SK. A summary of all of the systematics parameters is given in Table 5.4.

The specifics of the systematic errors will be described in the following sections.

5.6.1 ND280 Detector systematic error parametrization

The detector systematic errors are incorporated by having 40 parameters that scale the content of each of the p_μ, θ_μ bins as is represented by the parameter d^{nd} in Eq. 5.13.

Category	Source	Detector	# of parms.
Oscillation	$\sin^2 2\theta_{12}$, $\sin^2 2\theta_{13}$, Δm^2_{21}	—	3
Beam	ND280 ν_μ	ND280	11
	SK ν_μ	SK	11
	SK $\bar{\nu}_\mu$	SK	5
Detector	ND280 Detector Systematics	ND280	40
	SK Detector Systematics	SK	7
	SK Energy Scale	SK	1
Cross section	M_A^{QE}, M_A^{RES}. Norm for CCQE,		
	CC1π, NC1π^0	ND280&SK	8
	^{12}C p_F, E_b, SF etc	ND280	4
	^{16}O p_F, E_b, SF etc	SK	9
Total			99

Table 5.4: List of all nuisance parameters used in the analysis.

.

The prior probability for these parameters is described by a multivariate Gaussian, whose covariance is evaluated with analyses that assess uncertainties for different aspects of the detector response and event reconstruction. Fig. 5.4 shows the detector error matrix, the maximum relative error for any bin is about 10%. Section 4.5.1 shows how the systematic error was evaluated for the effect on the momentum due to magnetic field distortions. A summary of the error sources is shown in Table 5.5.

The normalization uncertainties on the CCQE, CCnonQE and inclusive selections from the detector systematics are 2.3%, 2.7% and 1.6% respectively.

5.6.2 SK Detector systematic error parametrization

The SK detector systematic parameters are included to account for both the reconstruction errors in the SK detector as well as the uncertainties from final state and secondary interactions (FSI+SI) in the detector.

SK detector errors consist of the systematic errors of the detection efficiency and the energy scale. A dominant error source in the detection efficiencies is the ring counting error which was evaluated by using atmospheric neutrino events with special event selections. The error size of the ring counting is assigned as the 68% C.L. upper limit of the difference of the number of events between the atmospheric neutrino measurement and the MC prediction. The CCQE $\nu_\mu, \bar{\nu}_\mu$ selection efficiency is evaluated in three energy bins with correlations. Also considered are the inclusive

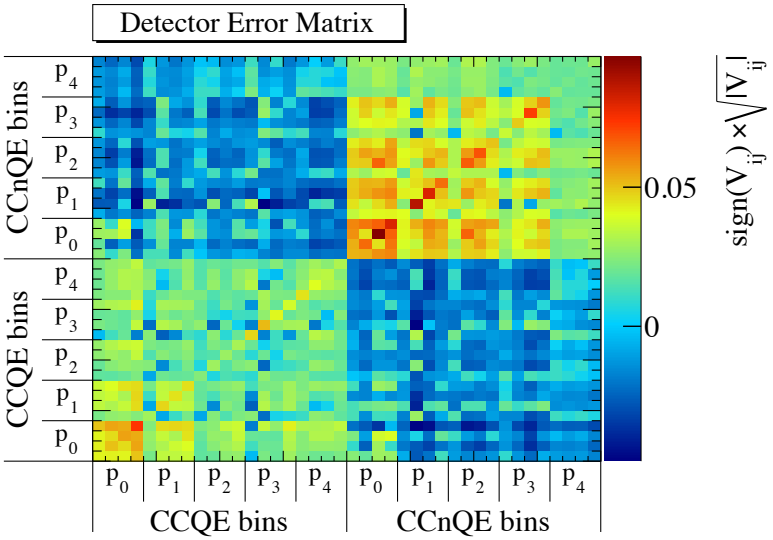

Figure 5.4: The detector error matrix for the 40 p_μ, θ_μ bins described in Section 5.2. To judge the relative importance of the covariance matrix elements, the signed square root of the terms are shown. The p_μ bins are labeled by p_i in increasing momentum [95].

Systematic error	Error Size (%)	
Pion absorption	special MC	3.0
Track Quality Cut	beam data/MC	0.1
TPC single track eff.	beam data/MC	0.5
TPC double track eff.	beam data/MC	0.6
TPC particle ID (PID)	beam data/MC	0.1
TPC momentum scale	external measurements	0.51
TPC momentum distortion	special MC	1–7
TPC momentum resolution	beam data/MC	2.0
TPC-FGD matching efficiency	sand interactions+cosmics	< 1
Fiducial Mass	external measurements	0.67
Charge mis-ID	beam data/MC	< 0.3
Michel electron	cosmics	0.49
Cosmic rays	special MC	0.1
Upstream interactions	special MC	1.5
Out of Fiducial Volume	several samples	$\sim$1–9
Pileup	beam data/MC	0.2
Track Multiplicity	beam data/MC	1.5

Table 5.5: Summary of all the ND280 detector systematic errors. Included are references to the T2K technical notes where the systematic error calculations are detailed.

CC, CCnonQE, NC, and overall efficiencies.

The error of the energy scale was assigned as 2.3%. This error is a quadratic sum of the uncertainty of the absolute scale (2.19%) and the stability (0.4%). The uncertainty of the absolute energy scale is evaluated by comparing data and MC, and the stability is checked by using cosmic-ray data.

The SK detector systematics are summarized in Table 5.6 and further detailed in T2K-TN-065 [99].

Uncertainties due to FSI were estimated by applying weights, calculated by NEUT, to SK MC events to account for modified interaction probabilities for quasi-elastic scattering, absorption, charge exchange and pion production. The systematic error due to uncertainty of the pion hadronic secondary interactions (SI) in SK is estimated by varying the interaction probabilities in the NEUT microscopic cascade model for the pion interactions. The procedure for generating the FSI+SI errors is detailed in T2K-TN-108 [100].

The FSI+SI systematics are calculated for the same interaction modes and energy bins as the reconstruction systematics and the two are added together in the analysis.

Error	Error size
$\nu_\mu, \bar{\nu}_\mu$ CCQE efficiency ($E_{rec} < 0.4$ GeV)	1.7%
$\nu_\mu, \bar{\nu}_\mu$ CCQE efficiency ($E_{rec} = 0.4 - 1.1$ GeV)	3.5%
$\nu_\mu, \bar{\nu}_\mu$ CCQE efficiency ($E_{rec} > 1.1$ GeV)	9.3%
$\nu_\mu, \bar{\nu}_\mu$ CCnonQE efficiency	20%
$\nu_e, \bar{\nu}_e$ CC efficiency	100%
NC efficiency	111%
Overall efficiency	1.7%
Energy scale error	2.3%

Table 5.6: Systematic errors for the SK detector efficiencies and energy scale error.

5.6.3 Flux parametrization

A description of the flux simulation is outlined in Section 2.2. The flux systematic uncertainty is simply described by normalization parameters in bins of neutrino energy and unoscillated flavour at a given detector. The covariance of these parameters, V_b, describes the variation of the flux due to the systematic uncertainties on the flux prediction. The description of the tuned flux and uncertainty for the oscillation analysis can be found in T2K-TN-099 [101].

Studies that incorporate uncertainties related to hadron production and beam-line components for Runs 1-3, weighted by POT, were done to create the overall covariance.

Eqs. 5.13 and 5.14 show the relation between the flux parameters and the number of predicted events at ND280 and SK respectively. For the ND280 sample, only ν_μ flux parameters are considered and for SK, parameters for ν_μ and $\bar{\nu}_\mu$ are taken into account. For ν_e and $\bar{\nu}_e$ the flux is considered flxed. For SK the 84 E_i^{sk} bins used to calculate the oscillation probabilities are grouped together to model the flux parameters.

Choice of flux binning

The binning of the flux parameters ($\vec{b}(E_i)$) is chosen with the following criteria:

1. The binning should be finer around the oscillation maximum.
2. The binning should be finer in regions contributing more to the data samples.
3. The flux error should not change too rapidly inside the bins.

4. The bins that are more highly correlated in the original flux covariance should be binned together.

The binning used was optimized during the BANFF ν_μ disappearance studies. Fig. 5.5 shows the flux uncertainties at SK provided by the T2K beam group with the BANFF analysis binning overlaid, showing that the error does not vary too rapidly in bins. Fig. 5.6 shows the flux correlations at SK, showing that bins with large correlations are combined.

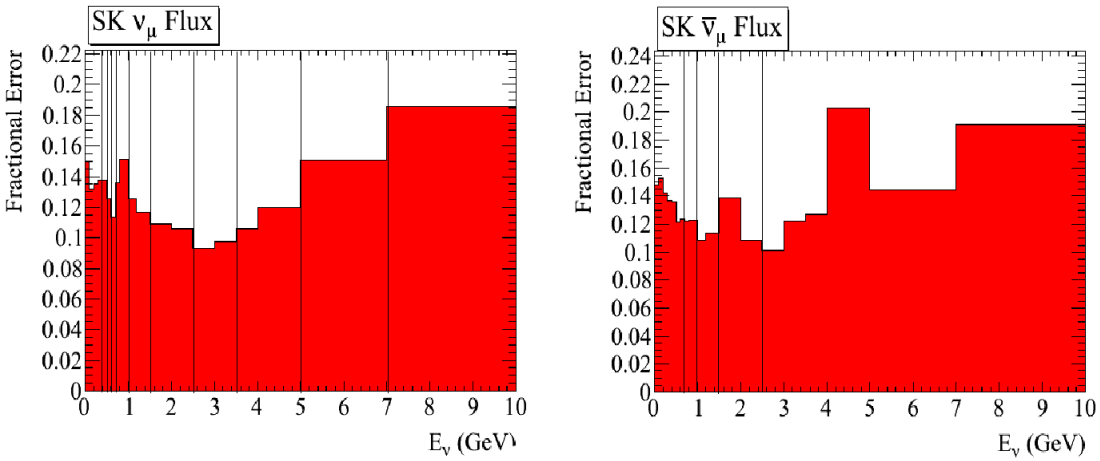

Figure 5.5: Flux errors at SK in the binning provided by the beam group. The vertical black lines mark bin edges in the BANFF binning [95].

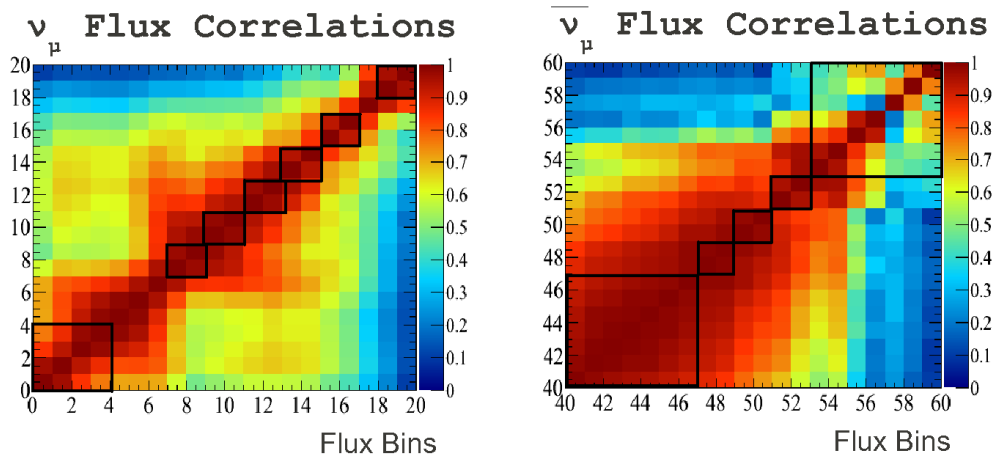

Figure 5.6: Parts of the correlation matrix for the SK flux in the binning provided by the beam group. Where black boxes are shown, the bins inside the box are combined for the BANFF binning [95].

The binning for the neutrino flavours are:

- ν_μ: 0–0.4, 0.4–0.5, 0.5–0.6, 0.6–0.7, 0.7–1.0, 1.0–1.5, 1.5–2.5, 2.5–3.5, 3.5–5.0, 5.0–7.0, 7.0–30.0 GeV
- $\bar{\nu}_\mu$: 0–0.7, 0.7–1.0, 1.0–1.5, 1.5–2.5, 2.5–30.0 GeV

The same binning is used for the ND280 ν_μ and SK ν_μ parameters. The ND280 ν_μ parameters are constrained by the analysis of the ND280 sample. The strong correlations between the ND280 and SK flux parameters allow the ND280 data to also constrain the SK flux parameters. Figure 5.7 shows the correlations between the ND280 and SK flux parameters.

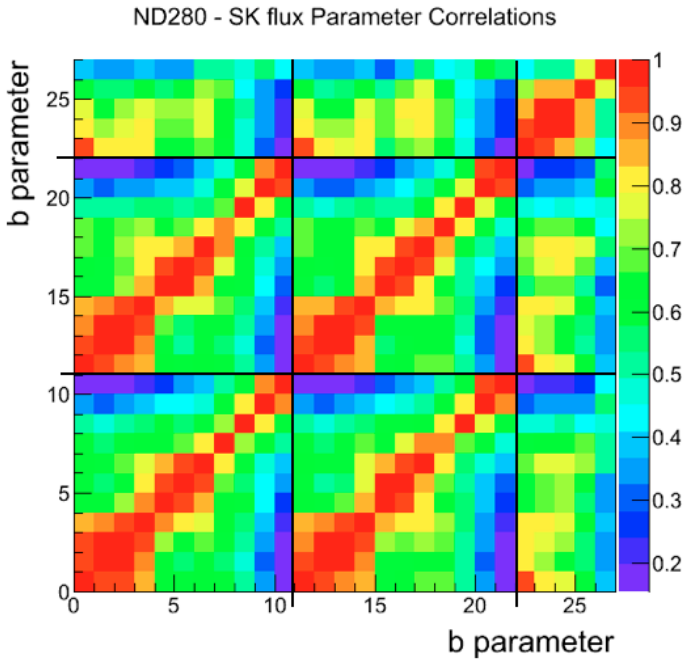

Figure 5.7: Correlations between the ND280 and SK flux parameters. Bin numbers are 0-10 ND280 ν_μ, 11-21 SK ν_μ, 22 - 26 SK $\bar{\nu}_\mu$ parameters.

5.6.4 Cross section parametrization

Neutrino interactions in the ND280 and SK detectors are simulated with the NEUT Monte Carlo generator [60]. External data, primarily from the MiniBOONE experiment [102], is used to tune some of the NEUT neutrino interaction parameters, as well as determine their prior uncertainties.

The models used in the NEUT interaction simulation are outlined in Section 2.3.1 and the cross section parameterization, developed by the T2K neutrino interactions working group, is described in T2K-TN-113 [103].

In NEUT the parameters M_A^{QE}, M_A^{RES} model the axial masses of the CCQE and resonance neutrino-production events respectively.

Energy dependent scaling factors have been introduced to provide additional freedom in energy regions of interest. These are included for CCQE, CC1π and NC1π interactions.

The Relativistic Fermi Gas (RFG) model implementation depends on two parameters, the Fermi momentum level and the nucleon binding energy, whose values are extracted from external quasi-elastic electron scattering data. The parameter p_F

takes into account changes in the Fermi momentum level while E_B models the binding energy. Both parameters depend on the detector material and differ for ND280 and SK.

This analysis considers the effect of switching between the RFG model and a better-motivated spectral function (SF) model. A single parameter is introduced to allow an arbitrary combination of the two models.

In resonant pion production processes the resonance (Δ) can interact with nucleons before it decays to produce nucleons but no pions, which will be misidentified as a CCQE like event. This is modelled by a π-less Δ decay parameter which changes the fraction of resonances that have π-less decays.

Misidentification of CC1π interactions also occurs when pions are produced but absorbed in a final state interaction. It has been observed that pion momentum distributions in resonance interactions show poor agreement with data [104] so that the "W shape" parameter is used to modify the shape of the initial pion distribution. As the W shape parameter decreases, the mean pion momentum reduces and this increases the probability of pion absorption in a final state interaction.

Uncertainty in the CC multi-pion, CC deep inelastic scattering and CC η, K and photon production is modelled by the variance of the CC other shape parameter.

At SK, uncertainties are considered for the CC coherent, NC, ν_e CC and $\bar{\nu}$ CC cross sections. The effect of these parameters on the SK μ-like sample will be small and they are considered to be energy independent.

5.6.5 Response functions

When determining the effect of adjusting cross section parameters, ideally one would like to recalculate the likelihood for each candidate event, however this approach is very computationally intensive. A reasonable approximation is to model the response of the detectors due to changes in the underlying cross section parameters. In the analysis the response functions $w(\vec{x}, E_i^{nd}, I_j, p, \theta)$ and $w(\vec{x}, E_i^{sk}, \nu_k, I_j, E_{rec})$ are used and are calculated in terms of the event selection templates T_{ND} and T_{SK} which are calculated with Monte Carlo using nominal cross section parameter values.

For example, in the case of SK, under a new set of cross section parameters, $\vec{x}_\alpha$, each event in a E_{rec}, E_i^{sk}, I_j bin for neutrino type ν_k is given a weight which is a ratio of the new cross section to the nominal one:

$$W_e(\vec{x}_\alpha, E_i^{sk}, \nu_k, I_j, E_{rec}) = \frac{\sigma(\vec{x}_\alpha, E_i^{sk}, \nu_k, I_j)}{\sigma(\vec{x}, E_i^{sk}, \nu_k, I_j)}. \tag{5.19}$$

The correction to the template is then the sum of these weights over all events e in the $E_{rec}, E_i^{sk}, \nu_k, I_j$ bin:

$$w(\vec{x}_\alpha, E_i^{sk}, \nu_k, I_j, E_{rec}) = \frac{\sum_e W_e(\vec{x}_\alpha, E_i^{sk}, \nu_k, I_j, E_{rec})}{T_{SK}(E_i^{sk}, \nu_k, I_j, E_{rec})}. \tag{5.20}$$

This is the response function, that is, the fractional change to a T_{SK} (or T_{ND}) bin for a given shift in one of the cross section parameters.

In practice, the cross section parameters, $\vec{x}$, are each varied independently, and the effect on the template is calculated for 7 points corresponding to -3σ, -2σ, -1σ, 0σ, +1σ, +2σ, +3σ (variations in terms of the standard deviation of each parameter). For an arbitrary change to a cross section parameter, the fractional change to the template is found using an interpolation through the 7 points with a spline function. Figure 5.8 [105] shows the response function of M_A^{QE} for one ν_μ CCQE energy bin at SK (E_ν is 0.6-0.7 GeV and E_{rec} is 0.65-0.7 GeV).

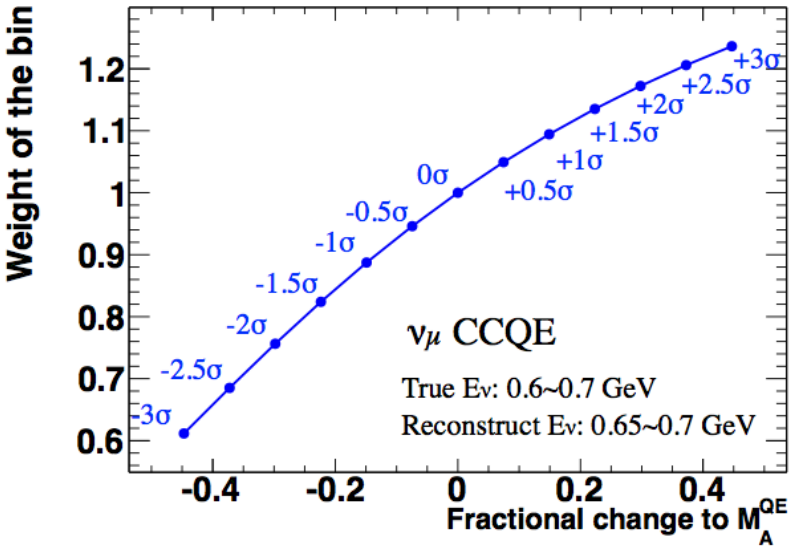

Figure 5.8: The M_A^{QE} response function for the bin true E_i^{sk} 0.6-0.7 GeV and E_{rec} 0.65-0.7 GeV for ν_μ CCQE events. The σ represents the error size of M_A^{QE} [105].

For ND280 the spline functions were provided by the BANFF group [95] whereas for SK the spline functions were generated by T2K collaborators from Kyoto and Tokyo Universities and Imperial College London [105].

At the near detector, the true neutrino binning for the response functions is the same as the true neutrino binning for the flux (see Section 5.6.3).

For SK the response function true neutrino bins for ν_μ and $\bar{\nu}_\mu$ are the same as ND280. For ν_e there are 7 bins:

- 0–0.5, 0.5–0.7, 0.7–0.8, 0.8–1.5, 1.5–2.5, 2.5–4.0, 4.0–30.0 GeV,

and for $\bar{\nu}_e$ there are 2 bins:

- 0–2.5, 2.5–30.0 GeV.

In terms of reconstructed energy, there are 41 E_{rec} bins as follows:

- Low energy bin: 0.00–0.30 GeV
- 50 MeV bins: 0.30–1.00 GeV
- 100MeV bins: 1.00–3.00 GeV
- High energy bins: 3.00–3.50, 3.50–4.00,4.00–5.00,5.00–7.00,7.00–30.00 GeV

These are optimized to be finer near the oscillation maximum. It has been observed that there were no large variations between the bin by bin response functions when using the 73 E_{rec} bins used in the SK selection. The coarser binning was used to improve computational time.

Modelling Cross Section Uncertainty

Uncertainties in the cross sections are incorporated into the likelihood function in three different terms:

A. Parameters that allow direct adjustment to the energy dependent cross section scaling factors, $X^{norm}(E_i^{nd}, I_j)$ and $X^{norm}(E_i^{sk}, \nu_k, I_j)$.

B. Parameters that are included within the response functions, $w(\vec{x}, E_i^{nd}, I_j, p, \theta)$ and $w(\vec{x}, E_i^{sk}, \nu_k, I_j, E_{rec})$.

C. Parameters that are included along with detector systematic errors. For ND280 the W shape, CC coherent normalization, NC other normalization and FSI uncertainties are included in the analysis as uncertainties on d_i^{nd}, which scale the content of each p_μ, θ_μ bin. For SK, the FSI uncertainties are included as

the uncertainties on d_i^{sk}. The covariance of d_i for each of these error sources is calculated by evaluating the effect of adjusting the parameters by $\pm 1\sigma$ and then summing them with the detector covariance. For ND280

$$V_{d^{nd}} = V_{det} + V_{FSI} + V_{Wshape} + V_{CCCOH} + V_{NCOTH}, \tag{5.21}$$

and for SK

$$V_{d^{sk}} = V_{det} + V_{FSI}. \tag{5.22}$$

ND280 and SK cross section parameters

Some cross section parameters are specific to each detector while others are common to both detectors. The categorization of the parameters is as follows:

1. Parameters specific to ND280: these include the spectral function, Fermi momentum and binding energy on carbon.

2. Parameters specific to SK: these include the spectral function, Fermi momentum and binding energy on oxygen.

3. Parameters common to ND280 and SK: these include M_A^{QE}, M_A^{RES}, and the CCQE and CC1π normalization parameters.

All the cross section parameters following categories A and B are summarized in Table 5.7, the parameters are also categorized in terms of whether they are specific or common to the ND280 and SK detectors.

5.6.6 Oscillation Parameters

Priors for the oscillation parameters under study in this analysis, $\sin^2(2\theta_{23})$ and Δm^2_{32} are taken to be uniform. Priors for the other oscillation parameters are taken to be normally distributed about the world average values. The priors are summarized in Table 5.8.

The parameter δ_{CP} is fixed at 0^o. Matter effects are included and the baseline and crust density are set as in Table 5.3. The normal mass hierarchy is used.

Parameter	E_ν Range	Nominal	Error	Class/Cat.
M_A^{QE}	all	1.21 GeV/c^2	0.45	B/3
M_A^{RES}	all	1.41 GeV/c^2	0.11	B/3
CCQE E1	$0 < E_\nu < 1.5$	1.0	0.11	A/3
CCQE E2	$1.5 < E_\nu < 3.5$	1.0	0.30	A/3
CCQE E3	$E_\nu > 3.5$	1.0	0.30	A/3
CC1π E1	$0 < E_\nu < 2.5$	1.15	0.43	A/3
CC1π E2	$E_\nu > 2.5$	1.0	0.40	A/3
p_F ^{12}C	all	217 MeV/c	30	B/1
E_B ^{12}C	all	25 MeV	9	B/1
SF ^{12}C	all	0 (off)	1 (on)	B/1
CC Oth shp ND280	all	0.0	0.40	B/1
NC1π^0	all	0.96	0.43	A/1
p_F ^{16}O	all	225 MeV/c	30	B/2
E_B ^{16}O	all	27 MeV	9	B/2
SF ^{16}O	all	0 (off)	1 (on)	B/2
CC Oth shp SK	all	0.0	0.40	B/2
W shape SK	all	0.0	0.20	B/2
π-less Δ decay SK	all	1.0	0.20	B/2
CC Coh norm	all	1.0	1.0	C/1 & A/2
NC1π norm	all	1.0	0.30	B/2
NC oth norm	all	1.0	0.30	C/1 & A/2
$\nu/\bar{\nu}$ norm	all	1.0	4.0	A/2

Table 5.7: Cross section parameters for the analysis, showing the applicable range of neutrino energy, nominal value and prior error. Shown in the table are the parameters with type A or B Class. The Class/Category of each parameter is defined in the text.

Parameter	Prior
$\sin^2(2\theta_{12})$	Normal $\mu = 0.857,\ \sigma = 0.024$
$\sin^2(2\theta_{23})$	Uniform between 0.6 -1.0
$\sin^2(2\theta_{13})$	Normal $\mu = 0.098,\ \sigma = 0.013$
$\Delta m^2_{21}(\mathrm{eV}^2)$	Normal $\mu = 7.50 \times 10^{-5},\ \sigma = 0.20 \times 10^{-5}$
$\Delta m^2_{23}(\mathrm{eV}^2)$	Uniform between $1.0 \times 10^{-3} - 4.0 \times 10^{-3}$

Table 5.8: Oscillation parameter priors.

5.7 Near Detector Data Analysis

An analysis of the ND280 tracker data alone was done as a cross check to ensure that the analysis software behaves as expected. Using the ND280 sample only, the likelihood reduces to be almost identical to that of the BANFF analysis. The results of the ND280-only analysis are compared to the BANFF result to ensure there are no large deviations between the two analyses for the SK flux parameters and cross section parameters common to ND280 and SK.

5.7.1 Biases in Parameter Estimates

The properties of the parameter estimates are investigated for 500 toy experiments; each analysis uses a chain of 1.0×10^6 post burn-in steps. These toy experiments were generated with the nominal value for all of the systematic parameters. When they were analyzed, the central value of the Gaussian prior was chosen randomly from the prior distribution. A pull [106] was defined for each parameter as

$$Pull = \frac{\hat{\mu} - \mu_{prior}}{\sqrt{\sigma^2_{prior} - \hat{\sigma^2}}} \tag{5.23}$$

where $\hat{\mu}$ is the parameter estimate, μ_{prior} is the central value used in the analysis, and σ_{prior} and $\hat{\sigma}$ are the prior uncertainty and the estimated parameter uncertainty, respectively. The pulls are expected to have a standard normal distribution.

The mean value of the parameter pulls is shown in Fig 5.9. The pull distributions for each of the parameters is shown in Appendix C. It can be seen that many of the pulls are not standard normal distributed. There are two likely sources of these small biases in the parameter pulls.

- The parameter errors come from fitting the posterior distributions with a Gaus-

sian. If the posterior distributions are slightly non Gaussian this could cause a slight error in the parameter error estimation.

- The maximum likelihood estimator may have an intrinsic bias that is proportional to $\sim 1/N_{bins}$, where N_{bins} is the number of bins used in the likelihood analysis. This is more of an issue for the low statistics case where fewer bins can be used.

We take the approach that if the bias in the pull mean is significantly less than 1, then the bias can be neglected.

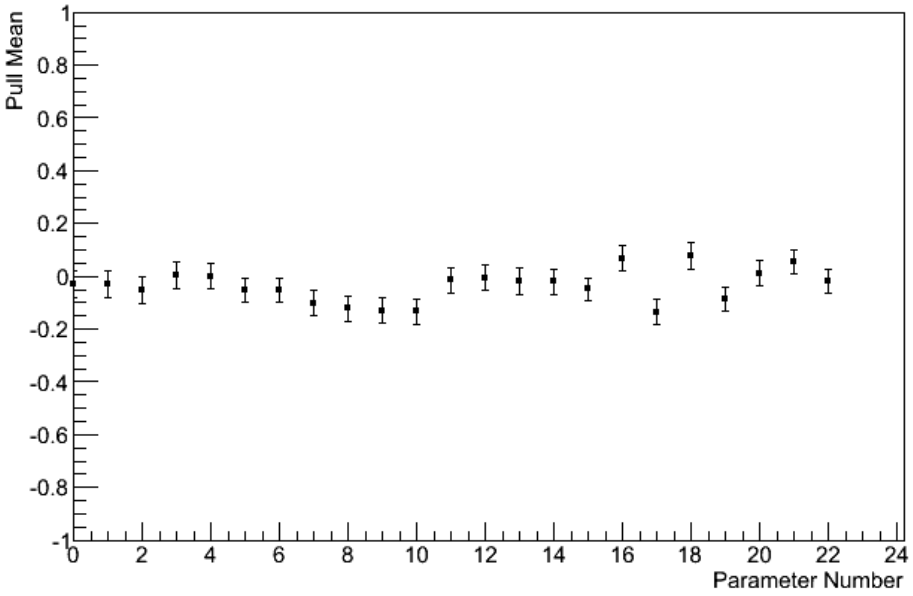

Figure 5.9: Pull means for the ND280-only analysis for the SK flux parameters and cross section parameters common between ND280 and SK. Parameter numbers are 0–15 SK flux parameters, 16 = M_A^{QE} , 17 = M_A^{RES}, 18–20 CCQE norms, 21–22 CC1π norms.

5.7.2 ND280 Only Analysis

For further validation, the parameter estimates and errors were compared to the BANFF analysis using the Run 1-3 ND280 data. A Markov chain of 20×10^6 post-burn-in steps was used. In this analysis, the step size was chosen to be 0.1 times the

prior error of each systematic parameter. This resulted in an acceptance probability of about 0.40 which is the same as the value of recommended by the Particle Data Group review concerning this topic [71]. In practice, chains of a length of 1.2×10^5 steps were used, removing the first 20,000 steps as the burn-in and combining the remaining steps. This approach was used to decrease computation time. Fig. 5.10 shows a comparison of the parameter estimates and errors between this analysis (MCMC) and the BANFF analysis. The results show compatibility between the two analyses. From Fig 5.10, it can be seen that the largest deviations are the parameter estimates and errors for the CCQE E2, E3 parameters. The MCMC analysis estimates values for CCQE E2, E3 slightly further away from the nominal values than the BANFF estimates. Also the MCMC estimated parameter uncertainties are generally slightly smaller. The numerical values for the parameters for the two analyses are listed in Table 5.9.

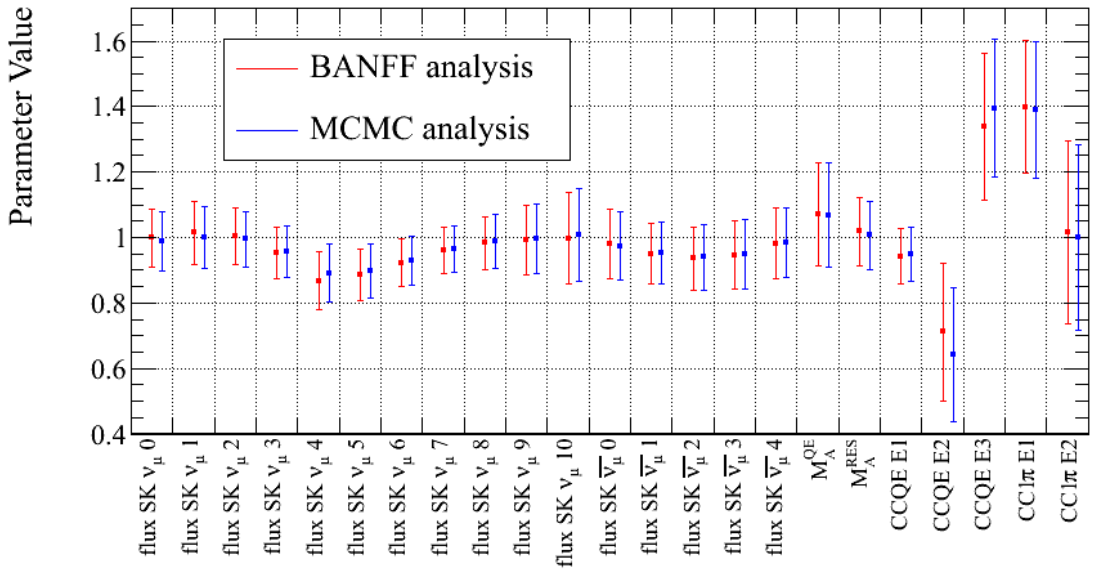

Figure 5.10: ND280-only MCMC parameter estimates compared with the results of the BANFF analysis. Shown are the SK flux parameters and cross section parameters common to ND280 and SK.

The posterior probability used in the near detector analysis is a simplified version of Eq. 5.12, where all terms dependent on SK are neglected. This posterior probability is almost identical to the likelihood used in the BANFF fit (Equation 14 in [95]). However the BANFF likelihood has an additional term which takes into account the effect of the flux and cross section parameters on the detector covariance,

parameter	MCMC	BANFF
SK $\nu_\mu b_0$	0.988 ± 0.089	0.999 ± 0.090
SK $\nu_\mu b_1$	0.999 ± 0.095	1.014 ± 0.095
SK $\nu_\mu b_2$	0.995 ± 0.086	1.005 ± 0.087
SK $\nu_\mu b_3$	0.956 ± 0.078	0.952 ± 0.079
SK $\nu_\mu b_4$	0.891 ± 0.090	0.868 ± 0.088
SK $\nu_\mu b_5$	0.899 ± 0.083	0.886 ± 0.080
SK $\nu_\mu b_6$	0.928 ± 0.076	0.923 ± 0.074
SK $\nu_\mu b_7$	0.963 ± 0.071	0.961 ± 0.069
SK $\nu_\mu b_8$	0.987 ± 0.083	0.983 ± 0.082
SK $\nu_\mu b_9$	0.996 ± 0.105	0.991 ± 0.107
SK $\nu_\mu b_{10}$	1.008 ± 0.141	0.998 ± 0.141
SK $\bar{\nu}_\mu b_0$	0.974 ± 0.105	0.981 ± 0.106
SK $\bar{\nu}_\mu b_1$	0.952 ± 0.094	0.951 ± 0.093
SK $\bar{\nu}_\mu b_2$	0.940 ± 0.100	0.936 ± 0.096
SK $\bar{\nu}_\mu b_3$	0.949 ± 0.105	0.946 ± 0.105
SK $\bar{\nu}_\mu b_4$	0.984 ± 0.106	0.982 ± 0.107
$M_A^{QE}(GeV)$	1.068 ± 0.161	1.070 ± 0.157
$M_A^{RES}(GeV)$	1.006 ± 0.104	1.018 ± 0.104
$CCQE\ E1$	0.949 ± 0.083	0.942 ± 0.084
$CCQE\ E2$	0.642 ± 0.204	0.711 ± 0.210
$CCQE\ E3$	1.395 ± 0.211	1.339 ± 0.224
$CC1\pi\ E1$	1.390 ± 0.208	1.399 ± 0.203
$CC1\pi\ E2$	1.001 ± 0.284	1.016 ± 0.281

Table 5.9: Values of parameter estimates from the ND280-only analysis. Parameters listed are the SK flux parameters and cross section parameters common to ND280 and SK.

$$\ln\left(\frac{|V_d(\vec{b},\vec{x})|}{|V_d^{nom}|}\right), \tag{5.24}$$

where V_d^{nom} is the covariance for the nominal parameters and $V_d(\vec{b},\vec{x})$ is the covariance for non-nominal values. The determinant of the covariances is taken and for the variations in the flux and cross section the ratio of these determinants is very close to 1; this leads the overall term being very small. Due to its small effect this term was ignored in the MCMC near detector analysis in order to reduce the CPU time requirements. The additional term used in the BANFF analysis is the possible source of the slight differences seen between the two analyses. However the overall differences between the two analyses are small, well within the parameter errors.

5.7.3 Power of ND280 Tracker ν_μ Sample

The ND280 analysis shows the ability of the tracker ν_μ sample to constrain the SK flux parameters and cross section parameters that are common to ND280 and SK. Using the same 500 toy experiments that were used for the calculations of the pulls, the posterior errors were found and compared to the prior errors. Figs. 5.11 and 5.12 show the prior and posterior errors for the cross section and flux parameters respectively. It can be seen that for the majority of the parameters the errors are reduced.

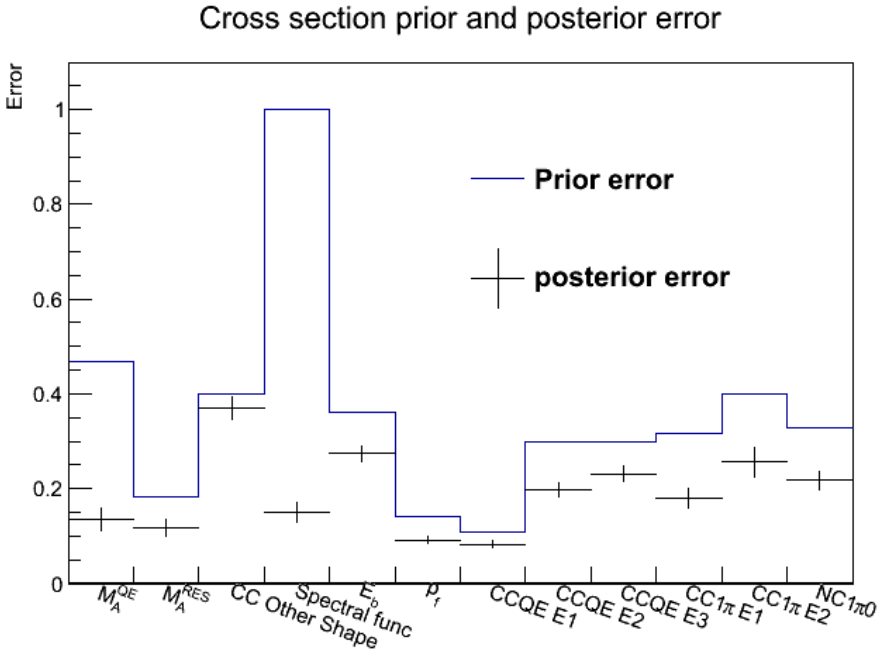

Figure 5.11: Error reduction for the cross section parameters for the ND280-only analysis.

Since there is reasonable agreement between this analysis and the BANFF analysis, and the pull studies show no significant biases, the validation checks are extended for the simultaneous analysis.

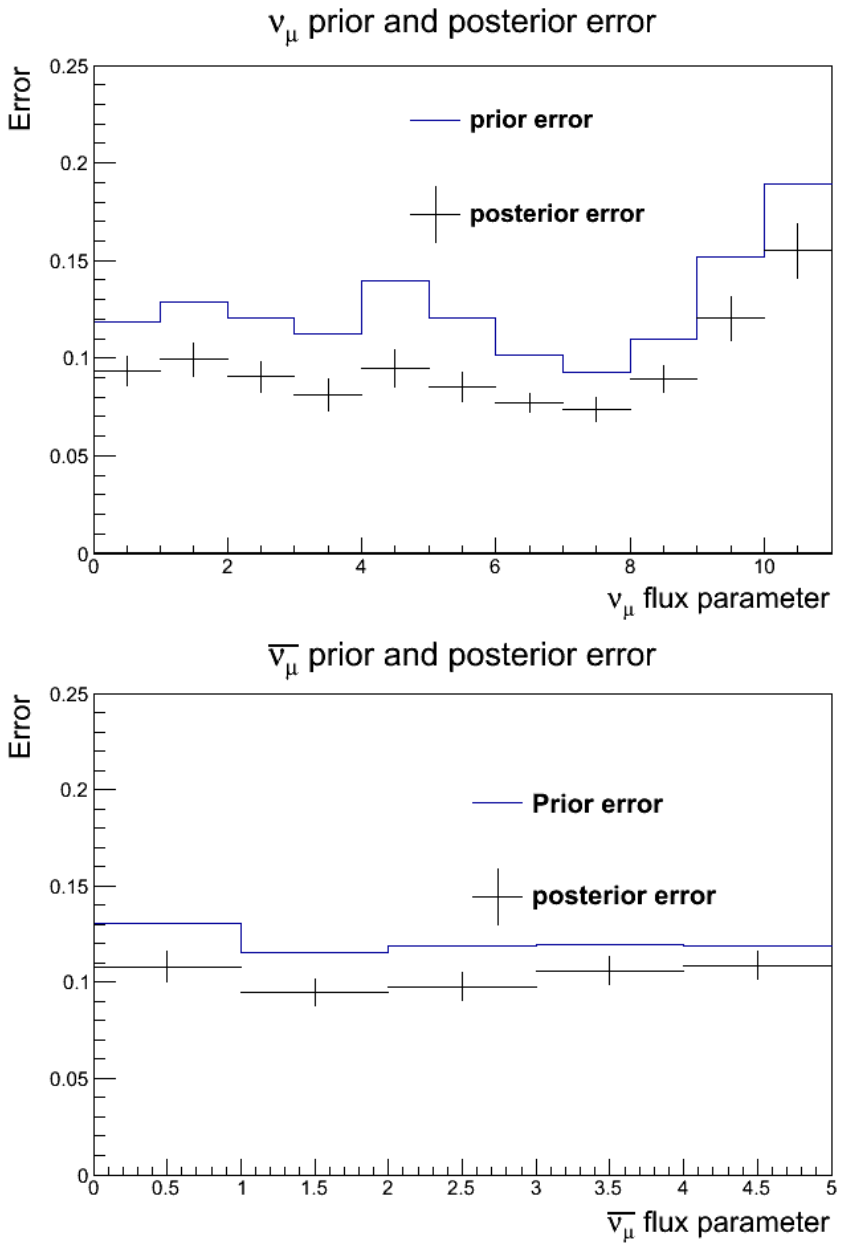

Figure 5.12: Error reduction for the SK ν_μ (top) and $\bar{\nu}_\mu$ (bottom) in the ND280-only analysis.

5.8 Simultaneous ND280 and SK Analysis

5.8.1 Parameter Estimates

As an additional validation check, pulls for the parameters are evaluated for the simultaneous ND280 and SK analysis. The cross section parameters common to ND280 and SK are considered as well as the oscillation parameters and the SK flux and detector parameters, to check for any biases.

Due to the long CPU time required to do the simultaneous analysis, only 100 toy experiments were used in the pull studies; each using a Markov chain of 0.5×10^6 post burn-in steps. Fig. 5.13 shows the pull means for the SK flux parameters and cross section parameters common to ND280 and SK.

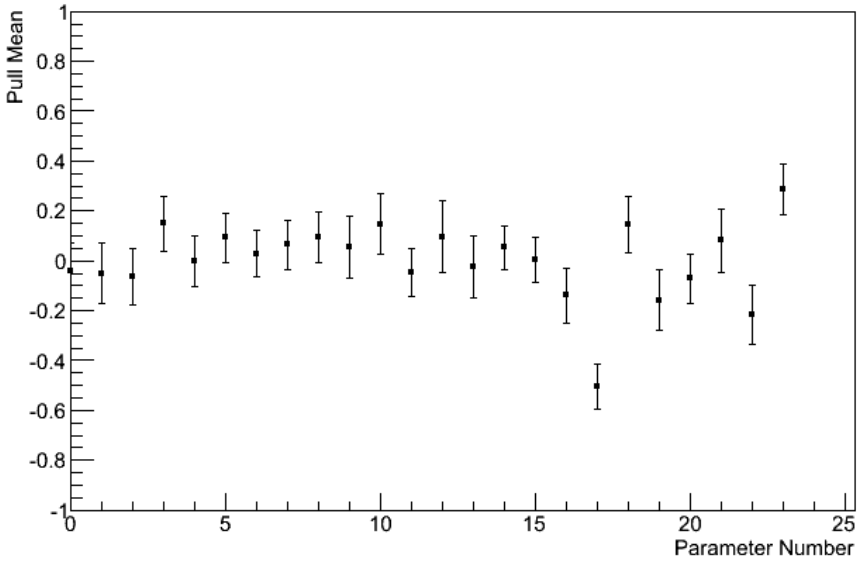

Figure 5.13: Pull means for the SK flux parameters and cross section parameters common to ND280 and SK. Parameter numbers are 0–15 SK flux parameters, 16 = M_A^{QE} , 17 = M_A^{RES}, 18–20 CCQE norms, 21–22 CC1π norms, 23 NC 1π norm.

The pull distributions for the flux parameters in the simultaneous analysis are quite similar to those from the ND280-only analysis. Some of the cross section parameters have a mean pull further away from zero than the ND280-only case. However, all of the pulls have means less than 0.5.

For the SK detector parameters and the three nuisance oscillation parameters, it

is expected that the SK data will not further reduce the uncertainties. In this case, the prior and posterior errors will be the same, as will the prior and posterior point estimates, and Eq. 5.23 will become 0/0. As a result, a different definition of the pull is required for the SK detector parameters and the oscillation parameters. A pull definition of

$$Pull = \frac{\hat{\mu} - \mu}{\hat{\sigma}}, \tag{5.25}$$

is used, where μ is the true value of the parameter and $\hat{\mu}$, $\hat{\sigma}$ are the parameter estimate and the estimated parameter uncertainty, respectively. For cases where the sample does not constrain the parameters, Eq. 5.25 should give pulls that have a standard normal distribution. Fig. 5.14 shows the pull means for the SK detector parameters and the nuisance oscillation parameters. The pull distributions for all of the parameters are shown in Appendix C.

Fig. 5.15 shows the pull distributions for $\sin^2(2\theta_{23})$ and Δm^2_{32}. A true value of $(\sin^2(2\theta_{23}) = 1.00, \Delta m^2_{32} = 2.4 \times 10^{-3}\text{eV}^2)$ was used to generate the toy experiment samples. Eq. 5.25 is used for the pull calculation since a uniform prior (in the physical range) was assumed for these parameters. For Δm^2_{32}, fitting the pull distributions with a Gaussian gives a mean which is consistent with zero. For $\sin^2(2\theta_{23})$, the pull distribution is asymmetric due to the physical limit at 1.0. Here, the majority of entries are in the bin closest to zero pull, showing no significant bias in the parameter. For the 100 toy experiments, 4 analysis jobs failed in the final processing.

5.8.2 SK Systematic Parameter Uncertainties

With the same 100 toy experiments, the posterior errors were found and compared to the prior error. Due to the low statistics of the SK sample, it will not strongly constrain the SK specific parameters, nor further constrain the parameters common to ND280 and SK. Fig. 5.16 shows the SK specific cross section parameters, it can be seen that the samples do not significantly reduce the errors. Similar behaviour for the SK detector parameters can be seen in Fig. 5.17.

Fig. 5.18 shows the errors in the cross section parameters that are common to ND280 and SK. Posterior errors are compared for the case of the ND280-only analysis and the simultaneous analysis and it is seen that the simultaneous analysis does not yield significantly smaller errors.

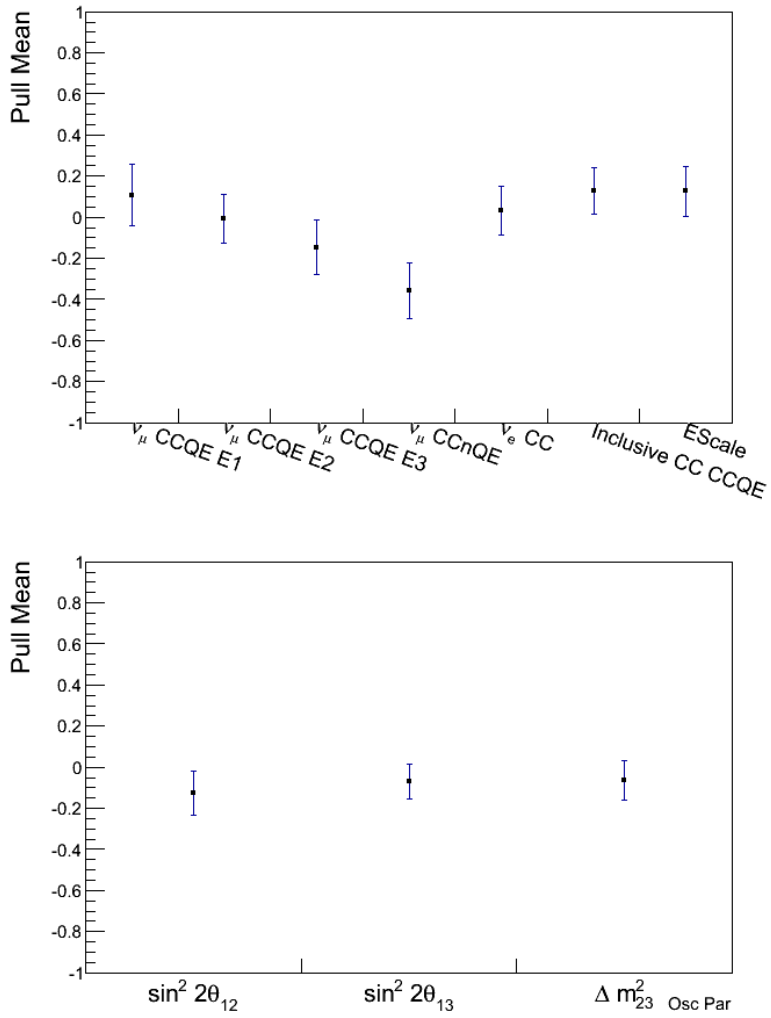

Figure 5.14: Pull means for SK detector parameters (top) and nuisance oscillation parameters (bottom).

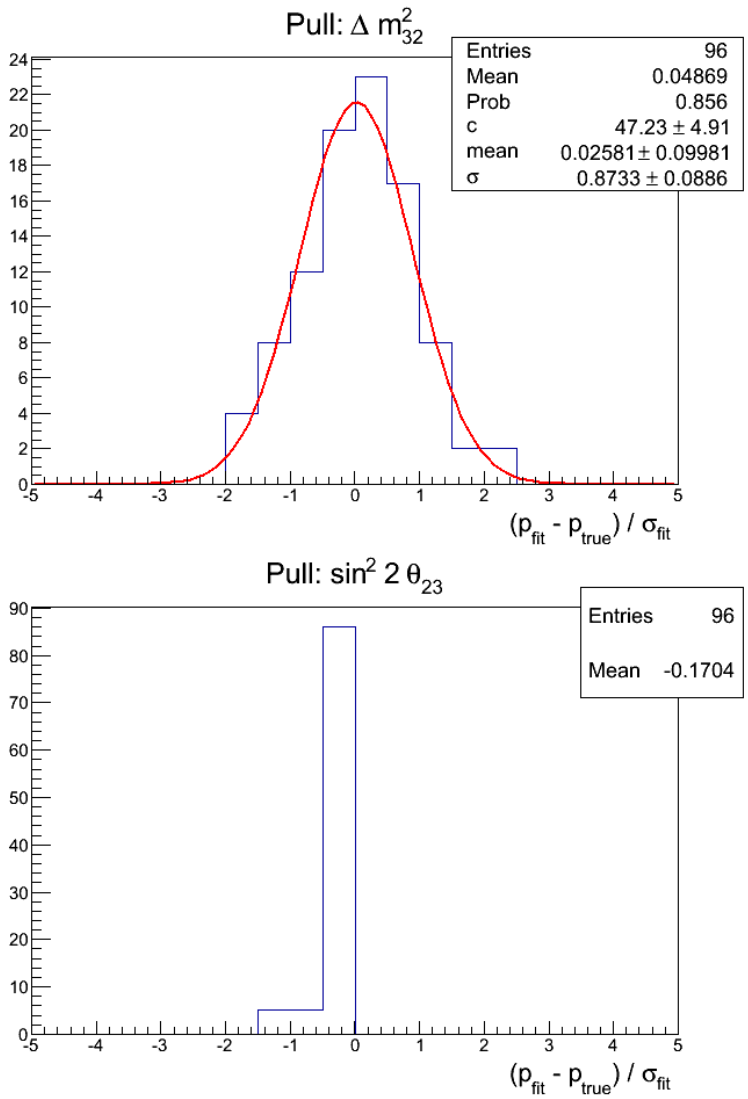

Figure 5.15: Pull distributions for oscillation parameters Δm^2_{32} (top) and $\sin^2(2\theta_{23})$ (bottom).

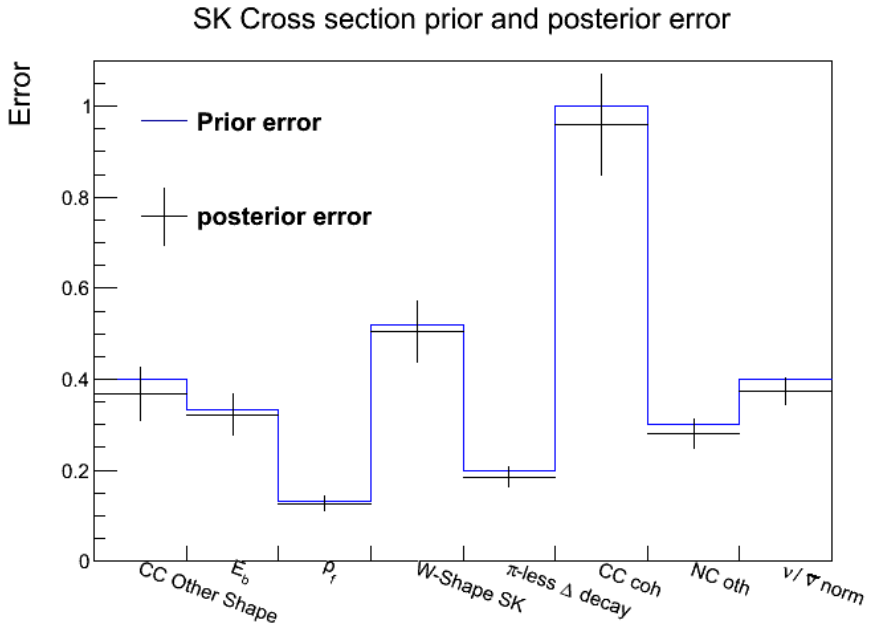

Figure 5.16: Prior and posterior error for cross section parameters specific to SK.

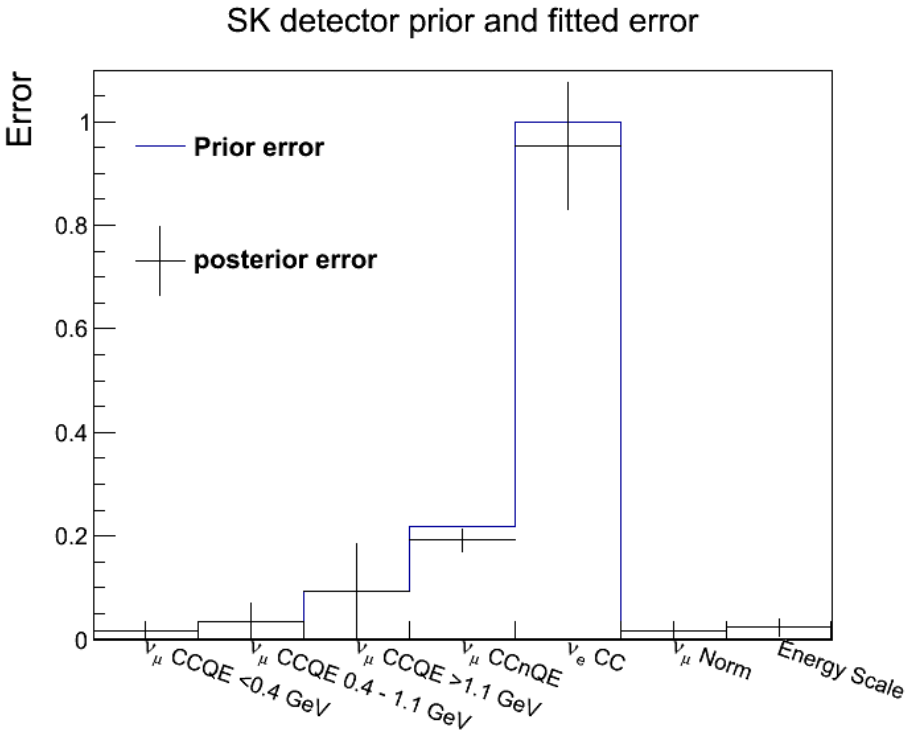

Figure 5.17: Prior and posterior error for SK detector parameters.

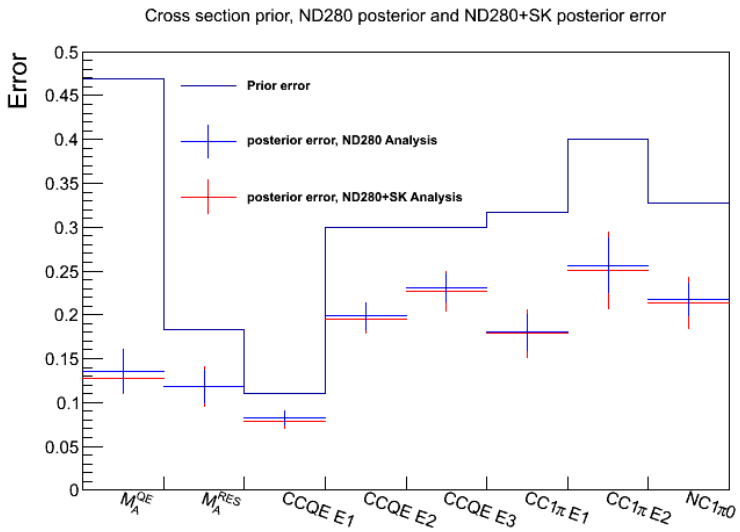

Figure 5.18: Prior and posterior error for cross section parameters. The posterior error is shown for the case of the ND280-only analysis and the simultaneous analysis.

5.8.3 Data Analysis

The SK and ND280 Run 1+2+3 data was analyzed with the MCMC using 40×10^6 post-burn-in steps. In this analysis, the step size was chosen to be 0.1 times the prior error of each systematic parameter. For the oscillation parameters of interest, a step size of 0.005 for $\sin^2(2\theta_{23})$ and a step size of 7×10^{-5} for Δm^2_{32} were used.

Similar to the ND280-only analysis, chains of length 1.2×10^5 with a burn-in of 20,000 steps were used. Fig. 5.19 shows the posterior probability plotted against the first approximately 60,000 steps of a chain. The visible burn-in section of the chain runs to about 5,000 steps, and we extend the burn-in period by a factor of four in order to ensure that the burn-in is entirely removed. The acceptance probability of the chain after burn-in is 0.43.

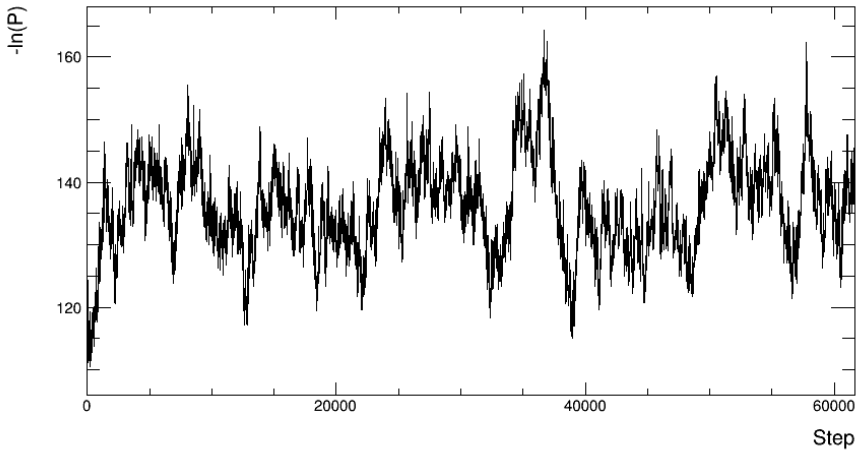

Figure 5.19: The posterior probability for the first approximately 60,000 steps of a simultaneous ND80+SK analysis. The visible burn-in period runs to about 5,000 steps; the burn-in cut is extended to 20,000 steps to ensure that all burn-in steps are removed.

The oscillation parameters point estimates are

$$\sin^2(2\theta_{23}) = 0.999 \tag{5.26}$$

$$\Delta m^2_{32} = 2.45 \times 10^{-3}\text{eV}^2 \tag{5.27}$$

and the 90% 1D bayesian credible intervals:

$$0.9340 < \sin^2(2\theta_{23}) < 1.000$$
$$2.22 \times 10^{-3} < \Delta m^2_{32}[\mathrm{eV}^2] < 2.74 \times 10^{-3}$$

It should be noted that the point estimates are taken to be the centre of the bin containing the largest probability, and therefore the largest possible point estimate for $\sin^2(2\theta_{23})$ in this analysis is 0.999.

The posterior is plotted in the $(\Delta m^2_{32}, \sin^2(2\theta_{23}))$ plane, in Fig 5.20, after marginalizing over all systematics. The resultant 2D, 68% and 90% credible intervals are shown in Fig. 5.21. The expected SK spectrum and the ratio to the no oscillation scenario are shown in Fig. 5.22 and Fig. 5.23. For these plots the systematic parameters are set at their point estimates, marginalized over all other parameters. For clarity the binning shown in the figures is coarser than the binning used for the analysis.[1] At SK the total number of observed events is 58 and the number of expected events for these parameter values is 59.81.

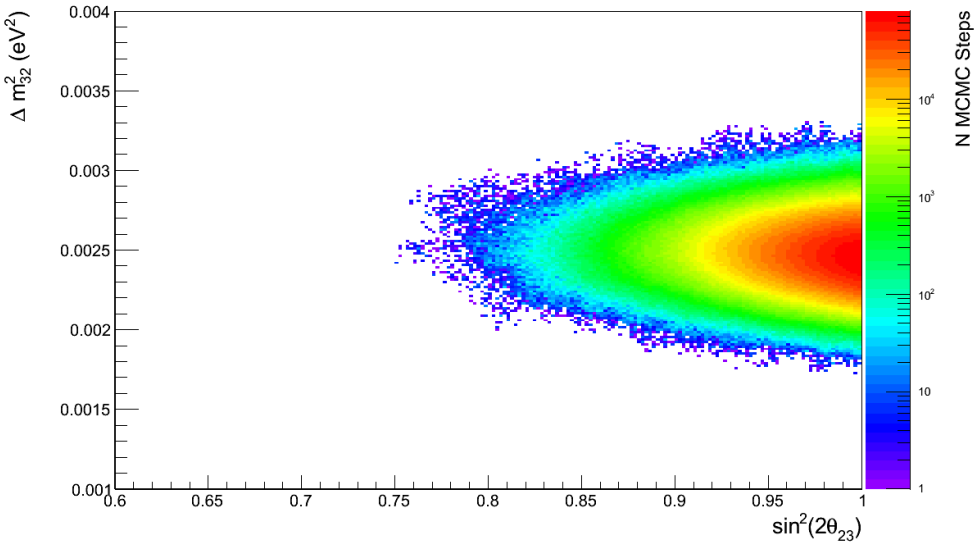

Figure 5.20: The posterior distribution of Δm^2_{32} and $\sin^2(2\theta_{23})$ from the simultaneous Run1+2+3 data analysis. All other parameters are marginalized.

[1] Bin boundaries are: 0, 0.3, 0.4, 0.5, 0.6, 0.7, 0.8, 0.9, 1.0, 1.1, 1.25, 1.5, 2, 3, 4, 6, 30 GeV

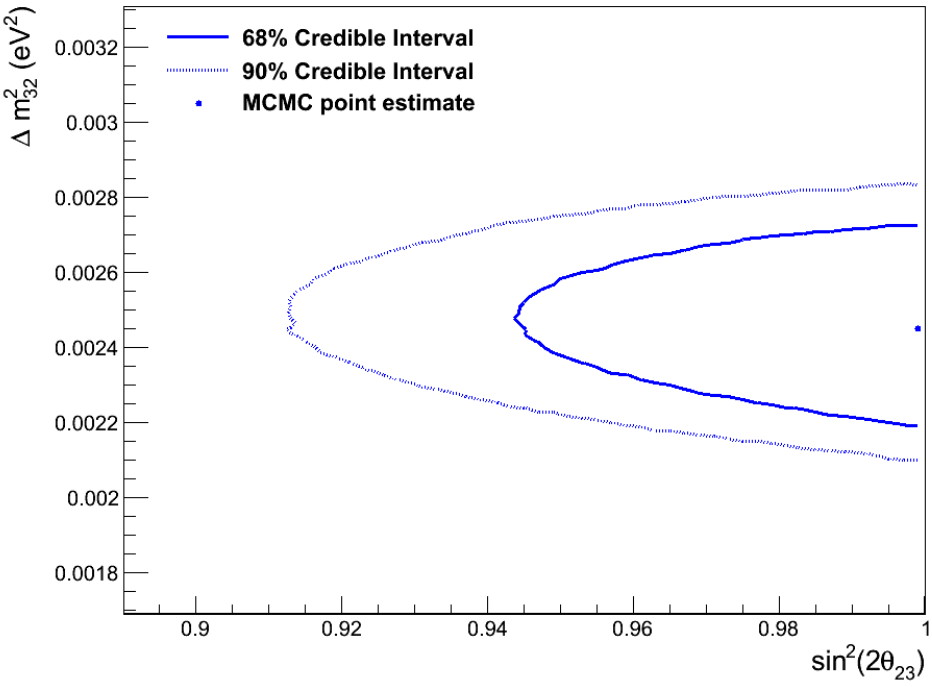

Figure 5.21: The 68% and 90% credible interval contours and the point estimate in the $\Delta m^2_{32} - \sin^2(2\theta_{23})$ plane. The contours were constructed using the method described in Section 5.5.2.

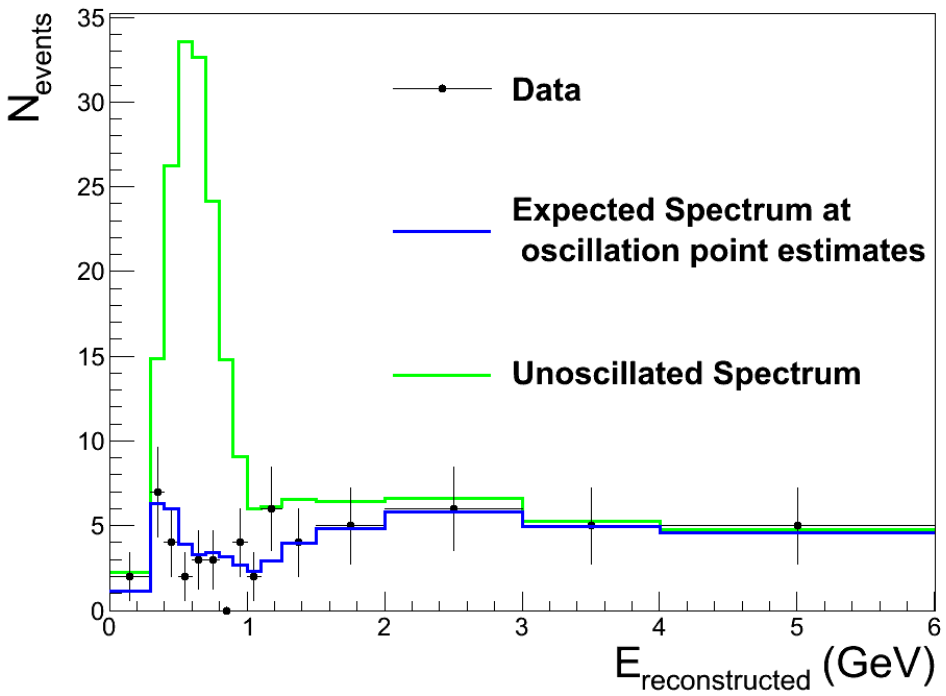

Figure 5.22: The reconstructed energy spectrum for neutrino candidates in SK, compared to the expected distribution with no oscillation, and for the oscillation parameter point estimates. The systematic parameters are set at their point estimates, marginalized over all other parameters. The binning of this plot is coarser than the binning used in the analysis.

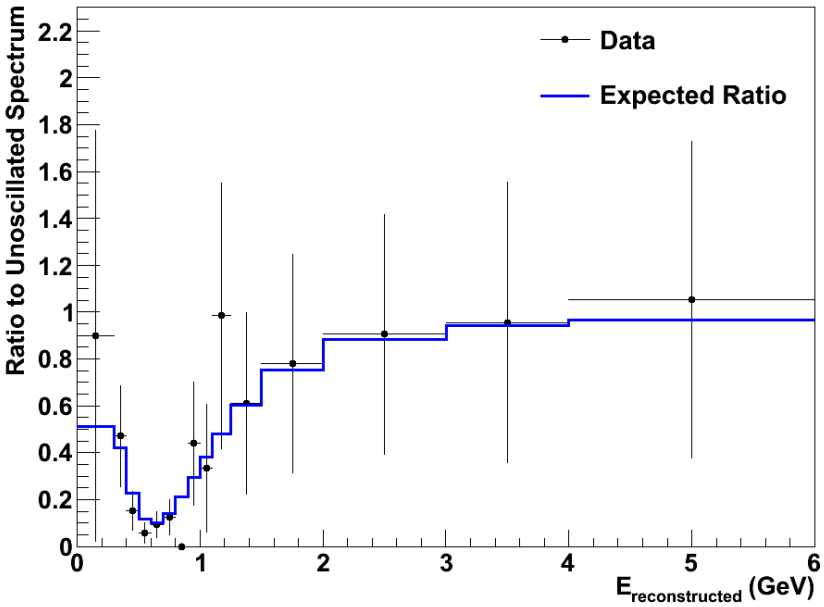

Figure 5.23: The ratio to the unoscillated reconstructed energy spectrum for the data compared to the expected ratio for the oscillation parameter point estimates. The systematic parameters are set at their point estimates, marginalized over all other parameters. The binning of this plot is coarser than the binning used for the analysis.

The pulls of the systematic parameters are evaluated using Eq 5.25. Fig. 5.24 shows the pulls for the nuisance oscillation parameters and all SK specific parameters, including SK detector systematics, and SK-only cross section parameters. Fig 5.25 shows the pulls for the flux, ND280-specific, and ND280-SK common cross section parameters. In the case of the SK systematics, absolute pull means are much less than 1, as is expected for poorly constrained parameters. For the flux and cross section parameters, the pulls are very similar to the ND280-only pulls, as is expected.

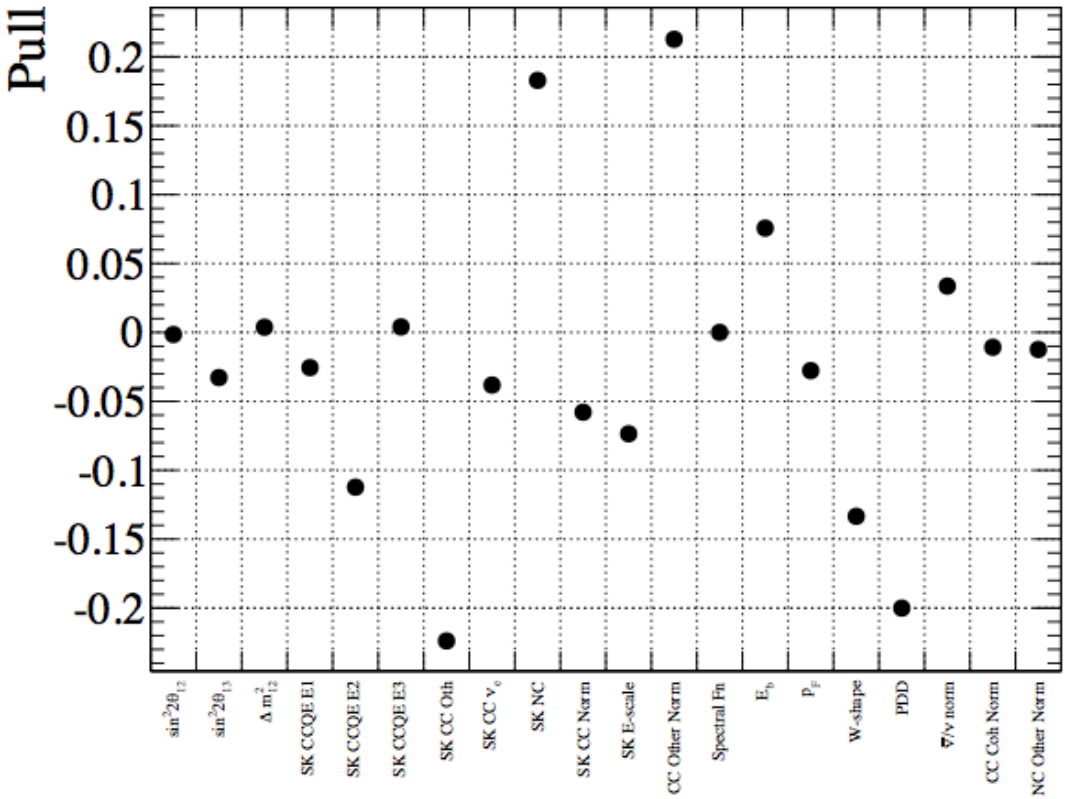

Figure 5.24: Pulls for nuisance oscillation parameters and SK specific parameters, including SK detector systematics and SK-only cross section parameters.

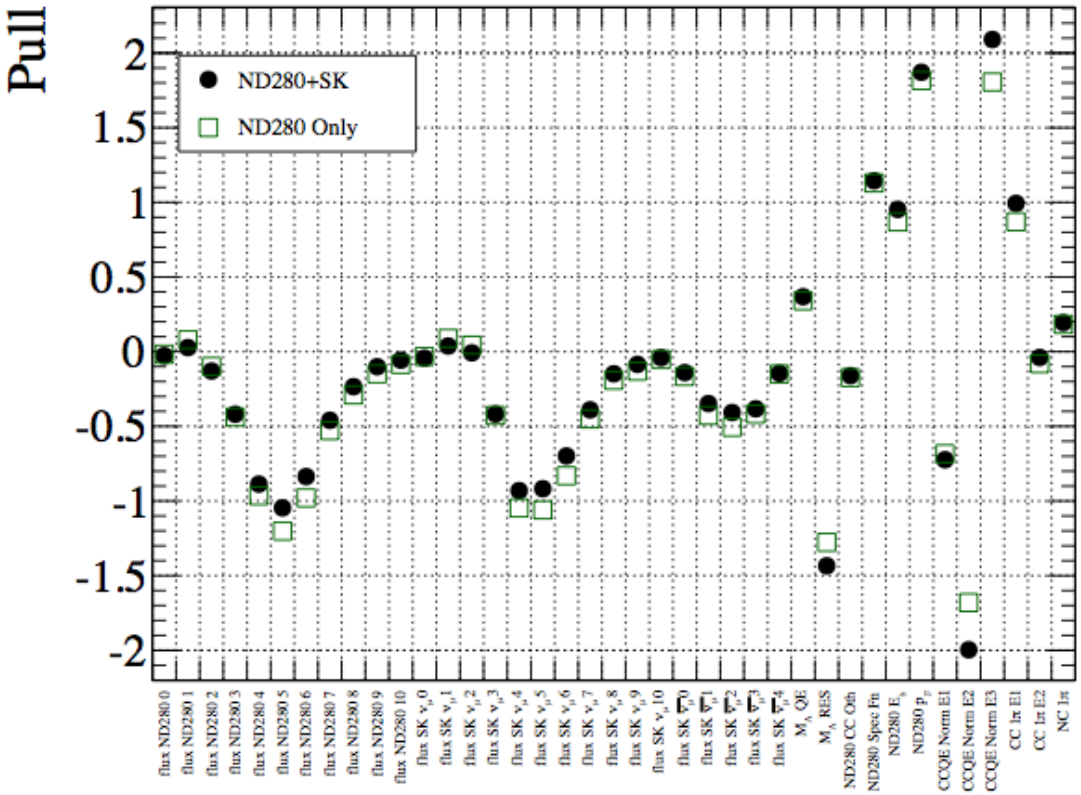

Figure 5.25: Pulls for flux and cross section parameters. Black circles show the pulls for the simultaneous analysis and open green squares show the pulls for the ND280-only analysis.

A comparison between the results of this analysis and results from other experiments is shown in Fig. 5.26, non-T2K results are from the Neutrino 2012 conference [107]. The 90% credible interval is slightly larger than the SK 3ν 90% C.L., which is currently the world's best. Direct comparisons between credible intervals and confidence intervals cannot be made, but we note that the MINOS and SK results fall within the 90% interval of this analysis, and so there is no inconsistency among the experimental results.

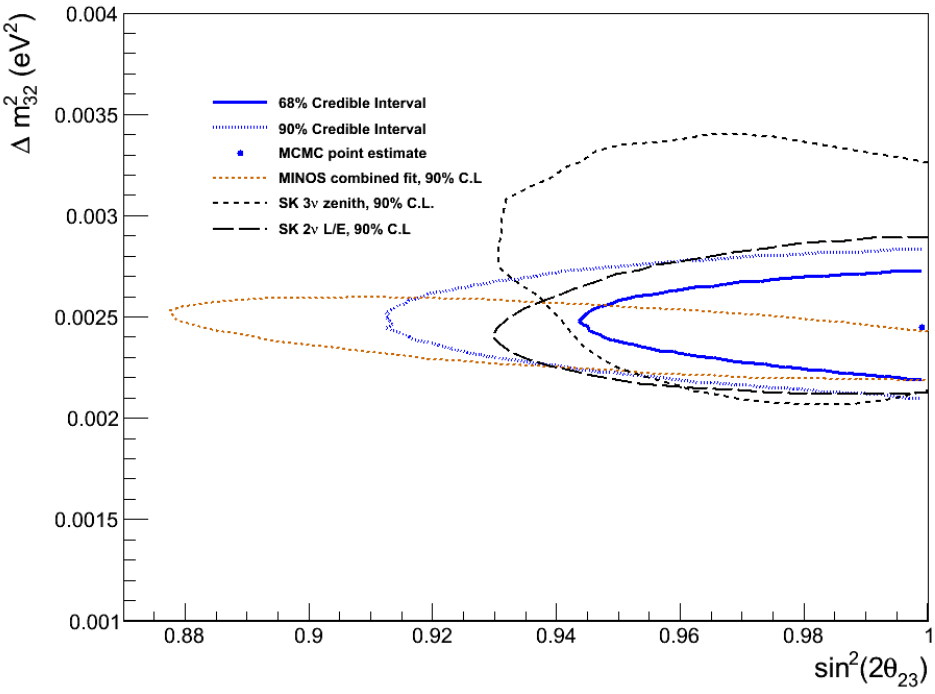

Figure 5.26: The 68% and 90% credible interval contours and the point estimate in the $\Delta m^2_{32} - \sin^2(2\theta_{23})$ plane. Also shown are the MINOS combined 90% C.L., SK 3ν Zenith 90% C.L, and the SK 2ν L/E 90% C.L. [107].

The analysis is also consistent with the two other ν_μ disappearance analyses done by other T2K collaborators. The other two analyses use a frequentist approach, using the Run 1-3 data set. The oscillation parameters are estimated using slightly different approaches, one analysis maximizes a binned likelihood ratio the other maximizes an unbinned likelihood. The analyses use the SK reconstructed neutrino energy sample binned in the same way as described in Section 5.3.1. In total 48 systematic parameters are considered which include the same SK detector parameters listed in Table 5.6, the same flux parameters described in Section 5.6.3 as well as the B and C type cross section parameters listed in Table 5.7. The analyses differ from the simultaneous analysis in that the central values and uncertainties of the flux parameters and the B type cross section parameters use information from the BANFF analysis. The output from the BANFF analysis is used as input for the oscillation analyses.

The 2D confidence regions for the oscillation parameters from the binned likelihood

ratio method are shown in Fig. 5.27 the analysis is done for octant 1 ($\theta_{23} < \pi/4$) and octant 2 ($\theta_{23} > \pi/4$).

The analysis yields the best-fit point for octant 1(2) at $\sin^2(2\theta_{23}) = 1.000(0.999)$ and $\Delta m^2_{32} = 2.44(2.44) \times 10^{-3}\text{eV}^2$. The contours and best fit result are very similar for the unbinned likelihood analysis. The 90% credible interval from the simultaneous analysis in Fig. 5.21 which uses both octants falls in between the octant 1 and octant 2 confidence intervals in Fig. 5.27.

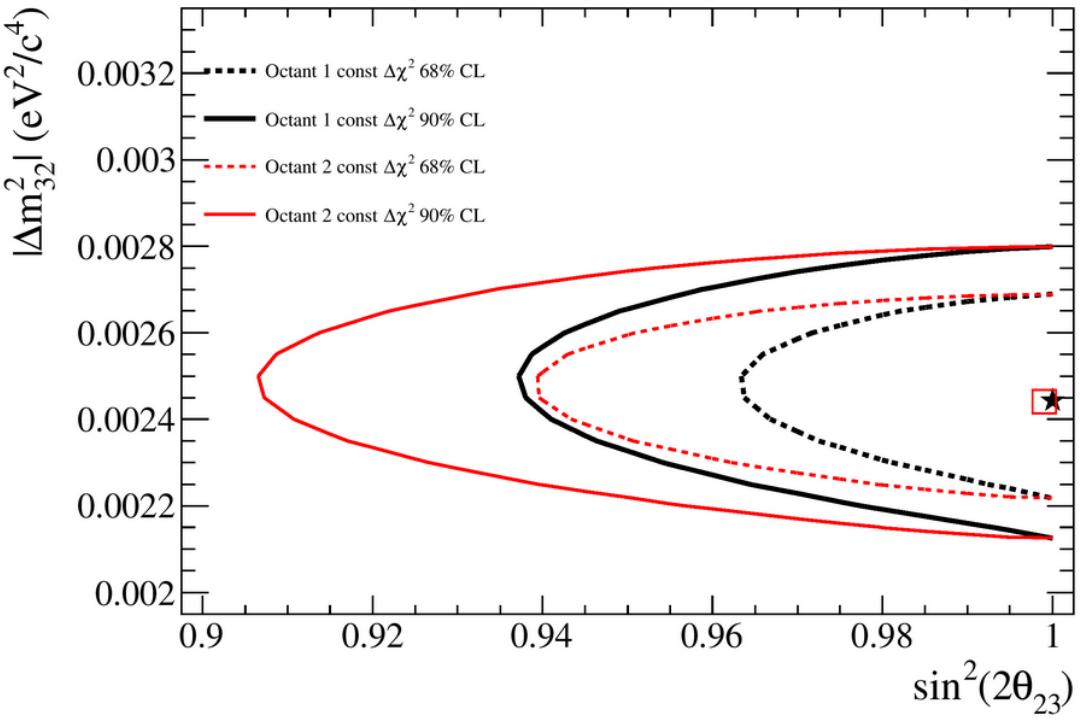

Figure 5.27: The 68% and 90% C. L. allowed contour regions for $\sin^2(2\theta_{23})$ and Δm^2_{32} for the T2K binned likelihood ratio analysis for the octant 1 (black) and octant 2 (red).

5.9 Posterior Credible Interval Checks

A check was made that the posterior intervals would contain the true value for the correct fraction of an ensemble of experiments whose oscillation parameters are distributed according to the prior. For this analysis it is assumed that the prior distri-

bution for $(\Delta m^2_{32}, \sin^2(2\theta_{23}))$ is uniform over ([0.001–0.004],[0.6–1.0]) .

To perform this check, the following ensemble of fake data is made:

- Fake data sets are made distributing the true value for the oscillation parameters $(\Delta m^2_{32}, \sin^2(2\theta_{23}))$ uniformly in a grid.
- In total 135 toy experiments are produced, corresponding to values of $\sin^2(2\theta_{23})$ = [0.625 ,0.650, 0.675, 0.700, 0.725, 0.750, 0.775, 0.800, 0.825, 0.850, 0.875, 0.900, 0.925, 0.950, 0.975] and Δm^2_{32} = [0.0015, 0.00175, 0.002, 0.00225, 0.0025, 0.00275, 0.003, 0.00325, 0.0035]
- The prior is uniform inside the region $\sin^2(2\theta_{23})$ 0.6-1.0 and Δm^2_{32} 0.001-0.004 and zero outside.
- Different values for the systematic parameters are thrown for each toy experiment.

Each toy experiment is analyzed using a Markov chain of 1.0×10^6 post burn-in steps. For each toy experiment, the credible interval contour on which the true value falls on is found, which is denoted as the "credible interval value". For correctly constructed credible intervals, the distribution of credible interval values should be uniform 0-1. Fig. 5.28 shows an example from one toy experiment where the true value ($\sin^2(2\theta_{23}) = 0.9, \Delta m^2_{32} = 0.003$) of the parameters falls on the 68% credible interval contour (credible interval value = 0.68).

Fig. 5.29 shows the distribution of the credible interval values obtained from the 135 toy experiments..

Doing a Kolmogorov-Smirnov test of the credible interval distribution under the hypothesis that it is uniform gives a p-value of 0.15. Additionally, there appears to be no strong dependency on the credible interval values as a function of $\sin^2(2\theta_{23})$ or Δm^2_{32}.

5.10 Data Analysis With World Average Prior

A simultaneous analysis of the SK and ND280 samples was also done using prior information for the oscillation parameters $\sin^2(2\theta_{23})$ and Δm^2_{32}. The prior is taken from world average values quoted in the Particle Data Group review of leptons [108], listed in Table 5.10.

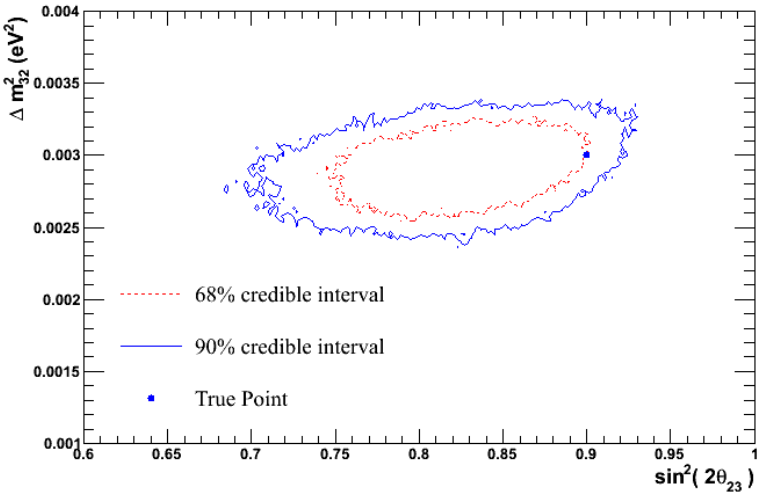

Figure 5.28: Point estimate and credible intervals for the toy experiment generated with $\sin^2(2\theta_{23}) = 0.9, \Delta m^2_{32} = 0.003$. The true value falls very close to the 68% credible interval contour. The analysis was done with a Markov chain of 1.0×10^6 steps.

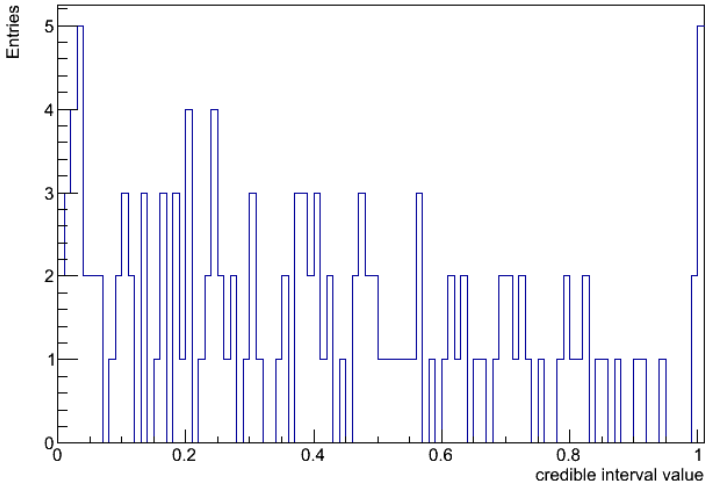

Figure 5.29: Credible interval distribution for toy experiments in the region of $\sin^2(2\theta_{23}) = [0.6 - 1.0], \Delta m^2_{32} = [0.001 - 0.004]$.

Parameter	Average Value	Error(-)	Error(+)
$\sin^2(2\theta_{23})$	0.974	-0.019	+0.051
$\Delta m^2_{32}[10^{-3}\text{eV}^2]$	2.35	-0.09	+0.12

Table 5.10: World average values of $\sin^2(2\theta_{23})$ and Δm^2_{32}, used as the prior hypothesis.

The posterior distribution is obtained from Eq. 5.9 using the same likelihood as the analysis above and using the PDG values in the prior probability density for the oscillation parameters. This method yields a new world average with the inclusion of the T2K data set.

The analysis done with 40×10^6 post burn-in steps, gives the oscillation parameter point estimates,

$$\sin^2(2\theta_{23}) = 0.999 \quad (5.28)$$

$$\Delta m^2_{32} = 2.40 \times 10^{-3}\text{eV}^2 \quad (5.29)$$

and the 1D, 90% bayesian credible intervals of $2.26 \times 10^{-3} < \Delta m^2_{32}[\text{eV}^2] < 2.56 \times 10^{-3}$ and $0.960 < \sin^2(2\theta_{23}) < 1.000$.

Figure 5.30 shows PDG world average values and 68% and 90% error contours used as the prior constraint on the oscillation parameters. Also shown is the result

from the MCMC analysis using the world average prior constraint.

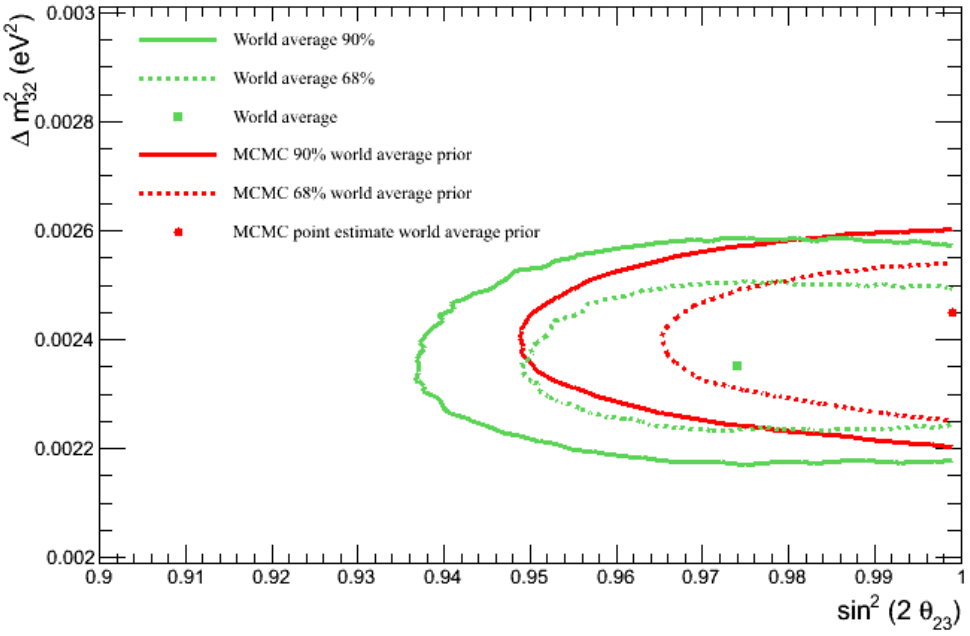

Figure 5.30: The PDG world average values and 68% and 90% contours (green) used as a prior constraint in the $\Delta m^2_{32}-\sin^2(2\theta_{23})$ plane. Also shown are the point estimate and 68% and 90% credible interval contours (red) obtained from the MCMC analysis.

It can be seen that the T2K data further reduces the error and pulls the point estimate for $\sin^2(2\theta_{23})$ to a maximal value. Compared to the prior world average the point estimate for Δm^2_{32} is pulled to a higher value and the error is not significantly reduced. There is not a significant change in the world average as the PDG world average values are still within the 68% credible interval of the MCMC analysis.

Figure 5.31 shows the results when a uniform prior is assumed compared to when the world average prior is assumed.

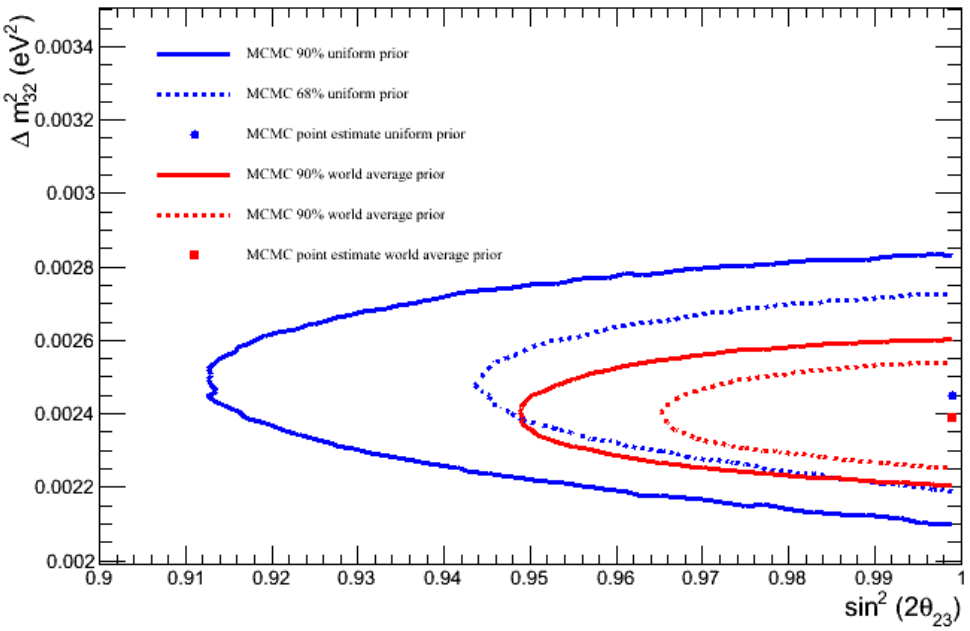

Figure 5.31: The 68% and 90% credible interval contours and point estimates with uniform prior (blue) and the world average prior (red) in $\Delta m^2_{32} - \sin^2(2\theta_{23})$.

Chapter 6

Systematic and Oscillation Parameter Correlations

The T2K experiment has a goal to collect a data set of 7.8×10^{21} POT. With increased statistics the error on Δm^2_{32} and $\sin^2(2\theta_{23})$ could be dominated by systematic errors. In this regime, if there are any strong correlations between systematic and oscillation parameters further reducing the error on the systematic parameters will yield a higher sensitivity to the oscillation parameters.

One benefit of the MCMC approach is that correlations between different parameters can be found by sampling points from the posterior probability distribution. The distributions of any two parameters in the Markov chain can be used to calculate correlations.

Monte Carlo Data Analysis

With the systematic parameterization described in the previous chapter a study was done to determine any correlations between the systematic and oscillation parameters. To obtain a desired sample the Monte Carlo data described in Sections 5.2.2 and 5.3.1 is scaled to 7.8×10^{21} POT at SK and the POT at ND280 is unchanged. For the oscillation parameters the true values used are $(\sin^2(2\theta_{23}), \Delta m^2_{32}) = (1.0, 2.4 \times 10^{-3}\text{eV}^2)$.

A MCMC analysis of the Monte Carlo was done with 20×10^6 post burn in steps and gives the point estimates:

$$\begin{aligned} \sin^2(2\theta_{23}) &= 0.999 \\ \Delta m^2_{32} &= 2.40 \times 10^{-3}\text{eV}^2 \end{aligned}$$

and the 1D 90% bayesian credible intervals of $2.32 \times 10^{-3} < \Delta m^2_{32}[\text{eV}^2] < 2.50 \times 10^{-3}$ and $0.986 < \sin^2(2\theta_{23}) < 1.000$. The 68% and 90% credible intervals and point estimates are shown in Fig. 6.1. For this analysis the mixing angle θ_{23} is set to be less that $\pi/4$.

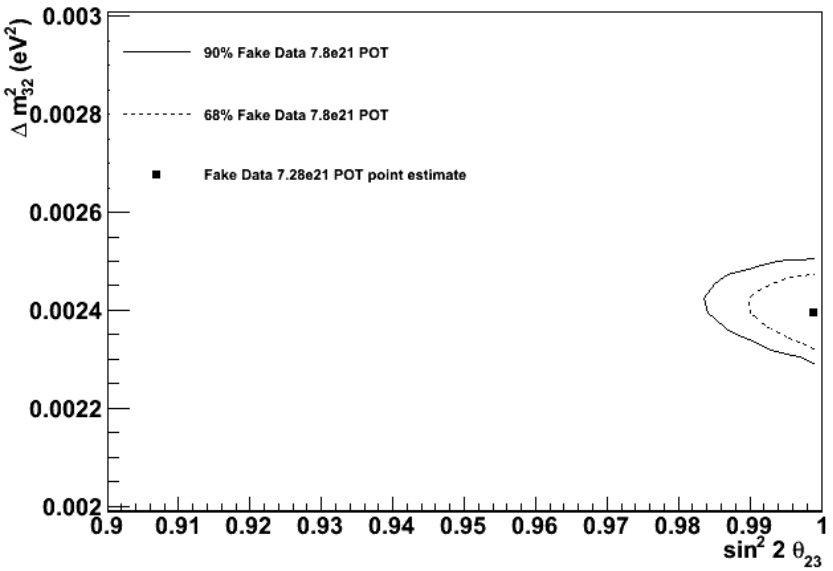

Figure 6.1: The 68% and 90% credible interval contours and the point estimate in the $\Delta m^2_{32} - \sin^2(2\theta_{23})$ plane. The Monte Carlo used true values $(\sin^2(2\theta_{23}), \Delta m^2_{32}) = (1.0, 2.4 \times 10^{-3}\text{eV}^2)$ and 7.8×10^{21} POT at SK.

A sub-sample of 2×10^6 steps is used to calculate correlations between the systematic and oscillation parameters. Visually the correlations can be inspected by projecting the posterior probability distribution onto a 2 dimensional plane, one axis set to a systematic parameter and the other set to Δm^2_{32} or $\sin^2(2\theta_{23})$.

Binding Energy on Oxygen

The largest correlation found between a systematic and oscillation parameter is the the binding energy on oxygen ($E_B\,{}^{16}O$) at SK and Δm^2_{32}. Fig. 6.4 shows the 68% and 90% credible intervals for the projection onto the $E_B\,{}^{16}O - \Delta m^2_{32}$ plane.

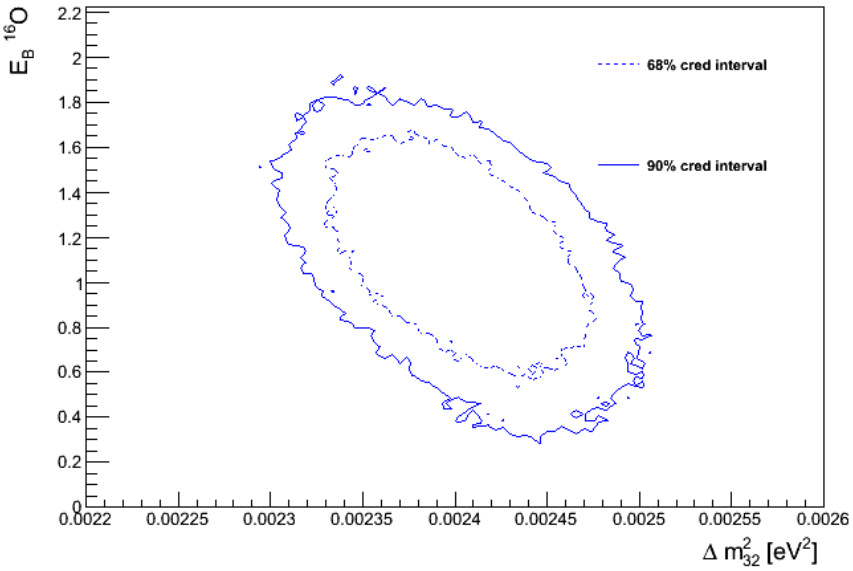

Figure 6.2: The 68% and 90% credible intervals for the posterior distribution projected onto the $E_B\ ^{16}O - \Delta m^2_{32}$ plane.

The effect the correlation has on the error of Δm^2_{32} can be estimated by projecting the posterior probability onto the Δm^2_{32} axis for different marginalizations of $E_B\ ^{16}O$. Figure 6.3 shows the Δm^2_{32} distribution when marginalizing over all possible values of $E_B\ ^{16}O$ and when marginalizing over a limited range which is centred about the estimated parameter value ($1.0 < E_B\ ^{16}O < 1.14$). Fitting both projections with a Gaussian, the error on Δm^2_{32} when marginalizing over all possible values of E_B is $4.61 \times 10^{-5}\text{eV}^2$ and marginalizing over the limited range gives an error of $4.07 \times 10^{-5}\text{eV}^2$, a difference of 12%.

These results show that further reducing the error on the binding energy on oxygen can improve the measurement of Δm^2_{32} by a significant amount.

The uncertainties on the binding energy are found from external electron scattering data [109]. It is of interest if ND280 can further reduce the error of $E_B\ ^{16}O$. Although it does not provide direct constraints, information from analyses done on carbon provides insight into the ability of ND280 to constrain the errors for parameters associated with oxygen.

For analyses of interactions in FGD 1 the analysis of the near detector data does provide a constraint on the binding energy on carbon ($E_B\ ^{12}C$). Figure 5.11 shows the error reduction for the cross section parameters, for $E_B\ ^{12}C$ there is a reduction

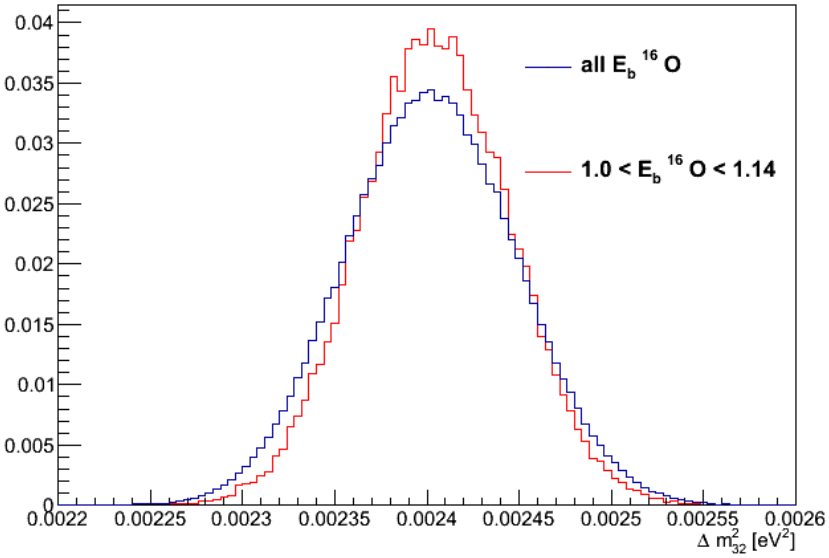

Figure 6.3: Projection on the Δm^2_{32} axis marginalizing over all values of the binding energy on oxygen at SK $E_B\ ^{16}O$ (blue) and marginalizing over a limited range $1.0 < E_B\ ^{16}O < 1.14$ (red).

in the fractional error from 36% to 27%.

Inspecting Eq. 2.4 it can be seen that in the region of T2K energies, the momentum scales as $-E_B$ to first order. From this linear relationship it follows that the uncertainty on the binding energy as determined by ND280 would be proportional to momentum scale uncertainty of ND280. The momentum scale uncertainty is important in comparing analyses done with in FGD 1 - TPC 2 and FGD 2 - TPC 3. As discussed in Chapter 4, tracks in TPC 3 have a larger momentum scale uncertainty due to the larger difference between the data and MC magnetic field distortions.

Another important consideration for analyses done in FGD 2 is the inactive material in the water panels that will lead to a reduced momentum resolution when compared to FGD 1.

The limitations in FGD 2 - TPC 3 will affect the constraints that can be applied to $E_B\ ^{16}O$. Due to the degraded resolution and larger momentum scale error, ND280 will not be able to constrain errors on oxygen as well as carbon.

Comparisons of electron scattering data with the spectral function model [110] suggest that it is a more correct representation of the nuclear potential [111]. Future oscillation analyses may use a parameterization of the spectral function model and not include the binding energy parameter. The spectral function model is not yet

included in NEUT and it is unknown if there are any correlations between parameters modelling the spectral function and oscillation parameters.

These studies show that E_B ^{16}O is an important systematic limiting the sensitivity of Δm^2_{32}. Analyses to further constrain the error on E_B ^{16}O or the determine the behaviours when modelling the cross section uncertainties with out using the binding energy parameter are of particular interest for the future sensitivity of T2K.

SK Energy Scale

Another parameter that is correlated with Δm^2_{32} and has an effect on the sensitivity is the SK energy scale error. Fig. 6.4 shows the 68% and 90% credible intervals for the projection onto the SK energy scale – Δm^2_{32} plane.

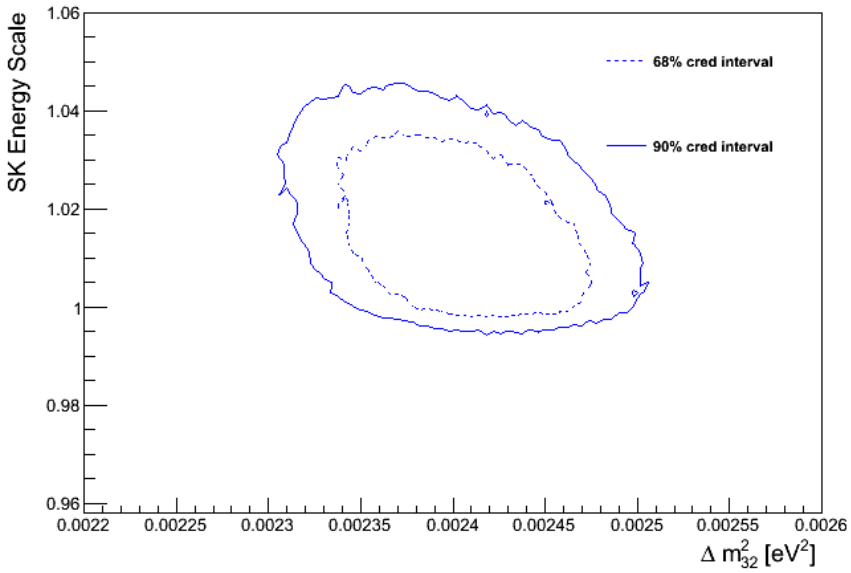

Figure 6.4: The 68% and 90% credible intervals for the posterior distribution projected onto the SK energy scale – Δm^2_{32} plane.

Fitting the projections on the Δm^2_{32} axis with a Gaussian, the error on Δm^2_{32} when marginalizing over all possible values of the energy scale parameter is $4.61 \times 10^{-5}\text{eV}^2$ and marginalizing over a limited range ($1.006 <$ energy scale < 1.017) gives an error of $4.35 \times 10^{-5}\text{eV}^2$, a difference of 6%. The projections onto the Δm^2_{32} axis are shown in Fig. 6.5.

The error on the energy scale at SK is evaluated using cosmic-ray stopping muons and associated decay-electrons, as well as π^0's produced by atmospheric neutrinos

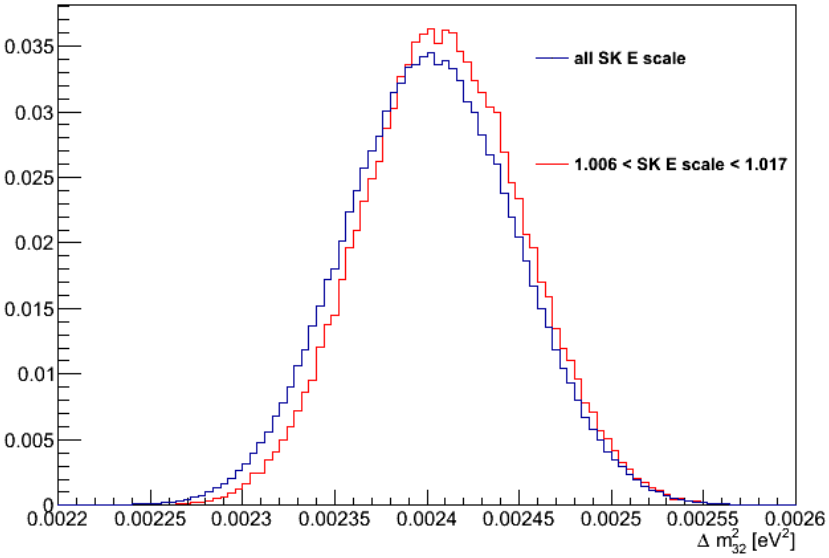

Figure 6.5: Projection on the Δm^2_{32} axis marginalizing over all values of the SK energy scale (blue) and marginalizing over a limited range $1.006 <$ energy scale < 1.017 (red).

and has an uncertainty of 2.3%. The already precise knowledge of the energy scale makes it difficult to further reduce.

Other Parameters

It has been observed that there are weak correlations between other systematic parameters and the oscillation parameters, these correlations do not have a significant impact on the sensitivity of the oscillation parameter measurements and are not presented.

Chapter 7

Conclusion

A ν_μ disappearance oscillation measurement was performed using a simultaneous analysis of the ND280 ν_μ tracker sample and SK ν_μ sample. The analysis used a Markov Chain Monte Carlo method for parameter estimation and interval construction. With a uniform prior for $\sin^2(2\theta_{23})$ and Δm^2_{32} the point estimates are:

$$(\sin^2(2\theta_{23}), \Delta m^2_{32}) = (0.999, 2.45 \times 10^{-3}[\mathrm{eV}^2]),$$

and the 1D 90% bayesian credible intervals:

$$0.9340 < \sin^2(2\theta_{23}) < 1.000$$
$$2.22 \times 10^{-3} < \Delta m^2_{32}[\mathrm{eV}^2] < 2.74 \times 10^{-3}$$

This result is consistent and competitive with the measurements made by other experiments and other analyses done by T2K collaborators. The T2K result will improve with more data as currently the sensitivity of the disappearance analyses is limited by the statistical uncertainty.

Performing the analysis using the current world average as prior information for the oscillation parameters $\sin^2(2\theta_{23})$ and Δm^2_{32} gives an updated world average with point estimates:

$$(\sin^2(2\theta_{23}), \Delta m^2_{32}) = (0.999, 2.40 \times 10^{-3}[\mathrm{eV}^2]),$$

$$0.960 < \sin^2(2\theta_{23}) < 1.000$$
$$2.26 \times 10^{-3} < \Delta m^2_{32}[\mathrm{eV}^2] < 2.56 \times 10^{-3}$$

The MCMC framework provides a method to find the correlations between systematic and oscillation parameters to determine parameters that will limit the sensitivity of the experiment. Tests done with Monte Carlo data show that with the parameterization used for the analysis in the regime where the systematic errors dominate, reducing the error on E_B ^{16}O will increase the sensitivity on Δm^2_{32}. There is potential for future studies investigating interactions in water at ND280 to further limit the uncertainty on E_B ^{16}O.

Further data collection and analysis upgrades at T2K will continue to improve the precision on measurements of the oscillation parameters $\Delta m^2_{32}, \theta_{23}$ and T2K will be able to provide the world leading measurements of these parameters.

Bibliography

[1] W. Pauli, "Letter to the Physical Society of Tubingen," 1930. Unpublished. Reprint Translation into English Physics Today vol. 31, p. 23, 1978.

[2] J. Chadwick *Nature*, vol. 192, 1932.

[3] H.Bethe and R. Peierls *Nature*, vol. 133, 1934.

[4] F. Reines and C. Cowan *Nature*, vol. 178, 1956.

[5] B. Pontecorvo *Sov. Phys. JETP*, vol. 10, pp. 1236–1240, 1960.

[6] G. Danby *et al. Phys. Rev. Lett.*, vol. 51, 1962.

[7] K. Kodama and others (DONUT Collaboration) *Phys. Lett. B*, vol. 504, 2001.

[8] S. Glashow *Nucl. Phys.*, vol. 22, 1961.

[9] F. J. Hasert *et al. Phys. Lett. B*, vol. 46, 1973.

[10] S. Schael *et al.*, "Precision electroweak measurements on the Z resonance," *Phys. Rept.*, vol. 427, 2006.

[11] B. T. Cleveland *et al. Astrophys. J.*, vol. 496, 1998.

[12] J. Bahcall, *Neutrino Astrophysics*. Cambridge University Press, 1989.

[13] S. Oser, "Neutrino Physics: A Select Overview," 2006. Proceedings of Lake Louise Winter Institute.

[14] P. Anselmann *et al. Phys. Lett. B*, vol. 285, pp. 376–389, 1992.

[15] A. I. Abazov *et al. Phys. Rev. Lett.*, vol. 67, pp. 3332–3335, 1991.

[16] K. S. Hirata *et al. Phys. Rev. Lett.*, vol. 63, 1989.

[17] K. S. Hirata *et al. Phys. Rev. Lett.*, vol. B205, 1988.

[18] T. J. Haines *et al. Phys. Rev. Lett.*, vol. 57, pp. 1987–1989, 1986.

[19] B. Pontecorvo *Sov. Phys. JETP*, vol. 6, 1957.

[20] M. N. Z. Maki and S. Sakata *Prog. Theor. Phys.*, vol. 28, 1962.

[21] B. Pontecorvo *Sov. Phys. JETP*, vol. 26, pp. 984–988, 1969.

[22] C. Amsler *et al. Phys. Lett.*, vol. B2667, 2008.

[23] P. Peebles *Phys. Rev. Lett.*, vol. 16, 1966.

[24] M. Maltoni *et al. Nucl. Phys. B.*, vol. 643, 2002.

[25] S. P. Mikheyev and A. Y. Smirnov *Sov. J. Nucl. Phys*, vol. 42, 1985.

[26] L. Wolfenstein *Phys. Rev. D*, vol. 17, 1979.

[27] S. Collaboration *Nucl. Instr. and Meth.*, vol. A449, 2000.

[28] B. Aharmin *et al. Phys. Rev.*, vol. C72, 2005.

[29] T. Araki *et al. Phys. Rev. Lett.*, vol. 94, 2003.

[30] S. Abe and others (KamLAND Collaboration) *Phys. Rev. Lett.*, vol. 100, 2008.

[31] T. Kajita *Advances in High Energy Physics*, vol. 2012, 2012.

[32] K. Abe and others (Super Kamiokande Collaboration) *Phys. Rev. Lett.*, vol. 107, 2011.

[33] P. Adamson and others (MINOS Collaboration) *Phys. Rev. Lett.*, vol. 110, 2013.

[34] K. Abe and others (T2K Collaboration) *Phys. Rev. D*, vol. 85, 2012.

[35] D. Ayres and others (NOVA Collaboration) *arXiv:hep-ex/0503053*, 2005.

[36] M. Apollonio *et al. Eur. Phys. J.*, vol. C27, pp. 331–374, 2003.

[37] K. Abe and others (T2K Collaboration) *Phys. Rev. Lett.*, vol. 107, 2011.

[38] P. Adamson and others (MINOS Collaboration) *Phys. Rev. Lett.*, vol. 107, 2011.

[39] F. P. An *et al. arXiv:1203.1669v2*, 2012.

[40] J. K. Ahn and others (RENO collaboration) *arXiv:1204.0626v2*, 2012.

[41] V. Aseev *et al. Phys. Rev. D84*, vol. 112003, 2011.

[42] K. Eitel *et al. Nucl. Phys. (Proc. Supp.)*, vol. B143, 2005.

[43] K. Abazajian *et al. Astopart. Phys.*, vol. 35, 2011.

[44] M. Danilov *Phys. Lett. B*, vol. 480, 2000.

[45] A. Barabash *et al. Physics of Atomic Nuclei*, vol. 67, 2004.

[46] J. Christenson *et al. Phys. Rev. Lett.*, vol. 13, 1964.

[47] B. Aubert and others (BABAR collaboration) *Phys. Rev. Lett.*, vol. 87, 2001.

[48] M.-C. Chen, "TASI 2006 Lectures on Leptogenesis," *arXiv:hep-ph/0703087*, 2007.

[49] A. Strumia, "Baryogenesis via Leptogenesis," *arXiv:hep-ph/0608347*, 2006.

[50] K. Abe and others (T2K Collaboration), "The T2K Experiment," *Nucl. Instrum. Meth. A*, vol. 659, 2011.

[51] S. Kopp, "Accelerator Neutrino Beams," *Phys.Rept.*, vol. 439, pp. 101–159, 2007.

[52] K. Abe and others (T2K Collaboration), "The T2K Neutrino Flux Prediction," *Phys. Rev. D*, vol. 87, 2013.

[53] N. Abgrall *et al.*, "Report from the NA61/SHINE Experiment at the CERN SPS," *Technical Report CERN-SPSC-2010-025*, 2010.

[54] "Fluka version 2008.3c http://www.fluka.org/fluka.php," 2008.

[55] A. S. G. Computing and C. Networks Division, "GEANT3, a Detector Description and Simulation Tool," 1993.

[56] C. Zeitnitz and T. A. Gabriel, "International Conference on Calorimetry in High Energy Physics," 1993.

[57] "Unpublished Official T2K Collaboration Plot," 2012.

[58] P. Lipari *Nucl. Phys. Proc. Suppl.*, vol. 112, 2002.

[59] "T2K ND280 Conceptual Design Report," tech. rep., 2005.

[60] Y. Hayato *Nucl.Phys.Proc.Suppl.*, vol. 112, pp. 171–176, 2002.

[61] C. L. Smith, "Neutrino Reactions at Accelerator Energies," *Phys.Rept.*

[62] R. Smith and E. Moniz, "Neutrino Reactions on Nuclear Targets," *Nucl. Phys. B*, vol. 43.

[63] D. Rein and L. M. Sehgal, "Neutrino-Excitation of Baryon Resonances and Single Pion Production," *Annals of Physics*, vol. 133, pp. 79–153, 1981.

[64] D. Rein and L. M. Sehgal, "Coherent π^0 Production in Neutrino Reactions," *Nuclear Physics B*, vol. 223, pp. 29–44, 1983.

[65] E. R. M. Gluck and A. Vogt, "Dynamical Parton Distributions Revisited," *Eur.Phys.J.*, vol. C5, pp. 461–470, 1998.

[66] R. D. Woods and D. S. Saxon, "Diffuse Surface Optical Model for Nucleon-Nuclei Scattering," *Phys. Rev.*, vol. 95, pp. 577–578, 1954.

[67] S. Agostinelli *et al. Nucl. Instrum. Meth. A*, vol. 506, pp. 250–303, 2003.

[68] M. Ikeda, *Precise Measurement of Solar Neutrinos with Super-Kamiokande III.* PhD thesis, University of Tokyo, 2010.

[69] T. G. C. Zeitnitz *Nucl.Instrum.Meth. A*, vol. 349, pp. 106–111, 1994.

[70] W. R. Leo, *Techniques for Nuclear and Particle Physics Experiments.* Springer-Verlag, 1994.

[71] J. Beringer and others (PDG), "The Review of Particle Physics ," *Phys.Rev.*, vol. D86, 2012.

[72] H. Bichsel, "A Method to Improve Tracking and Particle Identification in TPCs and Silicon Detectors," *Nuclear Instruments and Methods in Physics Research A.*

[73] D. Nygren and J. Marx *Physics Today*, vol. 31, 1978.

[74] I. G. G. Charpak *Nucl. Instrum. Methods A*, vol. 29, 1996.

[75] C. Giganti, *Particle Identification in the T2K TPCs and Study of the Electron Neutrino Component in the T2K Neutrino Beam.* PhD thesis, Institut de Recherche sur les lois Fondamentales de lUnivers, 2010.

[76] N. Abgrall *et al.*, "Time Projection Chambers for the T2K Near Detectors," *Nucl. Instrum. Meth. A*, vol. 637, 2011.

[77] "www.comsol.com."

[78] I. Giomataris *et al.*, "Micromegas in a Bulk," *Nucl. Instr. and Meth.*, vol. A560, pp. 405–408, 2006.

[79] J. Bouchez *et al.*, "Bulk Micromegas Detectors for Large TPC Applications," *Nucl. Instr. and Meth.*, vol. A574, pp. 415–420, 2007.

[80] "https://midas.psi.ch/."

[81] "http://root.cern.ch/drupal/."

[82] A.Hillairet, "ND280 Reconstruction," tech. rep., 2011.

[83] A. S. R. Fruhwirth and W. Waltenberger, "Helix Fitting by an Extended Riemann Fit," *Nucl. Instr. and Meth.*, vol. A490, 2002.

[84] D. Karlen, P. Poffenberger, and G. Rosenbaum, "TPC Performance in Magnetic Fields with GEM and Pad Readout," *Nucl. Instr. and Meth.*, vol. A555, 2005.

[85] F. James, "MINUIT Reference Manual," tech. rep., CERN, 2000.

[86] "http://evalu29.ific.uv.es/recpack/welcome.html."

[87] R. L. Gluckstern *Nucl. Instr. and Meth.*, vol. 24, 1963.

[88] L. Escudero, "T2K-TN-095, study of TPC Momentum Resolution from Tracks that Cross Multiple TPCs and the Associated Systematic Error on the ν_μ CC and CCQE Analyses," tech. rep., 2012.

[89] "Figure made by T2K Collaborator Andre Gaudin.," 2011.

[90] E. Frank *et al.*, "A Dedicated Device for Measuring the Magnetic Field of the ND280 Magnet in the T2K Experiment," *Journal of Instrumentation*, vol. 7, 2012.

[91] C. Giganti *et al.*, "Study of Neutrino Charged Current Interactions in the ND280 Tracker," Tech. Rep. TN-015, T2K, 2011.

[92] C. Bojechko *et al.*, "QE-like and non-QE-like numu event selections in the ND280 tracker using Run 1+2 data," Tech. Rep. TN-93, T2K, 2012.

[93] S. Brooks, A. Gelman, G. Jones, and X. Meng, *Handbook of Markov Chain Monte Carlo: Methods and Applications*. Chapman & Hall, 2010.

[94] R. Neal *et al.*, "Probabilistic Inference using Markov Chain Monte Carlo Methods," 1993.

[95] P. de Perio *et al.*, "Constraining the Flux and Cross Section with Data from the ND280 Detector for the 2012a Oscillation Analysis," Tech. Rep. TN-106, T2K, 2012.

[96] R. Wendall, "http://www.phy.duke.edu/ raw22/public/prob3++/," 2012.

[97] K. Nakamura *et al.*, "Review of particle physics," *Journal of Physics G: Nuclear and Particle Physics*, vol. 37, no. 7A, p. 075021, 2010.

[98] R. Cousins and V. Highland, "Incorporating Systematic Uncertainties into an Upper Limit," *Nucl. Instrum. Methods*, vol. A320, 1992.

[99] M. Otani *et al.*, "Super-K events and Updated systematic errors for ν_μ disappearance analysis with T2K 1.431×10^{20} POT," Tech. Rep. TN-065, T2K, 2011.

[100] P. de Perio *et al.*, "Cross section parameters for 2012a oscillation analysis," Tech. Rep. TN-108, T2K, 2012.

[101] N. Abgrall *et al.*, "Neutrino Flux Prediction for the 2011a Analysis," Tech. Rep. TN-99, T2K, 2011.

[102] A.Aguilar and others (MiniBooNE Collaboration) *arXiv:1007.1150v1*, 2010.

[103] P. de Perio *et al.*, "Implementation of the NIWG Cross Section Parametrization," Tech. Rep. TN-113, T2K, 2012.

[104] A. A. Aguilar-Arevalo *et al.*, "Measurement of ν_μ and $\bar{\nu_\mu}$ Induced Neutral Current Single π^0 Production Cross Sections on Mineral Oil at $E_\nu \sim \mathcal{O}(1\text{GeV})$," *Phys. Rev. D*, vol. 81, 2010.

[105] M. Murakami *et al.*, "Run 1+2+3 numu Disappearance Analysis with Maximum Likelihood Fit," Tech. Rep. TN-139, T2K, 2012.

[106] L. Demortier and L. Lyons, "Everything you Always Wanted to Know About Pulls," *CDF note*, vol. 49, no. 1, pp. 45–49, 2002.

[107] "Neutrino 2012, the XXV International Conference on Neutrino Physics and Astrophysics (Kyoto, Japan, 2012), neu2012.kek.jp."

[108] K. Nakamura and others (Particle Data Group) *JPG*, vol. 37, 2010.

[109] E. J. Moniz *et al.*, "Nuclear Fermi Momenta from Quasielastic Electron Scattering,"

[110] M. Ankowski and J. T. Sobczyk., "Construction of Spectral Functions for Medium-mass Nuclei," *Phys. Rev. C*, vol. 77, 2008.

[111] P. de Perio *et al.*, "T2K-TN-113, Implementation of the NIWG Cross Section Parametrization.," tech. rep., 2012.

Appendices

Appendix A

Magnetic Field Distortions Plots Monte Carlo

Magnetic field distortions plots generated from Monte Carlo simulation. Circles represent nominal location of dots. Lines represent the difference between the fit centroid of the targets for perfect field and measured field simulation. Lines are magnified by a factor of 20 to make visible on the plot. Referencing the Langevin equation the parameters used in the simulation are in Table 4.1.

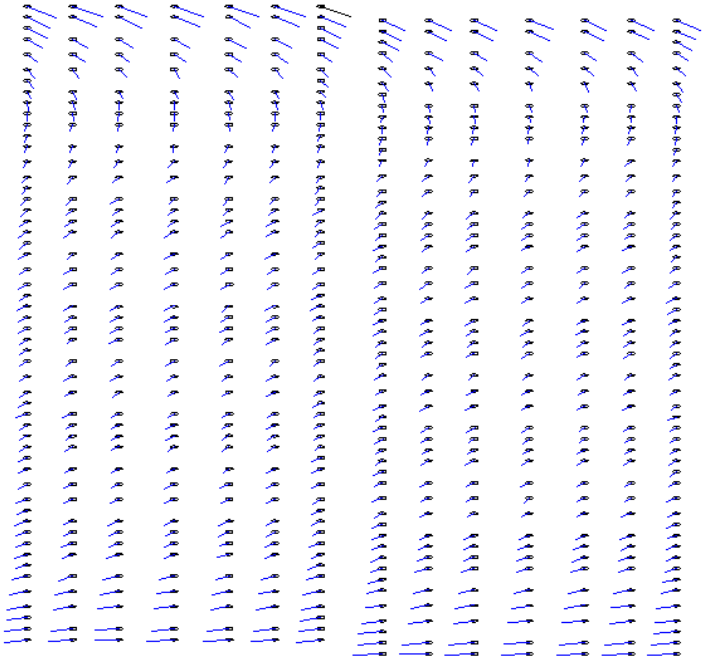

(a) TPC1 RP0

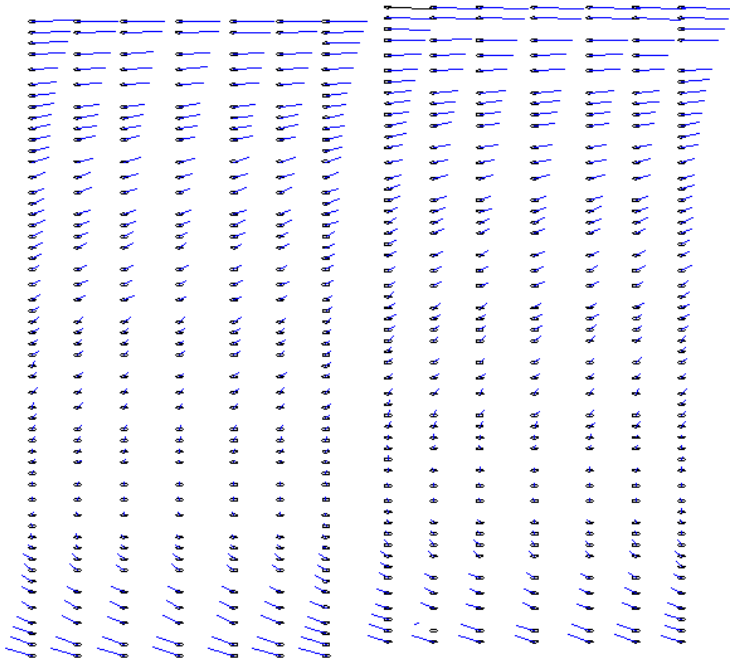

(b) TPC1 RP1

Figure A.1: Magnetic field distortions for TPC 1 Monte Carlo

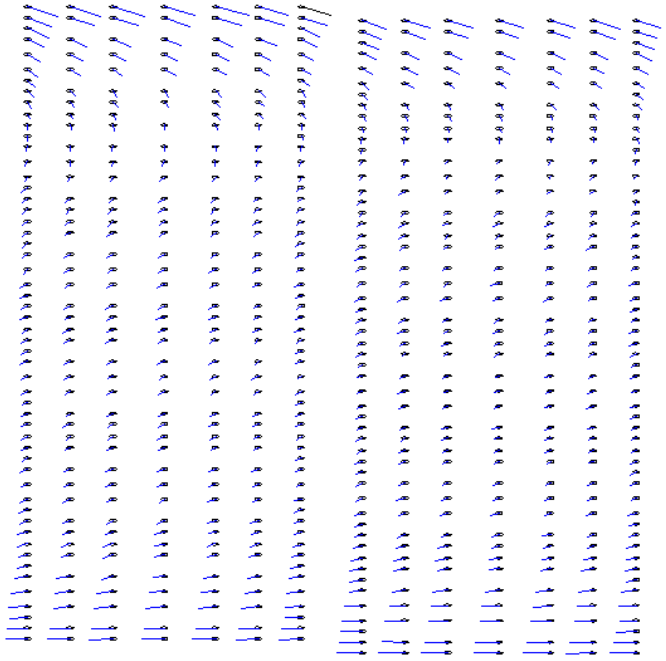

(a) TPC2 RP0

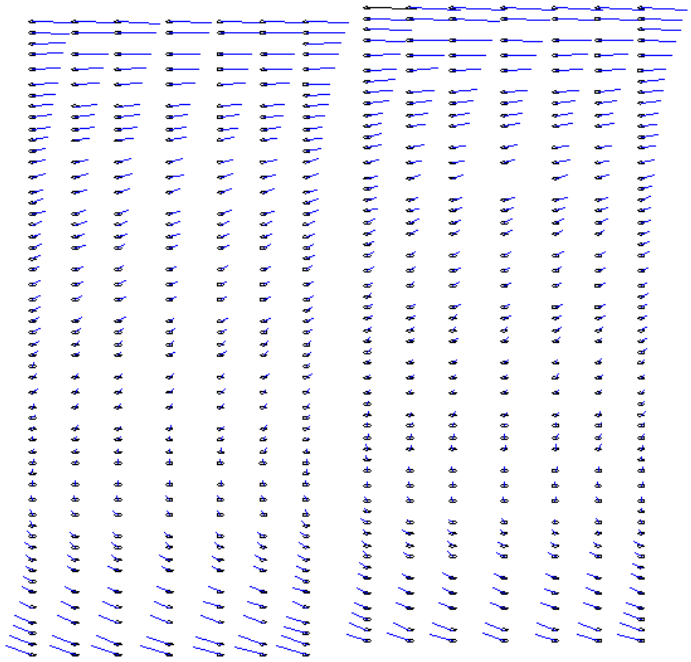

(b) TPC2 RP1

Figure A.2: Magnetic field distortions for TPC 2 Monte Carlo

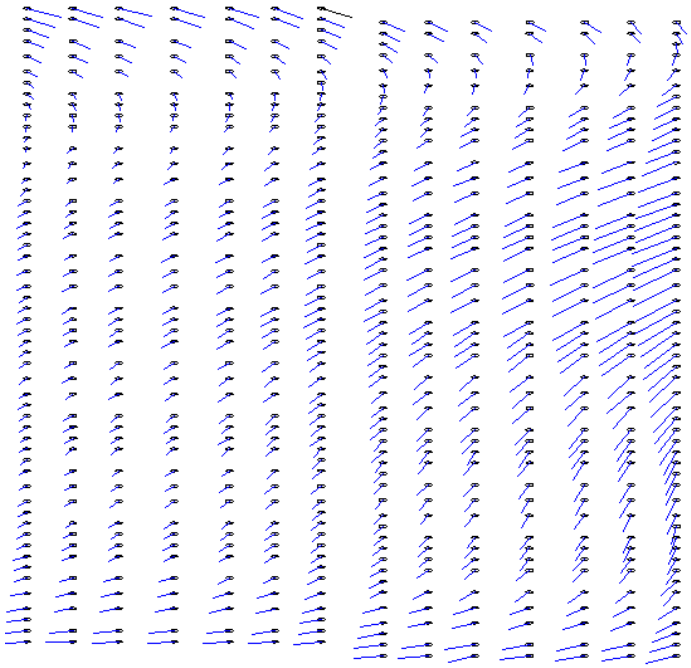

(a) TPC3 RP0

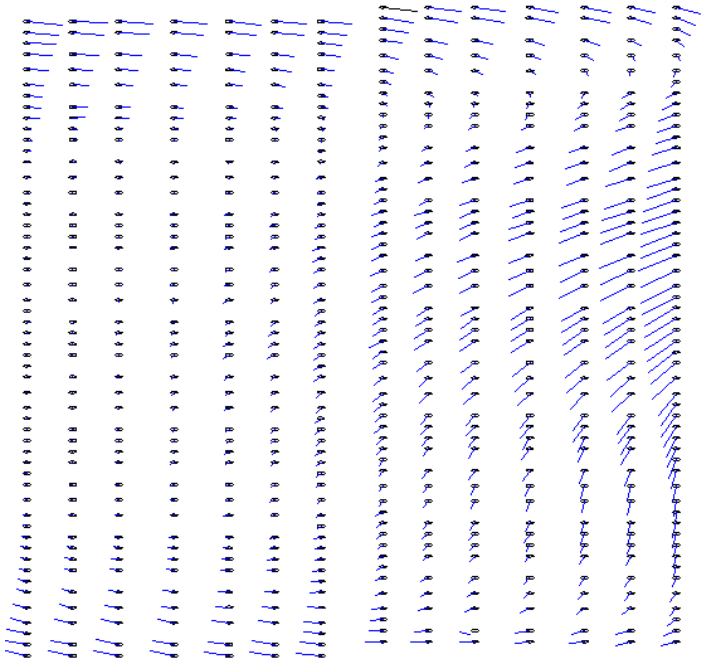

(b) TPC3 RP1

Figure A.3: Magnetic field distortions for TPC 3 Monte Carlo

Appendix B

Magnetic Field Distortions Plots Data

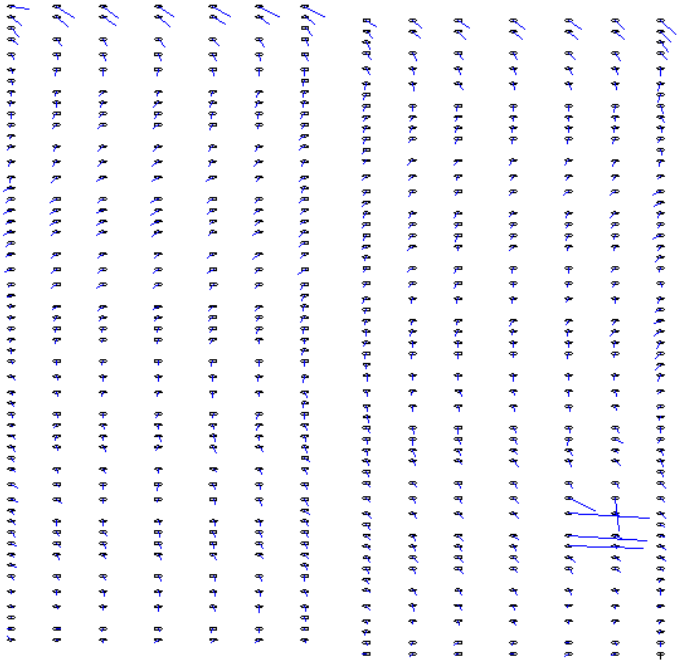

(a) TPC1 RP0

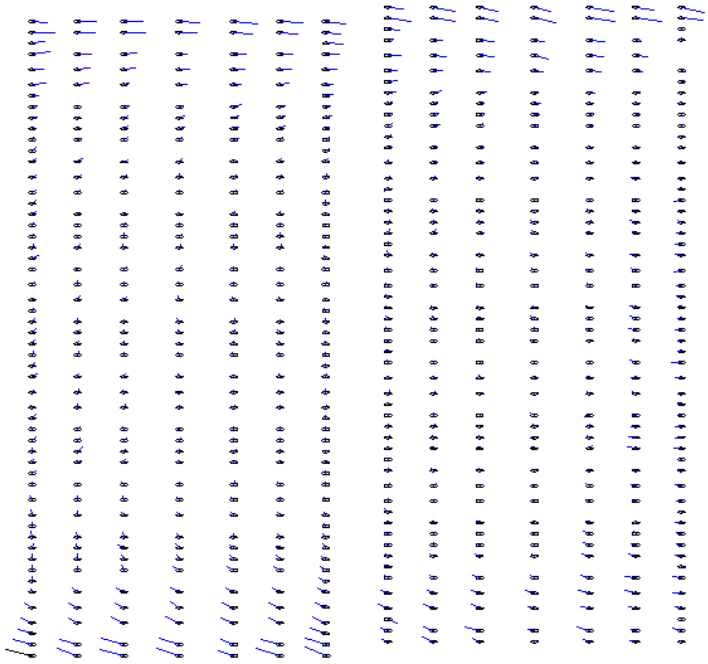

(b) TPC1 RP1

Figure B.1: Magnetic field distortions for TPC 1 data

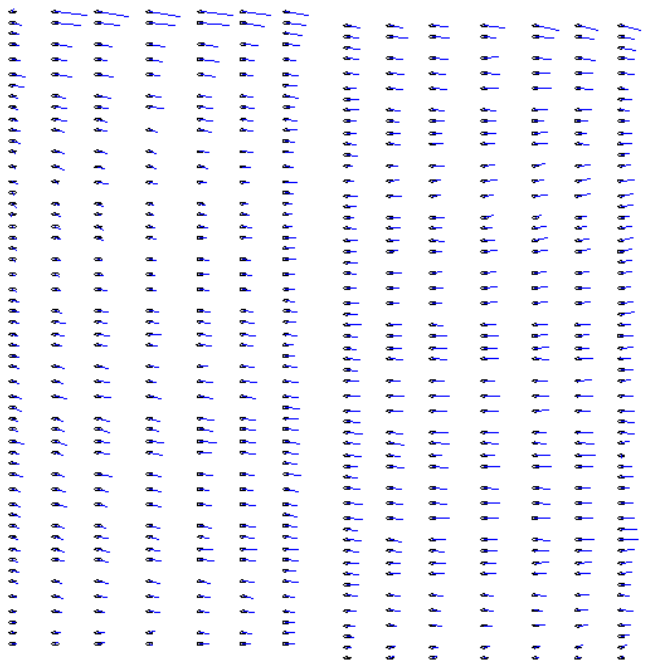

(a) TPC2 RP0

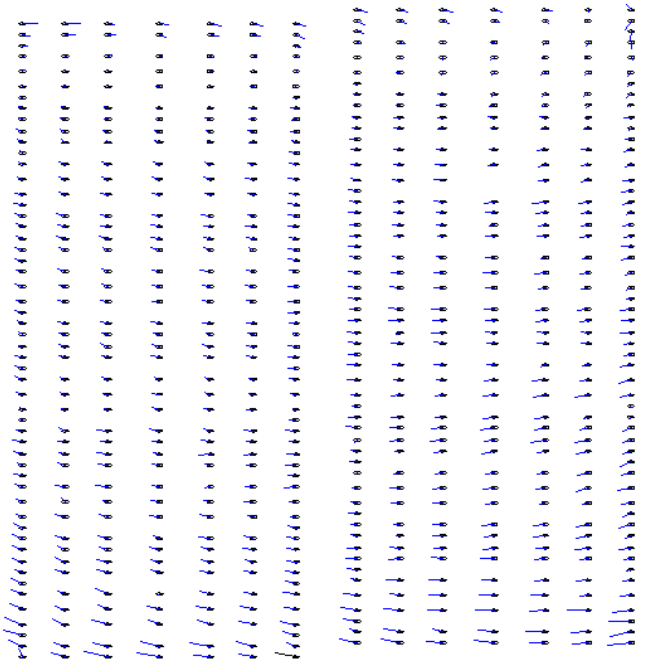

(b) TPC2 RP1

Figure B.2: Magnetic field distortions for TPC 2 data

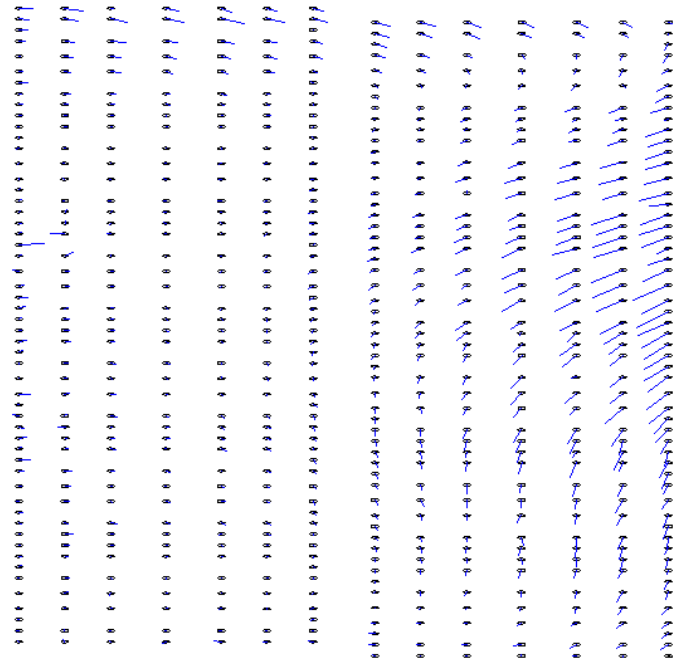

(a) TPC3 RP0

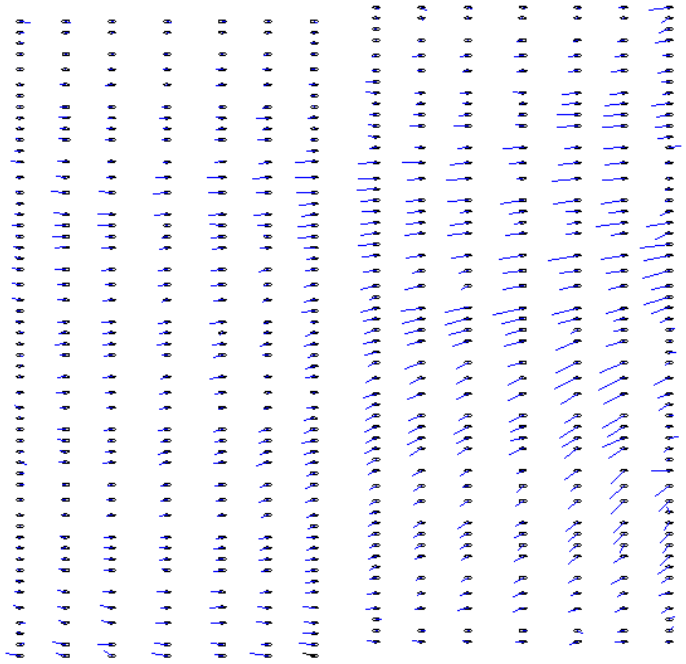

(b) TPC3 RP1

Figure B.3: Magnetic field distortions for TPC 3 data

Appendix C

Pull distributions

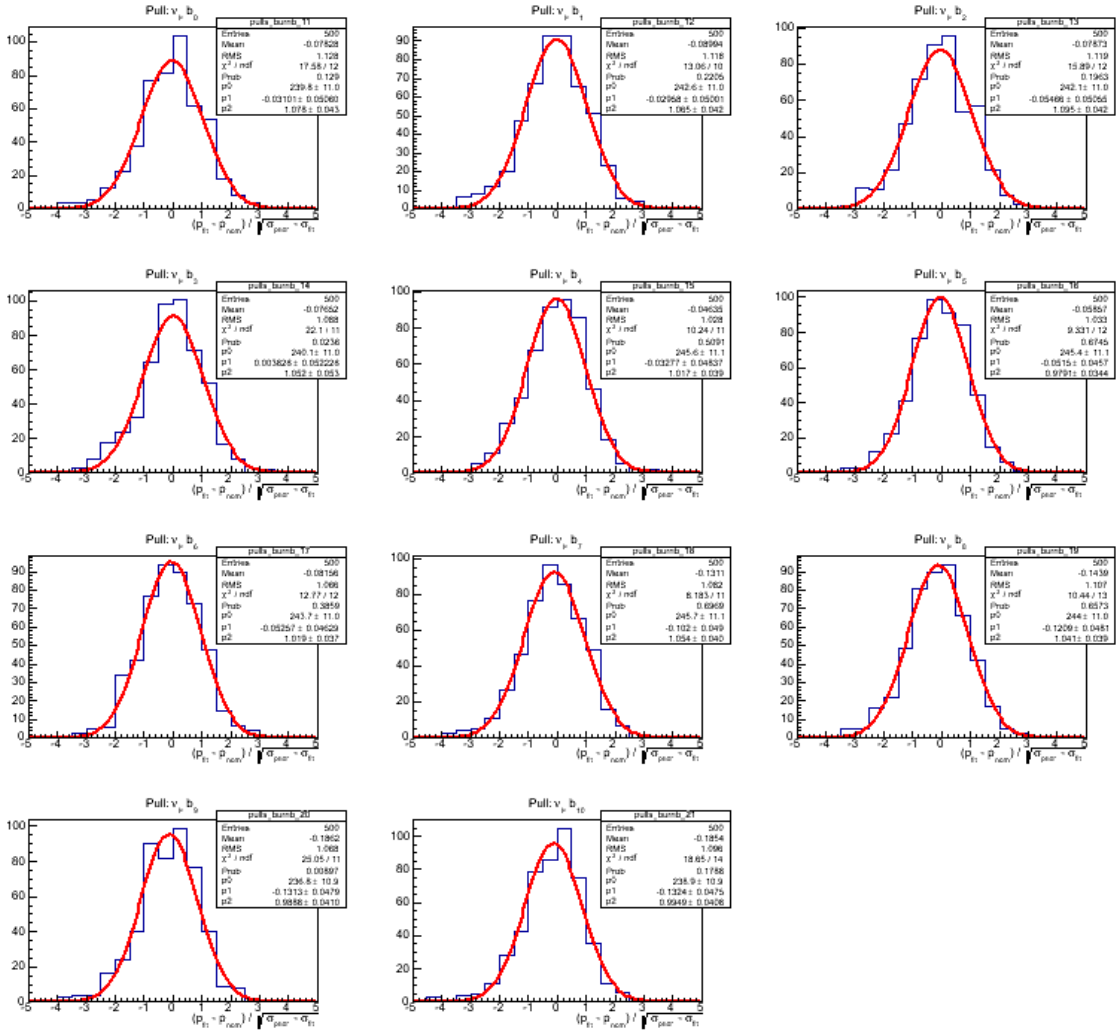

Figure C.1: Pull distributions for the SK ν_μ flux parameters. For ND280 fit only.

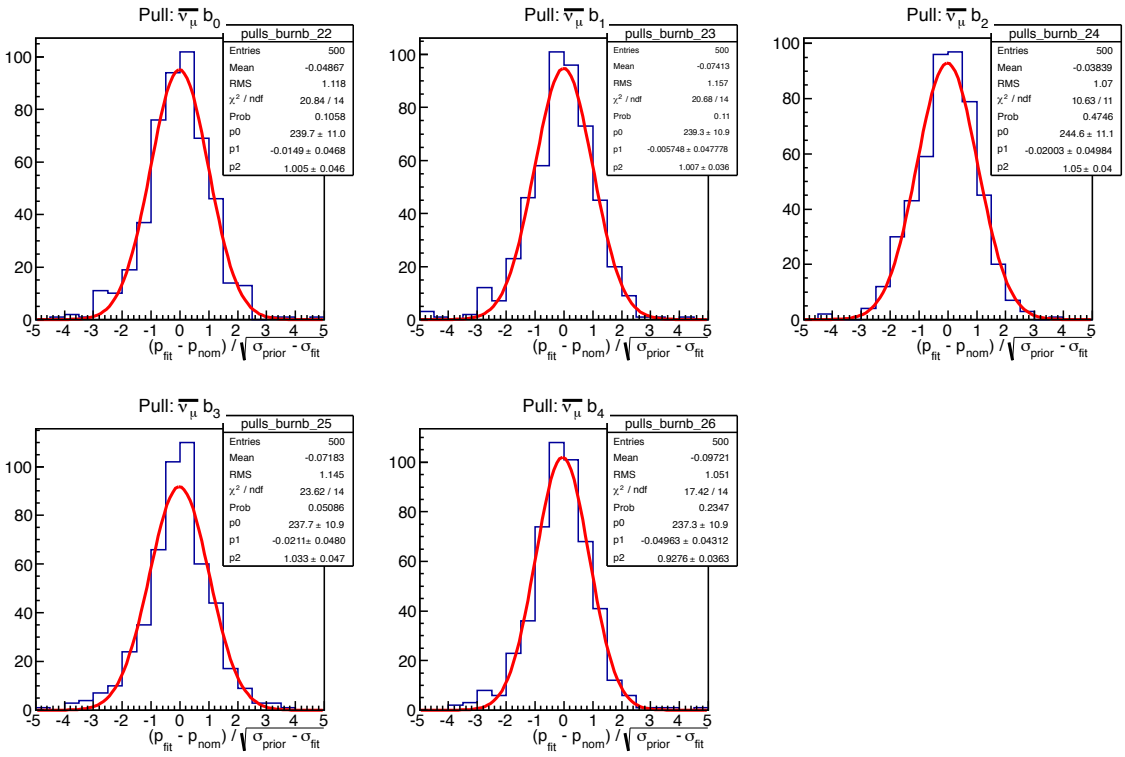

Figure C.2: Pull distributions for the SK $\bar{\nu_\mu}$ flux parameters. For ND280 fit only.

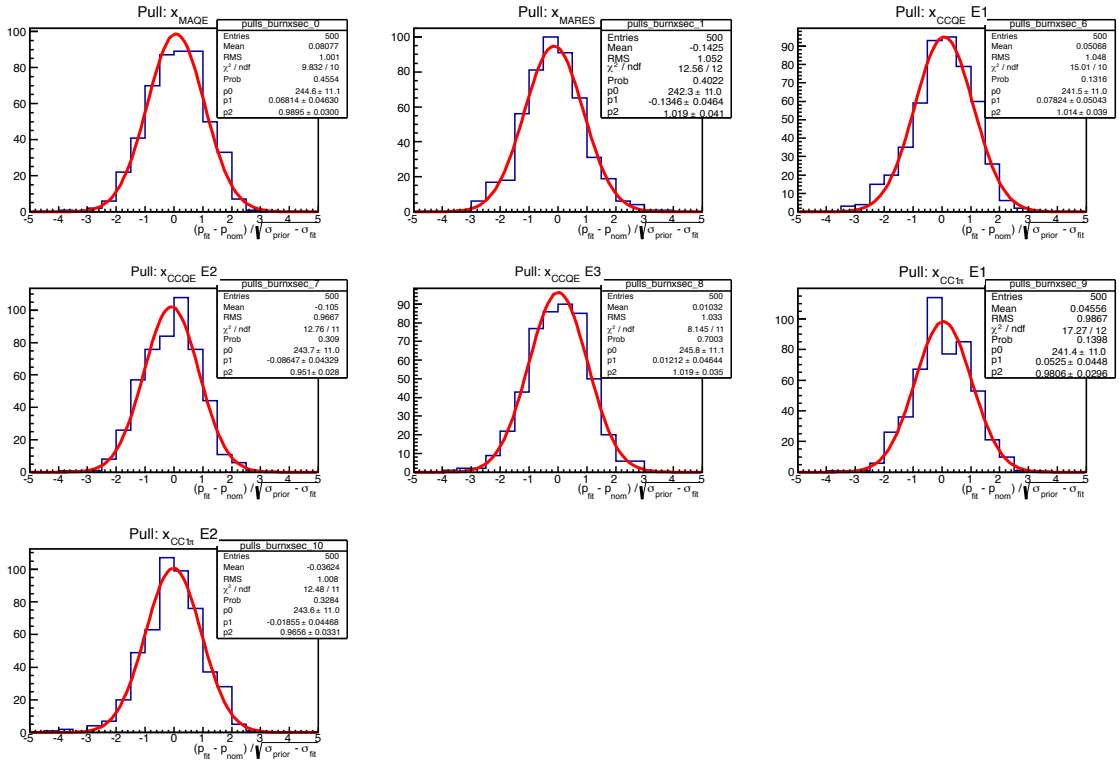

Figure C.3: Pull distribution for cross section parameters that are shared with SK in the ND280+SK fits. For ND280 fit only.

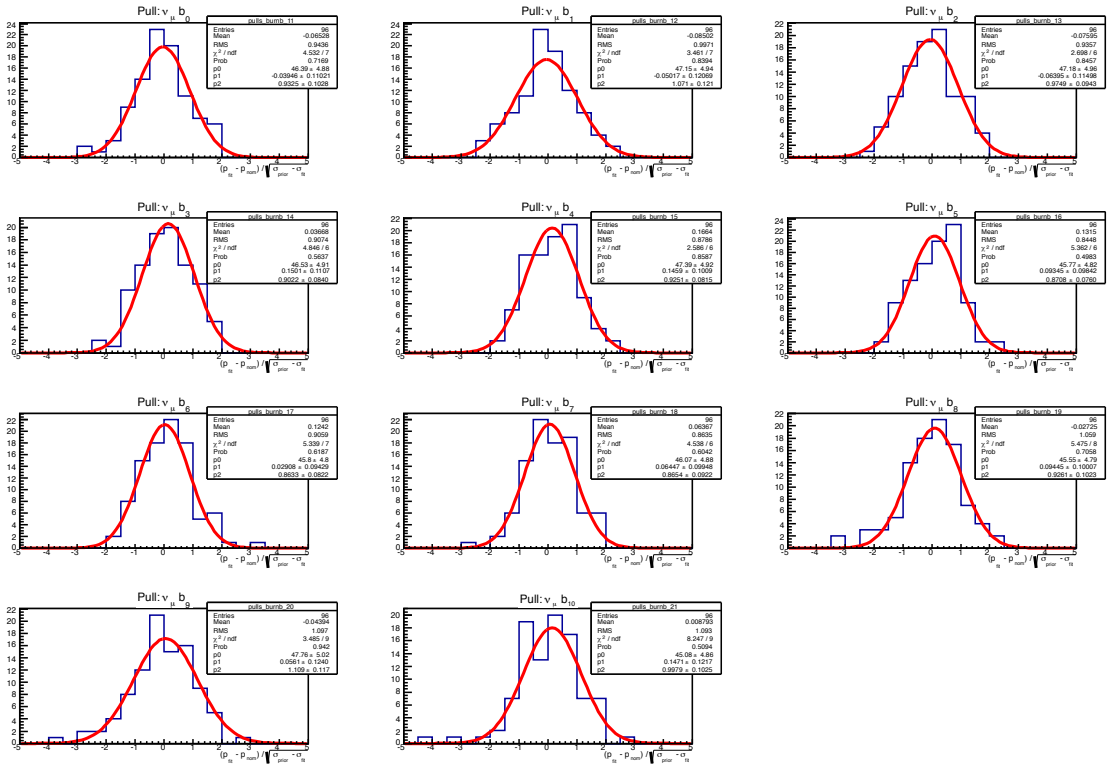

Figure C.4: Pull distribution for the SK ν_μ flux parameters. For ND280 and SK simultaneous fit.

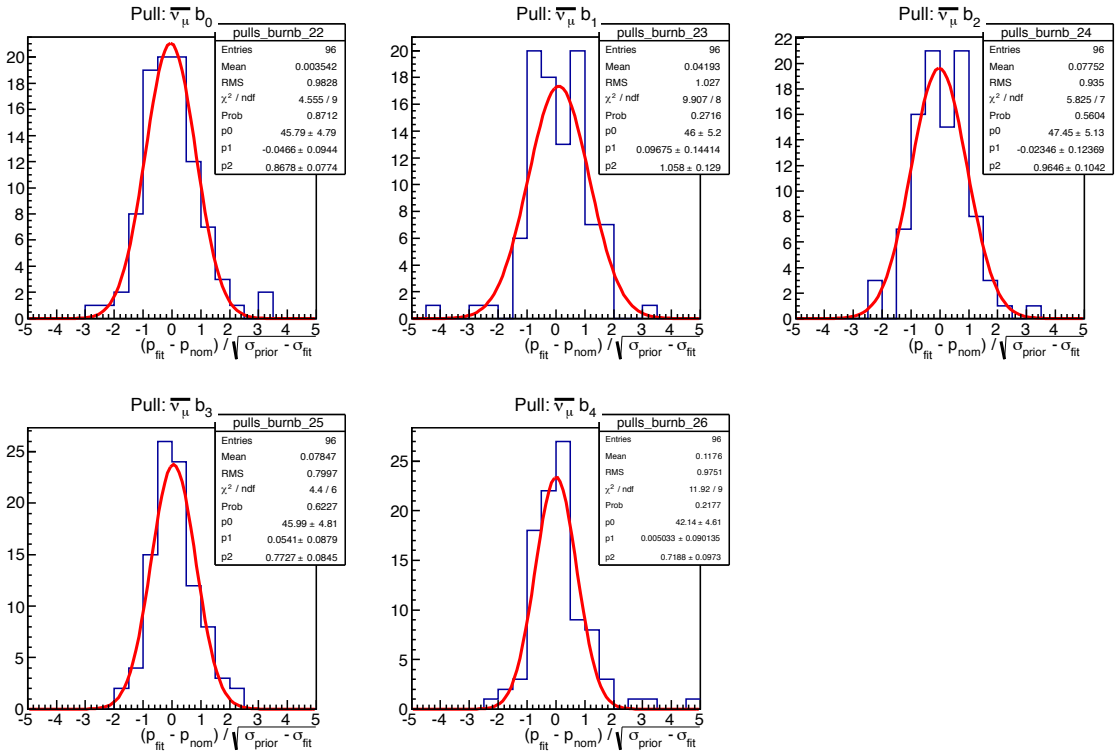

Figure C.5: Pull distribution for the SK $\bar{\nu_\mu}$ flux parameters. For ND280 and SK simultaneous fit.

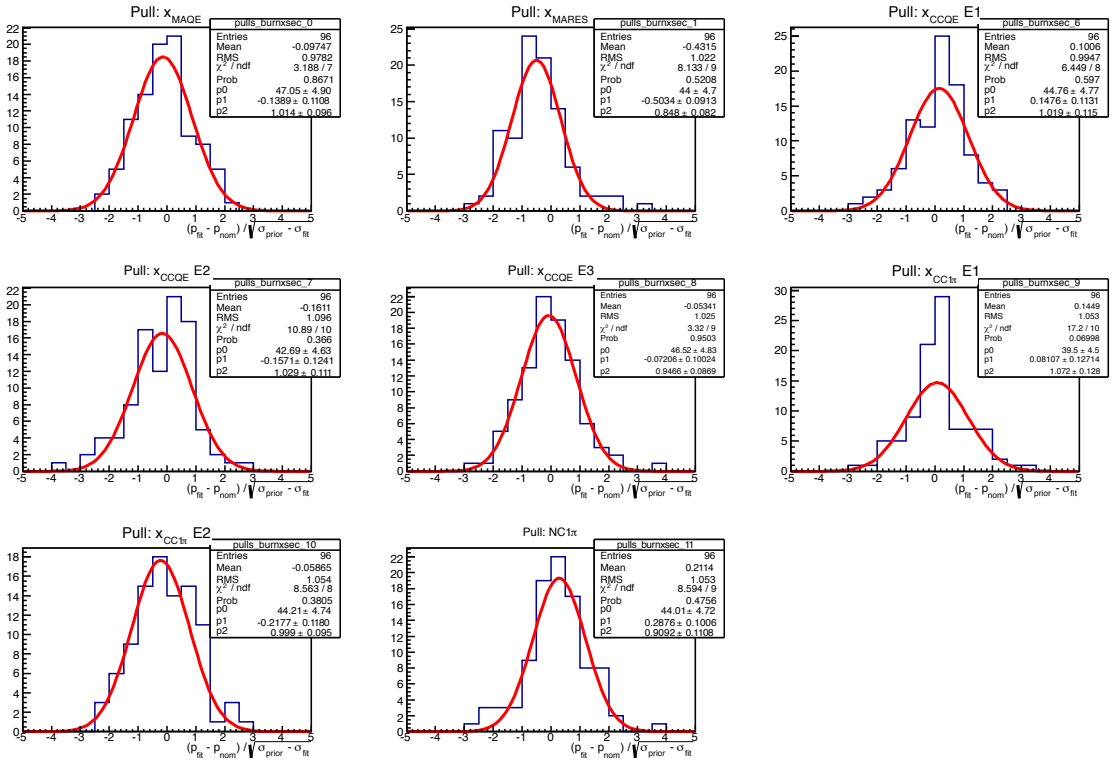

Figure C.6: Pull distribution for cross section parameters that are shared with between ND280 and SK. For ND280 and SK simultaneous fit.

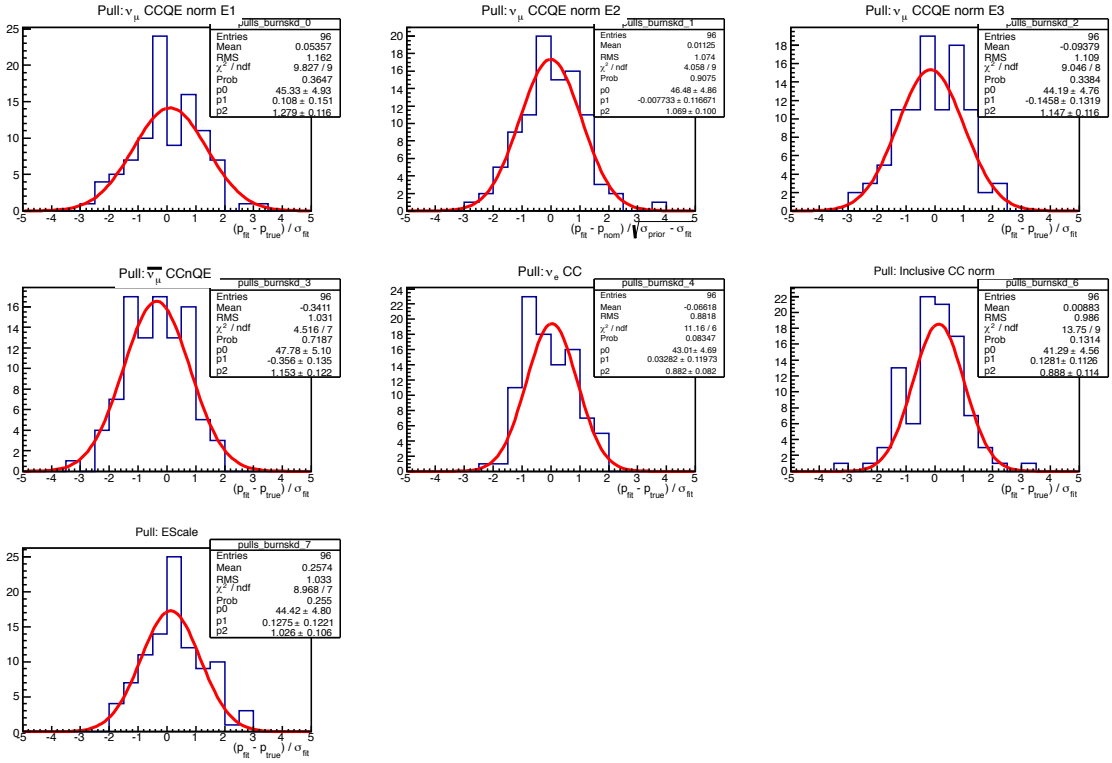

Figure C.7: Pull distribution SK detector parameters.

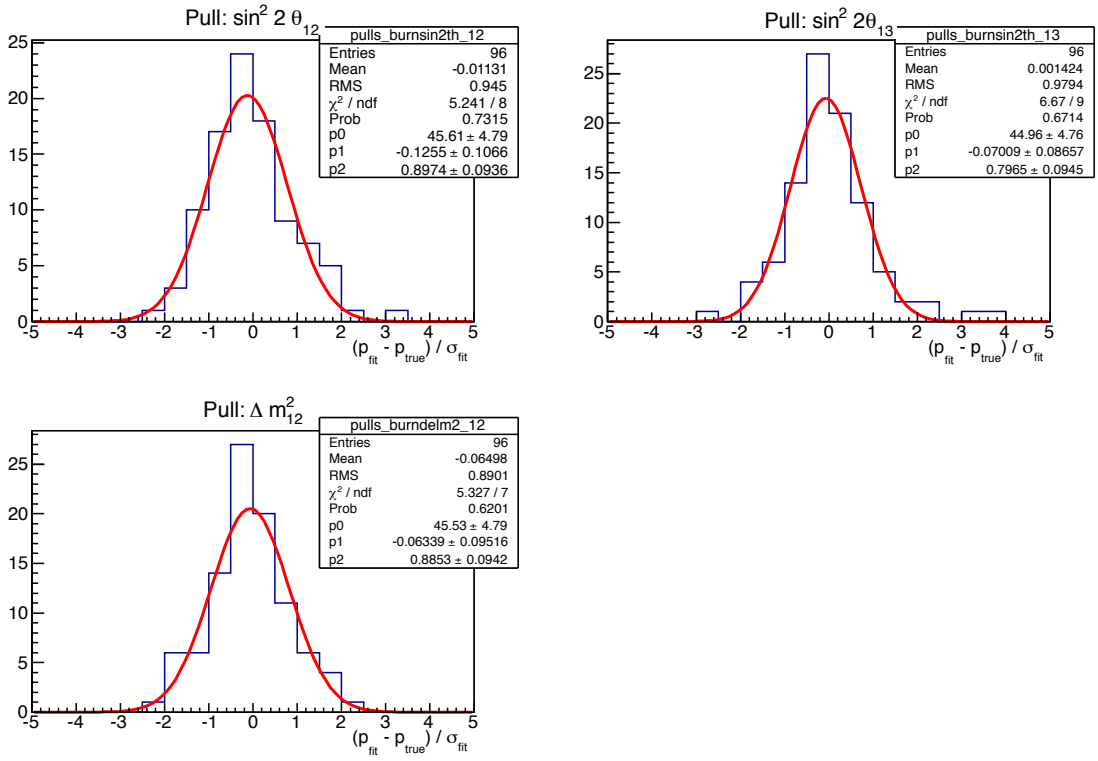

Figure C.8: Pull distribution oscillation parameters that are not of interest in the fit.

Appendix D

Changes to SK Spectrum Systematic Parameter Variations

Studies were done checking variations in the SK spectrum and the total number of events at SK due to variations in the systematic parameters. The oscillation parameters used are the same as in Table 5.3. The values for the cross section parameters are outlined in Table 5.7 giving slightly different number of events as shown in Figs 5.2, 5.3. The nominal number of events in the study is 64.46. Tables D.1, D.2, D.3 give the change in the total number of events and % change with respect to the nominal for flux, cross section and SK detector parameters respectively. Figs D.1 - D.41 shows the change in the E_{rec} spectrum for $\pm 3\sigma, \pm 1\sigma$ variations of the systematic parameters. It should be noted that for M_A^{QE} (Fig D.17) the -3σ variation and SK detector NC normalization (Fig D.39) the -1σ variation result in the parameters going to a negative value so the parameters are forced to a value of 0.0.

Parameter	+1 σ N event	% change	-1 σ N event	% change
ν_μ 0	64.98	0.008	63.94	-0.008
ν_μ 1	64.89	0.007	64.04	-0.007
ν_μ 2	64.54	0.001	64.39	-0.001
ν_μ 3	64.65	0.003	64.28	-0.003
ν_μ 4	65.99	0.024	62.94	-0.024
ν_μ 5	65.69	0.019	63.23	-0.019
ν_μ 6	65.60	0.018	63.32	-0.018
ν_μ 7	65.11	0.010	63.82	-0.010
ν_μ 8	65.30	0.013	63.62	-0.013
ν_μ 9	64.88	0.006	64.04	-0.006
ν_μ 10	64.57	0.002	64.35	-0.002
$\bar{\nu_\mu}$ 0	64.48	0.000	64.44	-0.000
$\bar{\nu_\mu}$ 1	64.49	0.000	64.43	-0.000
$\bar{\nu_\mu}$ 2	64.57	0.002	64.36	-0.002
$\bar{\nu_\mu}$ 3	64.64	0.003	64.29	-0.003
$\bar{\nu_\mu}$ 4	64.62	0.002	64.30	-0.002

Table D.1: Change in the number of events at SK for $\pm 1\sigma$ variations for SK ν_μ and $\bar{\nu_\mu}$ flux parameters.

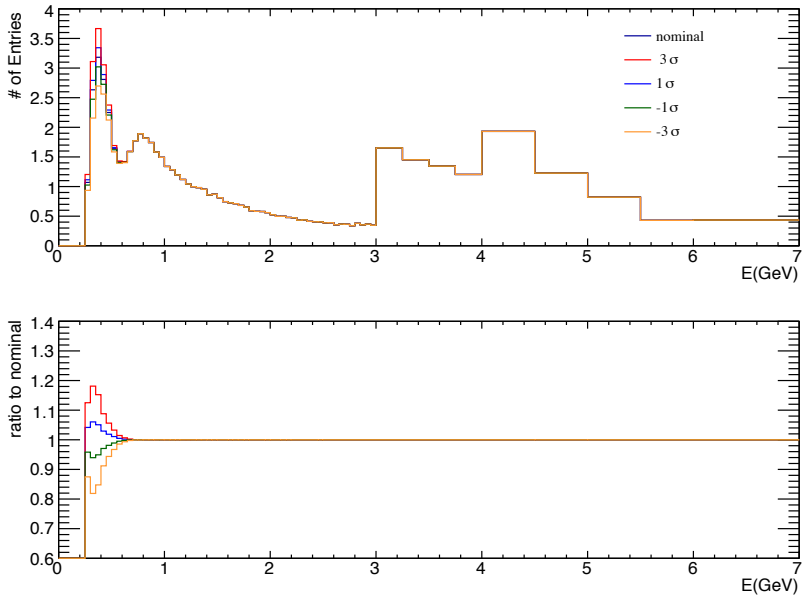

Figure D.1: Effect of SK ν_μ 0

Parameter	+1 σ N event	% change	-1 σ N event	% change
M_A^{QE}	76.13	0.181	49.82	-0.227
M_A^{RES}	68.84	0.068	60.18	-0.066
CCQE E1	67.16	0.042	61.76	-0.042
CCQE E2	66.98	0.039	61.94	-0.039
CCQE E3	65.23	0.012	63.69	-0.012
CC1π E1	67.63	0.049	61.29	-0.049
CC1π E2	67.97	0.054	60.95	-0.054
NC1π	65.19	0.011	63.74	-0.011
CC oth shp	64.96	0.008	63.96	-0.008
SF	64.02	-0.007	64.91	0.007
E_B	64.36	-0.002	64.67	0.003
p_F	64.57	0.002	64.44	-0.000
W shape	64.73	0.004	64.15	-0.005
πless Δ decay	68.53	0.063	60.39	-0.063
CC coh norm	65.00	0.008	63.93	-0.008
NC oth norm	65.00	0.008	63.93	-0.008
$\nu/\bar{\nu}$ norm	66.02	0.024	62.90	-0.024

Table D.2: Change in the number of events at SK for $\pm 1\sigma$ variations for cross section parameters.

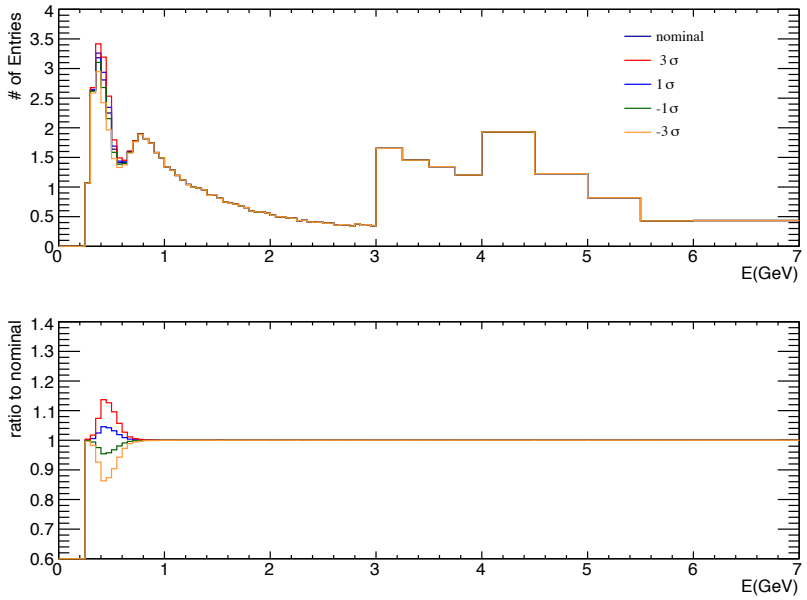

Figure D.2: Effect of SK ν_μ 1

Parameter	+1 σ N event	% change	-1 σ N event	% change
$\nu_\mu, \bar{\nu_\mu}$CCQE norm shape1 $0.0 < E_{rec} < 0.4$ GeV	64.53	0.001	64.40	-0.001
$\nu_\mu, \bar{\nu_\mu}$CCQE norm shape2 $0.4 < E_{rec} < 1.1$ GeV	65.00	0.008	63.92	-0.008
$\nu_\mu, \bar{\nu_\mu}$CCQE norm shape3 $E_{rec} > 1.1$ GeV	65.97	0.023	62.95	-0.023
$\nu_\mu, \bar{\nu_\mu}$ CCnQE norm	69.88	0.084	59.04	-0.084
$\nu_e, \bar{\nu_e}$ CCnQE norm	64.61	0.002	64.31	-0.002
NC norm	68.82	0.068	60.55	-0.061
CC norm	65.55	0.017	63.37	-0.017
Energy scale	64.46	-0.000	64.46	-0.000

Table D.3: Change in the number of events at SK for $\pm 1\sigma$ variations for SK detector parameters.

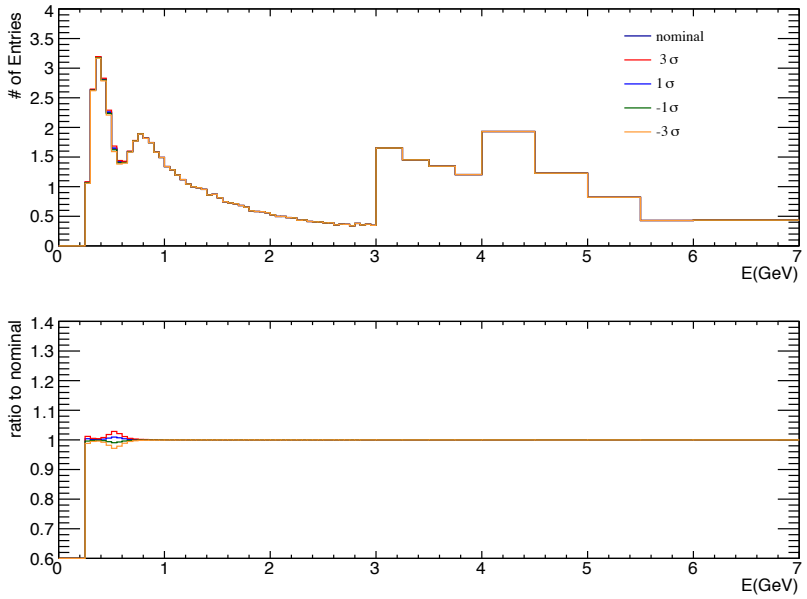

Figure D.3: Effect of SK ν_μ 2

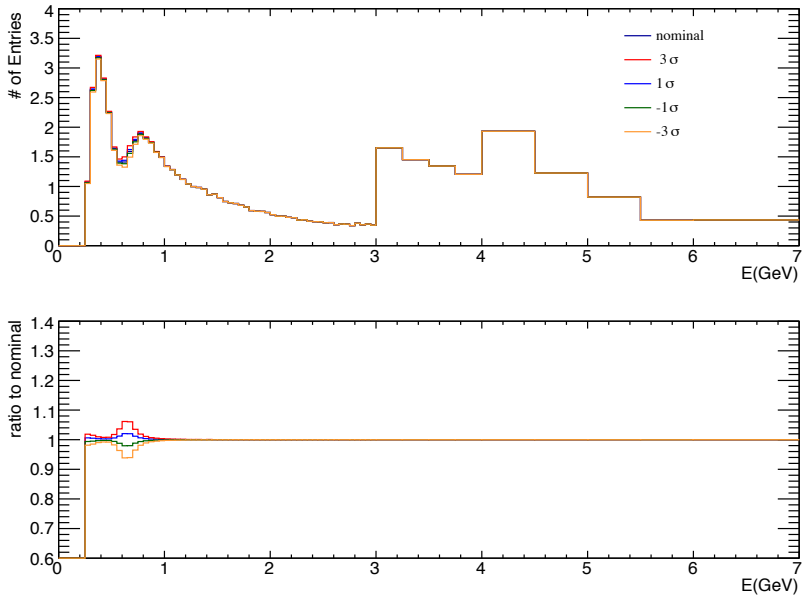

Figure D.4: Effect of SK ν_μ 3

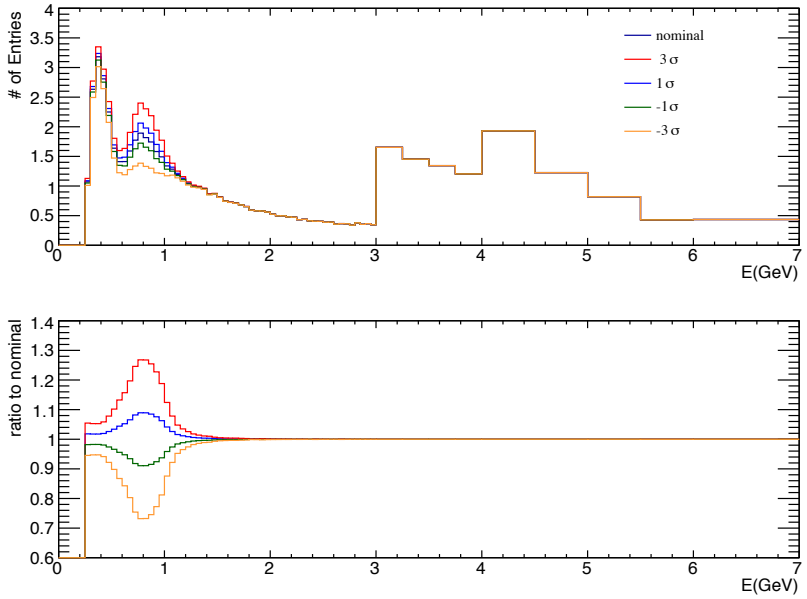

Figure D.5: Effect of SK ν_μ 4

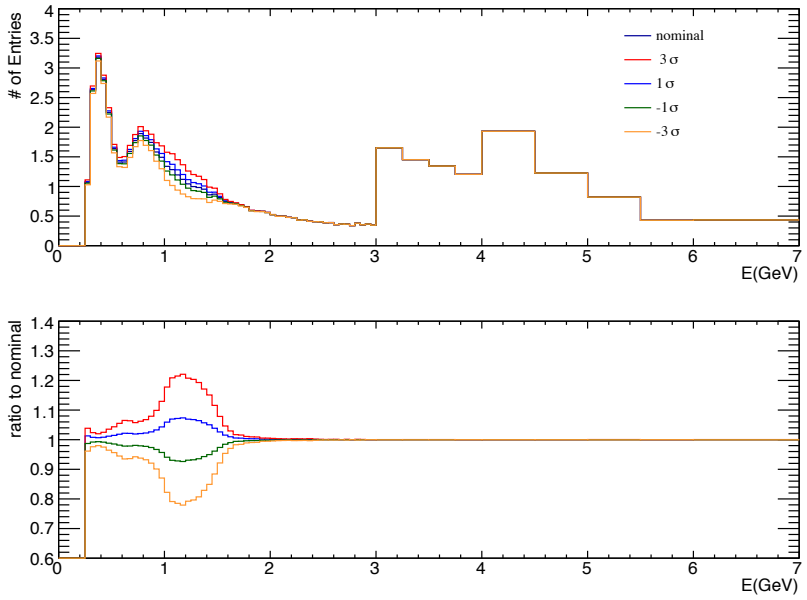

Figure D.6: Effect of SK ν_μ 5

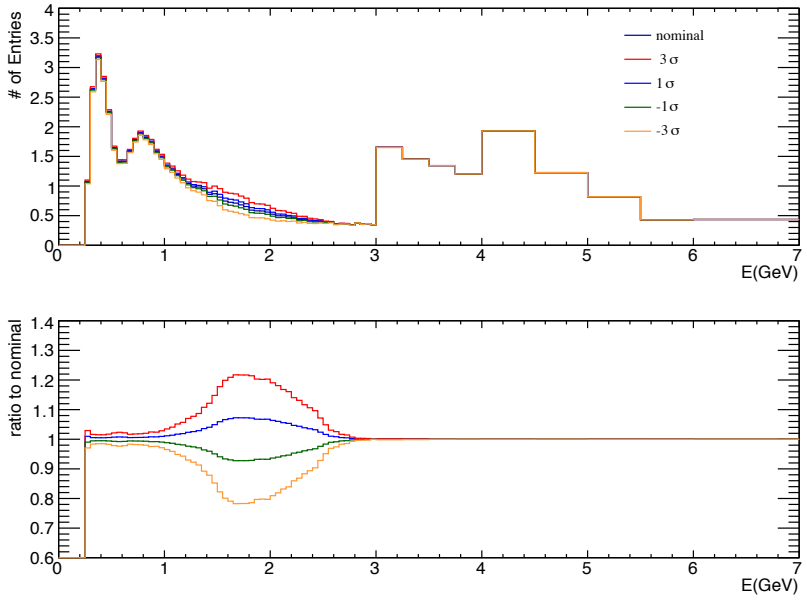

Figure D.7: Effect of SK ν_μ 6

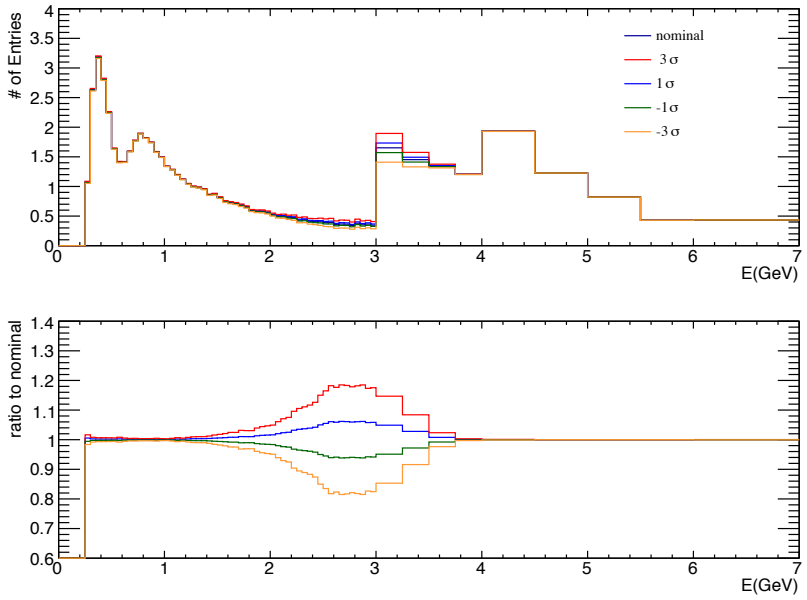

Figure D.8: Effect of SK ν_μ 7

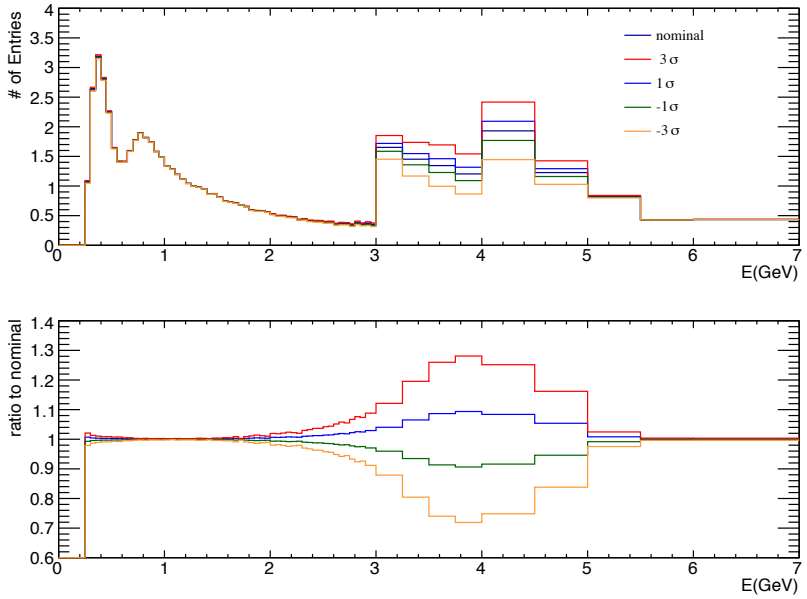

Figure D.9: Effect of SK ν_μ 8

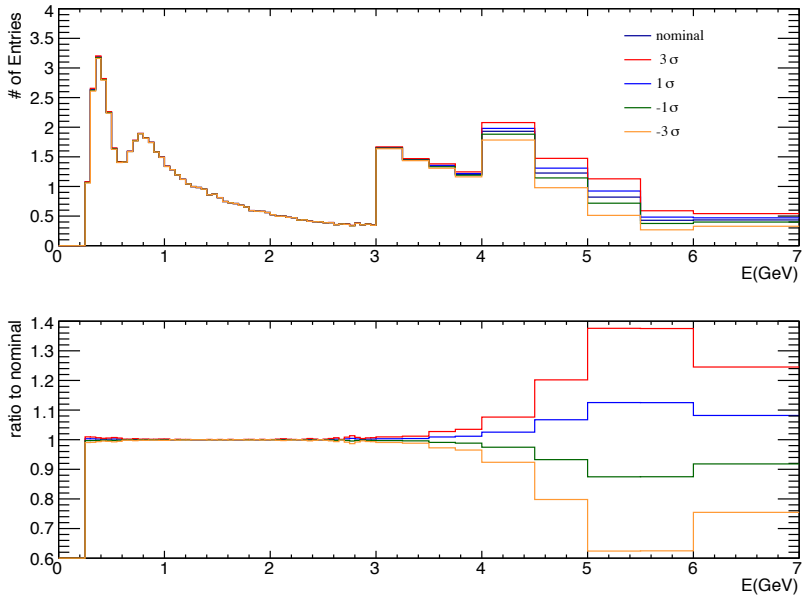

Figure D.10: Effect of SK ν_μ 9

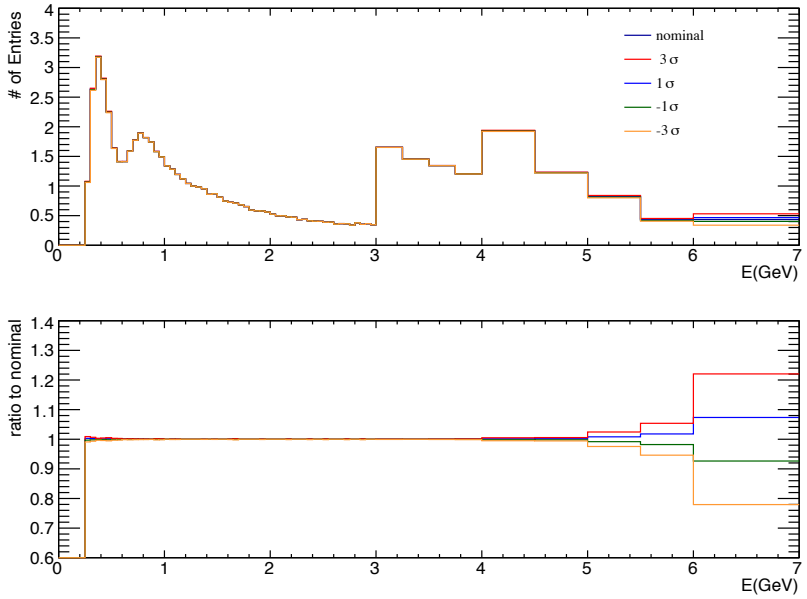

Figure D.11: Effect of SK ν_μ 10

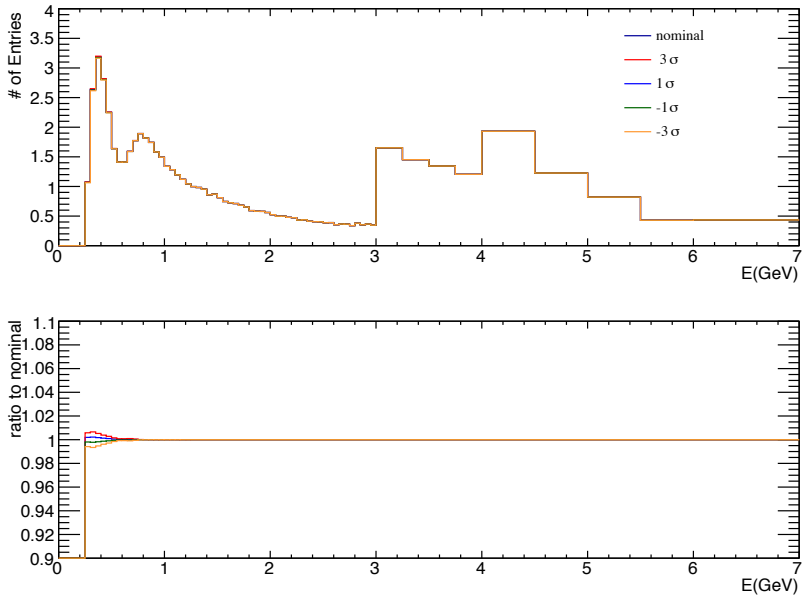

Figure D.12: Effect of SK $\bar{\nu_\mu}$ 0

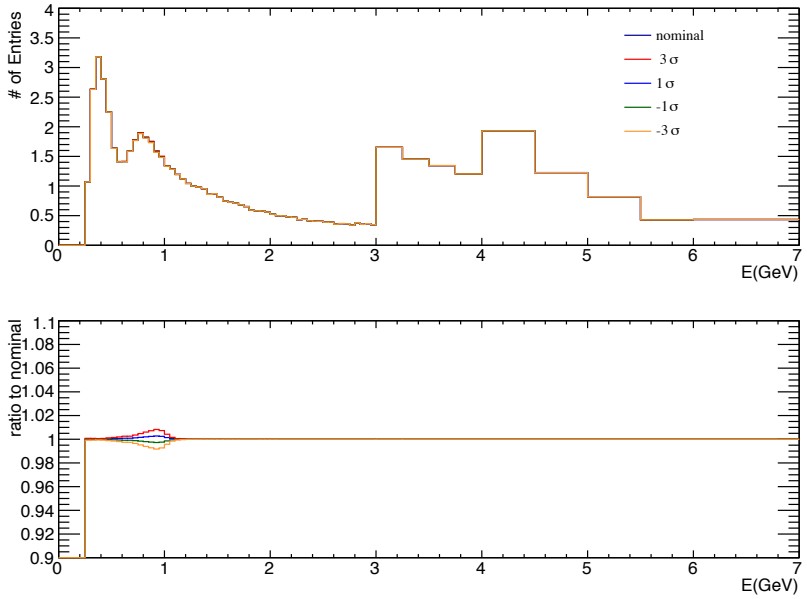

Figure D.13: Effect of SK $\bar{\nu_\mu}$ 1

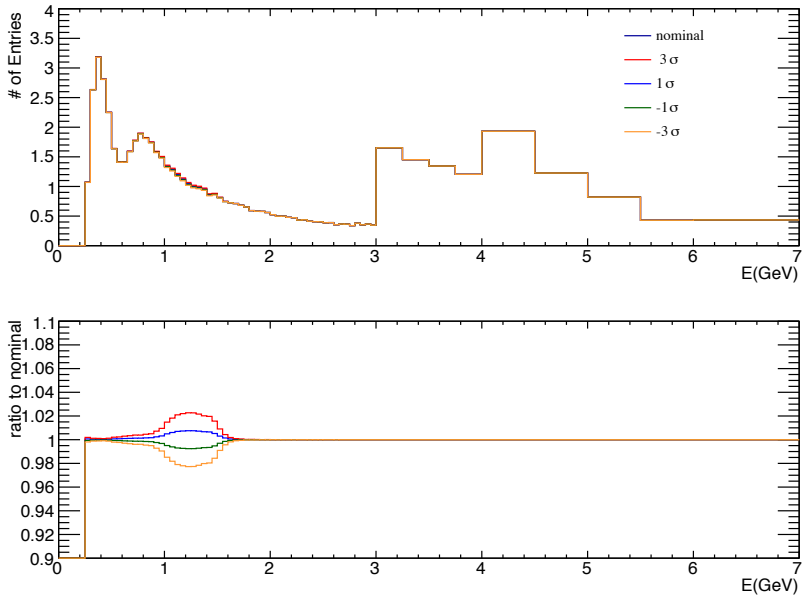

Figure D.14: Effect of SK $\bar{\nu_\mu}$ 2

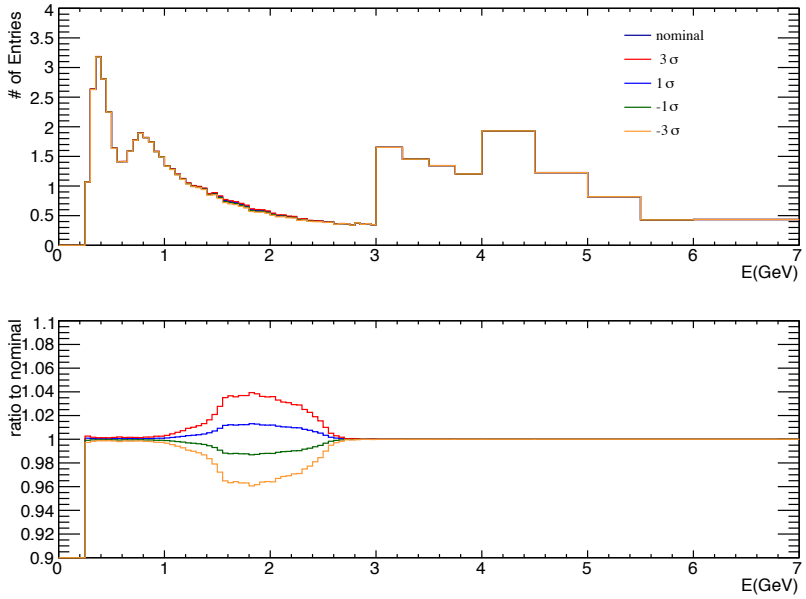

Figure D.15: Effect of SK $\bar{\nu_\mu}$ 3

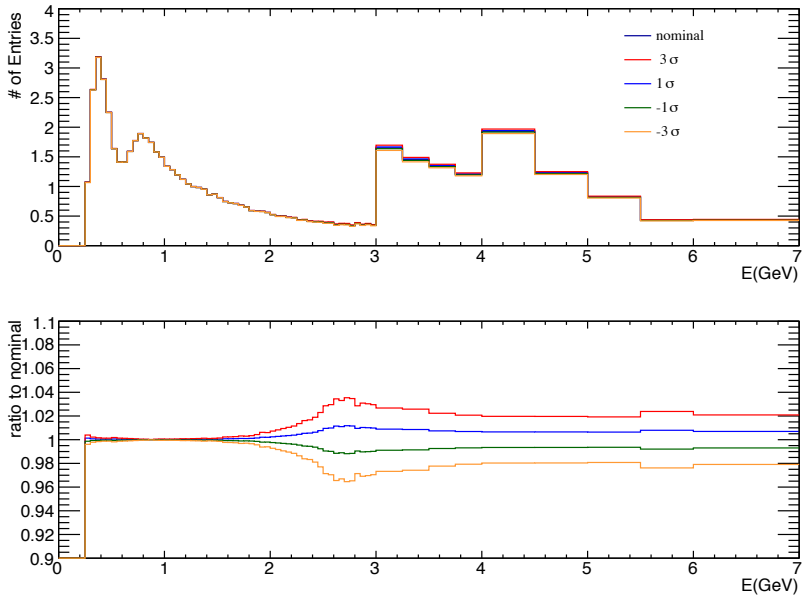

Figure D.16: Effect of SK $\bar{\nu_\mu}$ 4

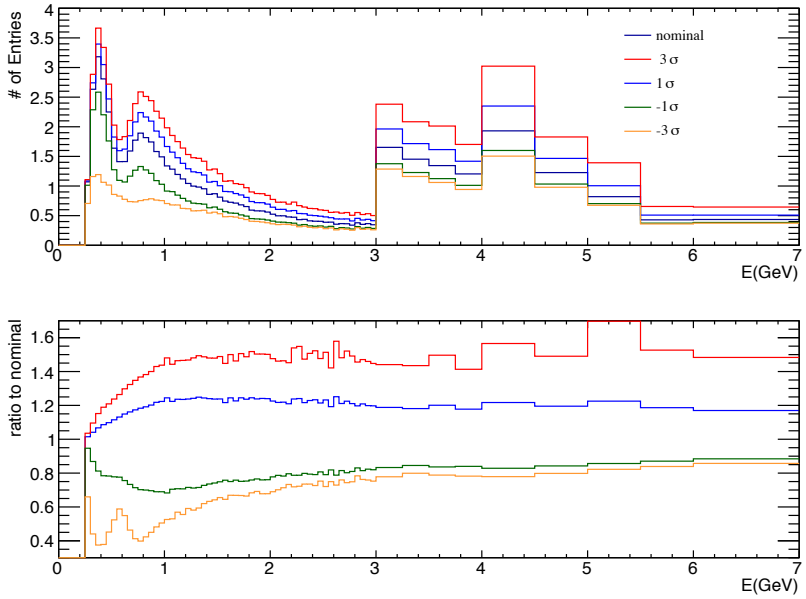

Figure D.17: Effect of M_A^{QE}

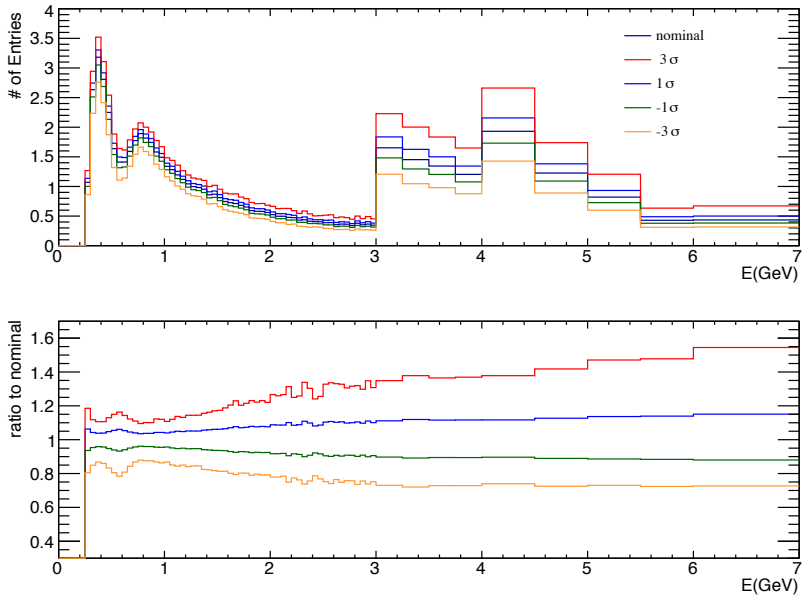

Figure D.18: Effect of M_A^{RES}

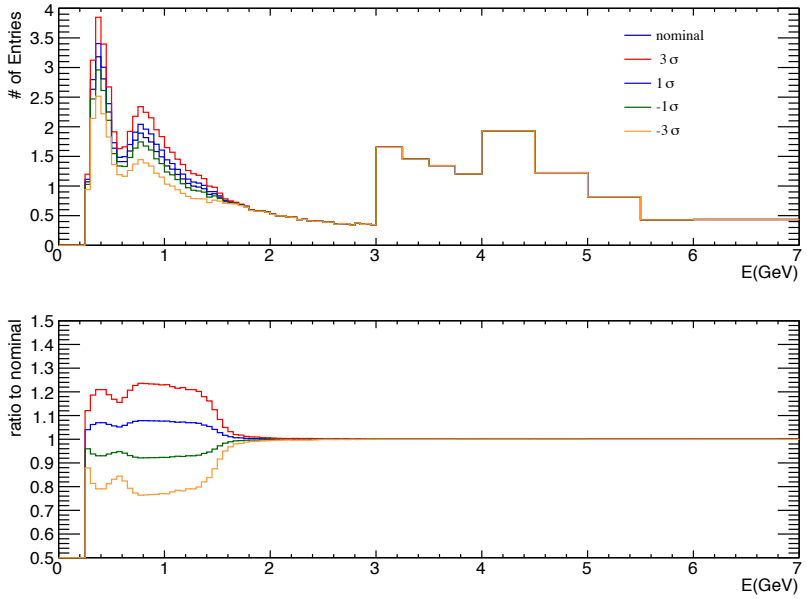

Figure D.19: Effect of CCQE E1

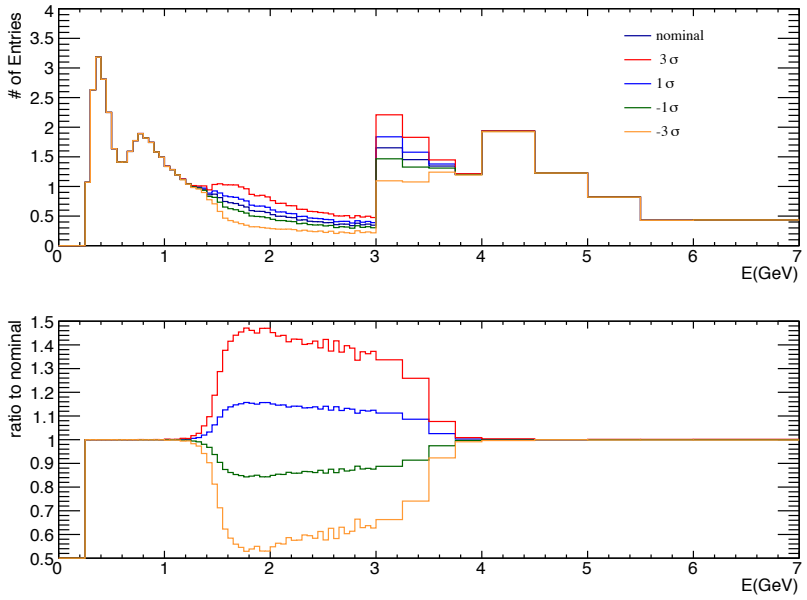

Figure D.20: Effect of CCQE E2

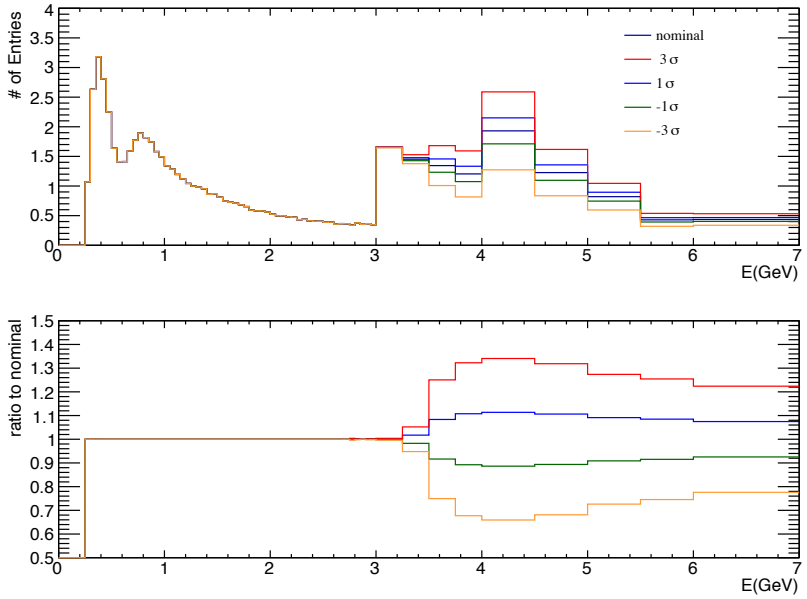

Figure D.21: Effect of CCQE E3

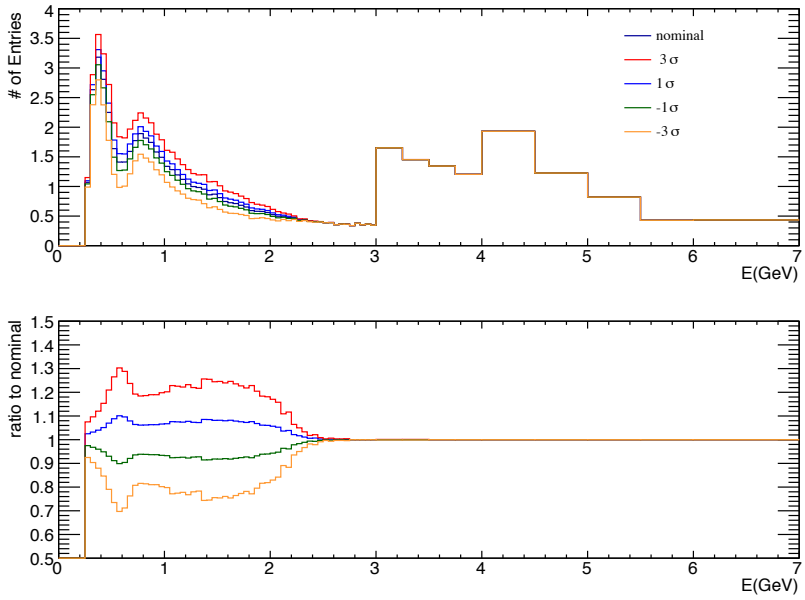

Figure D.22: Effect of CC1π E1

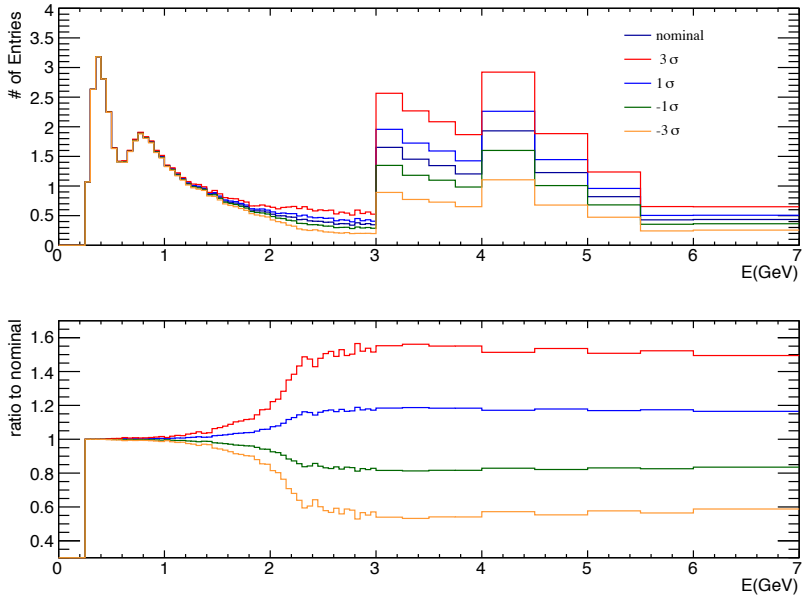

Figure D.23: Effect of CC1π E2

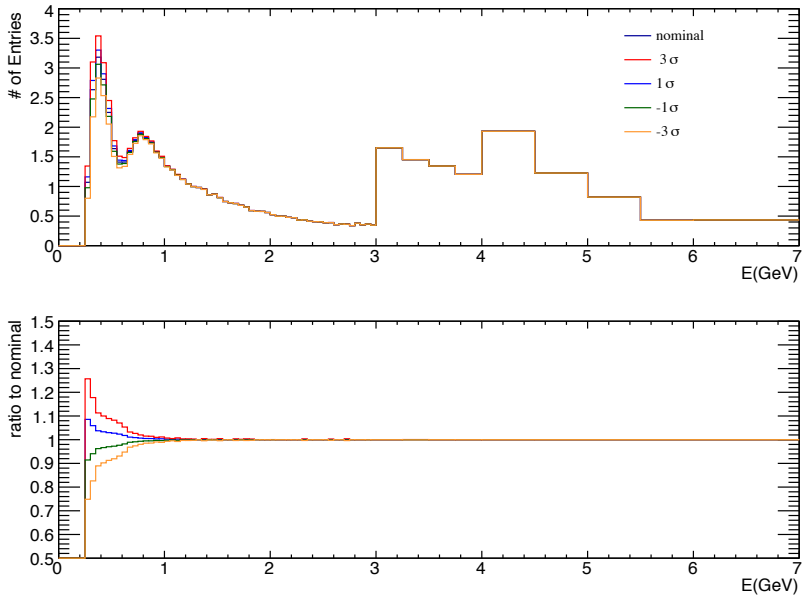

Figure D.24: Effect of NC 1π

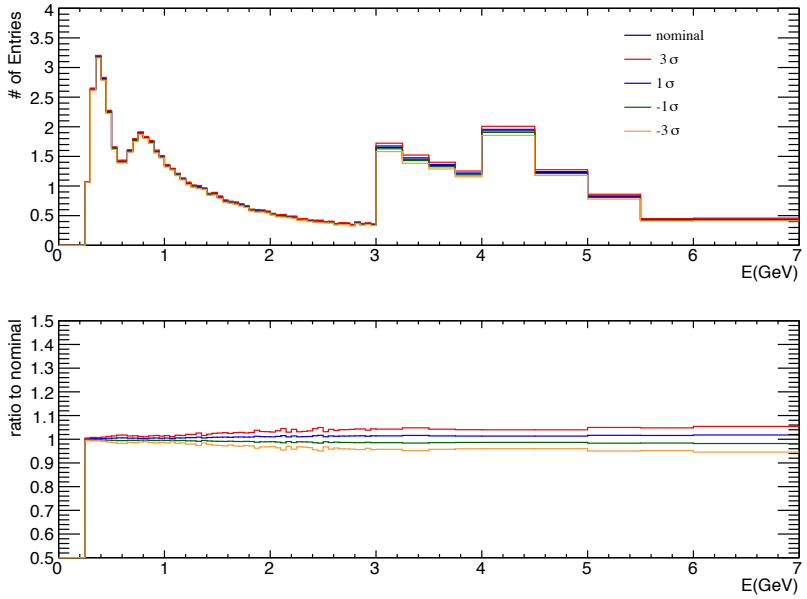

Figure D.25: Effect of CC other shape

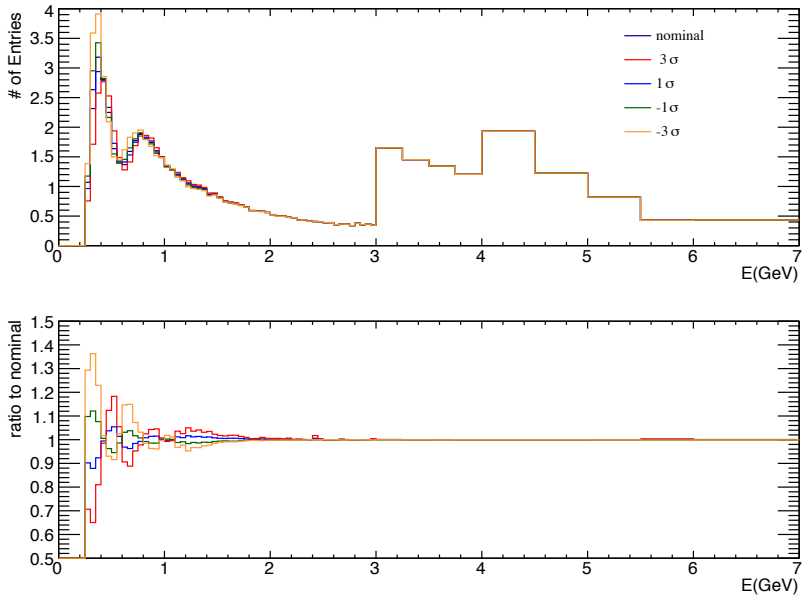

Figure D.26: Effect of SF

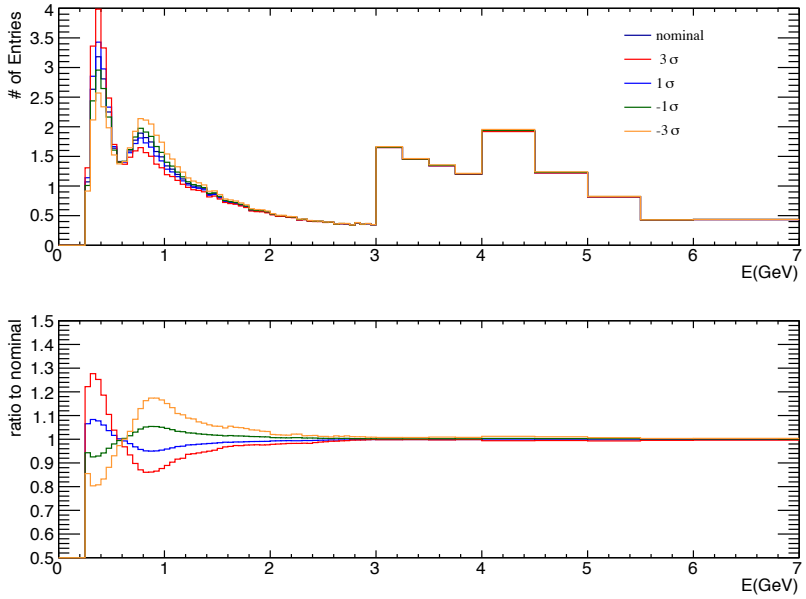

Figure D.27: Effect of p_F

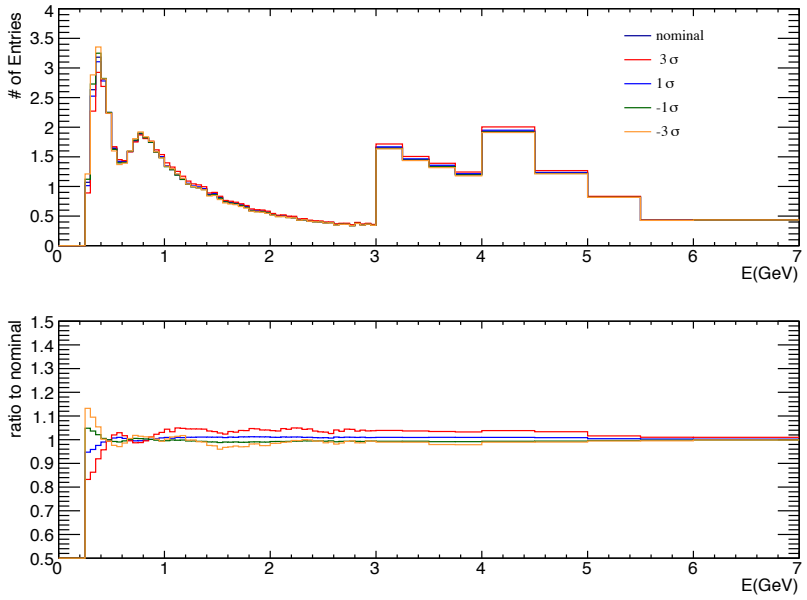

Figure D.28: Effect of E_B

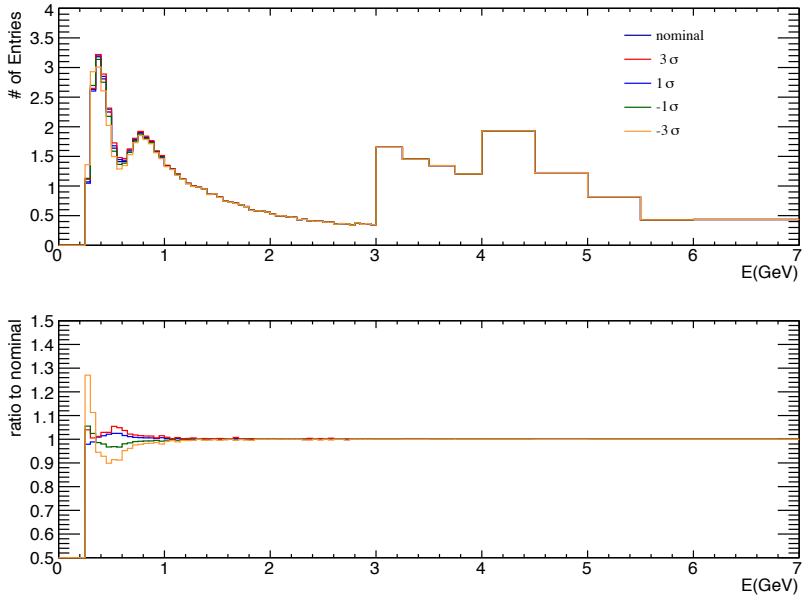

Figure D.29: Effect of W shape

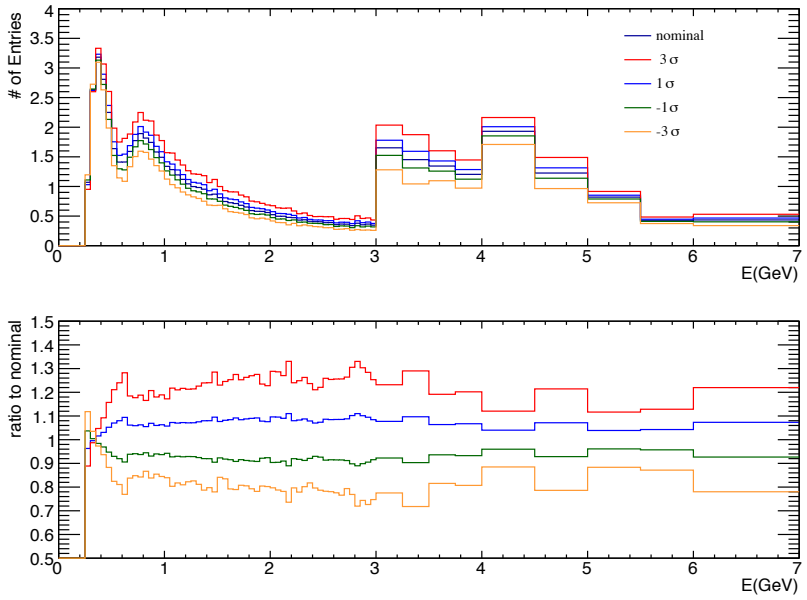

Figure D.30: Effect of π less Δ decay

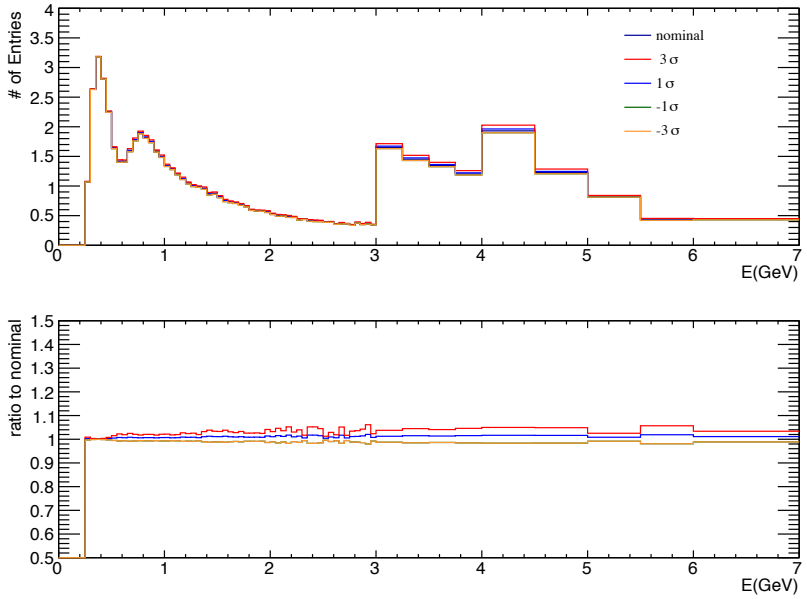

Figure D.31: Effect of CC coherent normalization

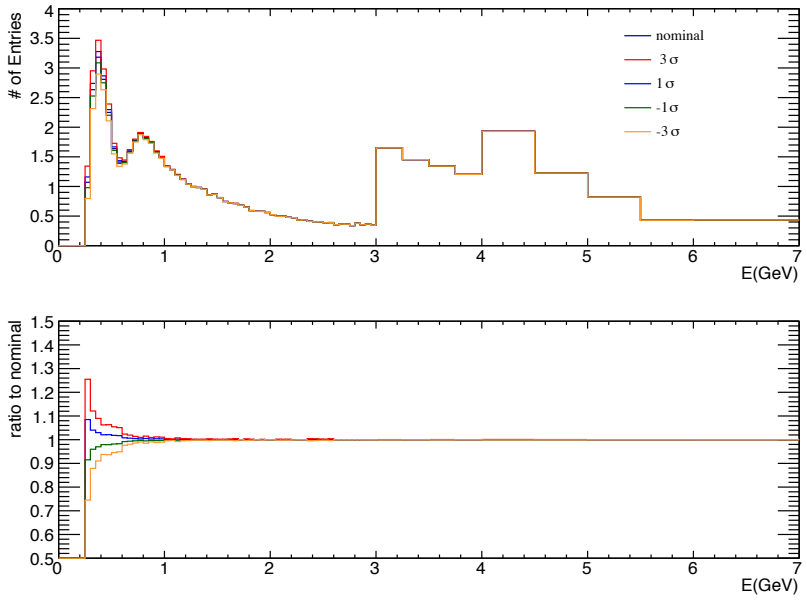

Figure D.32: Effect of NC other normalization

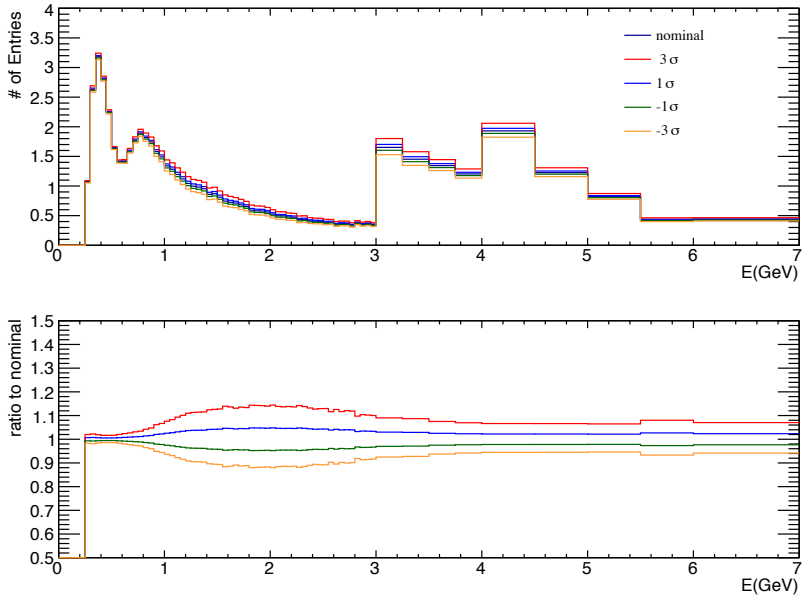

Figure D.33: Effect of $\nu/\bar{\nu}$ normalization

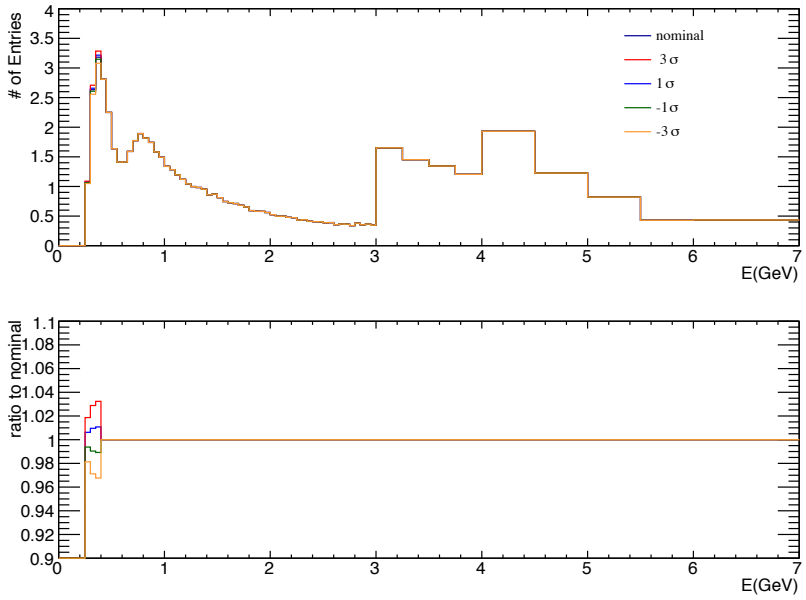

Figure D.34: Effect of $\nu_\mu, \bar{\nu_\mu}$ CCQE norm shape1 $0.0 < E_{rec} < 0.4$ GeV

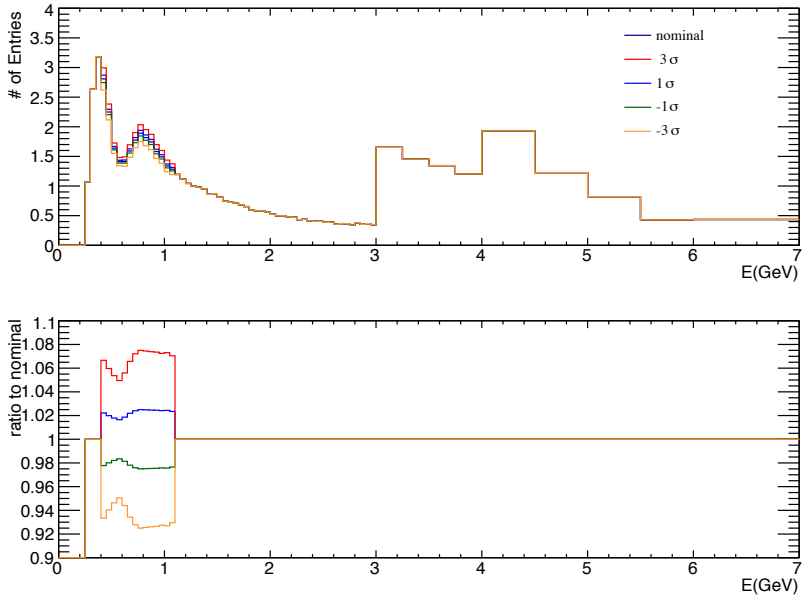

Figure D.35: Effect of $\nu_\mu, \bar{\nu_\mu}$ CCQE norm shape2 $0.4 < E_{rec} < 1.1$ GeV

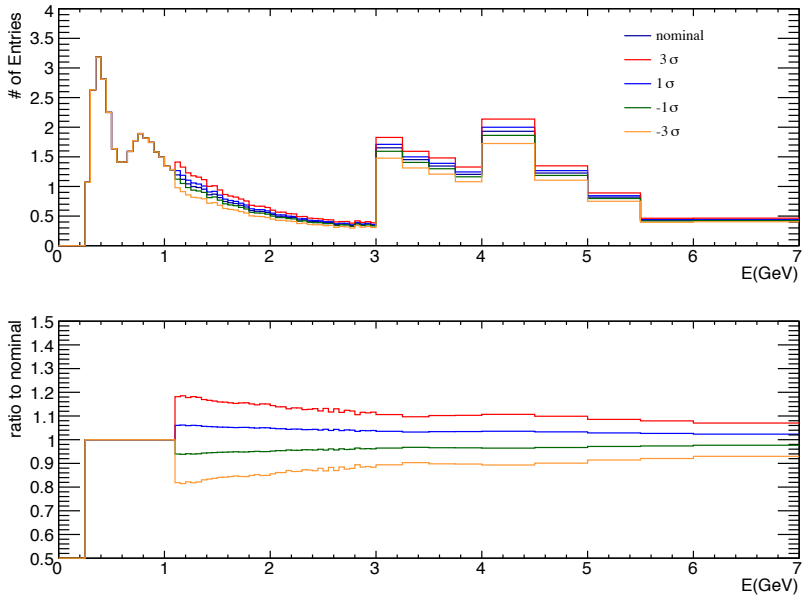

Figure D.36: Effect of $\nu_\mu, \bar{\nu_\mu}$ CCQE norm shape3 $E_{rec} > 1.1$ GeV

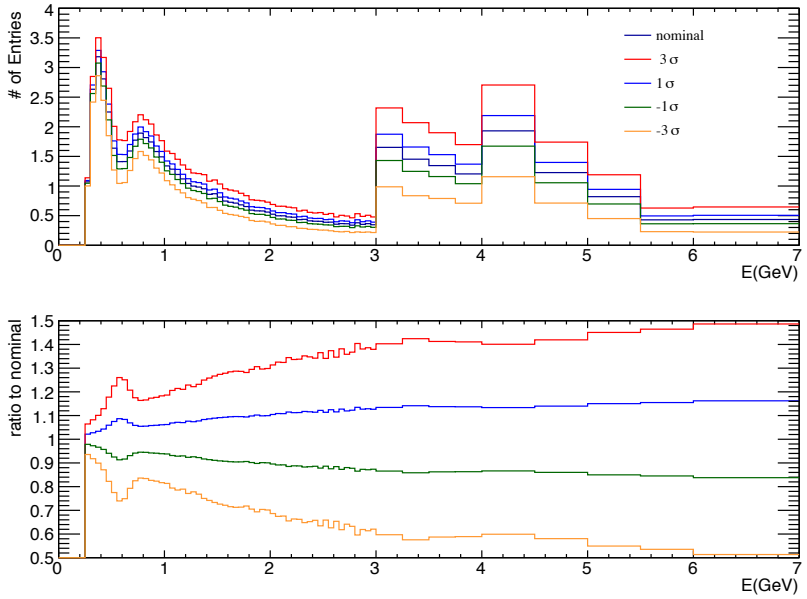

Figure D.37: Effect of $\nu_\mu, \bar{\nu_\mu}$ CCnQE norm

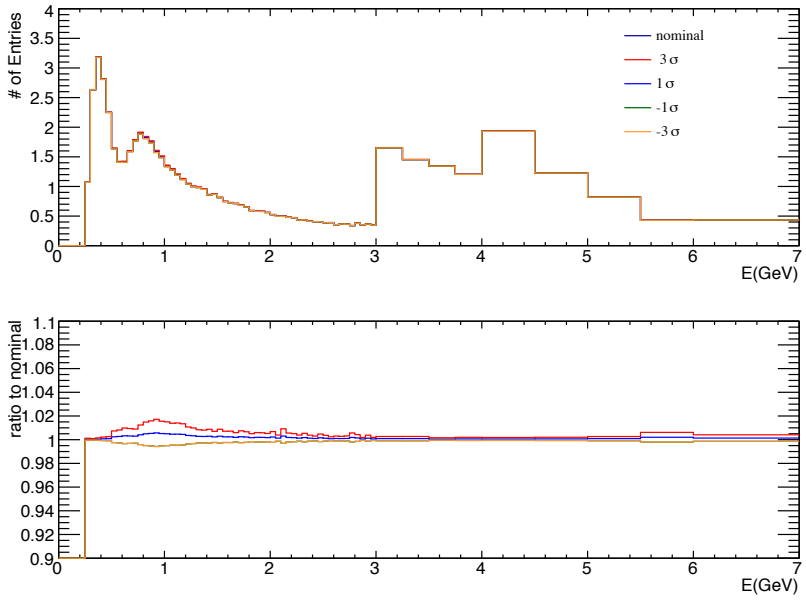

Figure D.38: Effect of $\nu_e, \bar{\nu_e}$ CCnQE norm

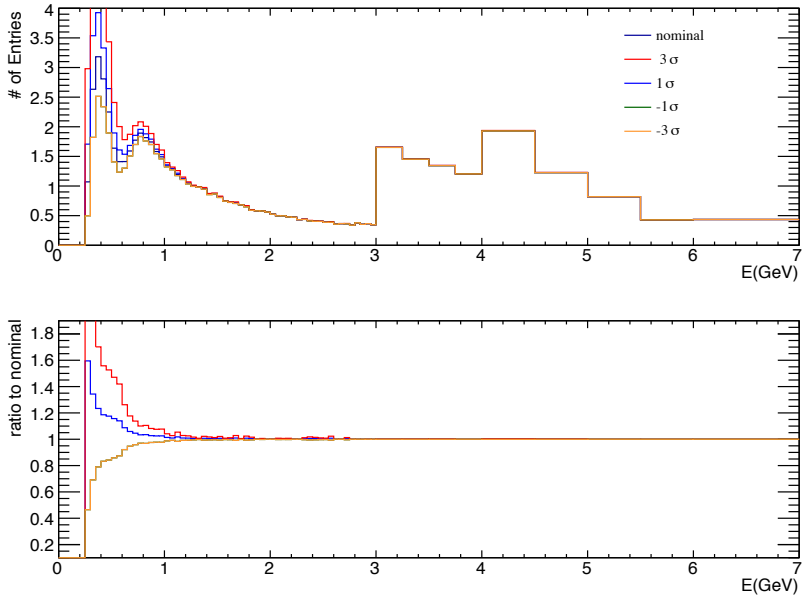

Figure D.39: Effect of NC norm

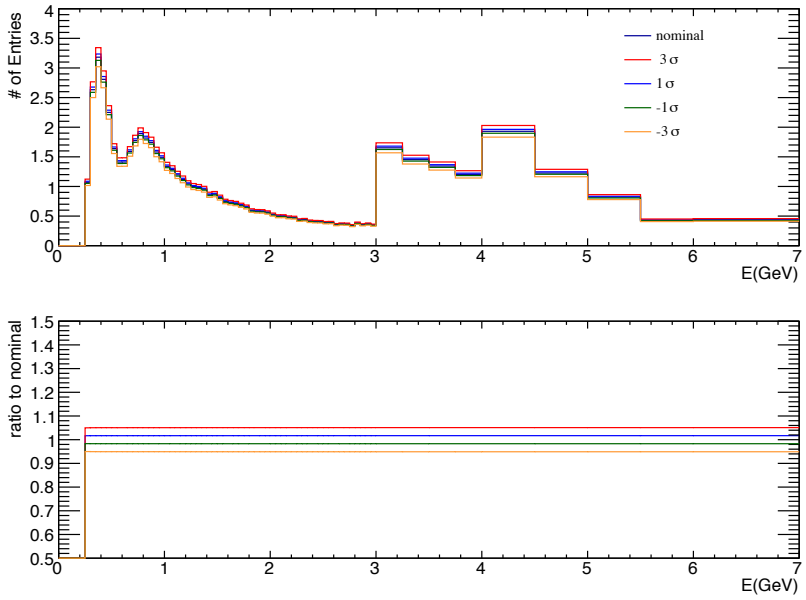

Figure D.40: Effect of CC norm

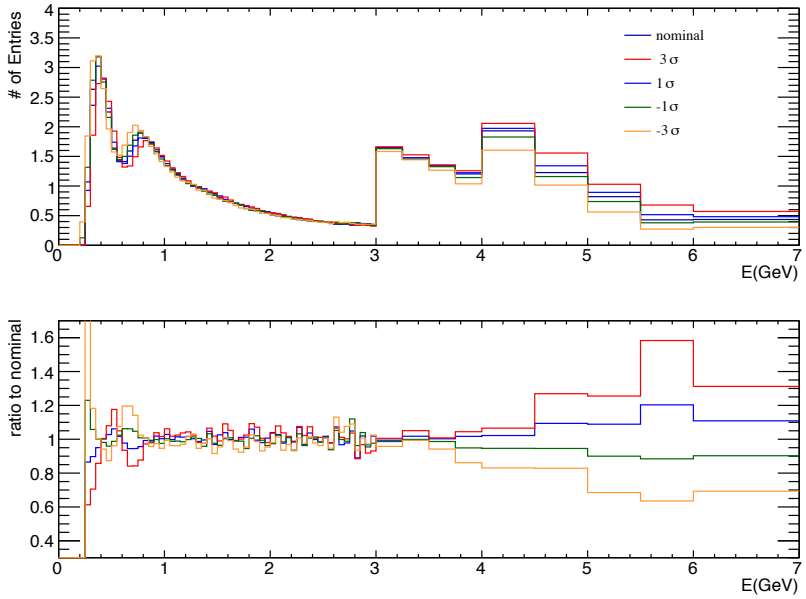

Figure D.41: Effect of Energy Scale